Tuning of Magnetic Exchange Interactions between Organic Radicals through Bond and Space

Dissertation

zur Erlangung des Grades

„Doktor der Naturwissenschaften“

am Fachbereich Chemie, Pharmazie und Geowissenschaften der

Johannes Gutenberg-Universität Mainz

vorgelegt von

Prince Ravat

geboren in Vadodara / India

Mainz, 2014

Dekan: Prof. Dr.

1. Berichterstatter: Prof. Dr.

2. Berichterstatter: Prof. Dr.

Tag der mündlichen Prüfung:

Die vorliegende Arbeit wurde in der Zeit von Juni 2011 bis Mai 2014 im Max-Planck-Institut für Polymerforschung in Mainz unter der Betreuung von Prof. Dr. Martin Baumgarten durchgeführt.

Ich danke Prof. Dr. Martin Baumgarten für seine wissenschaftliche und persönliche Unterstützung sowie für seine ständige Diskussionsbereitschaft.

Dedicated to my parents

Table of Contents

Abbreviations ..... **XI**

Chapter 1. Introduction: An Overview of Organic Radicals **1**

1.0 Prelude **2**

1.1 Appraise of different kinds of radicals **2**

1.1.1 Triphenylmethyl radical **2**

1.1.2 Nitroxide radicals **4**

1.1.3 Phenoxyl radicals **5**

1.1.4 Hydrazyl radicals **7**

1.1.5 Phenalenyl radicals **7**

1.1.6 Verdazyl radicals **8**

1.1.7 Dithiadiazolyl radicals **9**

1.1.8 "Kekulé" *versus* "Non-Kekulé" polycyclic hydrocarbons **10**

1.2 Applications of organic radicals **13**

1.2.1 Quantum computing or quantum information processing **14**

1.2.2 Organic radical batteries **15**

1.2.3 Catalysis **15**

1.2.3 Dye sensitized solar cell **16**

1.2.4 Organic Magnets-A Brief History **17**

1.3 Motivation and Objective **18**

1.3.1 Different approaches to tune the exchange interactions **20**

1.4 References **23**

Chapter 2. EPR Spectroscopy **31**

2.1 Introduction **32**

2.2 Molecules with S = 1/2 ..... **32**

2.3 Electron-Nuclear hyperfine interaction **34**

2.4 Molecules with S > 1/2 ..... **37**

2.5 Zero field splitting (*zfs*) **39**

2.6 Energy states in *zfs* **41**

2.7 Determination of *zfs* parameters *D* and *E* using EPR **42**

2.8 Ground State analysis and exchange-coupling constant (*J*) with EPR **45**

2.9 Instrumentation **46**

2.10 Summary **47**

2.11 Further reading **48**

Chapter 3. Tuning the Inter-molecular Exchange Interactions in Tolane-bridged NN Biradicals 49
3.1 Introduction 50
3.2 Synthesis of functionalized tolane bridge biradicals 51
3.3 UV-Vis analysis 54
3.4 EPR analysis 55
3.5 Crystal structure analysis 56
3.6 Magnetic measurements 59
3.7 DFT calculations 62
3.8 Coordination of NN with diamagnetic metal ion 65
3.8.1 Synthesis 65
3.8.2 Crystal Structure 65
3.8.3 Magnetic properties 68
3.9 Summary 69
3.10 Synthetic details 70
3.11 References 78

Chapter 4. Tuning the Intra-Molecular Exchange Interactions by Varying the Radical Moiety 81
4.1 Introduction 82
4.2 Synthesis 83
4.3 Optical Properties 84
4.4 Electrochemical analysis 85
4.5 Crystal structure analysis 87
4.6 EPR spectra 89
4.7 Magnetic measurements 91
4.8 DFT Calculations 94
4.9 Summary 95
4.10 Synthetic Details 95
4.11 References 99

Chapter 5. Tuning the Intra-Molecular Exchange Interactions by Synthesizing the Positional Isomers of Biradicals 101
5.1 Introduction 102
5.2 Mono radicals, 1-TMPNO and 2-TMPNO 104
5.3 Biradicals, 1,6-, 1,8- and 2,7-TMPNO 109
5.4 Tri and tetra radicals, 1,3,6-TMPNO and 1,3,6,8-TMPNO 112
5.5 Biradical 1,3-PyNO with triplet ground state 117

5.6 DFT calculations 120
5.7 Summary 123
5.8 Synthetic details 125
5.9 References 130

Chapter 6. Photo Excited High-Spin State of 2,7-TMPNO 133

6.1 Introduction 134
6.2 Synthesis 136
6.3 UV-Vis analysis 137
6.4 EPR analysis 140
6.5 Single crystal analysis 145
6.6 Magnetic measurement and DFT calculations 147
6.7 TREPR spectroscopy 149
6.8 Theoretical investigation of *zfs* parameters 155
6.9 Excited state dynamics through transient absorption spectroscopy 156
6.10 Summary 157
6.11 Synthetic details 158
6.12 References 159

Chapter 7. "Tschitschibabin type Biradicals": Benzenoid or Quinoid? .. 163

7.1 Introduction 164
7.2 Synthesis 168
7.3 Optical properties 169
7.4 EPR spectroscopy 171
7.5 Crystal structure analysis 174
7.6 DFT calculations 176
7.7 Summary 179
7.8 Synthetic details 181
7.9 References 185

Chapter 8. Positive Magneto-LC Effect in Conjugated Spin-bearing Hexabenzocoronene 189

8.1 Introduction 190
8.2 Synthesis 191
8.3 Thermotropic properties 192
8.4 EPR Spectroscopic analysis 195
8.5 Optical and electrochemical properties 197
8.6 Summary 200

8.7 Synthetic details **201**
8.8 References **204**

Appendix **207**
Appendix-I Analytical Techniques & DFT calculations **207**
Appendix-II Conversion tables **212**
Appendix-III Crystallographic tables **214**
Appendix-IV ORTEP diagrams **219**
Appendix-V Diamagnetic corrections **224**

List of Publications **231**

Curriculum Vitae **232**

Acknowledgements **233**

Symbols and Abbreviations

Symbols

a_{ij}	Hyperfine coupling constant
a_{iso}	Isotropic hyperfine coupling (Fermi contact)
a_N	Nitrogen hyperfine coupling
a_H	Proton hyperfine coupling
B_o	Applied external magnetic field tensor
$\Delta B_{1/2}$	Peak width (Full width at half maximum)
C	Curie constant
D	Zero-field splitting parameter (axial)
d_{rr}	Distance between two spins
E	Zero-field splitting parameter (rhombic)
ΔE_{ST}	Singlet-triplet energy difference
g_e	Electron g-factor, $g_e = 2.0023$
g	Observed g-value
h	Planck's constant $\hbar = h/(2\pi) = 1.0545\times10^{-34}$ J·s
H	Spin Hamiltonian
H_{Ze}	Electron-Zeeman interaction
H_{HF}	Hyperfine interaction
I	Nuclear spin angular momentum
J_{intra}	Intra-molecular spin-spin exchange coupling constant
J_{inter}	Inter-molecular spin-spin exchange coupling constant
k_B	Boltzmann constant
L	Orbital angular momentum
M	Magnetization
M_S	Magnetic quantum number
N_A	Avogadro number
S	Spin quantum number

$\hat{S}_a\hat{S}_b$	Electron-spin operators
T	Temperature
T_C	Curie temperature
T_N	Néel temperature
y	Degree of biradical character
E	Extinction coefficient ($cm^{-1}mol^{-1}$)
θ	Weiss constant
μ_B	Bohr magneton ($\beta = e\hbar/(2m_ec) = 9.2740 \times 10^{-24}\ J{\cdot}T^{-1}$)
μ_{eff}	Effective magnetic moment
v	Frequency
χ_{mol}	Molar magnetic susceptibility

Abbreviations

AF	Antiferromagnetic
AFM	Atomic force microscopy
UB3LYP	Unrestricted Becke 3-Parameter (Exchange), Lee, Yang and Parr
BEC	Bose-Einstein condensation
BHA	2,3-Dimethyl-2,3-bis(hydroxylamino)-butane
BS	Broken-symmetry
CV	Cyclic voltammetry
CW	Continuous wave
DCM	Dichloromethane
DEP	Dynamic electron polarization
DMF	N,N-dimethylformamide
DMSO	Dimethylsulfoxide
DPPH	N,N'-diphenyl-N'-picrylhydrazyl
DFT	Density functional theory
DSC	Differential scanning calorimetry
EPR	Electron paramagnetic resonance

ESR	Electron spin resonance
eV	Electron volt
FD-MS	Field desorption mass spectrometry
HBCs	Hexa-*peri*-hexabenzocoronenes
HC	Hydrocarbon
HDVV	Heisenberg-Dirac-van Vleck
HF	Hartree-Fock
hfc	Hyperfine coupling constant
HOMO	Highest occupied molecular orbital
HRMS	High resolution mass spectrometry
IN	Imino nitroxide
LUMO	Lowest unoccupied molecular orbital
M.P.	Melting point
NBMOs	Non-bonding molecular orbitals
NBS	N-bromosuccinimide
nm	Nanometer
NN	Nitronyl nitroxide
NMR	Nuclear magnetic resonance
OFETs	Organic field effect transistors
PL	Photoluminescence
QC	Quantum computing
QIP	Quantum information processing
RT	Room temperature
SOMO	Singly occupied molecular orbital
SQUID	Superconducting quantum interference device
TA	Transient absorption
TDAE	Tetrakis(dimethylamino) ethylene
TEMPO	2,2,6,6-Tetramethyl-4-piperidine-1-oxyl
TLC	Thin layer chromatography

THF	Tetrahydrofuran
TMP	4,5,9,10-Tetramethoxy pyrene
TREPR	Time-resolved EPR
UNOs	Unrestricted non-bonding orbitals
UV-Vis	Ultraviolet-visible
ZFS	Zero field splitting

CHAPTER 1 INTRODUCTION: AN OVERVIEW OF ORGANIC RADICALS

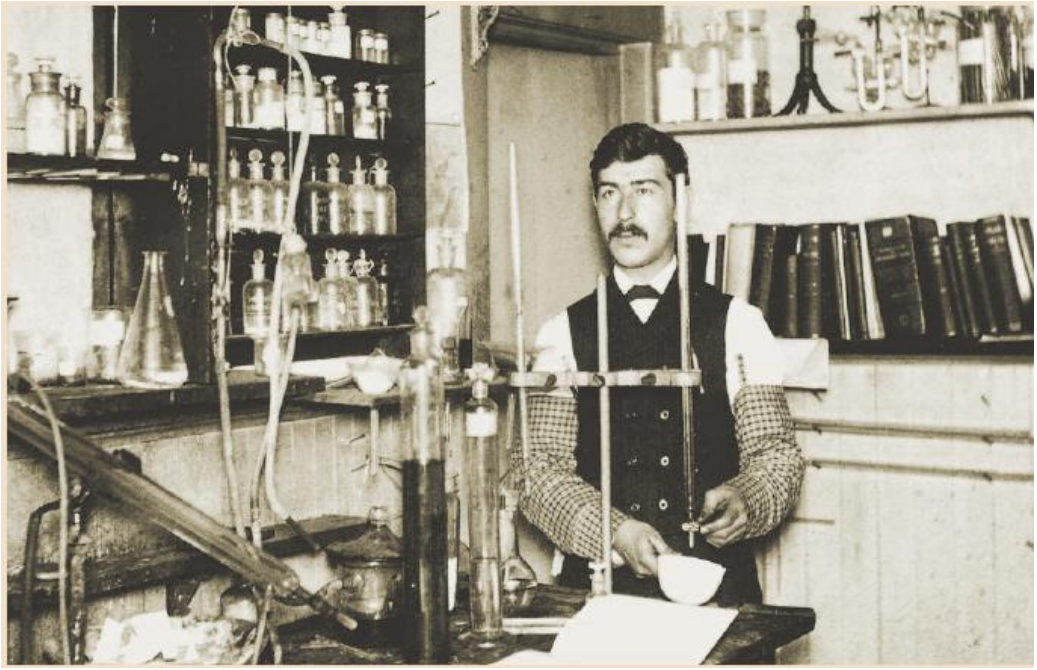

The discovery of stable radicals dates back 114 years when the first stable organic radical was synthesized by Prof. Gomberg (above photograph)[3] in 1900. Since then various types of stable organic radicals have been synthesized and utilized for various applications. This chapter starts with an overview of historical evolution of organic radicals thereafter some of their applications are discussed.

1.0 Prelude

Radicals can be defined as the molecules with at least one unpaired electron and are usually considered as highly reactive or transient species. Depending on the stability of radicals, they can be divided into (1) transient radicals- which undergo fast bimolecular self-reactions at or close to the diffusion controlled limit, (2) persistent radicals- which undergo much slower bimolecular self-reaction and slow or unimolecular decay reactions, and finally (3) stable radicals- which can be isolated, handled and stored as a pure compound for prolonged periods under normal laboratory conditions. Since the first report of stable radical in 1900 by Moses Gomberg many different classes of stable radicals were discovered.[1-3] Some of which include triphenylmethyl, phenalenyl, nitroxide, verdazyl, phenoxyls, dithiadiazolyl radicals etc.[4-7] Now the organic radicals are not only looked as molecules for studying fascinating fundamental aspects of spin coupling and exchange interactions but are also utilized for many practical applications.

1.1 Appraise of different kinds of radicals

1.1.1 Triphenylmethyl radical

The first stable organic radical Triphenylmethyl was accidently discovered in 1900 by Moses Gomberg.[1] The radical character of which was proven by its facile reaction with oxygen to form peroxide as shown in Scheme 1.1.

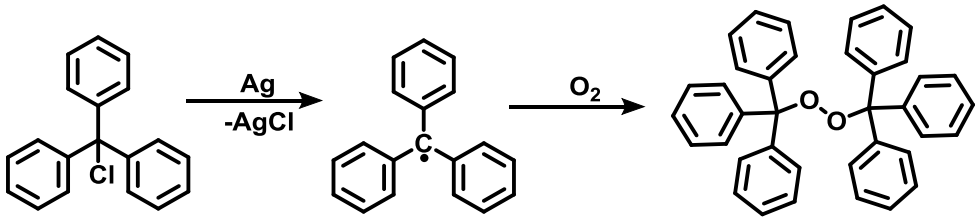

Scheme 1.1: Gomberg's synthesis of triphenylmethyl radical and its reaction with oxygen.

In Gomberg's synthesis, triphenylmethyl chloride was treated with Ag or Zn metal and a colored solution was obtained which upon oxidation yielded peroxide (Scheme 1.1).

In dilute deoxygenated solution it exists in equilibrium with its dimer (Figure 1.1). From this it was evident that the radical does not reside only on the central methyl carbon but is delocalized over the *ortho*- and *para*- positions. This was later proven by its EPR studies which showed larger hyperfine coupling for *ortho*- and *para*- hydrogen than for *meta* hydrogen.[8]

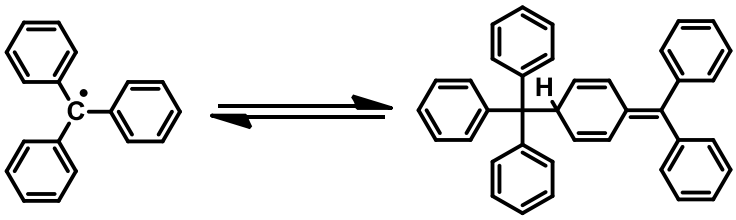

Figure 1.1: Equilibrium between triphenylmethyl radical and its dimer.

Thus in order to stabilize the triphenylmethyl radical various *ortho*- and *para*-substituted derivatives were synthesized.[9-10] The effect of substituents in stabilizing the radical was measured with EPR spectroscopy by determining the equilibrium constant for dissociation of dimers of radicals. Neumann *et al.* concluded that the captodative radicals are slightly more stable than the symmetrically disubstituted triaryls.[9]

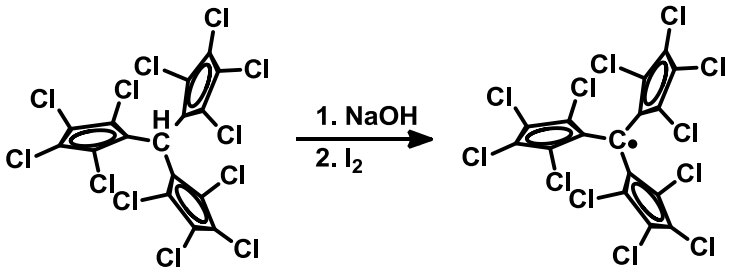

Scheme 1.2: Synthesis of perchlorotriphenylmethyl radicals.

In 1971 perchlorodiphenylmethyl and perchlorotriphenylmethyl radicals were synthesized (Scheme 1.2).[11-12] Both radicals showed high stability in air with lifetime of decades and were characterized as inert carbon free radicals. The *ortho*- chlorine atoms on the aryl rings shielded the central radical and preventing its dimerization or reaction with oxygen. Later on several other derivatives of perchlorinated triphenylmethyl

radical/biradical were synthesized and their optical, electronic, and magnetic properties have been studied extensively.[13-17]

1.1.2 Nitroxide radicals

After the discovery of the stable organic radical (triphenylmethyl), the first organic nitroxide (Figure 1.2a) was prepared by Piloty and Schwerin in 1901.[18] Half century later its radical character was elucidated by Holden *et al.* in 1951 with EPR spectroscopy.[19] The nitroxide radicals are most studied, class of stable radicals owing to very high stability of some of their derivatives with respect to air, water and other radical reactions. Later very important contribution came from Wieland *et al.*[20-21] and Mayer *et al.*[22] who synthesized diarylnitroxides (Figure 1.2b). In 1959, Lebedev *et al*. reported the synthesis of 2,2,6,6-tetramethyl-4-piperidone-1-oxyl (4-oxo-TEMPO) (Figure 1.2c), which initiated the development of TEMPO derivatives, a most widely used class of radicals as spin labels.[23-25]

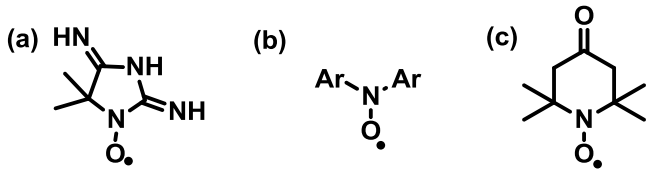

Figure 1.2: Structure of nitroxides.

In general nitroxide radicals can be classified as compounds containing >N—O· group, which has one unpaired electron. The π_{N-O} bond results from the overlapping of $2p_z$ orbitals of nitrogen and oxygen; it can be represented as following resonance structure (Scheme 1.3).[23] The spin density in nitroxide radicals mainly reside on nitrogen and oxygen atoms, but slightly higher on oxygen.

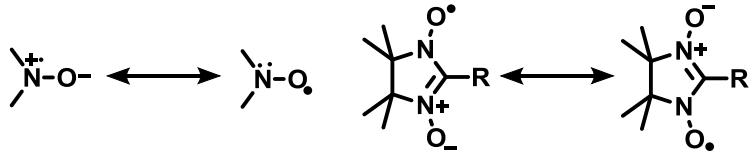

Scheme 1.3: Resonance delocalization of nitroxide and nitronyl nitroxide radical.

The chemistry of nitronyl nitroxides, the resonance delocalized nitroxide radical, was developed by Ullman *et al.*[26] Ullman's synthesis of nitronyl nitroxide involves condensation of aldehyde with bishydroxylamine followed by oxidation with lead oxide (Scheme 1.4). Same as in the nitroxides the spin density of nitronyl nitroxide also reside mainly on oxygen and nitrogen atom and very little spin density on the substituent R because of the presence of a nodal plane in π SOMO. Nitronyl nitroxides satisfy the prerequisite for stable nitroxide (i.e. no α-hydrogen) and thus can be synthesized with a large variety of R groups.[27-29]

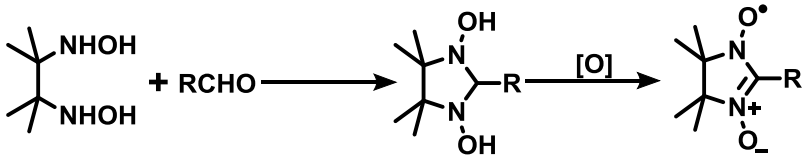

Scheme 1.4: Ullman's synthesis of nitronyl nitroxide.

Benzonitronyl nitroxide was first isolated in crystalline form by Tamura *et al.* in 1997.[30-31] Although this class of nitronyl nitroxide shows spin delocalization onto the annelated ring and adopts planar topology for strong intermolecular interactions, did not yet receive much attention.[32]

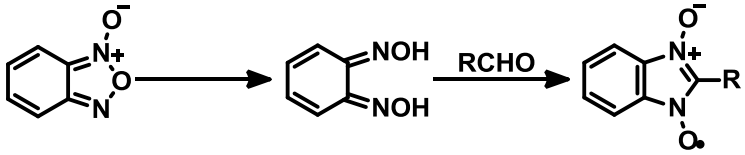

Scheme 1.5: Synthesis of benzo nitronyl nitroxide.

1.1.3 Phenoxyl radicals

Phenoxyls are a venerable class of radicals. Although the phenoxyl radicals were introduced by Plummer in 1914,[33] their existence by EPR was first demonstrated in 1960s.[34] Phenoxyls are electron deficient compounds, which make them highly reactive. The stabilization of phenoxyl radicals can be achieved by substituting bulky functional

group at *ortho*- and *para*- positions. This could be understood by considering following canonical forms (Figure 1.3). Computational studies suggested that spin density at oxygen atom is slightly higher than for *ortho*- and *para*- carbon atoms.[35] Studies by Lahti *et al.* showed that electron rich substituents at *para* position can possess as much spin density as the parent phenoxyl residue itself.[36] Reichard *et al.* proposed the generation of radicals related to phenoxyls can be from the mono-electronic oxidation of phenolic side chains of tyrosine in proteins and thus may be involved in some biological process. These residues are designated as tyrosyl.[37-38]

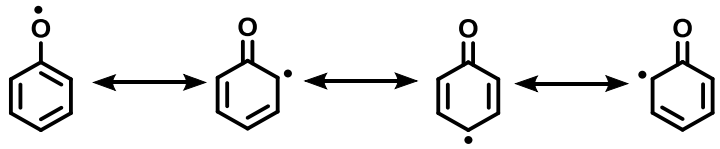

Figure 1.3: Resonance structure of phenoxyl radical.

The galvinoxyl radical also known as Coppinger's radical was synthesized in 1957,[39] and is of very special interest because of its exceptionally high stability and unusual magnetic properties.[40-41] Theoretical studies showed that, similar to simple phenoxyls there has been substantial spin density at *para* carbon atoms, thus it can be represented as two canonical forms (Figure 1.4).[42]

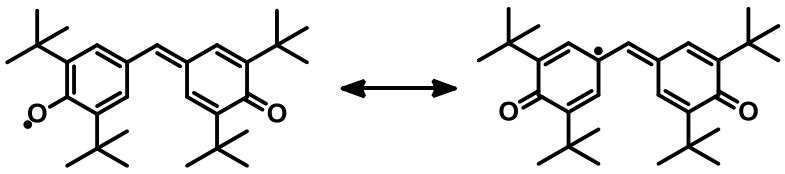

Figure 1.4: Galvinoxyl radical.

Another interesting molecule of this class is Yang's biradical prepared in 1960.[43] This biradical exist in triplet ground state. Nearly 50 % of spin density lies on three carbons attached to the central carbon, thus the Yang's biradical can be categorized as delocalized version of trimethylenemethane, prototypical triplet organic biradical (Figure 1.5).[44-45]

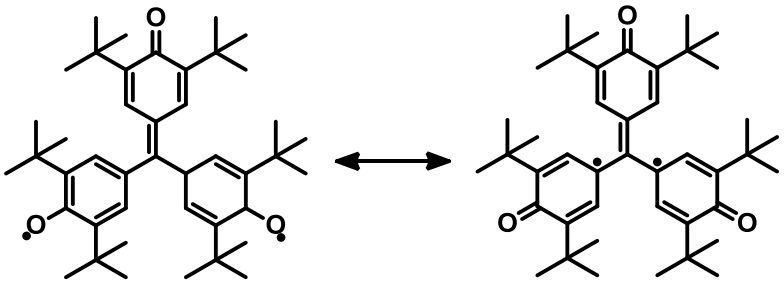

Figure 1.5: Yang's biradical.

1.1.4 Hydrazyl radicals

The hydrazyl radicals were discovered in 1922 by Goldschmidt.[2] While most of the hydrazyl radicals fall into the class of persistent radical, only few qualify as stable. One of the most stable derivatives of hydrazyl radical is DPPH (*N,N'*-Diphenyl-*N'*-picrylhydrazyl) (Figure 1.6). Most of the stable radicals of this class resemble the structure of DPPH. Owing to exceptional stability and selective reactivity of DPPH it has been extensively used as (1) standard for the EPR spectroscopy (g-marker, g = 2.0037), (2) radical scavenger in polymer chemistry, and (3) as an indicator for antioxidant chemistry.[46-47]

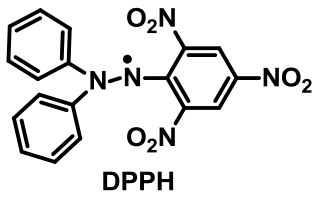

Figure 1.6: *N,N'*-Diphenyl-*N'*-picrylhydrazyl (DPPH) radical.

1.1.5 Phenalenyl radicals

The entire family of phenalenyl and higher analogous derivatives are known as non-Kekulé polynuclear benzenoid molecules and can be considered as triangular open-shell graphene fragments.[48] The first phenalenyl radical was prepared by Reid and Calvin independently in 1950s from the phenalene oxidation.[49-50] This radical was very sensitive

to air and in equilibrium with sigma dimer which further undergoes decomposition to yield highly fused polyaromatic hydrocarbon (Scheme 1.6).[49]

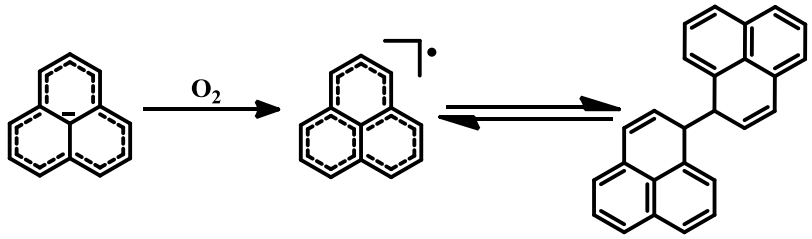

Scheme 1.6: Synthesis of phenalenyl radical and its equilibrium with a sigma dimer.

Computational studies have shown that although the spin density of the phenalenyl molecule is delocalized throughout the molecule, it mainly resides on six α-carbon atoms i.e. the periphery of molecule as shown in the resonance structure (Figure 1.7). Thus substituent at the edges will effectively tune the electron spin distribution.

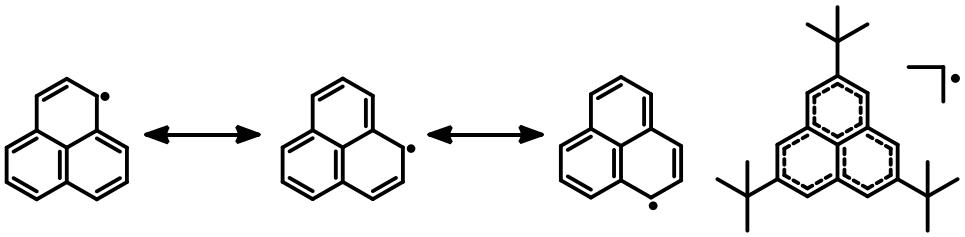

Figure 1.7: Resonance structure of phenalenyl radical and structure of 2,5,8-tri-*tert*-butyl-phenalenyl radical.

The first stable neutral phenalene derivative was synthesized by Nakasuji *et al*.[51] Substitution of *tert*-butyl group at *β*-positions (2,5,8-positions) of phenalenyl effectively prevented the sigma dimerization and gave stable product which forms π-dimer. The magnetic susceptibility measurements showed a large antiferromagnetic exchange interaction, indicating spin singlet ground state of π-dimer.[52]

1.1.6 Verdazyl radicals

The verdazyl radicals can be considered as the resonance delocalized class of

hydrazyl radicals. Richard Kuhn and H.Trischmann in 1963 reported the surprisingly stable nitogenous free radical *i.e.* Verdazyl radical.[53-54] Verdazyls are 7π-cyclic radicals with π-SOMOs, the nodal plane in this orbital passes through C6 and C3 carbon preventing the delocalization, but not the polarization, onto C-substituents (Figure 1.8a). In following years Neugebauer *et al.* developed the synthesis of two new kinds of verdazyl radicals, 3-phenyl-1,5-dimethyl-6-oxo- or thioxo- verdazyl (Figure 1.8b) in 1988,[55] and 1,3,5-triphenyl-6-oxo- or thioxo- verdazyl (Figure 1.8c) radicals in 1993,[56] the later radicals have higher stability than the former ones. Recently 1,5-diisopropyl substituted oxo-verdazyl radical derivatives were also synthesized.[57] The *N*-isopropyl derivatives were found to be more stable than the N-methyl substituted derivatives.

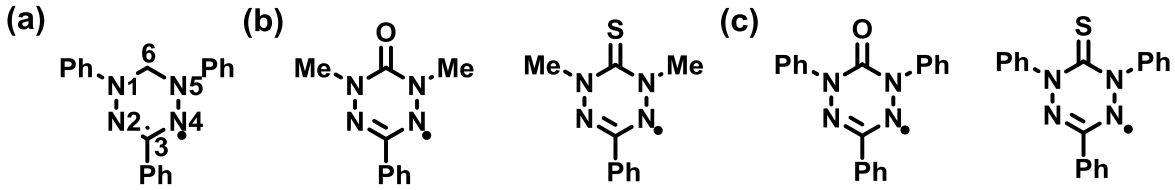

Figure 1.8: Verdazyl and 6-oxo- or 6-thioxo- verdazyl radicals.

Now the verdazyls can be characterized into two types depending on the nature of C6 carbon, (i) saturated carbon at C6 developed by Kuhn *et al.*,[53] and (ii) oxo- or thioxo group at C6 developed by Neugebauer *et al*.[55-56]

1.1.7 Dithiadiazolyl radicals

One of the most studied heterocyclic thiazyl radicals, 1,2,3,5-dithiadiazolyls, were first discovered in 1970s.[58-59] Synthesis of 1,2,3,5-dithiadiazolyl radicals always proceeded through the corresponding intermediate, dithiadiazolium cation, as shown in Scheme 1.7. The reduction of dithiadiazolium cation with metals or organo-metallic reagents or reducing anions gave corresponding 1,2,3,5-dithiadiazolyl radicals. Usually they are stable in oxygen free solution and in solid state. They show extremely high

thermal stability, as they are mostly purified by high vacuum sublimation.[60]

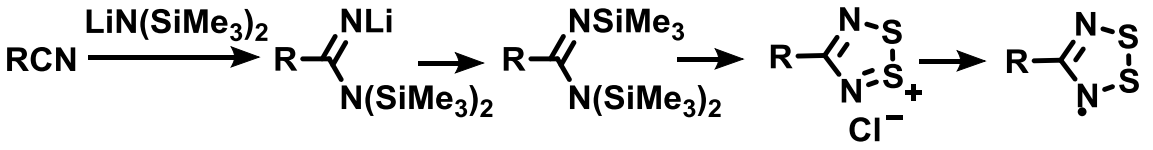

Scheme 1.7: General procedure for synthesis of 1,2,3,5-dithiadiazolyl radical.

In solution 1,2,3,5-dithiadiazolyl radicals are in equilibrium with dimers and nearly all the derivatives of these radicals adopt π-dimeric structures in solid state. A large number of 1,2,3,5-dithiadiazolyl radicals with different substituents have been structurally characterized by single crystal X-ray crystallography. Depending on the steric influence of substituent R as shown in Figure 1.9 mainly four different kinds of π-dimers are observed.[61-62]

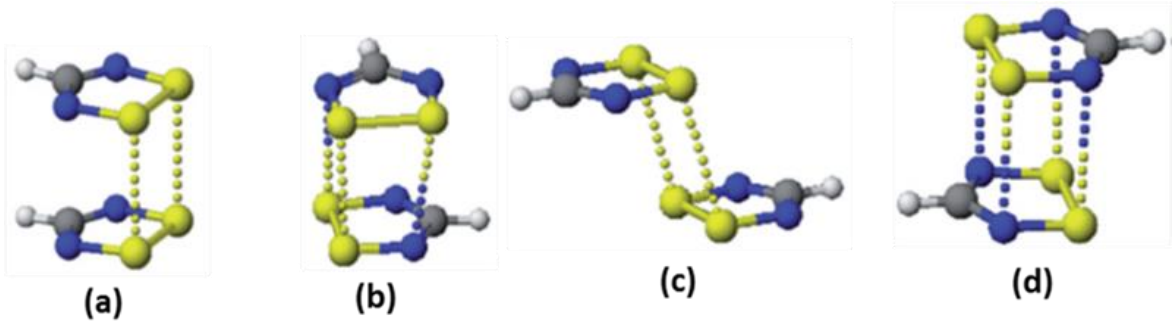

Figure 1.9: Different structural motifs of π-dimers of 1,2,3,5-dithiadiazolyl radicals (a) *cis-cofcial* (b) twisted (c) *trans-antrafacial* (d) *trans-cofacial* (blue: nitrogen, yellow: sulfur, gray: carbon) (Figure adopted from ref[61]).

1.1.8 "Kekulé" *versus* "Non-Kekulé" polycyclic hydrocarbons

Polycyclic conjugated biradicals can be divided into two parts, Kekulé and non-Kekulé biradicals. The simplest examples of Kekulé and non-Kekulé structures are *ortho*- or *para*- xylene and *meta*-xylene, respectively. While *meta*-xylene can only be drawn as biradical structure, the *ortho*- or *para*-xylene can be drawn as biradicaloid as well as quinonoid form (Figure 1.10).[63]

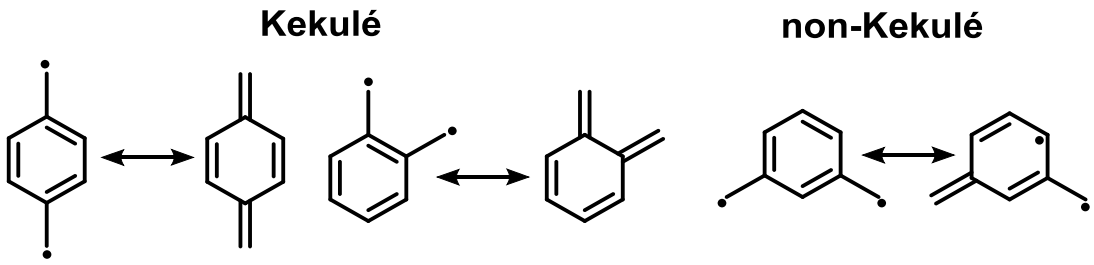

Figure 1.10: Kekulé versus non-Kekulé biradical structure.

Non-Kekulé molecules are conjugated hydrocarbons with two or more formal radical centers. Non-Kekulé biradicals can be classified into non-disjoint and disjoint depending on the shape of their two non-bonding molecular orbitals (NBMOs) (Figure 1.11).[64]

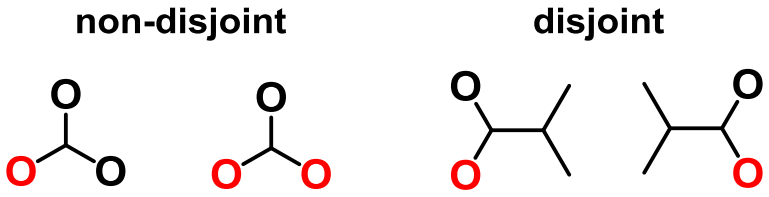

Figure 1.11: NBMOs of non-disjoint and disjoint non-Kekulé molecules.

Both NBMOs of molecules with non-disjoint characteristics such as trimethylenemethane have electron density at the same atom. According to Hund's rule, each orbital is filled with one electron with parallel spin, avoiding the Coulomb repulsion by filling one orbital with two electrons. Therefore, such molecules with non-disjoint NBMOs are expected to prefer a triplet ground state. In contrast, the NBMOs of the molecules with disjoint characteristics such as tetramethyleneethane can be described without having electron density at the same atom. With such MOs, the destabilization factor by the Coulomb repulsion becomes much smaller than for non-disjoint type molecules, and therefore the relative stability of the singlet ground state to the triplet ground state will be nearly equal, or even reversed because of the exchange interaction.[65-66]

The classical and most extensively discussed example Kekulé biradical is Tschitschibabin's biradical (Figure 1.12a), synthesized in 1907.[67-68] Non-Kekulé polynuclear aromatic hydrocarbons were proposed by Eric Clar in 1941. The simplest member of this class is triangulene. All the attempts to synthesize triangulene (Figure 1.12b) by Clar *et al.* failed.[69-70] The first polynuclear non-Kekulé structure, trioxotriangule (Figure 1.12c) was synthesized in 1995 by Bushby *et al*.[71-72]

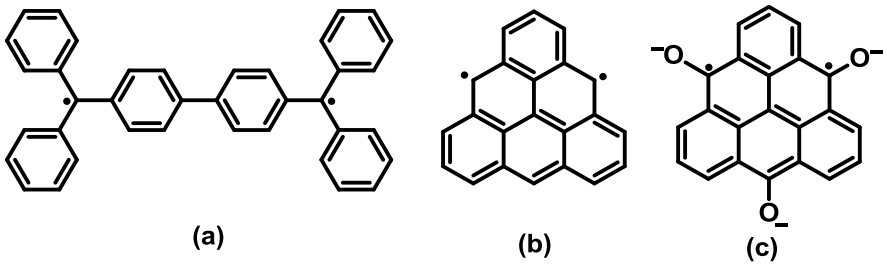

Figure 1.12: Tschitschibabin's and Clar's hydrocarbons.

	Historical overview of organic radicals	
Year	**Research group**	**Discovery**
1900	Moses Gomberg	Triphenylmethyl radical- first stable organic radical[1]
1901	Piloty and Schwerin	Synthesis of first organic nitroxide radical[18]
1907	Tschitschibabin	Synthesis of Tschitschibabin's biradical[68]
1914	Plummer *et al.*	Discovery of phenoxyl radicals[4]
1922	Goldschmidt *et al.*	Synthesis of DPPH-first hydrazyl based radical[7]
1957	Reid and Cavin	First phenalenyl radical reported[47, 50]
1959	Lebedev *et al.*	Synthesis of 4-oxo-TEMPO-gave birth to TEMPO derivatives, most widely used radical[23]
1963	Richard Kuhn and Trischmann	Nitrogeneous free radical (verdazy) reported
1968	Ullman *et al.*	First synthesis of nitronyl nitroxide[26]
1971	Donald Cram *et al.*	Perchlorotriphenylmethyl radical-inert carbon free radical[11]
1974	Banister et al.	The structure of first DTDA radical salt was elucidated[58]
1995	Bushby *et al*.	Synthesis of first Clar's hydrocarbon derivative[71]

1.2 Applications of organic radicals

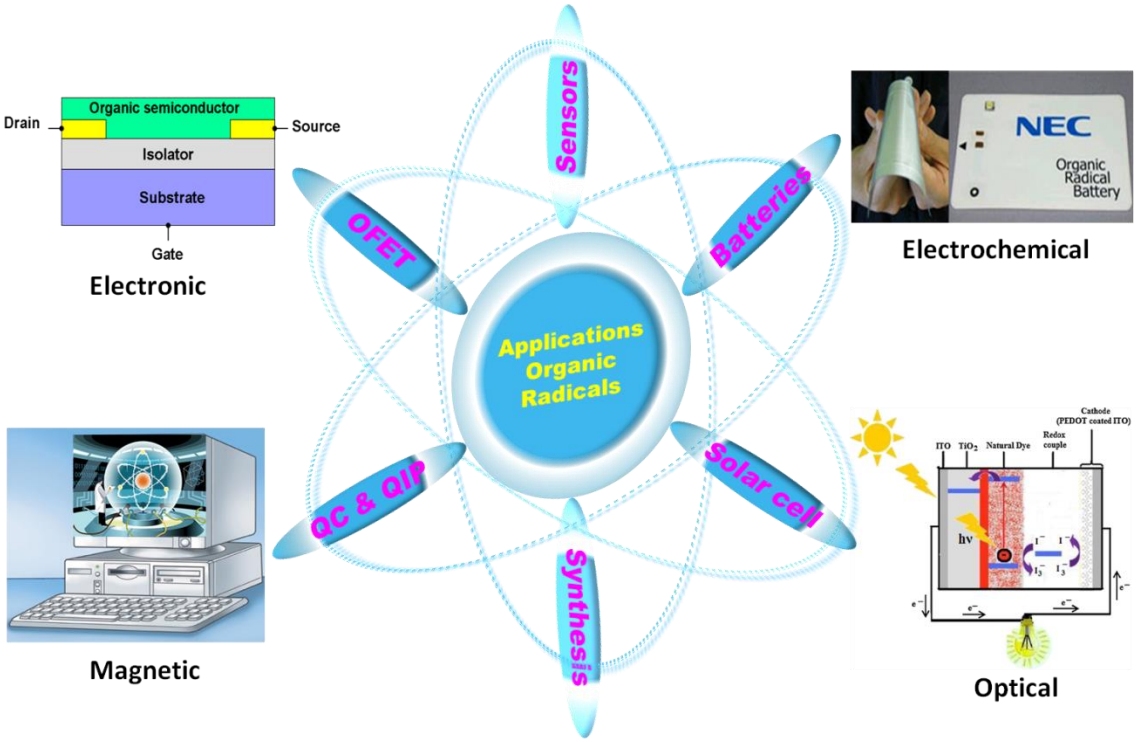

Figure 1.13: Some of the applications of organic radicals.

In last two decades stable organic radicals (open shell molecules) have attracted large attention of researchers from both fundamental and applied aspects because they showed unique structural electronic properties and spin nature based functionalities that are intrinsically different from closed-shell molecules.[4-5, 7] Radicals can act as donors or acceptors and/or redox active centers. These are the desirable requirements for molecule based materials. Organic materials are expected to be easy processible, light weight, soluble in organic solvents, and/or optically transparent. Organic radicals have shown potential variety of applications in catalysis,[73-74] organic field effect transistors (OFETs),[75-77] sensors,[78] magneto conducting materials,[79] dye sensitized solar cells,[80-81] photo excited spin systems,[82-83] quantum magnets,[84] and batteries.[48, 85] They also have been used as ligand to form metal-organic complexes with transition metals and observed ferromagnetism, ferrimagnetism or anti-ferromagnetism.[86-87] Some examples of organic

radicals showing practical applications are discussed as follows.

1.2.1 Quantum computing or quantum information processing

The most fascinating applications of organic radicals is in the development of Quantum computers.[88-89] Today's computers, like a Turing machine, work by manipulating bits that exist in one of two states, 0 or 1. Quantum computers aren't limited to two states; they encode information as quantum bits, or qubits, which can exist in superposition. Qubits represent atoms, ions, photons or electrons and their respective control devices that are working together to act as computer memory and processor. Because the quantum computer can contain these multiple states simultaneously, it has the potential to be millions of times more powerful than today's most powerful supercomputers. The quantum algorithms can reduce the CPU time by many orders of magnitude.[90-92]

Although in last decade the field of quantum computing (QC) or quantum information processing (QIP) developed rapidly the latest arrivals are the molecular qubits which links between both QC and chemistry. The existing qubits faces the problem of stability and scalability. The electron spin qubits have an advantage over nuclear spin qubits in the preparation of initialized states. This is because the gyromagnetic ratio for nuclear spin is 10^3 times smaller than that of electron spin which leads to low polarization of spin.[93-94]

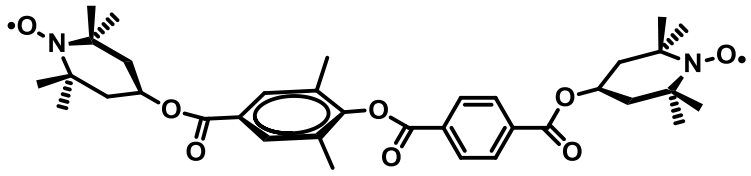

Figure 1.14: Biradical as a synthetic electron spin two-qubit system.

Takui *et al.* reported the two-qubit weakly coupled biradical (Figure 1.14) as fundamental unit for constructing QC which can afford Controlled-NOT (CNOT) gate operations.[95] CNOT gate operations are essentially important gates to constitute a

universal set of quantum gates together with well-defined single qubit operation.

1.2.2 Organic radical batteries

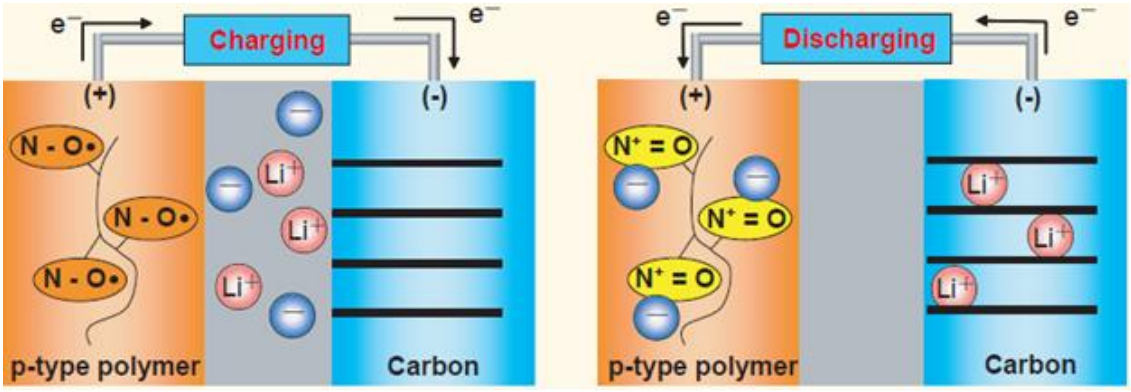

Figure 1.15: A lithium-ion battery based on a radical polymer cathode (Figure adopted from ref[96]).

One of the most studied applications of organic radical is their utilization as a cathode and/or anode materials in batteries (Figure 1.15). Their excellent electrochemical properties makes them ideal candidate as electrode active material for rechargeable batteries. While the nitroxide and phenoxyl radicals are used as p-type and n-type electrode material, respectively, the nitronyl nitroxide can serve as ambipolar material for constructing all organic batteries.[97] Recently organic radical or organic radical polymer based batteries with excelling charge-discharge capacity and cyclic stability exceeding that of Li-ion batteries have been reported.[98-101]

1.2.3 Catalysis

Nitroxides are found to be chemo/stereo selective organo-catalyst in several alcohol oxidation reactions of industrial application. Nitroxide catalyzed reactions are used for the oxidation of primary and secondary alcohols to aldehydes or carboxylic acids and ketones, respectively, in the presence of large functional groups. The observed chemoselectivity is mainly based on the relative oxidation rates. The large number of such

examples can be found in the literature.[74]

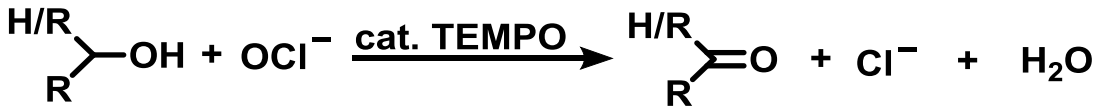

Scheme 1.15: TEMPO as organo-catalyst for oxidation of alcohols.

1.2.4 Dye sensitized solar cell

Recently Nishide *et al.* reported the significant enhancement in conversion efficiency of dye sensitized solar cell (DSSC) by using stable radical 2-azaadamantan-*N*-oxyl as highly reactive redox mediator (Figure 1.16).[81, 102] The increased conversion efficiency of DSSC can be attributed to high reactivity and yet reversible redox behavior of nitroxide radicals which dramatically enhanced the charge diffusion, electrode reaction rate, and the photovoltaic performance.

Moreover Vardeny *et al.* used 3 % doping of spin 1/2 galvinoxyl radical in P3HT/PCBM solar cell, which improved solar cell efficiency by 18 %. The enhanced organic photovoltaic solar cell efficiency was attributed to suppressed polaron pair recombination at the donor-acceptor domain interfaces by doping with galvinoxyl radical.[80]

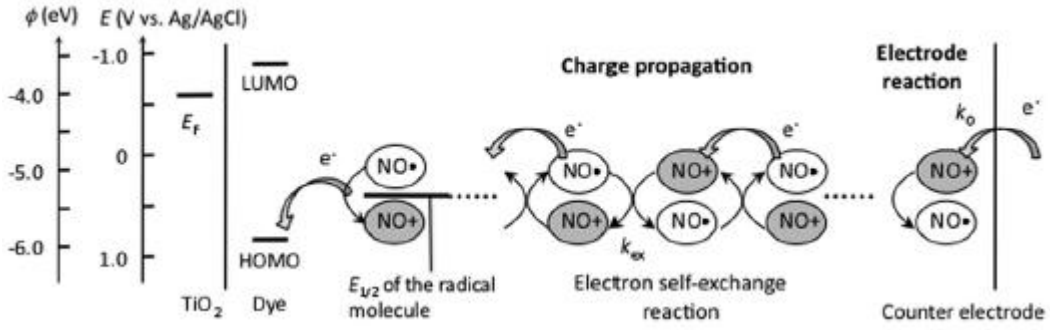

Figure 1.16: Redox mediation process with nitroxide radical redox couple in a DSSC(Figure adopted from ref[80]).

1.2.5 Organic Magnets-A Brief History

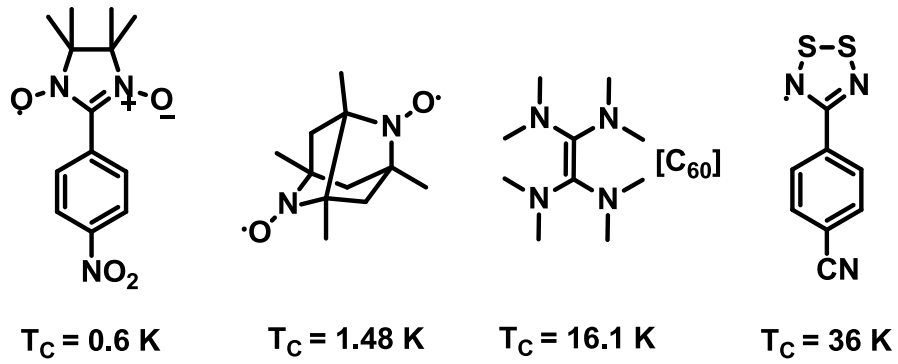

Figure 1.17: Organic magnets and ordering temperature.

Organic magnets can be defined as the materials exhibiting bulk magnetic ordering and possessing unpaired electron spin residing in p-orbitals that contribute to magnetic ordering.[7, 103-105] This is contradictory to Heisenberg's prediction in 1928 that the ferromagnetic long range order in an infinite lattice can be found only when it contains the heavy (metallic) element.[106] Later in 1963 theoretician McConnell derived the mechanism for ferromagnetic interaction between organic radicals containing atoms only from the first raw of periodic table.[107] After three decades the first of such material was found in 1991, p-nitrophenyl nitronyl nitroxide, which has critical temperature of 0.6 K (Figure 1.17).[108] Soon after 2 years Chiarelli *et al.* found nitroxide biradical showing ferromagnetic transition at 1.48 K.[109] This area of research became more promising when fullerene derivative [TDAE]-[C_{60}], was reported to show ferromagnetic ordering temperature as high as 16 K.[110] The highest reported ferromagnetic ordering temperature for a purely organic magnet is 36 K for β-phase of the dithiadiazolyl radical.[111] The inter-molecular interactions between unpaired electrons from different radicals is a necessary requirement for obtaining long range magnetic ordering in solid state.

In this chapter up to here different types of stable radicals, their properties were discussed and finally a few of their applications were shown. In the next part of the

chapter the motivation and outline of PhD thesis is presented.

1.3 Motivation and Objective

Stable neutral organic biradicals are of special interest because they offer the possibility to tune the magnetic interactions through appropriate design of a spacer.[4, 7, 112] Thus, by considering the topological rules of physics and at the same time employing the advanced methods of organic chemistry, molecules with predictable magnetic properties can be synthesized.[63, 113] Among the biradical family, antiferromagnetically (AF) coupled species can be considered as a source of interacting bosons.[114-115] Consequently, such biradicals can serve as molecular models of a gas of magnetic excitations which can be used for quantum computing (QC) or quantum information processing (QIP).[91-95, 116-117] Notably, initial small triplet state population in weakly AF coupled biradicals can be switched into larger in the presence of applied magnetic field. Such biradical systems are promising molecular models for studying the phenomena of magnetic field-induced Bose-Einstein condensation (BEC) in the solid state (Figure 1.18).[118-119]

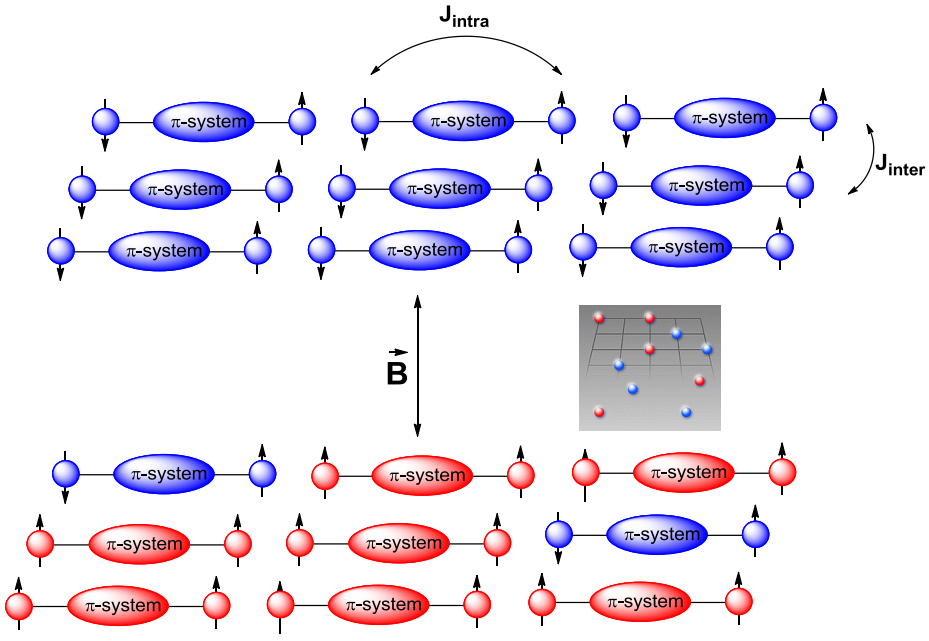

Figure 1.18: Schematic representation of magnetic field induced quantum phase transition.

"The understanding of BEC under various and sometimes extreme conditions is the heart of cooperative "Sonderforschungsbereich/Transregio-49" (SFB/TR-49) project between Frankfurt, Mainz, and Kaiserslautern."

To observe such phenomena it is very important to control intra as well as inter-molecular magnetic exchange interactions. The intra-molecular magnetic exchange interactions can be tuned by either changing the length of the π-spacer molecule carrying the radical moieties or by changing the radical moiety while maintaining the same π-spacer.[84, 120-121] The inter-molecular magnetic exchange interactions, which usually operate through hydrogen bond or other short inter-molecular contacts, highly depends on the crystal packing and are quite difficult to predict or control.[122-123] To some extent the inter-molecular magnetic exchange interactions can be regulated by employing the crystal engineering approach.[124-128] For instance, introduction of hydrogen bond donor or acceptor (or a combination of both) functional groups in the π-spacer fragment can result in additional hydrogen bonding, which in turn is advantageous for smooth transmission of magnetic interactions through the lattice. As a result multi-dimensional spin-networks can be constructed.

1.3.1 Different approaches to tune intra- and inter-molecular exchange interactions

In our laboratory we have utilized different approaches to tune inter- and intra-molecular exchange interactions as follows,

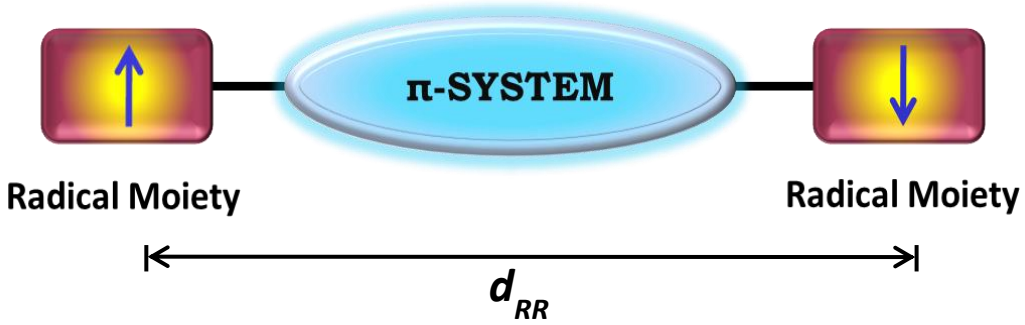

Scheme 1.16: Schematic representation of AF coupled biradical system; d_{RR} is the distance between two spin-centers.

Approach 1: Varying the length of the π-system- using this approach intra-molecular exchange interaction can be tuned predictably.

This is the most utilized approach to tune the intra molecular exchange interactions.[129-134] The experimental and theoretical investigation suggests that in nitronyl nitroxide radicals the electron spin-density is partially delocalized over the radical moiety. The magnetic exchange interactions between two radical moieties usually depend on the length and nature of the π-spacer. As shown in Table 1 bisnitronyl nitroxide (**1**) possesses the strongest intra-molecular antiferromagnetic exchange interaction among the nitronyl nitroxide biradical family. On moving from biradical **1** to **5** the exchange interaction decreases drastically from -923.0 K to -2.4 K by varying the spacer length from 0.15 nm to 1.45 nm. By introducing longer spacer unit the distance between localized spin centers increases leading to decrease in spin-spin interaction. Thus using this approach tuning of intra-molecular exchange interaction is achieved. The limitation of this approach is the very large change in interactions and fine tuning of

exchange interaction could not be obtained due to synthetic limitations.

Table 1: List of biradicals with their intra-molecular exchange interaction values.

Biradicals	d_{RR} **(nm)**	**Intra-molecular exchange interaction**
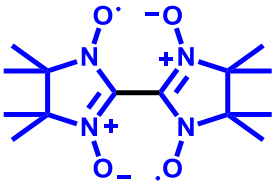 **(1)**	0.15	-923.0 K[129, 132]
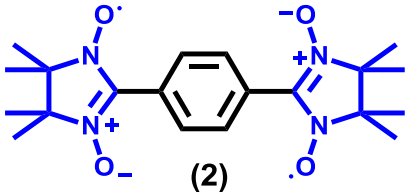 **(2)**	0.57	-72.3 K[130]
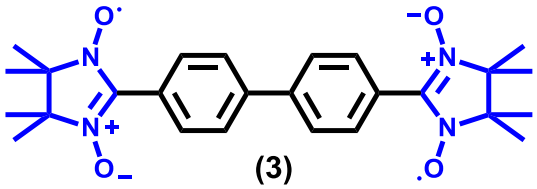 **(3)**	1.01	-14.0 K[84]
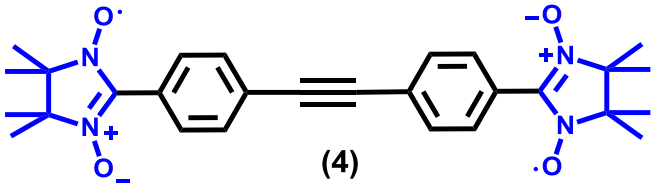 **(4)**	1.24	-4.6 K[121]
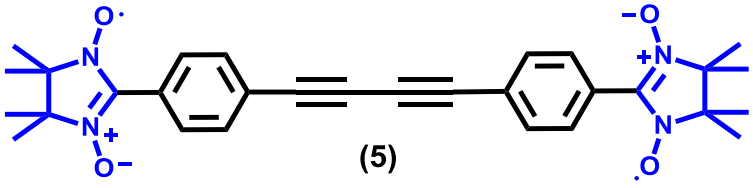 **(5)**	1.45	-2.4 K[121]

Looking forward in this direction during the course of my dissertation, different other approaches have been studied to tune intra- as well as inter-molecular exchange

interactions which are summarized in the forth coming chapters.

Approach 2: Functionalization of π-spacer- by this approach inter-molecular exchange interactions can be altered. (Discussed in chapter 3)

Approach 3: Complex formation with diamagnetic metal ion- this approach is also utilized to alter inter-molecular exchange interactions. (Discussed in chapter 3)

Approach 4: Varying the radical moiety- this is a novel approach to tune inter-molecular exchange interaction, as here the π-spacer is maintained the same. (Discussed in chapter 4)

Approach 5: Synthesizing positional isomers- in this approach the π-spacer and radical moieties were maintained and exchange interaction tuned by changing the position of radical moiety on the π-spacer. (Discussed in chapter 5)

Furthermore during our study on tuning of intra- and inter-molecular exchange interactions utilizing various approaches as mentioned above we have found the molecules 2,7-TMPNO and BPNO which exist in semi-quinoid form and exhibit exceptionally stronger magnetic exchange interactions.

2,7-TMPNO possesses the singlet-triplet energy gap of ΔE_{ST} = –1185 K. So it is nearly unrealistic to observe the magnetic field induced spin switching. So we planned to study the spin switching of this molecule by photo-excitation. (Discussed in chapter 6)

The similarity of molecule BPNO with Tschitschibabin's HC allowed us to dig discrepancies related to ground state of Tschitschibabin's HC. (Discussed in chapter 7)

Finally in chapter 8 the synthesis and characterization of neutral paramagnetic HBC derivative (HBCNO) is discussed. The magneto liquid crystalline properties of HBCNO were studied by DSC and EPR spectroscopy.

1.4 References

[1] M. Gomberg, *J. Am. Chem. Soc.* **1900**, *22*, 757.

[2] S. Goldschmidt, K. Renn, *Berichte der deutschen chemischen Gesellschaft (A and B Series)* **1922**, *55*, 628.

[3] http://bentley.umich.edu/exhibits/tappan/panel8.php.

[4] R. G. Hicks, in *Stable Radicals: Fundamentals and Applied Aspects of Odd-Electron Compounds*, John Wiley & Sons, NewYork, **2010**.

[5] Gertz I. Likhtenshtein, Jun Yamauchi, Shin'ichi Nakatsuji, Alex I. Smirnov, a. R. Tamura, in *Nitroxides Applications in Chemistry, Biomedicine, and Materials Science*, WILEY-VCH Verlag GmbH & Co. KGaA, Weinheim, **2008**.

[6] R. G. Hicks, *Org. Biomol. Chem.* **2007**, *5*, 1321.

[7] T. L. Makarova, F. Palacio, in *Carbon Based Magnetism* (Eds.: T. Makarova, F. Palacio), Elsevier, Amsterdam, **2006**.

[8] A. H. Maki, R. D. Allendoerfer, J. C. Danner, R. T. Keys, *J. Am. Chem. Soc.* **1968**, *90*, 4225.

[9] W. P. Neumann, A. Penenory, U. Stewen, M. Lehnig, *J. Am. Chem. Soc.* **1989**, *111*, 5845.

[10] W. P. Neumann, W. Uzick, A. K. Zarkadis, *J. Am. Chem. Soc.* **1986**, *108*, 3762.

[11] D. J. Cram, J. N. Roitman, *J. Am. Chem. Soc.* **1971**, *93*, 2225.

[12] M. Ballester, *Acc. Chem. Res.* **1985**, *18*, 380.

[13] N. r. Crivillers, S. Furukawa, A. Minoia, A. Ver Heyen, M. Mas-Torrent, C. Sporer, M. Linares, A. Volodin, C. Van Haesendonck, M. Van der Auweraer, R. Lazzaroni, S. De Feyter, J. Veciana, C. Rovira, *J. Am. Chem. Soc.* **2009**, *131*, 6246.

[14] N. Crivillers, M. Mas-Torrent, J. Vidal-Gancedo, J. Veciana, C. Rovira, *J. Am. Chem. Soc.* **2008**, *130*, 5499.

[15] O. Armet, J. Veciana, C. Rovira, J. Riera, J. Castaner, E. Molins, J. Rius, C. Miravitlles, S. Olivella, J. Brichfeus, *The Journal of Physical Chemistry* **1987**, *91*, 5608.

[16] L. Teruel, L. Viadel, J. Carilla, L. Fajarí, E. Brillas, J. Sañé, J. Rius, L. Juliá, *J. Org.*

Chem. **1996**, *61*, 6063.

[17] N. Crivillers, M. Mas-Torrent, S. Perruchas, N. Roques, J. Vidal-Gancedo, J. Veciana, C. Rovira, L. Basabe-Desmonts, B. J. Ravoo, M. Crego-Calama, D. N. Reinhoudt, *Angew. Chem. Int. Ed.* **2007**, *46*, 2215.

[18] O. Piloty, B. G. Schwerin, *Chem. Ber.* **1901**, *34*, 1870.

[19] A. N. Holden, W. A. Yager, F. R. Merritt, *J. Chem. Phys.* **1951**, *19*, 1319.

[20] H. Wieland, M. Offenbächer, *Chem. Ber.* **1914**, *47*, 2111.

[21] A. R. Forrester, R. H. Thomson, *Nature* **1964**, *203*, 74.

[22] K. H. Meyer, W. Reppe, *Berichte der deutschen chemischen Gesellschaft (A and B Series)* **1921**, *54*, 327.

[23] E. G. Rozantsev, V. D. Sholle, *Synthesis* **1971**, *1971*, 190.

[24] E. G. Rozantsev, V. D. Sholle, *Synthesis* **1971**, *1971*, 401.

[25] J. F. W. Keana, *Chem. Rev.* **1978**, *78*, 37.

[26] J. H. Osiecki, E. F. Ullman, *J. Amer. Chem. Soc.* **1968**, *90*, 1078.

[27] D. G. B. Boocock, R. Darcy, E. F. Ullman, *J. Amer. Chem. Soc.* **1968**, *90*, 5945.

[28] D. G. B. Boocock, E. F. Ullman, *J. Amer. Chem. Soc.* **1968**, *90*, 6873.

[29] R. W. Kreilick, J. Becher, E. F. Ullman, *J. Amer. Chem. Soc.* **1969**, *91*, 5121.

[30] Y. Kusaba, M. Tamura, Y. Hosokoshi, M. Kinoshita, H. Sawa, R. Kato, H. Kobayashi, *J. Mater. Chem.* **1997**, *7*, 1377.

[31] A. Zakrassov, V. Shteiman, Y. Sheynin, B. Tumanskii, M. Botoshansky, M. Kapon, A. Keren, M. Kaftory, T. E. Vos, J. S. Miller, *J. Mater. Chem.* **2004**, *14*, 1827.

[32] T. E. Gough, R. Puzic, *Journal of Magnetic Resonance (1969)* **1976**, *23*, 31.

[33] R. Pummerer, F. Frankfurter, *Chem. Ber.* **1914**, *47*, 1472.

[34] E. R. Altwicker, *Chem. Rev.* **1967**, *67*, 475.

[35] P. J. O'Malley, *J. Phys. Chem. B* **2002**, *106*, 12331.

[36] C. Xie, P. M. Lahti, C. George, *Org. Lett.* **2000**, *2*, 3417.

[37] J. Stubbe, D. G. Nocera, C. S. Yee, M. C. Y. Chang, *Chem. Rev.* **2003**, *103*, 2167.

[38] J. Stubbe, W. A. van der Donk, *Chem. Rev.* **1998**, *98*, 705.

[39] G. M. Coppinger, *J. Am. Chem. Soc.* **1957**, *79*, 501.

[40] B. Kirste, W. Harrer, H. Kurreck, K. Schubert, H. Bauer, W. Gierke, *J. Am. Chem. Soc.* **1981**, *103*, 6280.

[41] I. Novak, B. Kovač, *Chem. Phys. Lett.* **2005**, *413*, 351.

[42] F. Dietz, N. Tyutyulkov, M. Baumgarten, *J. Phys. Chem. B* **1998**, *102*, 3912.

[43] N. C. Yang, A. J. Castro, *J. Am. Chem. Soc.* **1960**, *82*, 6208.

[44] H. Bock, A. John, Z. Havlas, J. W. Bats, *Angew. Chem. Int. Ed.* **1993**, *32*, 416.

[45] P. Dowd, *Acc. Chem. Res.* **1972**, *5*, 242.

[46] G. J. Papariello, M. A. M. Janish, *Anal. Chem.* **1965**, *37*, 899.

[47] M. S. Blois, *Nature* **1958**, *181*, 1199.

[48] Y. Morita, S. Suzuki, K. Sato, T. Takui, *Nat. Chem.* **2011**, *3*, 197.

[49] D. H. Reid, *Tetrahedron* **1958**, *3*, 339.

[50] P. B. Sogo, M. Nakazaki, M. Calvin, *J. Chem. Phys.* **1957**, *26*, 1343.

[51] K. Goto, T. Kubo, K. Yamamoto, K. Nakasuji, K. Sato, D. Shiomi, T. Takui, M. Kubota, T. Kobayashi, K. Yakusi, J. Ouyang, *J. Am. Chem. Soc.* **1999**, *121*, 1619.

[52] Y. Takano, T. Taniguchi, H. Isobe, T. Kubo, Y. Morita, K. Yamamoto, K. Nakasuji, T. Takui, K. Yamaguchi, *J. Am. Chem. Soc.* **2002**, *124*, 11122.

[53] R. Kuhn, H. Trischmann, *Angew. Chem. Int. Ed.* **1963**, *2*, 155.

[54] R. Kuhn, F. A. Neugebauer, H. Trischmann, *Angew. Chem. Int. Ed.* **1964**, *3*, 232.

[55] F. A. Neugebauer, H. Fischer, R. Siegel, *Chem. Ber.* **1988**, *121*, 815.

[56] F. A. Neugebauer, H. Fischer, C. Krieger, *Journal of the Chemical Society, Perkin Transactions 2* **1993**, 535.

[57] E. C. Pare, D. J. R. Brook, A. Brieger, M. Badik, M. Schinke, *Org. Biomol. Chem.* **2005**, *3*, 4258.

[58] A. J. Banister, H. G. Clarke, I. Rayment, H. M. M. Shearer, *Inorganic and Nuclear Chemistry Letters* **1974**, *10*, 647.

[59] R. J. Gillespie, J. P. Kent, J. F. Sawyer, *Inorg. Chem.* **1981**, *20*, 3784.

[60] J. M. Rawson, A. J. Banister, I. Lavender, The Chemistry of Dithiadiazolylium and Dithiadiazolyl Rings. In *Advances in Heterocyclic Chemistry*, R. K. Alan, Ed. Academic Press: 1995; Vol. Volume 62, pp 137.

[61] C. S. Clarke, D. A. Haynes, J. N. B. Smith, A. S. Batsanov, J. A. K. Howard, S. I. Pascu, J. M. Rawson, *CrystEngComm* **2010**, *12*, 172.

[62] J. M. Rawson, A. Alberola, A. Whalley, *J. Mater. Chem.* **2006**, *16*, 2560.

[63] M. Baumgarten, High Spin Molecules Directed Towards Molecular Magnets. In *EPR of Free Radicals in Solids II*, A. Lund, M. Shiotani, Eds. Springer Netherlands: 2012; Vol. 25, pp 205.

[64] W. T. Borden, E. R. Davidson, *J. Am. Chem. Soc.* **1977**, *99*, 4587.

[65] P. Nachtigall, K. D. Jordan, *J. Am. Chem. Soc.* **1993**, *115*, 270.

[66] M. Baumgarten, S. Karabunarliev, *Chem. Phys.* **1999**, *244*, 35.

[67] L. K. Montgomery, J. C. Huffman, E. A. Jurczak, M. P. Grendze, *J. Am. Chem. Soc.* **1986**, *108*, 6004.

[68] A. E. Tschitschibabin, *Chem. Ber.* **1907**, *40*, 1810.

[69] E. Clar, D. G. Stewart, *J. Am. Chem. Soc.* **1953**, *75*, 2667.

[70] E. Clar, D. G. Stewart, *J. Am. Chem. Soc.* **1954**, *76*, 3504.

[71] G. Allinson, R. J. Bushby, J.-L. Paillaud, M. Thornton-Pett, *J. Chem. Soc., Perkin Trans. 1* **1995**, 385.

[72] G. Allinson, R. J. Bushby, M. V. Jesudason, J.-L. Paillaud, N. Taylor, *Journal of the Chemical Society, Perkin Transactions 2* **1997**, 147.

[73] W. Adam, C. R. Saha-Möller, P. A. Ganeshpure, *Chem. Rev.* **2001**, *101*, 3499.

[74] M. V. N. De Souza, *Mini-Rev. Org. Chem.* **2006**, *3*, 155.

[75] K. Aoki, H. Akutsu, J.-i. Yamada, S. i. Nakatsuji, T. Kojima, Y. Yamashita, *Chem. Lett.* **2009**, *38*, 112.

[76] T. M. Figueira-Duarte, K. Müllen, *Chem. Rev.* **2011**, *111*, 7260.

[77] Y. Wang, H. Wang, Y. Liu, C.-a. Di, Y. Sun, W. Wu, G. Yu, D. Zhang, D. Zhu, *J. Am. Chem. Soc.* **2006**, *128*, 13058.

[78] Y. B. Borozdina, V. Kamm, F. Laquai, M. Baumgarten, *J. Mater. Chem.* **2012**, *22*, 13260.

[79] T. Sugawara, H. Komatsu, K. Suzuki, *Chem. Soc. Rev.* **2011**, *40*, 3105.

[80] Y. Zhang, T. P. Basel, B. R. Gautam, X. Yang, D. J. Mascaro, F. Liu, Z. V. Vardeny, *Nat Commun* **2012**, *3*, 1043.

[81] F. Kato, A. Kikuchi, T. Okuyama, K. Oyaizu, H. Nishide, *Angew. Chem. Int. Ed.* **2012**, *51*, 10177.

[82] R. T. Hayes, C. J. Walsh, M. R. Wasielewski, *J. Phys. Chem. A* **2004**, *108*, 2375.

[83] Y. Teki, S. Miyamoto, K. Iimura, M. Nakatsuji, Y. Miura, *J. Am. Chem. Soc.* **2000**, *122*, 984.

[84] E. A. Mostovich, Y. Borozdina, V. Enkelmann, K. Remović-Langer, B. Wolf, M. Lang, M. Baumgarten, *Cryst. Growth Des.* **2012**, *12*, 54.

[85] Y. Morita, S. Nishida, T. Murata, M. Moriguchi, A. Ueda, M. Satoh, K. Arifuku, K. Sato, T. Takui, *Nat. Mater.* **2011**, *10*, 947.

[86] E. M. Fatila, R. Clérac, M. Rouzières, D. V. Soldatov, M. Jennings, K. E. Preuss, *J. Am. Chem. Soc.* **2013**, *135*, 13298.

[87] H. Oshio, T. Watanabe, A. Ohto, T. Ito, T. Ikoma, S. TeroKubota, *Inorg. Chem.* **1997**, *36*, 3014.

[88] A. Aspuru-Guzik, A. D. Dutoi, P. J. Love, M. Head-Gordon, *Science* **2005**, *309*, 1704.

[89] S. Lloyd, *Science* **1993**, *261*, 1569.

[90] S. Bone, M. Castro http://www.doc.ic.ac.uk/~nd/surprise_97/journal/vol4/spb3/.

[91] G. Aromi, D. Aguila, P. Gamez, F. Luis, O. Roubeau, *Chem. Soc. Rev.* **2012**, *41*, 537.

[92] F. Troiani, M. Affronte, *Chem. Soc. Rev.* **2011**, *40*, 3119.

[93] K. Sato, S. Nakazawa, S. Nishida, R. Rahimi, T. Yoshino, Y. Morita, K. Toyota, D. Shiomi, M. Kitagawa, T. Takui, Novel Applications of ESR/EPR: Quantum Computing/Quantum Information Processing. In *EPR of Free Radicals in Solids II*, A.

Lund, M. Shiotani, Eds. Springer Netherlands: 2012; Vol. 25, pp 163.

[94] K. Sato, S. Nakazawa, R. Rahimi, T. Ise, S. Nishida, T. Yoshino, N. Mori, K. Toyota, D. Shiomi, Y. Yakiyama, Y. Morita, M. Kitagawa, K. Nakasuji, M. Nakahara, H. Hara, P. Carl, P. Hofer, T. Takui, *J. Mater. Chem.* **2009**, *19*, 3739.

[95] S. Nakazawa, S. Nishida, T. Ise, T. Yoshino, N. Mori, R. D. Rahimi, K. Sato, Y. Morita, K. Toyota, D. Shiomi, M. Kitagawa, H. Hara, P. Carl, P. Höfer, T. Takui, *Angew. Chem.* **2012**, *124*, 9998.

[96] H. Nishide, T. Suga, *Electrochem. Soc. Interface* **2005**, *14*, 32.

[97] T. Suga, S. Sugita, H. Ohshiro, K. Oyaizu, H. Nishide, *Adv. Mater.* **2011**, *23*, 751.

[98] T. Janoschka, A. Teichler, B. Häupler, T. Jähnert, M. D. Hager, U. S. Schubert, *Advanced Energy Materials* **2013**, *3*, 1025.

[99] T. Janoschka, M. D. Hager, U. S. Schubert, *Adv. Mater.* **2012**, *24*, 6397.

[100] H. Nishide, K. Oyaizu, *Science* **2008**, *319*, 737.

[101] K. Nakahara, K. Oyaizu, H. Nishide, *Chem. Lett.* **2011**, *40*, 222.

[102] T. Murakami, F. Kato, K. Oyaizu, H. Nishide, *J. Photopolym. Sci. Technol.* **2010**, *23*, 353.

[103] J. S. Miller, *Adv. Mater.* **2002**, *14*, 1105.

[104] D. Gatteschi, *Adv. Mater.* **1994**, *6*, 635.

[105] E. Coronado, P. Delhaès, D. Gatteschi, J. Miller, in *Molecular Magnetism: From Molecular Assemblies to the Devices, Vol. 321* (Eds.: E. Coronado, P. Delhaès, D. Gatteschi, J. Miller), Springer Netherlands, **1996**.

[106] W. Heisenberg, *Z. Phys.* **1928**, *49*, 619.

[107] H. M. McConnell, *J. Chem. Phys.* **1963**, *39*, 1910.

[108] M. Tamura, Y. Nakazawa, D. Shiomi, K. Nozawa, Y. Hosokoshi, M. Ishikawa, M. Takahashi, M. Kinoshita, *Chem. Phys. Lett.* **1991**, *186*, 401.

[109] R. Chiarelli, M. A. Novak, A. Rassat, J. L. Tholence, *Nature* **1993**, *363*, 147.

[110] P.-M. Allemand, K. C. Khemani, A. Koch, F. Wudl, K. Holczer, S. Donovan, G. Grüner, J. D. Thompson, *Science* **1991**, *253*, 301.

[111] F. Palacio, G. Antorrena, M. Castro, R. Burriel, J. Rawson, J. N. B. Smith, N. Bricklebank, J. Novoa, C. Ritter, *Phys. Rev. Lett.* **1997**, *79*, 2336.

[112] M. Abe, *Chem. Rev.* **2013**, *113*, 7011.

[113] J. S. Miller, A. J. Epstein, *Angew. Chem. Int. Ed.* **1994**, *33*, 385.

[114] C. Rüegg, K. Kiefer, B. Thielemann, D. F. McMorrow, V. Zapf, B. Normand, M. B. Zvonarev, P. Bouillot, C. Kollath, T. Giamarchi, S. Capponi, D. Poilblanc, D. Biner, K. W. Krämer, *Phys. Rev. Lett.* **2008**, *101*, 247202.

[115] V. Gurarie, J. T. Chalker, *Phys. Rev. Lett.* **2002**, *89*, 136801.

[116] A. Collauto, M. Mannini, L. Sorace, A. Barbon, M. Brustolon, D. Gatteschi, *J. Mater. Chem.* **2012**, *22*, 22272.

[117] A. Ueda, S. Suzuki, K. Yoshida, K. Fukui, K. Sato, T. Takui, K. Nakasuji, Y. Morita, *Angew. Chem. Int. Ed.* **2013**, *52*, 4795.

[118] T. Giamarchi, C. Ruegg, O. Tchernyshyov, *Nat. Phys.* **2008**, *4*, 198.

[119] S. Jochim, M. Bartenstein, A. Altmeyer, G. Hendl, S. Riedl, C. Chin, J. Hecker Denschlag, R. Grimm, *Science* **2003**, *302*, 2101.

[120] P. Ravat, Y. Ito, E. Gorelik, V. Enkelmann, M. Baumgarten, *Org. Lett.* **2013**, *15*, 4280.

[121] B. Wolf, P. T. Cong, K. Remović-Langer, Y. D. Borozdina, E. Mostovich, M. Baumgarten, M. Lang, *J. Phys.: Conf. Ser.* **2010**, *200*, 012225.

[122] M. M. Matsushita, A. Izuoka, T. Sugawara, T. Kobayashi, N. Wada, N. Takeda, M. Ishikawa, *J. Am. Chem. Soc.* **1997**, *119*, 4369.

[123] P. Taylor, P. R. Serwinski, P. M. Lahti, *Chem Commun* **2003**, 1400.

[124] X. Pang, X. R. Zhao, H. Wang, H.-L. Sun, W. J. Jin, *Cryst. Growth Des.* **2013**, *13*, 3739.

[125] H. Akpinar, J. A. Schlueter, P. M. Lahti, *Chem. Commun.* **2013**, *49*, 3345.

[126] H. Tanaka, D. Shiomi, S. Suzuki, M. Kozaki, K. Okada, K. Sato, T. Takui, *CrystEngComm* **2010**, *12*, 526.

[127] G. R. Desiraju, *Acc. Chem. Res.* **2002**, *35*, 565.

[128] C. B. Aakeröy, K. R. Seddon, *Chem. Soc. Rev.* **1993**, *22*, 397.

[129] E. F. Ullman, D. G. B. Boocock, *Journal of the Chemical Society D: Chemical Communications* **1969**, 1161.

[130] A. Caneschi, P. Chiesi, L. David, F. Ferraro, D. Gatteschi, R. Sessoli, *Inorg. Chem.* **1993**, *32*, 1445.

[131] K. C. Ko, D. Cho, J. Y. Lee, *J. Phys. Chem. A* **2013**, *117*, 3561.

[132] M. E. Ali, S. N. Datta, *J. Phys. Chem. A* **2006**, *110*, 2776.

[133] M. Shinomiya, K. Higashiguchi, K. Matsuda, *J. Org. Chem.* **2013**, *78*, 9282.

[134] P. Wautelet, A. Bieber, P. Turek, J. L. Moigne, J.-J. André, *Molecular Crystals and Liquid Crystals Science and Technology. Section A. Molecular Crystals and Liquid Crystals* **1997**, *305*, 55.

CHAPTER 2 EPR SPECTROSCOPY

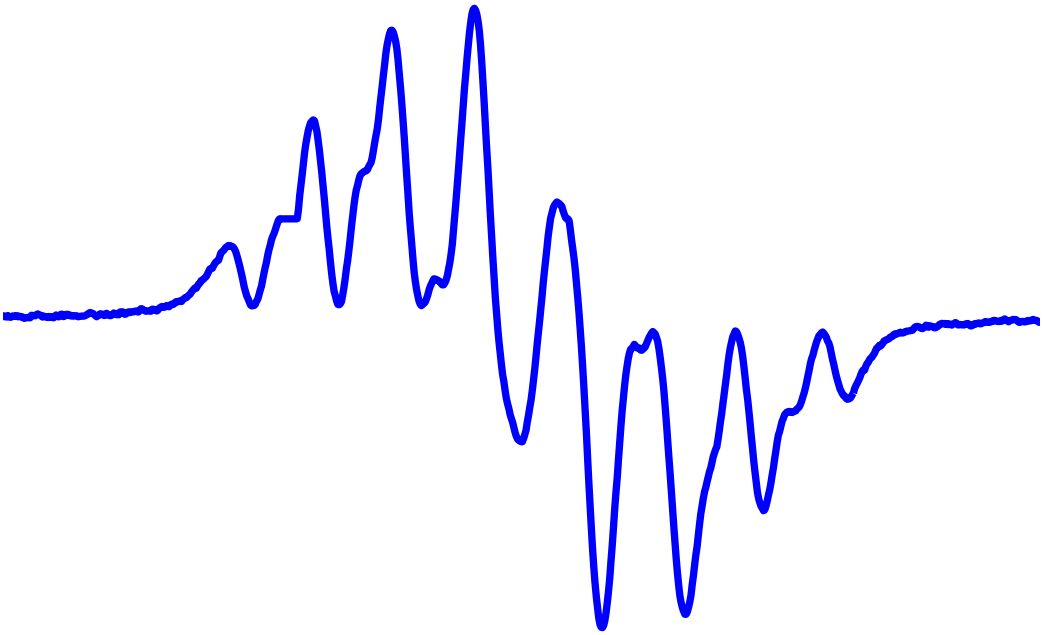

Twinkle Twinkle little Spin

Are you single or are you twin?

Are you real or are you false?

How I crave your resonant pulse

—JOHN A. WEIL

2.1 Introduction

Electron spin resonance (ESR) or electron paramagnetic resonance (EPR) spectroscopy was invented by the Russian physicist Zavoisky in 1945. EPR is resonant absorption of microwave radiation in the presence of applied magnetic field. The basis for EPR spectroscopy relies on the perturbation of the electron spin state by the application of applied magnetic field alike the NMR spectroscopy. According to Pauli's principle the spin quantum number of free electron is S = 1/2. In the presence of an applied magnetic field magnetic quantum number becomes effective (M_S = +1/2 or M_S = –1/2). Functions associated with magnetic quantum number (M_S) are denoted as α and β. Due to the spin, electron possesses effective magnetic moment (μ_e) which is proportional to spin angular momentum (*S*).

$$\mu_e = -g_e \mu_B S \qquad \textbf{2-1}$$

Where μ_B is Bohr magneton defined as $\mu_B = eh/4\pi m_e$, e and m_e are electron elementary charge and rest mass, respectively, and h is plank's constant. g_e is so called electron g-factor or landé g-factor. For free electron the g-factor is 2.0023.

2.2 Molecules with S = 1/2

For a system with one unpaired electron placed in magnetic field experiences the quantization of spin state and exhibits discrete spin states according to the spin multiplicity rule, 2S + 1. The interaction between spin and field is described by the Zeeman-effect. The interaction energy between the spin and the field is a negative value of the scalar product of effective magnetic moment and applied magnetic field.

$$E = -\mu_e \boldsymbol{B} \qquad \textbf{2-2}$$

When the field is chosen along the z-direction (**B** = (0, 0, *B*)), the scalar product simplifies to,

$$E = -\mu_{e,z} B = -(-g_e \mu_B M_S B) \qquad \textbf{2-3}$$

Therefore the energy for two different states,

$$E_\alpha = +\frac{1}{2} g_e \mu_B B \quad \textbf{2-4}$$

$$E_\beta = -\frac{1}{2} g_e \mu_B B \quad \textbf{2-5}$$

Zeeman splitting, $\Delta E = E_\alpha - E_\beta = h\nu = g_e \mu_B B$ **2-6**

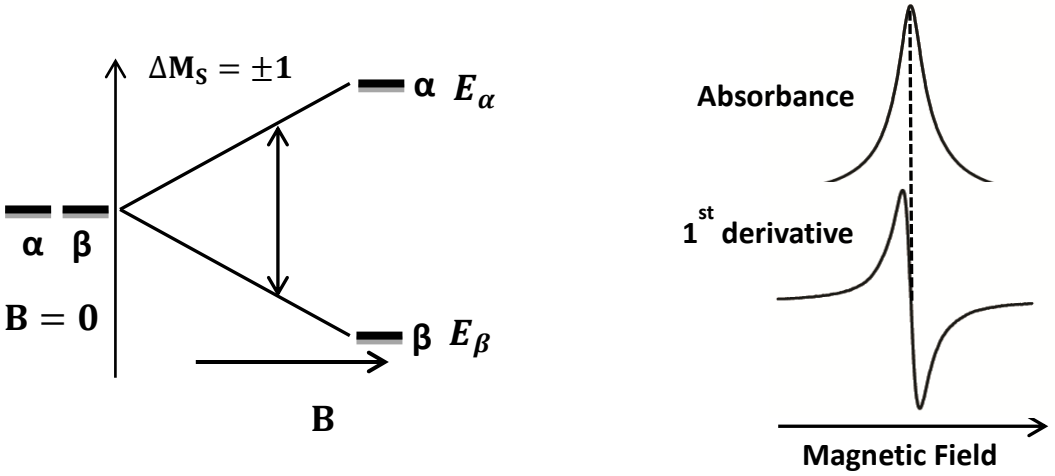

Figure 2.1: Electron-Zeeman splitting as a function of applied magnetic field and absorption curve for S = 1/2 system.

In the absence of an applied field α or β spin states of the electron are degenerate as shown in Figure 2.1. Application of an applied field perturbs the degeneracy of the two spin states. The α spin state with magnetic moment opposite to the applied field, rises in energy while the β spin state having magnetic moment aligned with the applied field, decreases in energy as the strength of the applied field increases. When a frequency of energy which matches the energy separation between the two spin states is applied, the absorption occurs; this causes a transition between two spin states. The energy difference between two spin states is proportional to the applied magnetic field. The selection rule for transition between two levels is $\Delta M_S = \pm 1$.

Generally, continuous wave EPR spectrometers work at constant frequency (v) and variable magnetic field (B). One of the commonly used frequency ranges for EPR spectrometers is the *X*-band (9-10 GHz). EPR spectra are usually represented as its first derivative. From this EPR measurement, one of the most important data is the g-value, which can be calculated from $g_e = hv/\mu_B B$, (simplifying this equation $g = 714.5 \times \frac{frequency\ of\ instrument\ (GHz)}{applied\ field\ (G)}$), where v is the frequency of the microwave radiation used. The g-value gives the information about the species of the atom on which the unpaired electron lies, the molecular orbitals in which the unpaired electron resides, the nature of the chemical bonds to which the unpaired electron belongs, and the surrounding molecular environments from which the unpaired electron experiences the interactions.

2.3 Electron-Nuclear hyperfine interaction

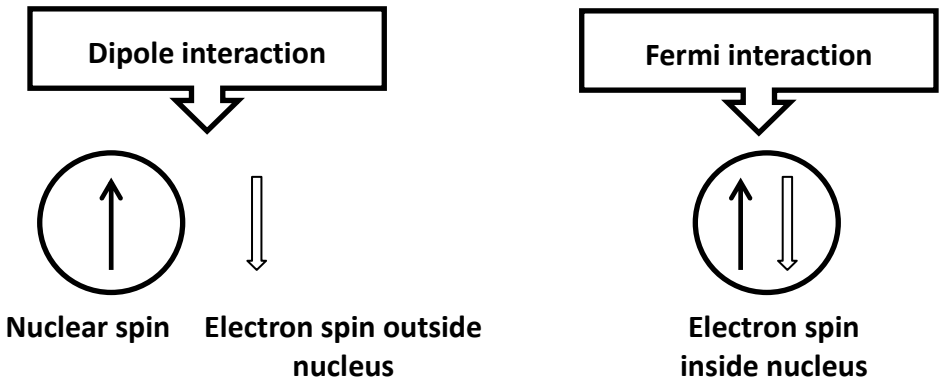

Figure 2.2: Schematic representation of dipole interaction and Fermi contact.

The notion hyperfine interaction comes from atomic physics, where it is used for the interaction of the electronic magnetic moment with the nuclear magnetic moment. Nuclei with an odd number of protons and an odd number of neutrons possess the property of nuclear spin angular momentum (I). Electron-nuclei interactions have several mechanisms, the most prevalent being the Fermi contact and dipolar interactions (Figure 2.2). While the Fermi contact interaction is isotropic, the dipole interaction is anisotropic in nature. Dipole interactions occur between the magnetic moments of the nucleus and electron as an electron moves around a nucleus. However, as an electron approaches a

nucleus, it has a magnetic moment associated with it. As this magnetic moment moves very close to the nucleus, the magnetic field associated with that nucleus is no longer entirely dipolar. The resulting interaction of these magnetic moments while the electron and nucleus are in contact is radically different from the dipolar interaction of the electron when it is outside the nucleus. This non-dipolar interaction of a nucleus and electron spin in contact is the Fermi contact interaction. The isotropic Fermi contact interaction is readily observed in solution EPR. The anisotropic coupling vanishes to zero in solutions because of the averaged motions of the system and can only be determined for radicals in a rigid matrix (crystals, powders, frozen solutions). Dipole interactions (or electron spin-spin interactions) depend on the distance between spin and nucleus. This interaction gives the information about the position of spin on the molecule in solid lattice.

The spin Hamiltonian for the unpaired electron of an organic radical in magnetic field experiencing hyperfine interaction is given by,

$$H = H_{Ze} + H_{hf} = g_e \mu_B B S + \sum_n A_n \boldsymbol{S}\, \boldsymbol{I_n} \qquad \textbf{2-7}$$

$$Thus\ the\ total, E = E_{Ze} + E_{hf} = g_e \mu_B B M_S + \sum_n A_n M_S M_{i,n} \qquad \textbf{2-8}$$

The first term is the Zeeman energy of electron, and the second term is the hyperfine coupling between electron and nucleus, where A_n is the hyperfine coupling constant. As explained earlier,

$$A_n = A_0 + A_{dip} \qquad \textbf{2-9}$$

where A_0 and A_{dip} are Fermi (isotropic) and dipolar (anisotropic) hyperfine coupling constants, respectively.

Figure 2.3 shows the hyperfine splitting by a nucleus X with I = 1/2 and I = 1 for a radical in magnetic field B. According to EPR selection rule $\Delta M_S = \pm 1$ and $\Delta M_I = 0$, two transition are allowed for I = 1/2 and three for I = 1. The numbers of hyperfine lines grow

multiplicatively with the number n of magnetic nuclei. Each additional nucleus splits every line to equidistant 2I + 1 lines of same intensity. For n number of equivalent nuclei the number of lines can be given by 2nI + 1.

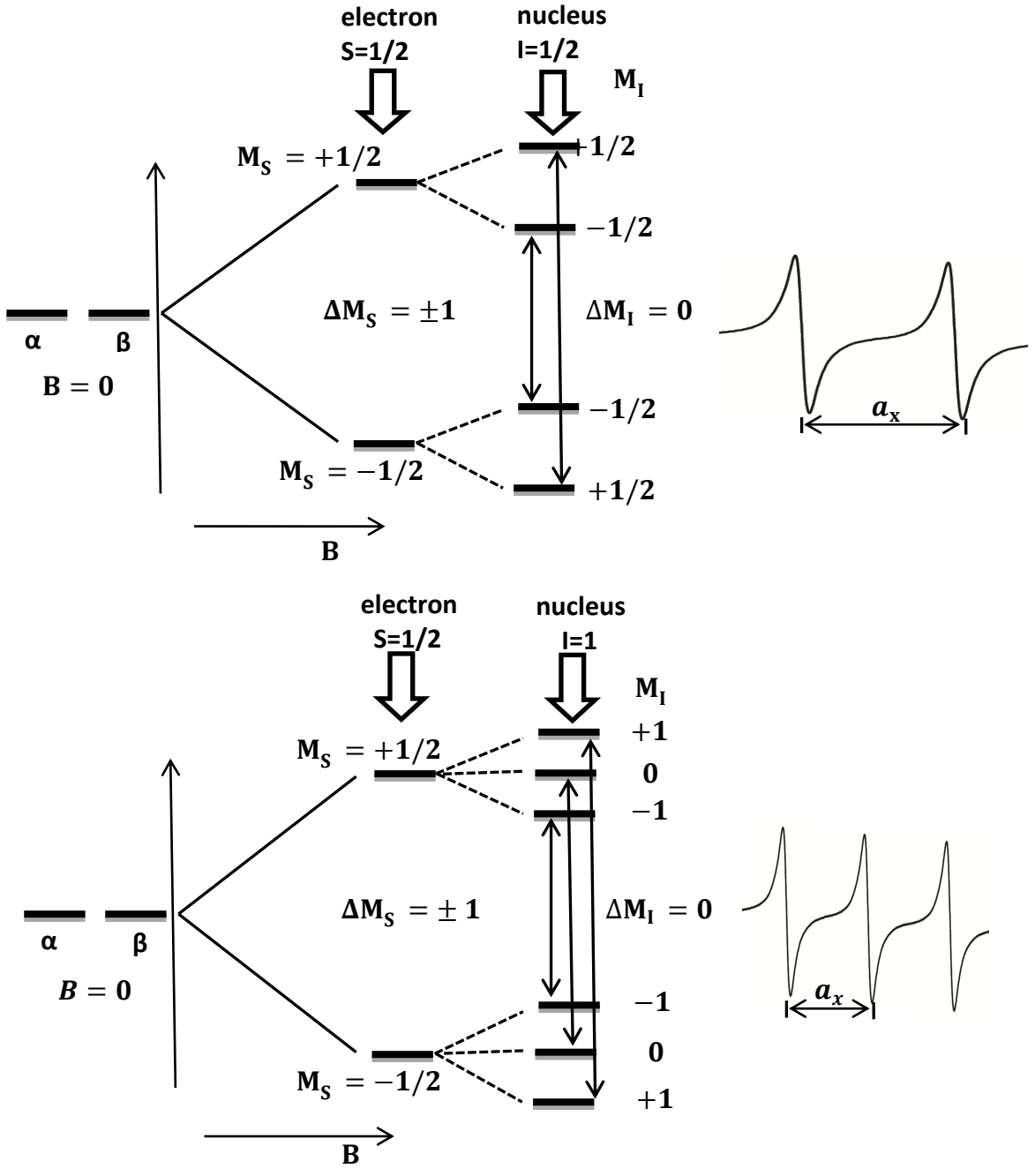

Figure 2.3: Hyperfine splitting of electron-Zeeman levels for nucleus with I = 1/2 and 1.

2.4 Molecules with S > 1/2

In case of biradicals two unpaired electrons are present in a system, thus the spin state depends on the alignment of two electrons. If unpaired electrons are aligned antiparallel (S = 0) the spin multiplicity is singlet (2S + 1 = 1), suggesting only a singlet state available, thus no EPR signal observed. In case of parallel aligned spin (S = 1) the multiplicity is triplet (2S + 1 = 3). So according to the selection rule, $\Delta M_S = \pm 1$, there are two allowed transitions as shown in Figure 2.4.

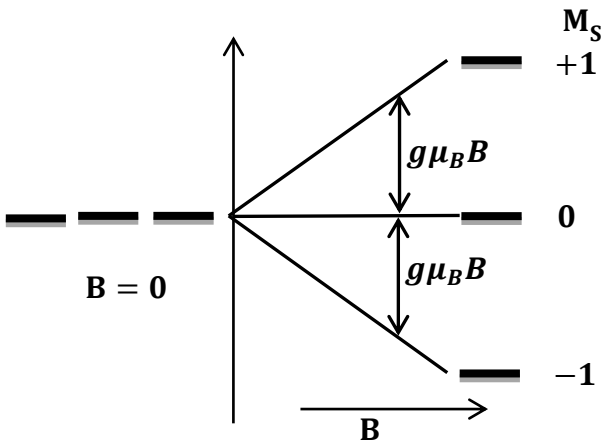

Figure 2.4: Energy diagram for S = 1 system.

For the biradicals, a simplest case of two spins system, the spin Hamiltonian can be written as,

$$H = g_e \mu_B B S_a S_b - 2J_{ab} S_a S_b + \sum_{ij} a_{xij} (S_a I_i + S_b I_j) \quad \textbf{2-10}$$

The empirical operator, $2JS_a S_b$, is the Heisenberg-Dirac-Van Vleck (HDVV) Hamiltonian and represents the exchange interactions. S_a and S_b are electron spin angular momentum operators and J_{ab} is the isotropic exchange coupling constant. The product of spin angular momentum operators can be expressed in terms of component and product (total) spin angular momentum operators,

$$S_{Tot}^2 = (S_a + S_b)^2 = S_a^2 + S_b^2 + 2S_a S_b \quad \textbf{2-11}$$

$$S_a\, S_b = 1/2(S_{Tot}^2 - S_a^2 - S_b^2) \quad \textbf{2-12}$$

Since, the Eigenvalue of S^2 is S^2 = S(S + 1), the total energy (E_{Tot}) of the state with S_{Tot} originating from interacting spins S_a and S_b is given by,

$$E_{Tot} = -2J_{ab}\, S_a\, S_b \quad \textbf{2-13}$$

$$\text{Therefore, } E_{Tot} = -2J_{ab}\,[S_{Tot}\,(S_{Tot} + 1) - S_a\,(S_a + 1) - S_b\,(S_b + 1)] \quad \textbf{2-14}$$

Thus coupling of two interacting spins results in a triplet and a singlet state (in total 4 spin states, Figure 2.5). For ferromagnetic coupling (J > 0), the energy of triplet state (S = 1) using above formula is,

$$E_T = -\frac{J}{2} \quad \textbf{2-15}$$

In case of antiferromagnetic coupling (J < 0), the energy of singlet state (S = 0) is,

$$E_S = \frac{3J}{2} \quad \textbf{2-16}$$

$$\text{The singlet triplet gap, } \Delta E_{S\,T} = E_S - E_T = 2J \quad \textbf{2-17}$$

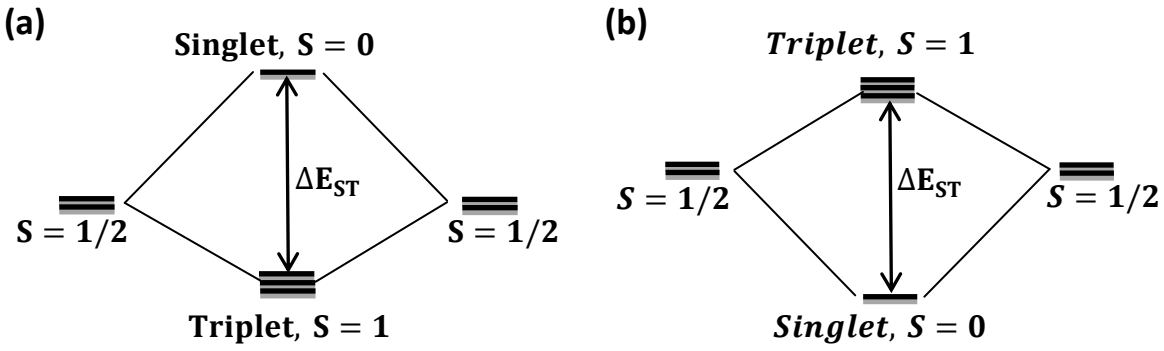

Figure 2.5: Energy level diagram for (a) ferromagnetic and (b) antiferromagnetic coupling.

The EPR spectral shape and number of lines highly depend on the relative magnitude of exchange coupling constant J and the hyperfine coupling constant a_x with

respect to each other. For the EPR spectra of biradicals in solution there are three possible cases,

1) $J >> a_x$, in the occasions when exchange interactions are much larger than the hyperfine coupling constant, for the n equivalent nuclei 2nI + 1 number of lines should be observed with a_x half of the same observed for related mono radical species. However the total width of the spectrum should be same as the observed for the mono radical.

2) $J < a_x$, in this case each of the radical species behave independently and can be treated as the uncorrelated spin-system. Here the observed EPR spectrum matches exactly as monoradical system with signal intensity doubled compared to later.

3) $J \sim a_x$, here the mixing of singlet and triplet state through hyperfine interaction is possible. The total spectral width would be larger and the number of spectral lines would be more than the observed for mono radical system.

2.5 Zero field splitting (*zfs*)

In frozen solution or powder sample the degeneracy of triplet sub states is lifted or quantization of spin state takes place at zero applied magnetic field. This is called zero field splitting and can be accounted for the anisotropic dipole-dipole interactions of the magnetic moments of two interacting spins. This phenomenon can be described by the *zfs* parameters *D* and *E*. The phenomenological Hamiltonian to describe the spin-spin interaction energy can be written as,

$$H = \boldsymbol{S} \cdot \boldsymbol{D} \cdot \boldsymbol{S} \qquad \textbf{2-18}$$

Where S is total spin operator of the two electrons ($S = S_1 + S_2$) and $\boldsymbol{D}$ is symmetrical traceless tensor. Since the dipole-dipole interactions are isotropic the Hamiltonian becomes,

$$H = D_{XX}S_X^2 + D_{YY}S_Y^2 + D_{ZZ}S_Z^2 \qquad \textbf{2-19}$$

Where D_{XX}, D_{YY}, and D_{ZZ} are Eigenvalues of ***D*** in *x*, *y* and *z* directions. As ***D*** is the traceless tensor ($D_{XX} + D_{YY} + D_{ZZ} = 0$), only two independent parameters exist, known as zero field splitting parameters *D* and *E*. The expressions for *D* and *E* are,

$$D = 3/2\, D_{ZZ} \quad \textbf{2-20}$$

$$E = 1/2|D_{XX} - D_{YY}| \quad \textbf{2-21}$$

Including these parameters the spin Hamiltonian for a molecule with S ≥ 1 can be written as,

$$H = \underbrace{g_e \mu_B B S_{a.b}}_{\text{Zeeman interactions}} \underbrace{- 2J_{ab}\, S_a\, S_b}_{\text{Exchange interactions}} + \underbrace{D\left\{\left(S_Z^2 - \frac{1}{3}\, S(S+1)\right)\right\} + E\left(S_x^2 - S_y^2\right)}_{\text{Electron-electron dipole interactions}} + \underbrace{\sum_n A_n \boldsymbol{SI_n}}_{\text{Hyperfine interactions}} \quad \textbf{2-22}$$

The spin-spin Hamiltonian consists of two different interactions, spin-spin and spin-orbit coupling. For the organic molecules the most contribution to ***D*** comes from spin-spin coupling as spin-orbit coupling is negligible for lighter nuclei. Following the classical dipole-dipole interaction the element D_{ij} for spin-spin coupling tensor ***D*** can be described as,

$$D_{ij} = -\left(\frac{\mu_0}{4\pi h}\right) g_e^2 \mu_B^2 \left\langle \frac{d^2 \delta_{ij} - 3ij}{d^5} \right\rangle \quad \textbf{2-23}$$

Simplifying above equation, for an axially symmetrical system E = 0, the average distance (d) between two unpaired electron in a molecule can be calculated as,

$$D = -\left(\frac{3\mu_0}{8\pi h}\right) g_e^2 \mu_B^2 \left\langle d^{-3} \right\rangle \quad \textbf{2-24}$$

Further simplifying the equation the value of *d* can be obtained as,

$d = 0.138/|D|^{1/3}$, where *d* and *D* are in nm and cm^{-1} units, respectively **2-25**

While *D* is inversely proportional to the cube of the distance between two spins, *E*

describes the deviation of electron distribution from axial symmetry. *D* and *E* also have been called the axial and rhombic *zfs* parameters, respectively.

2.6 Energy states in *zfs*

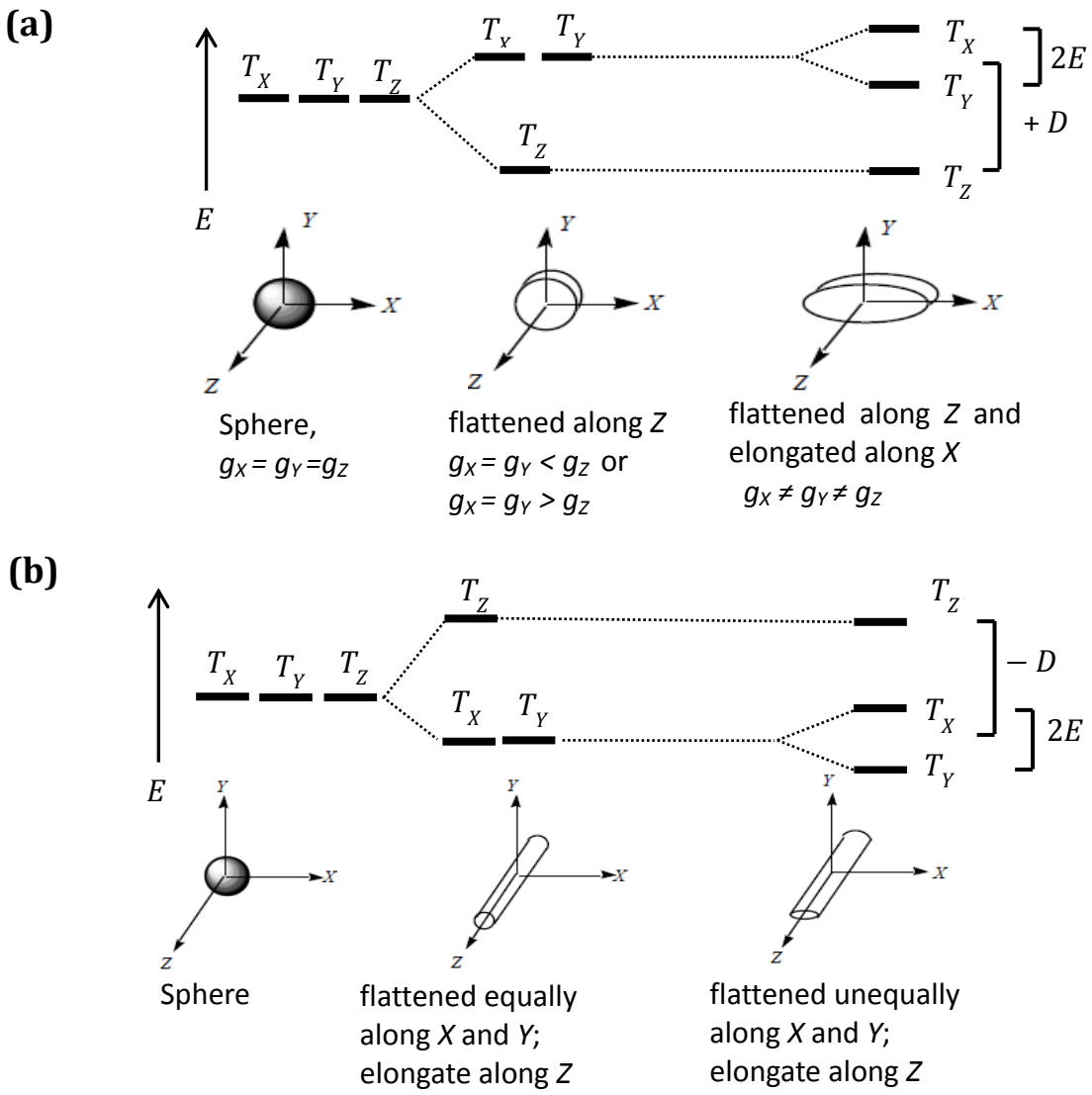

Figure 2.6: Energy states as a function of electron distribution for cubic, axial, and rhombic symmetry, (a) $D > 0$, (b) $D < 0$.

For an idealized triplet system experiencing dipole-dipole interactions, in the absence of external magnetic field the *zfs* of energy states highly depend on the electron spin distribution along the *X*, *Y*, and *Z* directions (Figure 2.6). Thus the triplets T_X, T_Y, and

T_Z are the spin states. While in the T_X-state spin axes is confined to the *ZY* plane with zero component along *X*-axis, for the T_Y-state the spin axis is confined to the *XZ* plane with zero component along *Y*-axis. Similarly for T_Z-state the spin axis is confined to the *XY* plane with zero component along *Z*-axis. The energetic effects in zero field are due to the anisotropic electron distribution and can be described by *zfs* parameters *D* and *E*. *D* is defined as energy difference in higher and lower energy states and the parameter *E* is half of the energy difference of higher energy states. As shown in Figure 2.6, *D* is positive for oblate spin distribution, a flattening in one direction, and negative for prolate spin distribution, an elongation in one direction. Thus a geometrical shape of the spin distribution can be estimated from *D* and *E*.

2.7 Determination of *zfs* parameters *D* and *E* using EPR

EPR is the technique used to determine energies of *D* and *E*. The simplest EPR spectrum of a triplet system is the one for cubic symmetry. There is no zero-field energy state splitting in the system with cubic symmetry as shown in Figure 2.4. Regardless of direction of applied magnetic field the splitting pattern remains the same. Moving from higher symmetric cubic system to lower symmetric axial system the two fold degeneracy of energy state is observed and the energy states of such triplet is described by *D* as shown in Figure 2.7. Here $E = 0$ because of the presence of axial symmetry. For this system the T_X and T_Y states remains degenerate at zero field and application of applied magnetic field in *X* and *Y* direction result in absorption at the same field. Two absorptions are observed for an axial system. Thus the axial system is generally characterized by a four line spectrum with the distance between two outer most peaks equal to 2*D* as shown in Figure 2.7c. On further propagating towards lower symmetric rhombic system the degeneracy is lifted completely at zero field. The zero field energy states are described by *D* and *E*. Three absorptions are observed for rhombic system giving a six line spectrum (Figure 2.8d), because each canonical orientation results in different spectrum i.e. $\Delta M_S = 1$ transitions occur at different field strengths. From the spectrum it is possible to calculate

the energy of *D* and *E* as shown in Figure 2.8d. It should be noted that for the axial and rhombic system $\Delta M_S = 2$ transitions may also be observed at half field (B/2) of the $\Delta M_S = \pm 1$ transition. The lower field, $\Delta M_S = 2$ transitions are usually forbidden. Here the selection rule is quite relaxed because at lower field the spin quantum numbers ($M_S = \pm 1, 0$) are not well defined.

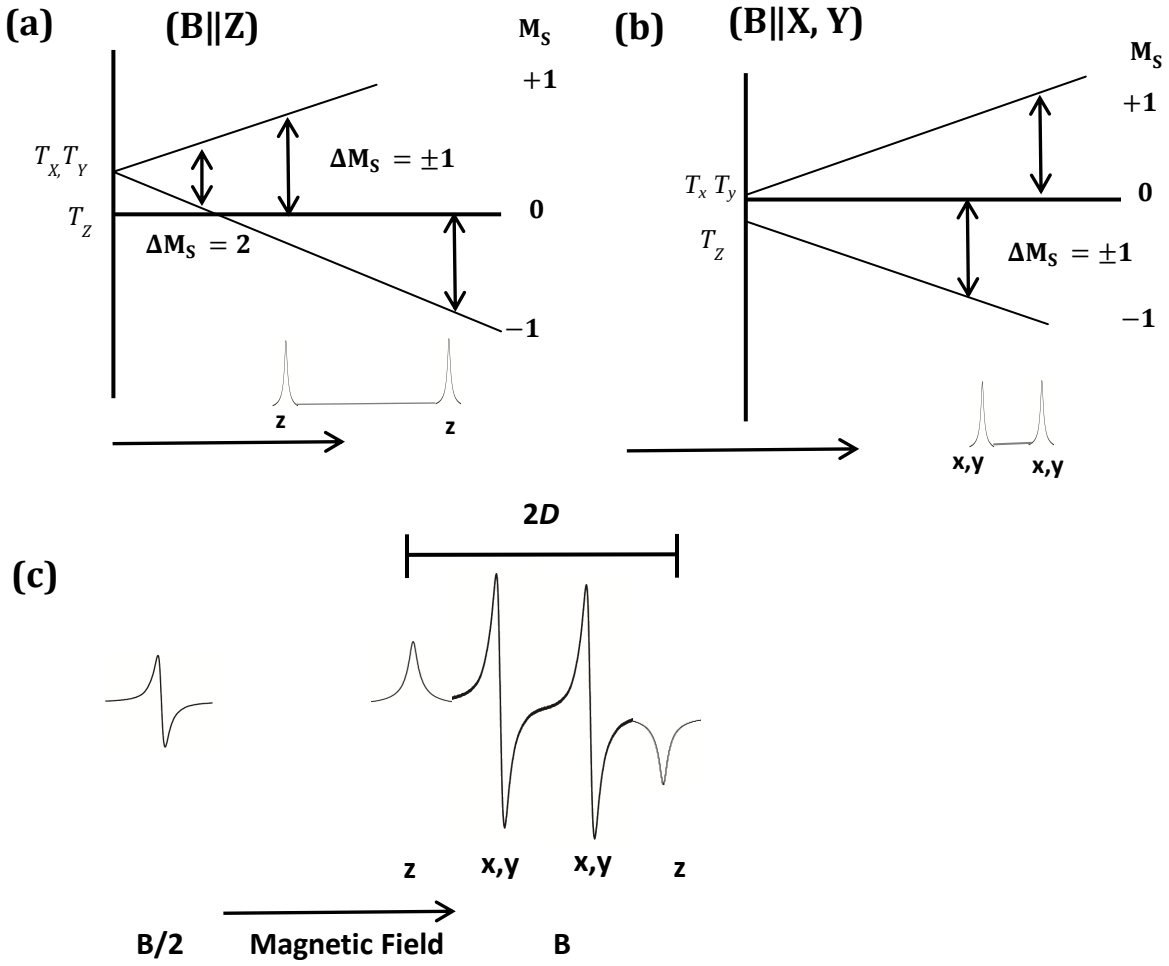

Figure 2.7: Energy diagram for axial system with S = 1 and *D* > 0. (a) Applied field aligned with molecular *Z*-axis. (b) Applied field aligned with molecular *X*- or *Y*- axis. (c) Simulated EPR spectra for this system.

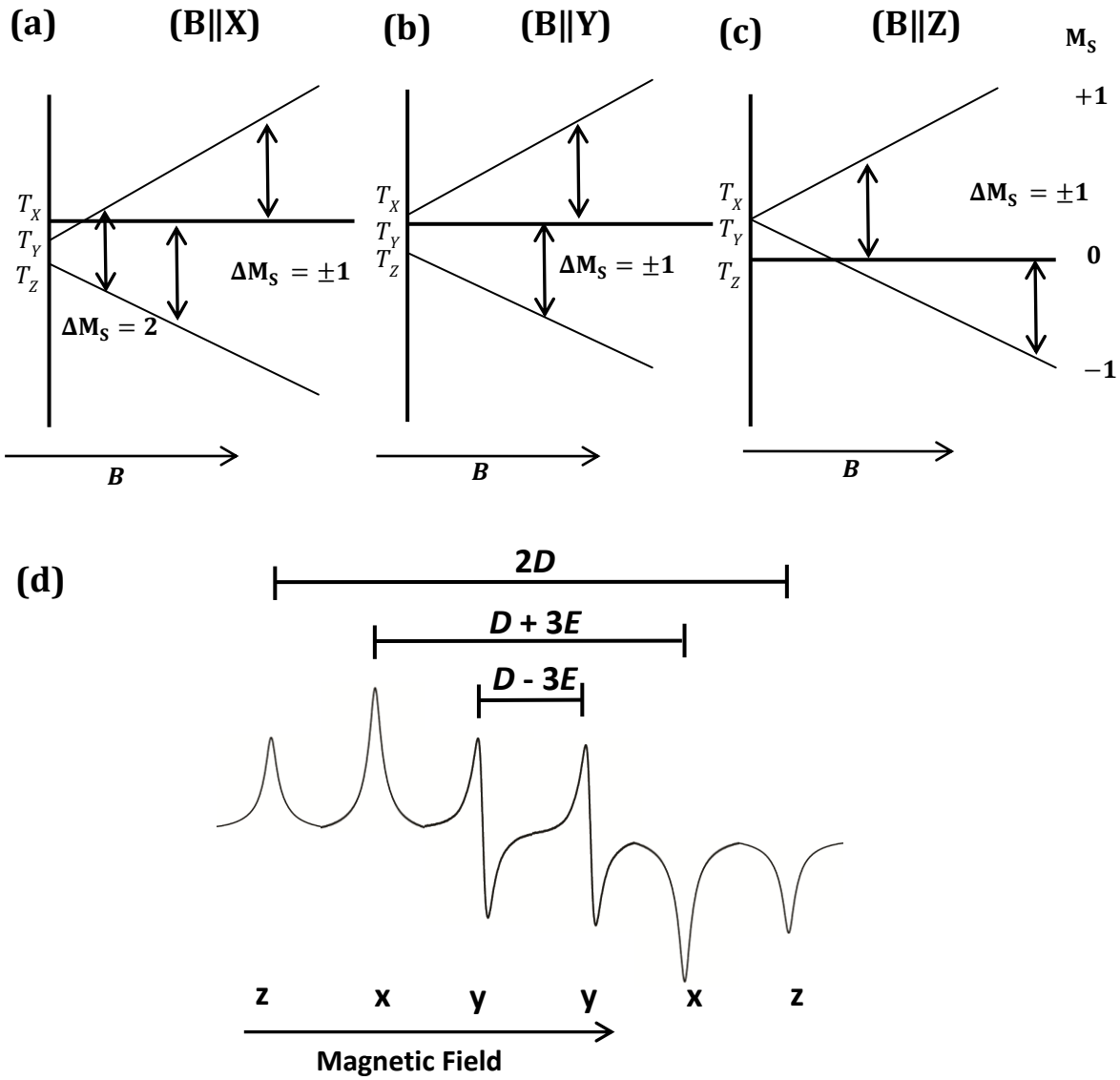

Figure 2.8: Energy diagram for rhombic system with S = 1, $D > 0$, and $|D| \neq 3\,|E|$. (a) Applied field aligned with molecular *X*-axis. (b) Applied field aligned with molecular *Y*-axis. (c) Applied field aligned with molecular *Z*-axis. (d) Simulated EPR spectra for this system and determination of *zfs* parameters.

2.8 Ground State analysis and exchange-coupling constant (*J*) with EPR

At thermal equilibrium and under the influence of the external applied magnetic field, according to the Maxwell–Boltzmann law the spin population splits between the two Zeeman levels, n_+ and n_-,

$$\frac{n_+}{n_-} = exp\left[-(E_\alpha - E_\beta)/k_B T\right] = exp\left[-\frac{g_e \mu_B B}{k_B T}\right] \quad \textbf{2-26}$$

Where k_B is the Boltzmann constant and T is the absolute temperature. Following the above equation all the spin levels are therefore populated above 0 K in a Boltzmann distribution of spins in upper and lower spin sub levels. At 298 K, in field of about 3300 G the n_+ / n_- is approximately 0.9986. Thus the population of two Zeeman level is almost equal, but the slight excess in lower level gives rise to net absorption. Further after the absorption the excess energy of upper level lost as consequences of the process called spin lattice relaxation. Thus the intensity of EPR signal is temperature dependent and follows the Curie law,

$$I_{EPR} = \frac{C}{T} \quad \textbf{2-27}$$

Where C is the Curie constant, and I_{EPR} is the intensity of EPR signal which is inversely proportional to temperature. From the temperature dependent EPR spectra of $\Delta M_S = \pm 1$ transition the exchange coupling constant (*J*) can be calculated owing to Bleaney-Bower's singlet-triplet model using the equation 2-28,

$$I_{EPR}T = C\frac{3}{\left(3 + exp\left(-\frac{2J}{k_B T}\right)\right)} \quad \textbf{2-28}$$

In precept the ground sate of a high spin molecule can be determined using temperature dependent EPR measurement data in a glass matrix. A linear increase of EPR signal intensity with temperature indicates no thermal population or depopulation of spin state

of molecule in given temperature range.

2.9 Instrumentation

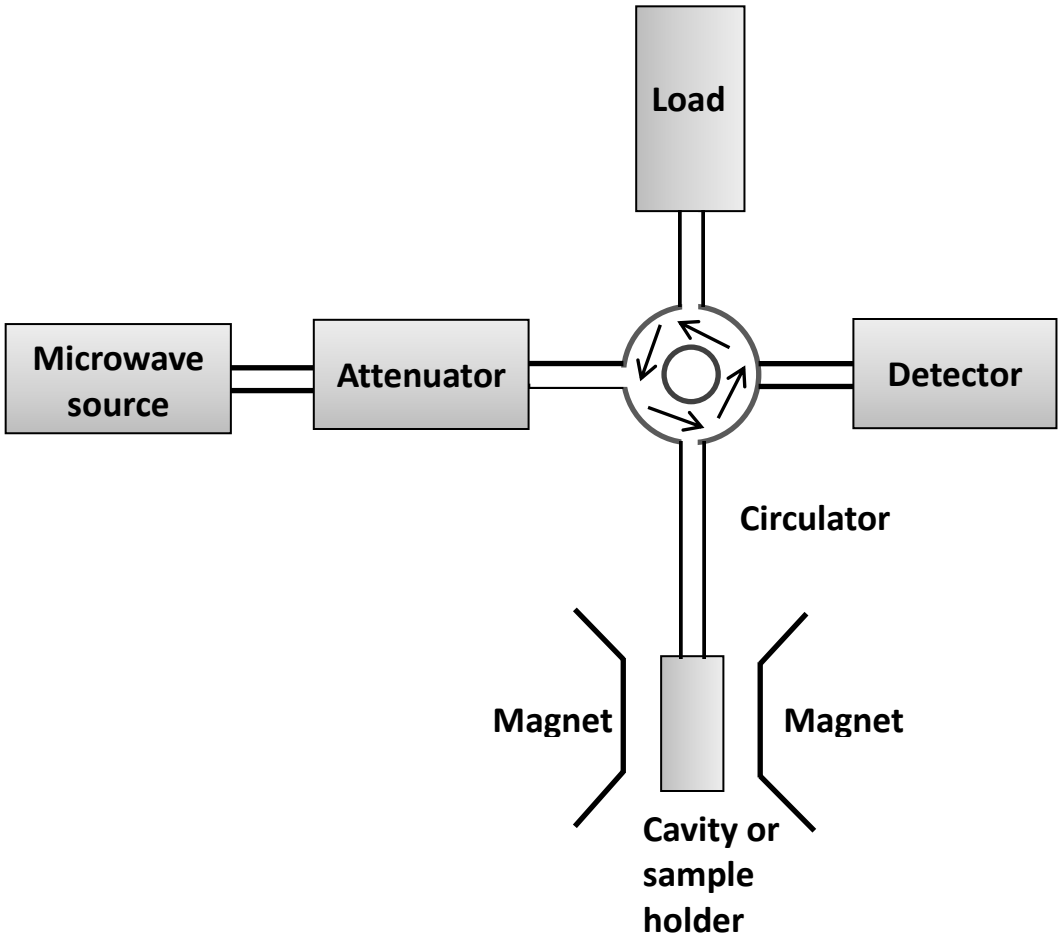

Figure 2.9: Schematic block diagram continuous wave EPR spectrometer.

The majority of CW EPR instruments are based on the general design shown in the schematic diagram (Figure 2.9). The plane polarized microwaves are generated by the klystron tube and the power level adjusted with the attenuator. The circulator behaves as a traffic circle and directs the microwaves to the cavity where the sample is mounted. At resonance, a portion of the microwaves are absorbed by the sample. The microwaves reflected back from the cavity are routed by the circulator to the diode detector. Excess of any microwave reflected from the diode are absorbed completely by the load.

2.10 Summary

After having basic information about the principles of EPR spectroscopy a vast amount of information can be extracted from the EPR spectra measured using different experimental conditions (concentration, temperature etc).

- The selection rules for EPR spectroscopy, $\Delta M_S = \pm 1$ and $\Delta M_I = 0$. Number of lines in EPR spectrum can be given by 2nI + 1.
- *g*-value calculated using formulae, $g = 714.5 \times \frac{frequency\ of\ instrument\ (GHz)}{applied\ field\ (G)}$.
- *g*-value gives the information about the species of the atom on which the unpaired electron lies, the molecular orbitals in which the unpaired electron resides, the nature of the chemical bonds to which the unpaired electron belongs, and the surrounding molecular environments from which the unpaired electron experience the interactions.
- The electron-nuclear hyperfine interaction pattern gives information about number and type of magnetic nuclei with which the unpaired electron interacts.
- *ZFS* parameters *D* and *E* are usually obtained from the EPR spectrum measured at low temperature in solvent glass matrix.
- Geometrical shape of spin distribution can be estimated from *zfs* parameters *D* and *E*.
- Distance between two spins is inversely proportional to the cube root of *zfs* parameter *D* and can be calculated using the formulae, $d = 0.138/|D|^{1/3}$, *d* and *D* are in nm and cm^{-1} units, respectively.
- The ground state of high spin molecule can be determined using variable temperature EPR measurement in glass matrix.
- From the variable temperature EPR spectrum exchange coupling constant can be calculated by fitting Bleaney-Bowers equation, $I_{EPR}T = C\frac{3}{\left(3+exp\left(-\frac{2J}{k_BT}\right)\right)}$ the sign of *J* gives information about the type of exchange interaction i.e.

antiferromagnetic or ferromagnetic.

Further reading, [1-12]

[1] P. H. Rieger, in *Electron Spin Resonance Analysis and Interpretation*, The Royal Society of Chemistry, Cambridge CB4 0WF, UK, **2007**.

[2] Fabian Gerson, W. Huber, in *Electron Spin Resonance Spectroscopy of Organic Radicals*, WILEY-VCH Verlag GmbH & Co. KGaA, Weinheim, **2004**.

[3] M. Baumgarten, High Spin Molecules Directed Towards Molecular Magnets. In *EPR of Free Radicals in Solids II*, A. Lund, M. Shiotani, Eds. Springer Netherlands: 2012; Vol. 25, pp 205.

[4] John A. Weil, J. R. Bolton, in *Electron Paramagnetic Resonance: Elementary Theory and Practical Applications, Second Edition*, John Wiley & Sons, Inc., New Jersey, **2006**.

[5] G. E. Uhlenbeck, S. Goudsmit, *Nature* **1926**, *117*, 264.

[6] D. L. Griscom, *J. Non-Cryst. Solids* **1980**, *40*, 211.

[7] D. J. Griffiths, *American Journal of Physics* **1982**, *50*, 698.

[8] N. J. Bunce, *J. Chem. Educ.* **1987**, *64*, 907.

[9] Gertz I. Likhtenshtein, Jun Yamauchi, Shin'ichi Nakatsuji, Alex I. Smirnov, a. R. Tamura, in *Nitroxides Applications in Chemistry, Biomedicine, and Materials Science*, WILEY-VCH Verlag GmbH & Co. KGaA, Weinheim, **2008**.

[10] K. A. Sandberg, D. A. Shultz, *J. Phys. Org. Chem.* **1998**, *11*, 819.

[11] B. Bleaney, K. D. Bowers, *Proc. R. Soc. London A* **1952**, *214*, 451.

[12] E. Wasserman, L. C. Snyder, W. A. Yager, *J. Chem. Phys.* **1964**, *41*, 1763.

CHAPTER 3

TUNING THE INTER-MOLECULAR EXCHANGE INTERACTIONS IN TOLANE-BRIDGED NN BIRADICALS

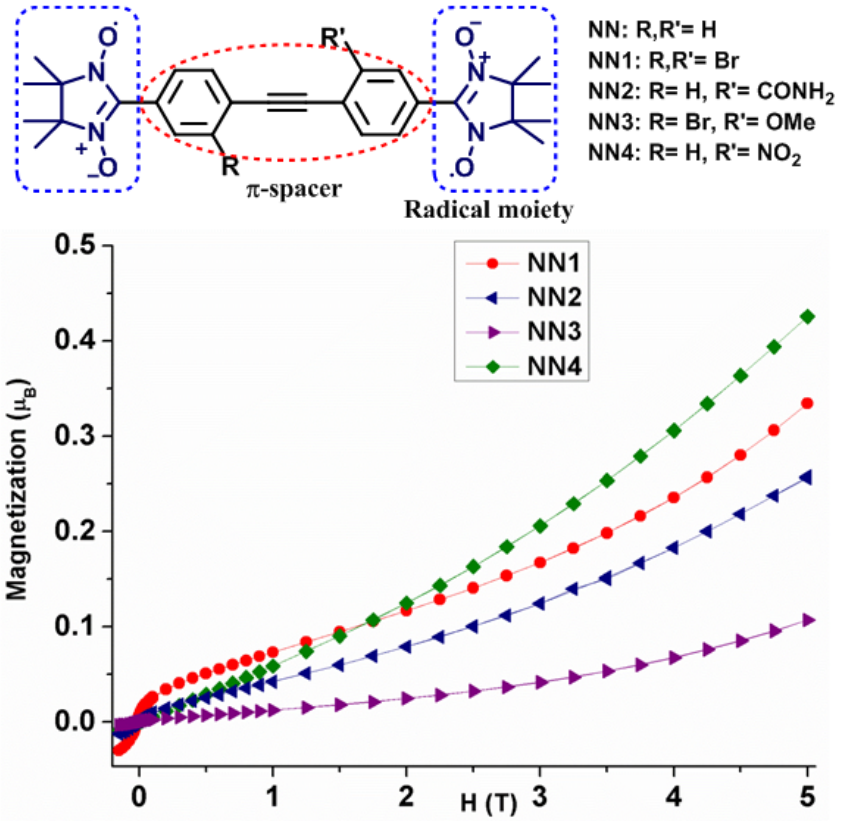

The intra-molecular magnetic exchange interactions can be tuned by either changing the radical moiety or the π-spacer in a predictable manner. The inter-molecular exchange interactions cannot be simply tuned because of the unpredictable molecular self-organization in a crystal lattice. In this chapter we have shown the tuning of inter-molecular magnetic exchange interactions, in the tolane bridged nitronyl nitroxide biradicals, utilizing the crystal engineering approach.

Note: Large part of this chapter has been published in Crystal Growth and Design, 2014, DOI: 10.1021/cg5010787.

3.1 Introduction

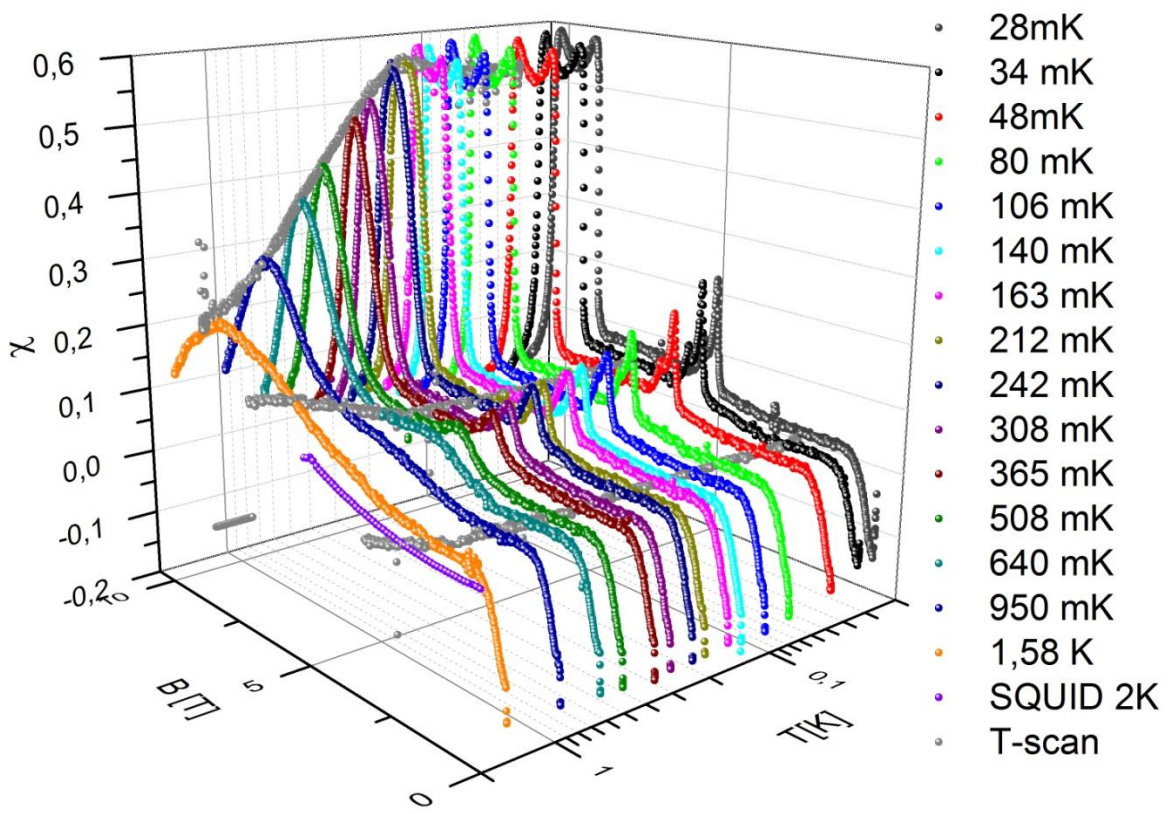

Figure 3.1: Magnetic field induced quantum phase transition.

Previously in our laboratory, it was found that tolane bridged nitronyl nitroxide biradical (**NN**, Scheme 3.1) undergoes quasi two dimensional magnetic field induced quantum phase transition at millikelvin temperatures in the routine laboratory magnetic field up to 11 T.[1] As shown in Figure 3.1, the AC susceptibility measurements were performed at sub Kelvin temperature under the applied magnetic field up to 11 T. The rounded double peak structure between lower critical field and the saturation field in the AC susceptibility measurements indicated the "Berezinskii-Kosterlitz-Thouless" type two-dimensional magnetic field induced phase transition.[2-3] In this case the estimated inter- and intra-molecular exchange interactions were −1 to −2 K and −4.8 K, respectively.[4] These findings demonstrated the prospective utilization of weakly AF coupled nitronyl nitroxide biradicals to generate quantum magnets. Continuing our investigations in this

direction the tolane bridged biradicals, decorated with hydrogen bond donor and/or acceptor functional groups, were designed (Scheme 3.1) to achieve the fine tuning of the inter-molecular magnetic exchange interactions and to obtain a three-dimensional hydrogen bonded spin-lattice in the crystalline form.

The focus of the present chapter was to study the structurally similar compounds exhibiting different magnetic behavior. It was expected to achieve such effect by retaining the intra-molecular exchange pathway through maintaining the geometry of the tolane bridge, and leaving the inter-molecular exchange interactions as the main variable. A functional group is a delicate, yet powerful tool with the potential to alter the motif of crystal packing. Therefore, it was intriguing to examine the influence of functional groups on the character and magnitude of the inter- and intra-magnetic exchange interactions.

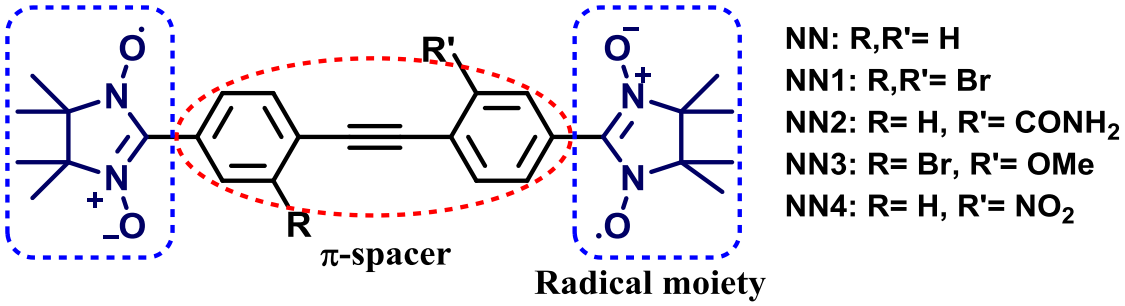

Scheme 3.1: Functionalized tolane bridged nitronyl nitroxide biradicals.

3.2 Synthesis of functionalized tolane bridged biradicals

The key precursor for the synthesis of nitronyl nitroxide biradicals are dialdehydes.[5] The general approach towards the synthesis of tolane bridged dialdehydes relied on Pd(II) catalyzed Sonogashira-Hagihara cross coupling reaction as shown in Scheme 3.2. Condensation of dialdehyde with 2,3-bis(hydroxylamino)-2,3-dimethyl butane (BHA) gave bisimidazolidine in quantitative yield. The oxidation of bisimidazole was performed with $NaIO_4$ in DCM/H_2O two phase mixtures.

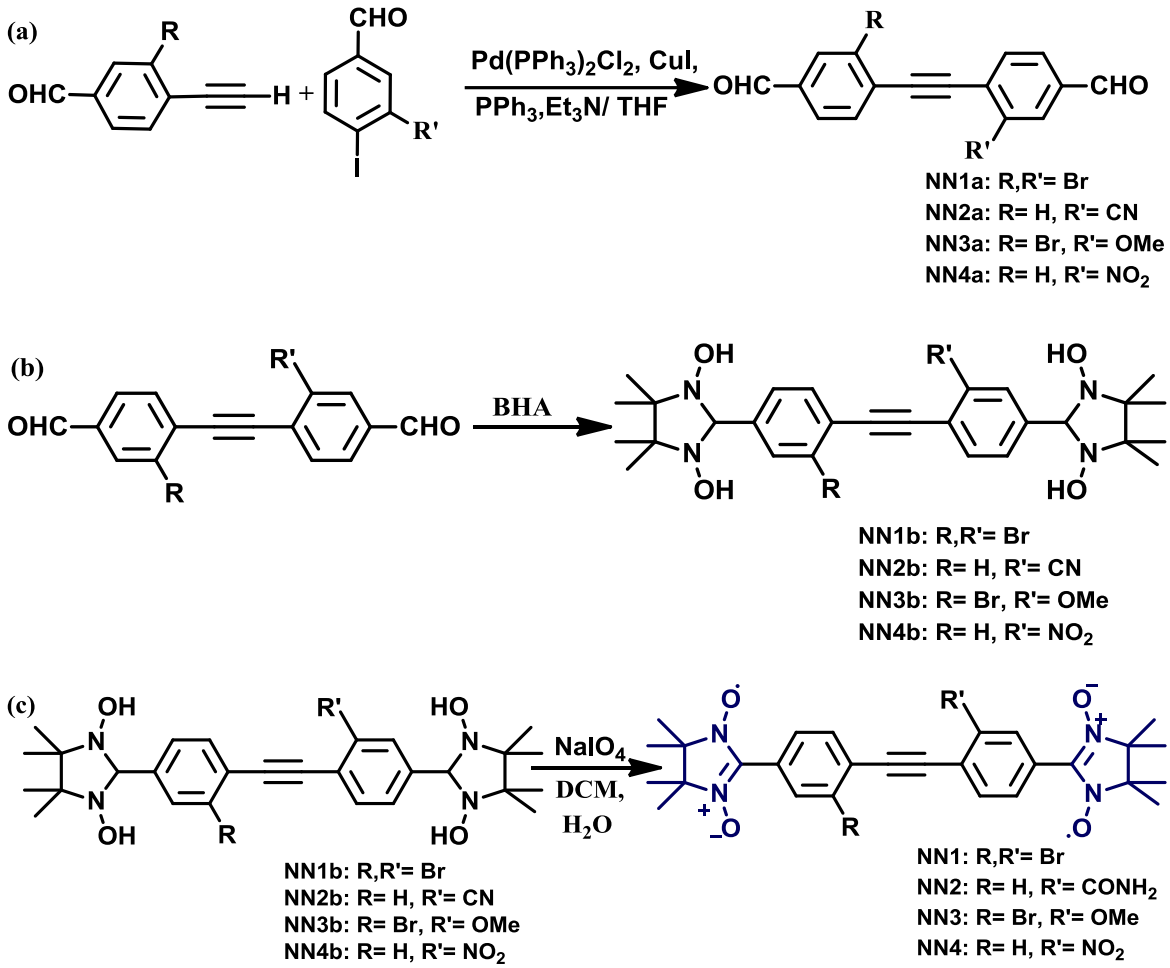

Scheme 3.2: General synthetic route to the synthesis of functionalized tolane bridged (a) dialdehyde, (b) bisimidazolidine and (c) nitronyl nitroxide derivatives.

Inspired by the literature procedures[6-7] for the synthesis of ethynylbisbenzaldehyde with good yields using one pot Pd catalyzed Sonogashira coupling reaction, as shown in Scheme 3.3a, Sonogashira coupling reactions were performed to obtain 4,4'-(ethyne-1,2-diyl)bis(3-bromobenzaldehyde) (**NN1a**). But the reaction ended in very poor yield with many side products. So it was necessary to find out an alternate route for the synthesis of **NN1a**. As shown in Scheme 3.3b the **NN1a** can be obtained by step wise Sonogashira coupling reaction of 4-iodo-3-bromo-benzaldehyde (**2**).[8-9] The Sonogashira coupling reaction of **2** with TMSA (trimethylsilylacetylene), yielded compound **6** (70% yield), which on deprotection of trimethylsilyl under mild basic

condition gave the product **7** in 90% yield. Further coupling of **7** with **2** resulted in the desired product **NN1a** in 65% isolated yield. Similarly aldehydes **NN2a** to **NN4a** were also synthesized in good yield following this stepwise Sonogashira reaction sequence.

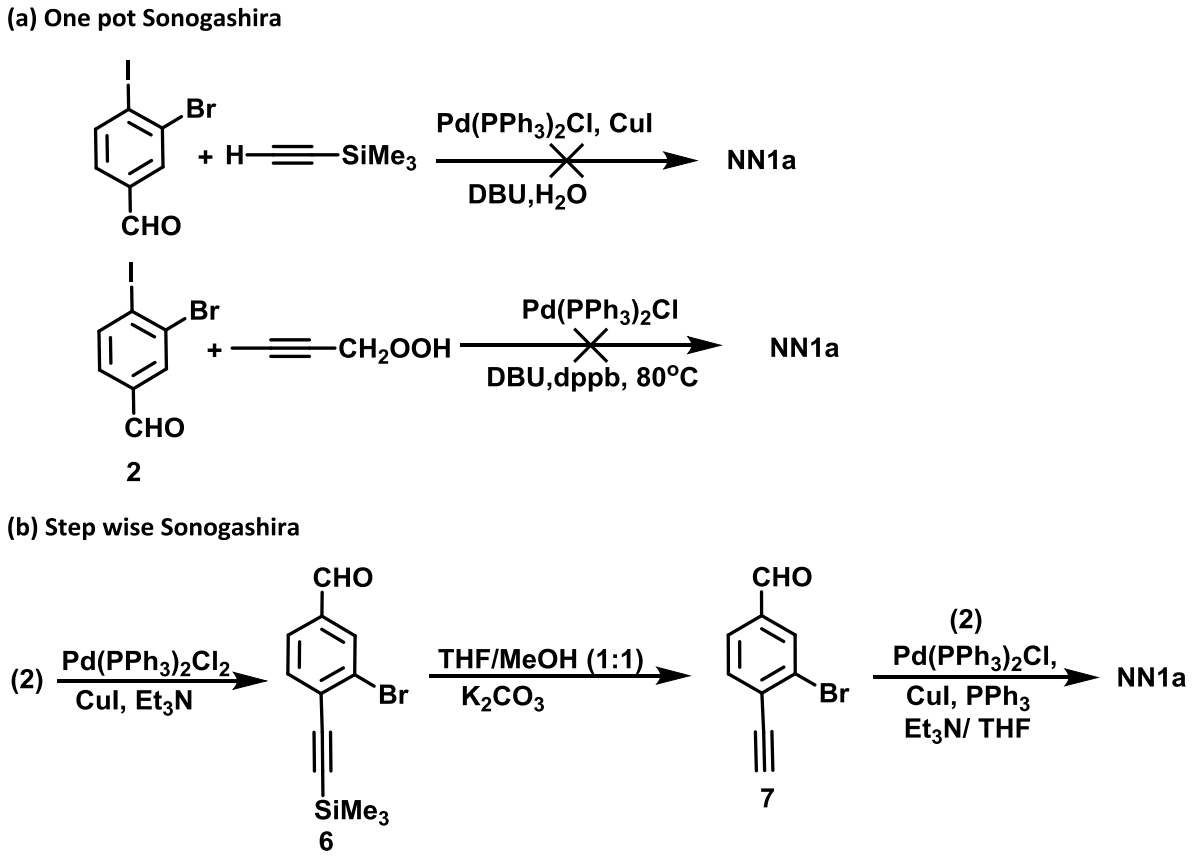

Scheme 3.3: (a) one pot and (b) stepwise Sonogashira coupling reaction for the synthesis of **NN1a**.

The condensation of dialdehyde with BHA was sensitive to reaction solvent and the temperature. The reaction of **NN1a** and **NN3a** with BHA in toluene at 90 ^{o}C for two days gave the desired product **NN1b** and **NN3b**, respectively, in quantitative yields. Under similar reaction conditions the condensation reaction of **NN2a** and **NN4a** with BHA did not form the desired product, probably because of the poor stability of condensation product under these conditions. After several trials using different solvents and reaction temperatures the optimized conditions listed in Table 3.1 gave the best yields. Oxidation of bishydroxylamines is a gentle process, and must be performed with care to avoid the

formation of imino nitroxide radicals or mixed species.[10] Thus, oxidation with equimolar $NaIO_4$ in an ice bath led preferably to the desired nitronyl nitroxide biradicals.[11]

Table 3.1: Optimized reaction conditions for synthesis of **NN1a-NN4a**.

Compound	Solvent	Temperature	Time
NN1a	Toluene	90 °C	2 days
NN2a	Toluene	90 °C	2 days
NN3a	Toluene	65 °C	5 days
NN4a	DCM/MeOH	Room temp.	7 days

The synthesized biradicals **NN1-4** were characterized by UV-Vis, EPR and single crystal X-ray analysis. Magnetic measurements and DFT calculations were performed to collect information about the electronic structure and magnetic properties of the biradical species.

3.3 UV-Vis analysis

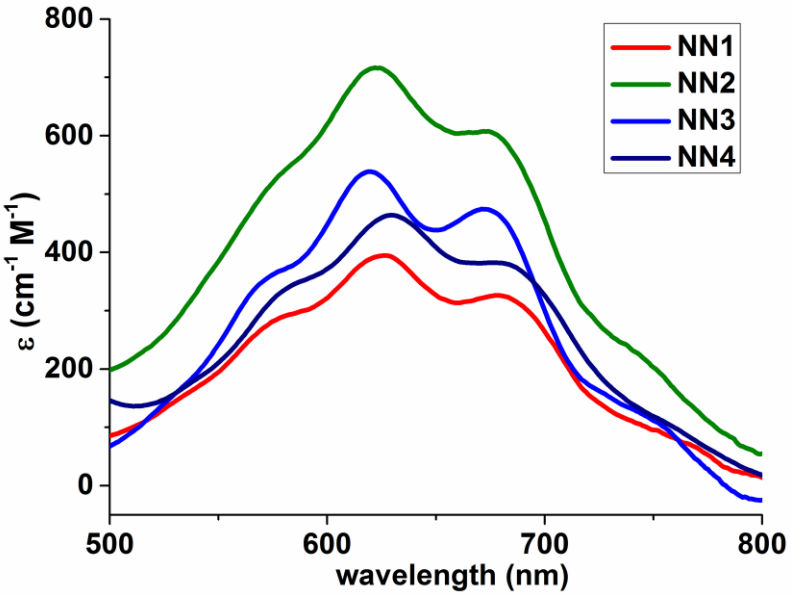

Figure 3.2: Characteristic n—π* transition of biradicals **NN1-4** in toluene (c ~ 10^{-4} M).

The obtained biradicals were fairly good soluble in polar organic solvents. As they show prolonged stability in aprotic solvent like toluene or benzene, the UV-Vis measurements were performed in toluene with concentration of ~10^{-4} molar. The UV-Vis spectrum of neutral radicals gave clear insight of the corresponding radical moieties. The biradicals **NN1-4** displayed nearly identical weak absorption around 620-630 nm (Figure 3.2). This weak absorption in visible range was a characteristic n—π* transition stemming from nitronyl nitroxide radical moiety. Thus the UV-Vis spectra confirmed the presence of radical moieties in the synthesized compounds.

3.4 EPR analysis

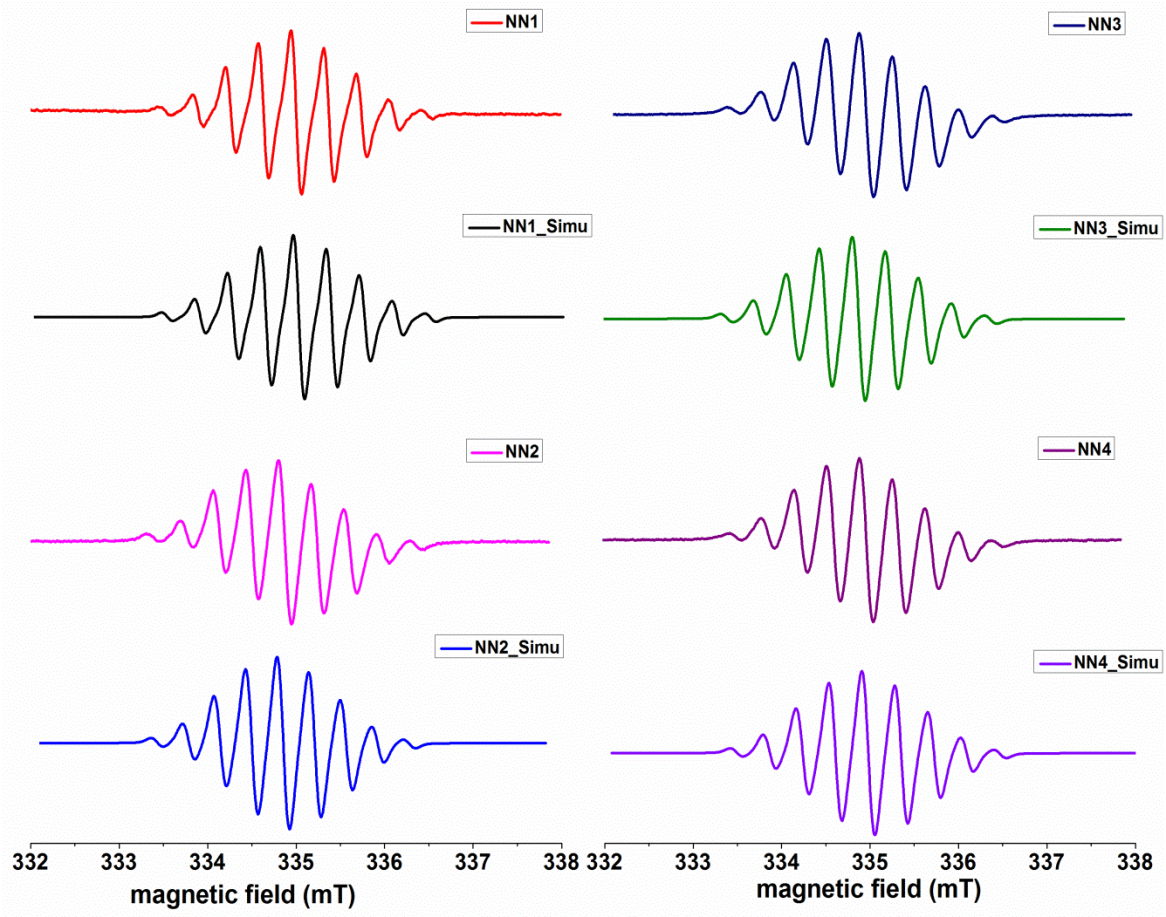

Figure 3.3. X-band EPR spectra of biradicals **NN1-4** in toluene (c ~ 10^{-4} M) at room temperature and simulated EPR spectra.

The EPR spectra of biradicals were measured in toluene at ~10^{-4} molar concentration. The typical EPR spectra of biradicals consisted of nine well-resolved lines due to hyperfine coupling (*hfc*) of two electron spins with four equivalent nitrogen atoms at g_{iso} = 2.0068 (Figure 3.3) following the formula, 2nI + 1, for exchange coupled biradicals. The *hfc* and g-values were calculated by spectral simulation and are listed in Table 3.2. The experimental EPR spectra were in agreement with simulated one. The obtained *hfc,* $a_{N1}/2$ = 0.372 mT, which is half of the *hfc* for mono nitronyl nitroxide. The EPR spectra for all biradicals demonstrated that the exchange interactions (*J*) between the radical moieties are much larger than the hyperfine coupling ($J >> a_N$).

3.5 Crystal structure analysis

Magnetic interactions highly depend on the geometry and packing of the molecules in the crystal lattice. Therefore single crystal analysis of the radicals is a vital requirement to understand their magnetic properties. The single crystals were grown by slow diffusion of hexane to a solution of biradical in DCM at room temperature. Good quality single crystals were obtained for the biradicals **NN1**, **NN2**, and **NN3**.[12-13] All the attempts to obtain single crystal of **NN4** failed. The unit cell parameters, space group and other crystallographic details are listed in crystallographic table (Appendix-III). Biradical **NN1** crystallized in non-centro symmetric monoclinic, $P2_1$, chiral space group. Crystal structure analysis revealed that **NN1** forms sheet structure. In the sheet molecules of **NN1** recognizes each other through C—H···O and C—H···Br hydrogen bonds, forming the planar herringbone pattern in two dimensions (Figure 3.2a). The >N—O group of radical moiety in **NN1** forms weak C—H···O hydrogen bonds with the phenyl and methyl protons of two neighboring molecules (highlighted blue area, Figure 3.4a). These sheets further stack through π—π interaction and C—H···O hydrogen bond (Figure 3.4b). Furthermore the torsion angles of the terminal nitronyl nitroxides with the benzene ring of the tolane bridge are 26.6° and 25.6°.

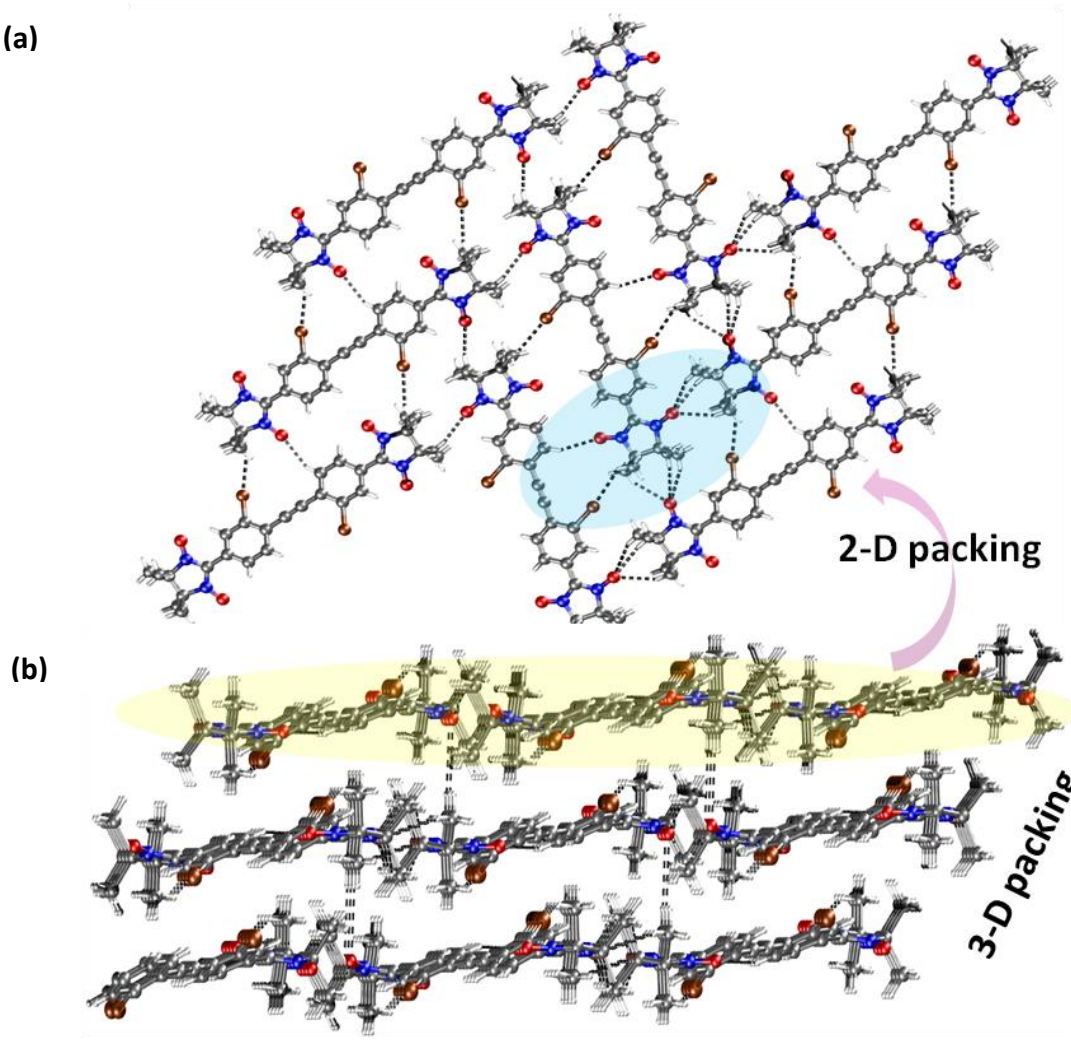

Figure 3.4: Crystal packing of **NN1**.

Biradicals **NN2** and **NN3** were crystallized in monoclinic, Pc, and tetragonal, $I4_1/a$, space groups, respectively. Careful structural analysis showed that while **NN1** exhibited only two dimensional hydrogen bonded network, interestingly the **NN2** and **NN3** formed three dimensional networks (Figure 3.5 and 3.6). This is probably due to more flexible and/or hydrogen bond donor functional groups attached to the tolane bridge in case of **NN2** and **NN3**. In two dimensions the molecules of **NN2** forms non planar herringbone pattern (Figure 3.5a). The molecules of **NN2** recognize each other through π—π stacking and strong N—H···O hydrogen bonds. This two dimensional herringbone structure further

extends in three dimensions through N—H···O and C—H···O hydrogen bonds (Figure 3.5b). It should be noted that the >N—O group of the radical moiety in **NN2** recognizes two neighboring molecules through amide functional group utilizing strong N—H···O hydrogen bond, thereby indicating the possible way to transmit magnetic exchange interaction through strong hydrogen bond. Interestingly **NN3** forms non planar layered structure in two dimensions in which the two radical moieties form two different kinds of hydrogen bonding motifs (highlighted with green and yellow strips in Figure 3.6a). While one of the radical moiety forms C—H···O hydrogen bond with methyl, the other radical moiety forms C—H···O hydrogen bond with the methoxy functional group and a phenyl ring. The Br functional group of **NN3** is involved in inter layer C—H···Br hydrogen bond. Moreover torsion angles of terminal nitronyl nitroxides with tolane bridge are 22.7° and 13.4° for **NN2** and 28.6° and 11.3° for **NN3**. One of the terminal radical moieties is more in plane with tolane compared to the other one. According to the crystal structure analysis we could significantly influence the pattern of the interacting spins in the lattice, and move from two to three dimensional order by directing new hydrogen bonding.

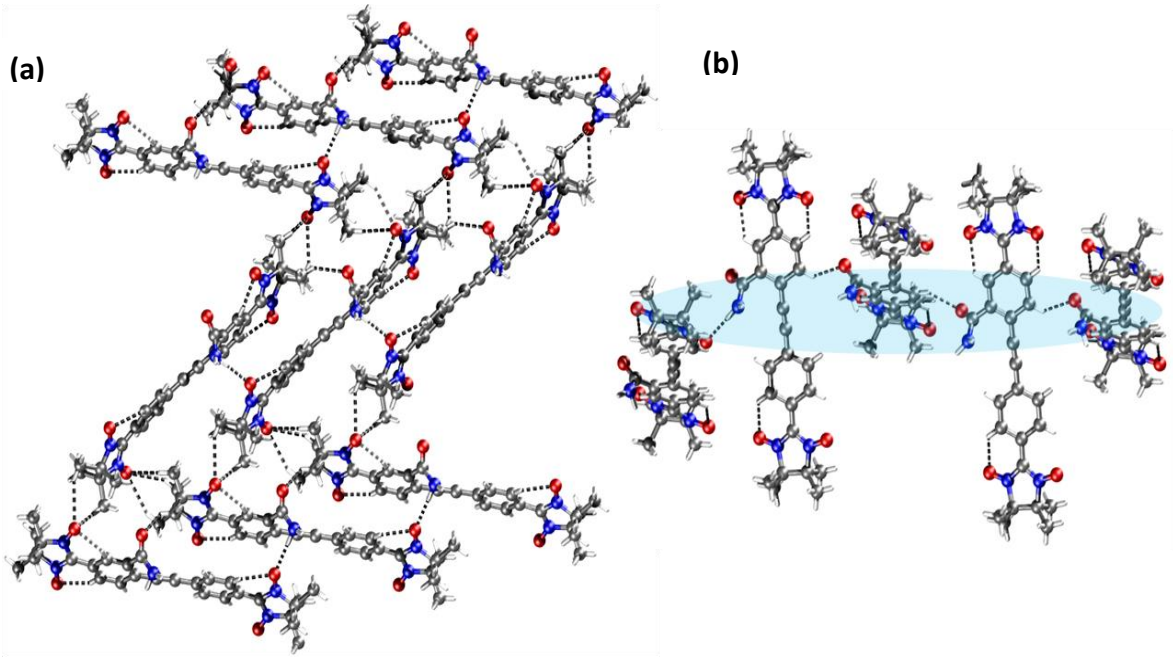

Figure 3.5: Crystal packing of **NN2.**

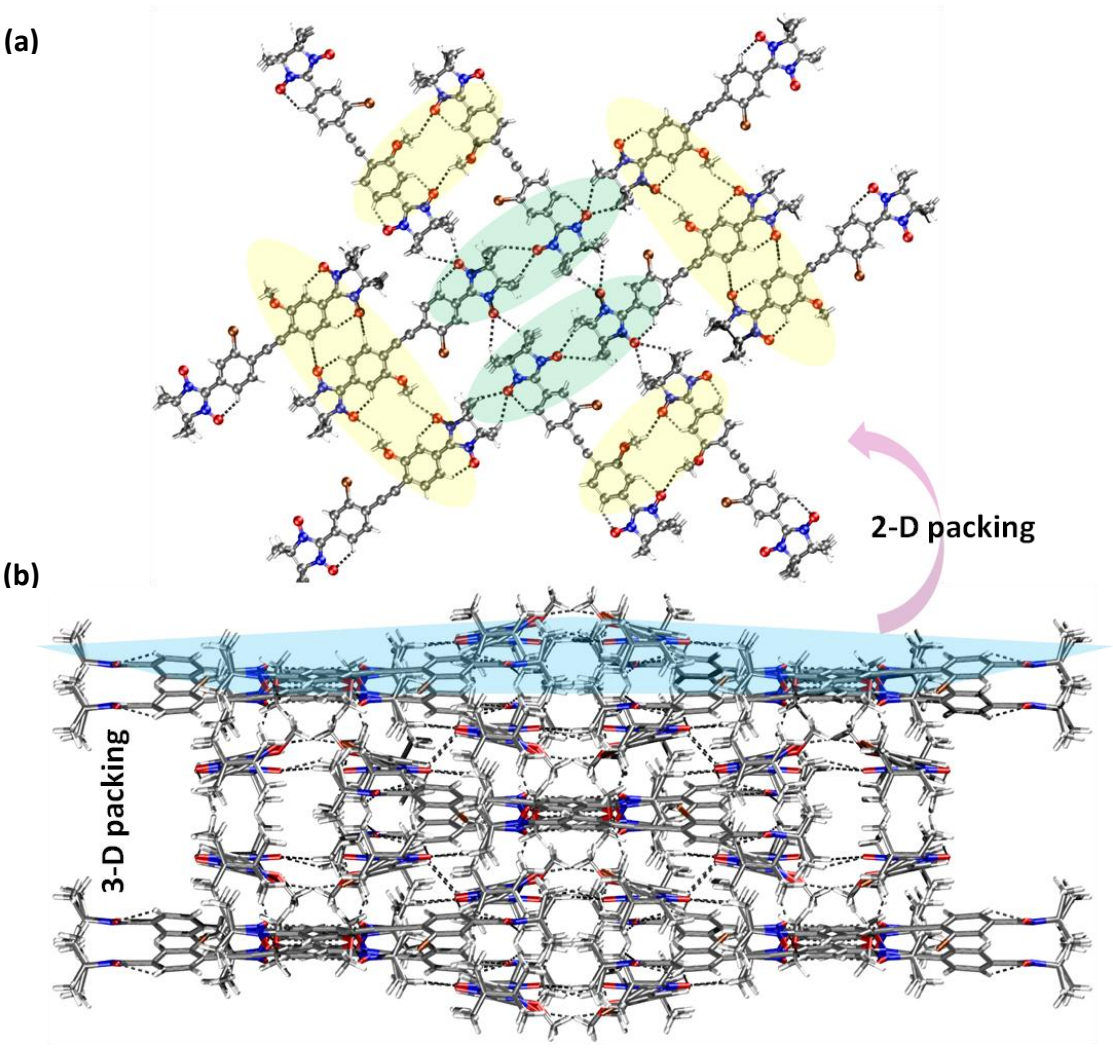

Figure 3.6: Crystal packing of **NN3.**

3.6 Magnetic measurements

Crystal structure analysis provided the evidence about the possible ways of transmitting magnetic interactions in the lattice. On the basis of crystal structure data the information about the magnitude of exchange interactions cannot be obtained precisely. Therefore, magnetic susceptibility and magnetization of polycrystalline sample of biradicals were measured in the temperature range 2 K ≤ T ≤ 200 K using a SQUID magnetometer to understand the nature and extent of the magnetic exchange interactions prevailing in the synthesized tolane bridged biradicals. Background signals of

sample holder and diamagnetic correction were subtracted.[14] The SQUID measurements were performed by Dr. Yoshikazu Ito.

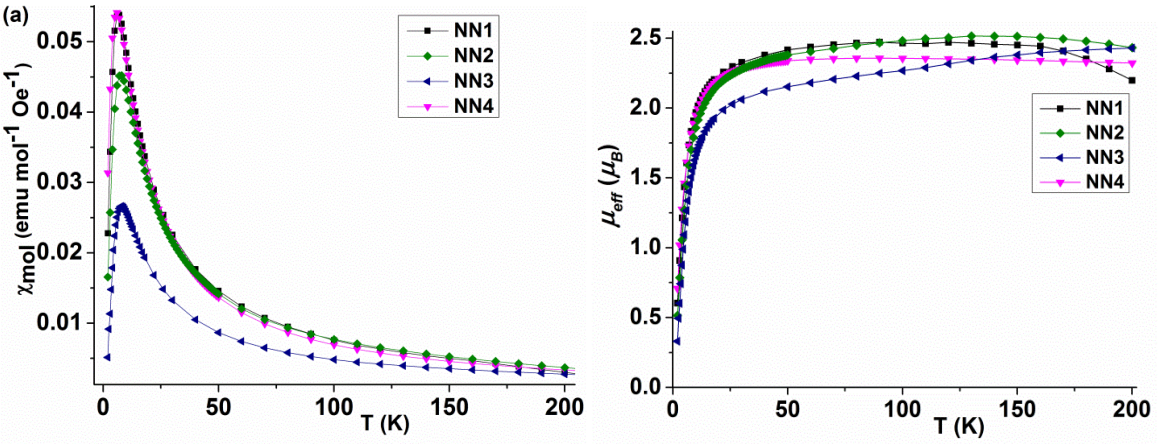

Figure 3.7: (a) Molar magnetic susceptibility, χ_{mol}, (emu/mol/Oe) as a function of temperature under magnetic field 0.1 T. (b) Effective magnetic moment as a function of temperature under magnetic field 0.1 T.

As shown in Figure 3.7a, the molar magnetic susceptibility (χ_{mol}) initially increased with the Curie-Weiss behavior at higher temperature region and decreased at lower temperature with a broad peak mainly caused by intra-molecular AF interactions. On further lowering the temperature, χ_{mol} abruptly decreases close to zero at 2 K which means the biradicals switch from a thermally populated magnetic spin triplet state to a non magnetic spin singlet ground state. All the biradicals exhibited T_{max} from 6 to 8 K. The intra-dimer coupling constant J_{intra} of R-tolane-R' was then estimated using an isolated dimer model ($H = -2J_{intra}S_R S_{R'}$).[15] The obtained intra-molecular exchange interaction values appeared in very narrow range from −3.2 to −4.5 cm^{-1} (Table 3.2). Notably the J_{intra} for functionalized tolane bridged biradicals **NN1**, **NN2** and **NN4** was very close to the non-functionalized tolane **NN** biradical (Table 3.2). Only in case of **NN3** the J_{intra} was slightly higher by 1 cm^{-1} compared to other functionalized tolane bridged biradicals. This very small change in J_{intra} may be originated from the captodative effect of two different functional groups (electron donor methoxy and electron acceptor bromo) attached to the tolane bridge in **NN3**.[16] These observations led to inference that the functionalization of

the tolane bridge didn't influence the intra-molecular magnetic exchange interactions significantly. The negative Weiss temperature was observed in all the biradicals indicating existence of AF intra- and inter-molecular magnetic exchange interactions. The observed effective magnetic moment (μ_{eff}) values for all biradicals were calculated from temperature dependence of magnetic susceptibility under 0.1 T (Figure 3.7b). At 200 K the magnetic moments were close to the theoretical value 2.45 μ_B for magnetically uncorrelated spins[17] of biradicals.

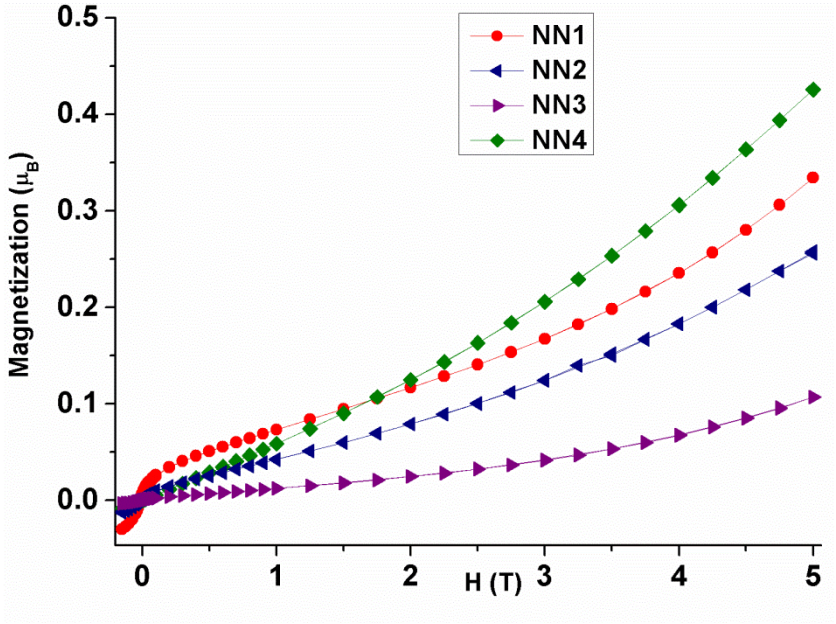

Figure 3.8: Magnetization as a function of magnetic field at 2 K.

The magnetization curves of all the biradicals **NN1-4** were measured at 2 K to understand the influence of hydrogen bonds on inter-molecular exchange interactions. Interestingly, despite of having similar intra-molecular AF interactions, **NN1**, **NN2** and **NN4** showed significant differences in the magnetization under the influence of an applied magnetic field up to 5 T (Figure 3.8). This difference can only be attributed to substantial alteration of the inter-molecular exchange interactions because the intra-molecular exchange interactions were quite similar. The **NN3** with relatively higher J_{intra} showed smallest magnetic field dependence in comparison with the other functionalized

tolane bridged biradicals. In the presence of an applied magnetic field the population of triplet state increases in the order **NN4** > **NN1** > **NN2** > **NN3**. These results are in accordance with the crystal structure analysis, where **NN2** and **NN3** possessing hydrogen bond donor functional group form hydrogen bonds with radical moiety, shows smaller raise in magnetic field induced triplet state population compared with **NN1** and **NN4**. Therefore the hydrogen bonds played an important role in transmitting inter-molecular exchange interactions.

Table 3.2. Magnetic properties of biradicals

	T_{max} (K)	Θ (K)[a]	J_{intra}(exptl) (cm^{-1})[b]	J_{intra}(calcd) (cm^{-1})[d]	g-factor	hfc (a_N/2) (mT)
NN	-	-	−3.3[c]	−6.3	-	-
NN1	6.5	−5.2	−3.6	−5.7	2.0068	0.372
NN2	7.5	−9.0	−3.5	−5.4	2.0067	0.372
NN3	8.0	−17.7	−4.5	−7.3	2.0072	0.372
NN4	6.0	−3.5	−3.2	−6.4	2.0067	0.372
NN+Ag	8.0	-	-	-	-	-

[a]Weiss temperature, [b]Estimated from the magnetic susceptibility measurements (Figure 3.7a) using an isolated dimer model (S = 1/2), [c]reference 1, [d]Calculated at UBLYP/6-31G(d) level of DFT.

3.7 DFT calculations

The intra-molecular exchange interaction energies of the biradical species were also estimated from the DFT calculations.[18] The geometry of biradical **NN1-3** was taken from the X-ray diffraction determinations without further optimization. The geometry of **NN4** obtained from the X-ray geometry of **NN1** by replacing two bromo functional groups by a nitro group and hydrogen. The broken-symmetry approach proposed by Noodleman *et al.* was employed to elucidate the magnetic properties of the biradical species under

study. The exchange coupling constant (*J*) was calculated by the generalized spin projection method suggested by Yamaguchi *et al*.[19-21] For the molecule with two exchange coupled unpaired electrons, the Heisenberg-Dirac-Van Vleck (HDVV) Hamiltonian,

$$H = -2J_{12}S_1S_2, \qquad \textbf{3-1}$$

S_1 and S_2 are the spin angular momentum operators.

$$Exchange\ interaction, \qquad J = \frac{(E(BS) - E(T))}{(S^2(T) - S^2(BS))} \qquad \textbf{3-2}$$

where, E(BS) is the energy of the broken-symmetry (BS) solution, a mixture of singlet and triplet states with $S_Z = 0$ and S^2(BS) close to 1, E(T) is the energy of the triplet state with S^2(T) close to 2, and S^2 are the Eigenvalues of the spin operator for these states.

$$\text{Thus the direct exchange yields, } J \approx E(BS) - E(T) \qquad \textbf{3-3}$$

All DFT calculations were performed with the Gaussian 09 program package.[22] For calculating *J* values the B3LYP is most commonly used functional[23-25] and to increase accuracy, polarization and diffuse functions were added to the basis set.[26] Thus we have initiated our calculation using unrestricted spin polarized density functional theory, UB3LYP/6-31G(d). However the calculated intra-molecular exchange interaction values J_{intra}*(calcd)* were much higher than the J_{intra}*(exptl)* obtained from the magnetic measurements (Table 3.2 & 3.3). Recently Lee *et al*. have used scaling approach to correlate the J_{intra}*(calcd)* with J_{intra}*(exptl)* and obtained scaling factor of 0.38 for *para* and *meta* substituted phenylene biradicals using UB3LYP/6-311++G(d,p) level of theory.[27] Even after applying this scaling factor for tolane bridged biradicals the calculated values deviated largely from experimental results. The observed over estimation of calculated *J* values using UB3LYP functional can be attributed to the spin contamination from Hartree-Fock.[28] Thus to avoid the Hartree-Fock contamination we calculated *J* with UBLYP functional using 6-31G(d) basis set. Interestingly UBLYP/6-31G(d) provided rather

accurate results. The calculated exchange interactions were very close to the same obtained from the magnetic measurements (Table 3.2). Additionally calculated spin density of triplet state of biradicals **NN1-4** was localized over the radical moiety and functionalization of tolane bridge didn't influence the distribution of the spin density (Figure 3.9).

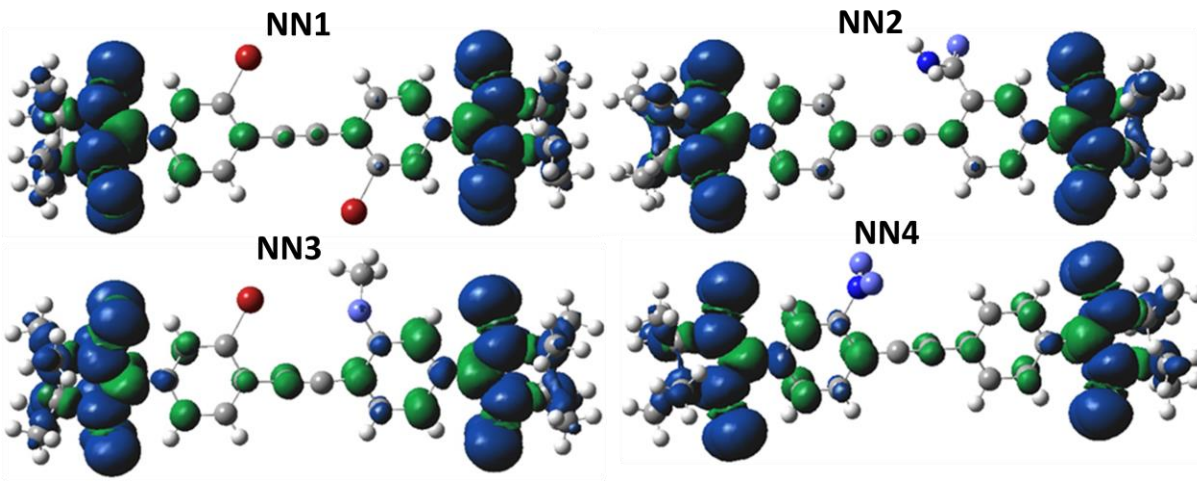

Figure 3.9. Spin density distribution in triplet state of **NN1-4**.

Table 3.3. Summary of DFT calculations.

	Method	*J* (cm^{-1})	E, eV (triplet)	S^2 (triplet)	E, eV (BS)	S^2 (BS)
NN	UB3LYP/6-31G(d)	−23.5	−43683.7450	2.1163	−43683.74792	1.1226
	UBLYP/6-31G(d)	−6.36	−43665.54415	2.0281	−43665.54494	1.0295
NN1	UBLYP/6-31G(d)	−5.77	−183593.6877	2.0274	−183593.6884	1.0287
NN2	UBLYP/6-31G(d)	−5.52	−48253.3057	2.0284	−48253.3063	1.0297
NN3	UBLYP/6-31G(d)	−7.36	−116740.9387	2.0336	−116740.9396	1.0356
NN4	UBLYP/6-31G(d)	−6.44	−49229.37964	2.0314	−49229.38044	1.0323

3.8 Co-ordination of NN with diamagnetic metal ion

In the previous section it was shown that the inter-molecular magnetic exchange interactions can be tuned by introducing hydrogen bond donor or acceptor functional group to the spacer molecule. Another approach, to increase the dimensionality and tuning of magnitude of exchange interactions, is the co-ordination complex formation with diamagnetic metal ion. The diamagnetic metal ions such as Ag(I) and Cu(I), are believed not to mediate magnetic interactions, when complexed with stable organic radical ligands. However it has been shown that antiferromagnetic interactions between the radicals were operative through the diamagnetic metal ions.[29-32] Thus to obtain three dimensional structure and better inter-molecular exchange interactions the metal complex of silver with tolane bridged nitronyl nitroxide biradical (**NN**) have been synthesized.

3.8.1 Synthesis

To the solution of $Ag(CF_3COO)$ in minimum amount of methanol, the solution of tolane nitronyl nitroxide biradical (**NN**) in DCM was added. The resulting clear solution was filled in NMR tube over which hexane was added and allowed for slow diffusion. After few days dark blue colored needle shaped crystals suitable for single crystal X-ray diffraction were obtained.

3.8.2 Crystal Structure

The co-ordination complex of **NN** and $Ag(CF_3COO)$ (**NNAg**) was crystallized in triclinic Pī space group. Careful structure analysis revealed that there are four different coordination environments present in each repeating unit of complex (Figure 3.10). Two different types of chains of silver are connected by co-ordination through the tolane biradical forming ladder type architecture in two dimensions (Figure 3.11). This discrete repeating unit further extends in three dimensions by co-ordination through tolane

biradical and by O—H···O hydrogen bond (2.25 Å) formation between two coordinated water molecules (Figure 3.12). The repeating NN biradicals are separated by layer of silver cluster and recognizes each other through Ag metal ion. This is quite undesirable as an excessive layer of silver may dilute the inter-molecular exchange interactions.

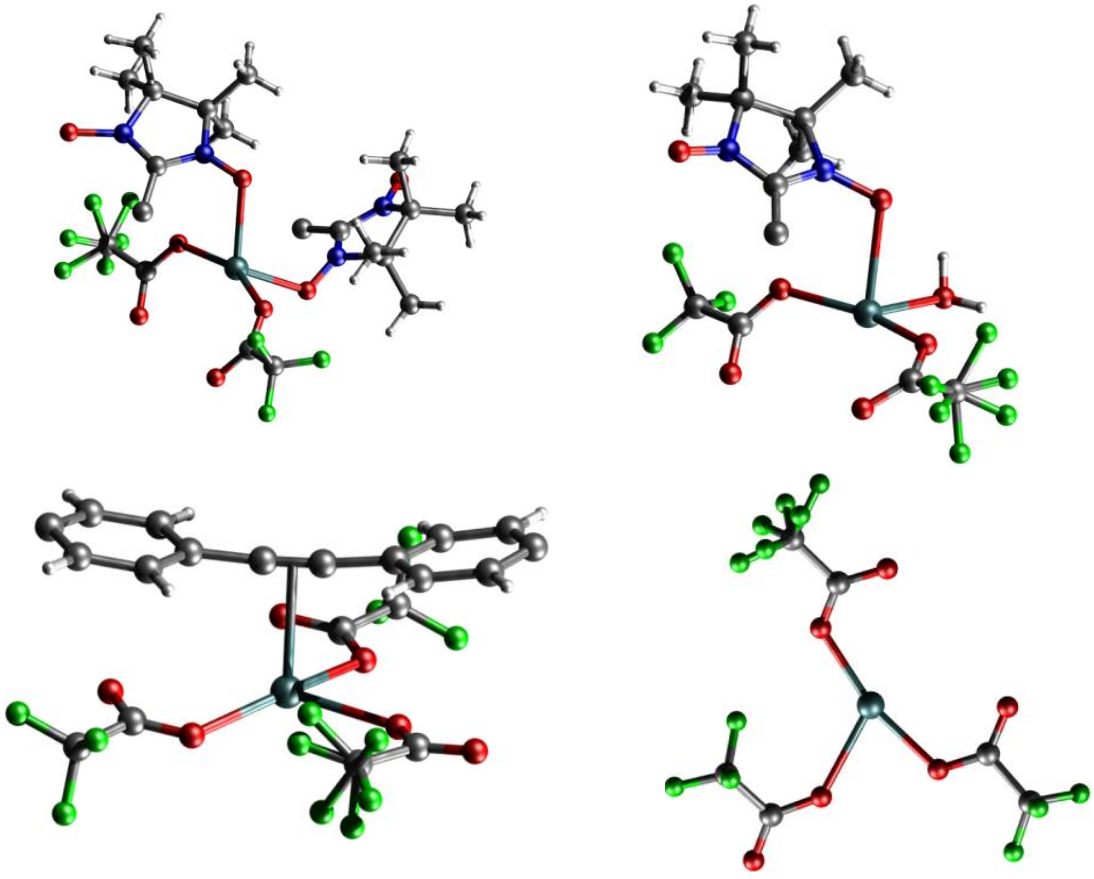

Figure 3.10. Four different coordination environments of Ag.

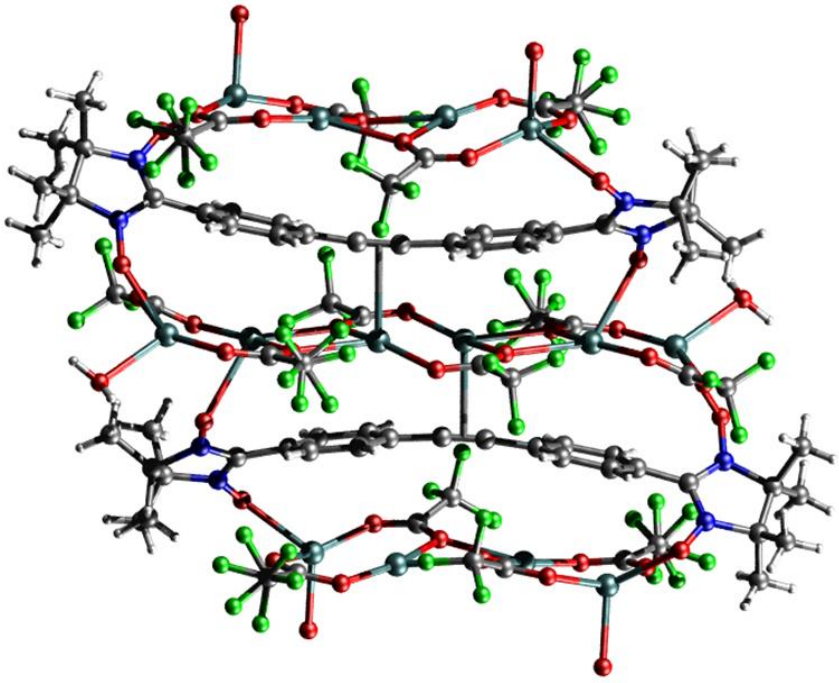

Figure 3.11. Discrete ladder type architecture formed by alternative ligand and silver chain.

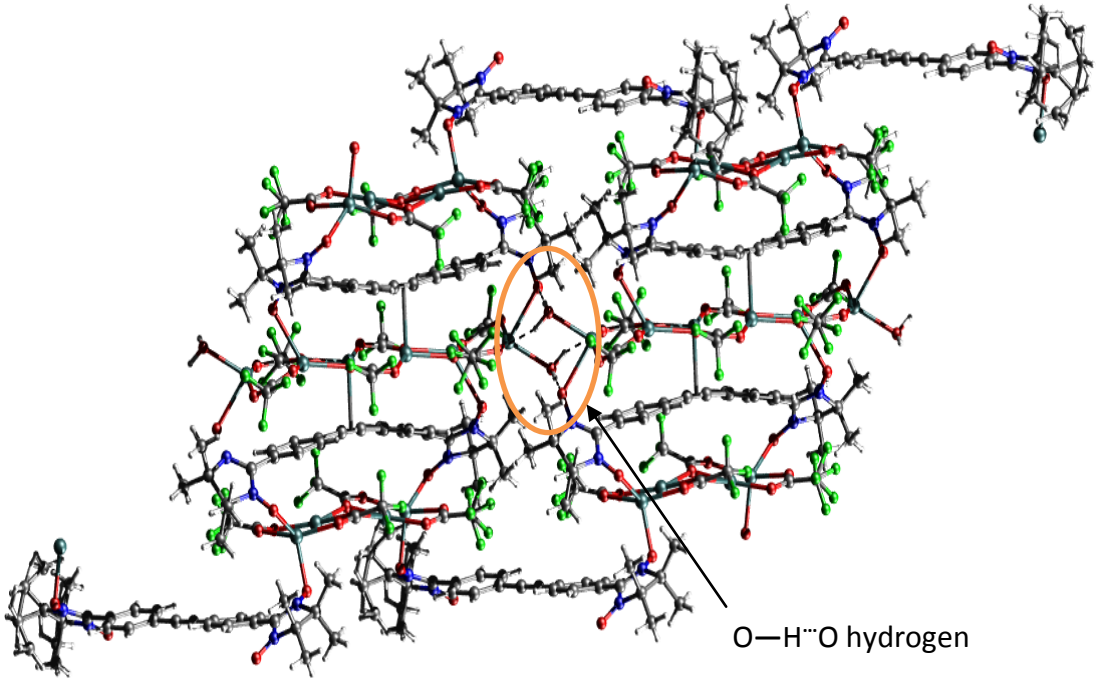

Figure 3.12. Further extension of repeating unit by coordination of ligand and hydrogen bond formation between coordinated water molecules.

3.8.3 Magnetic properties

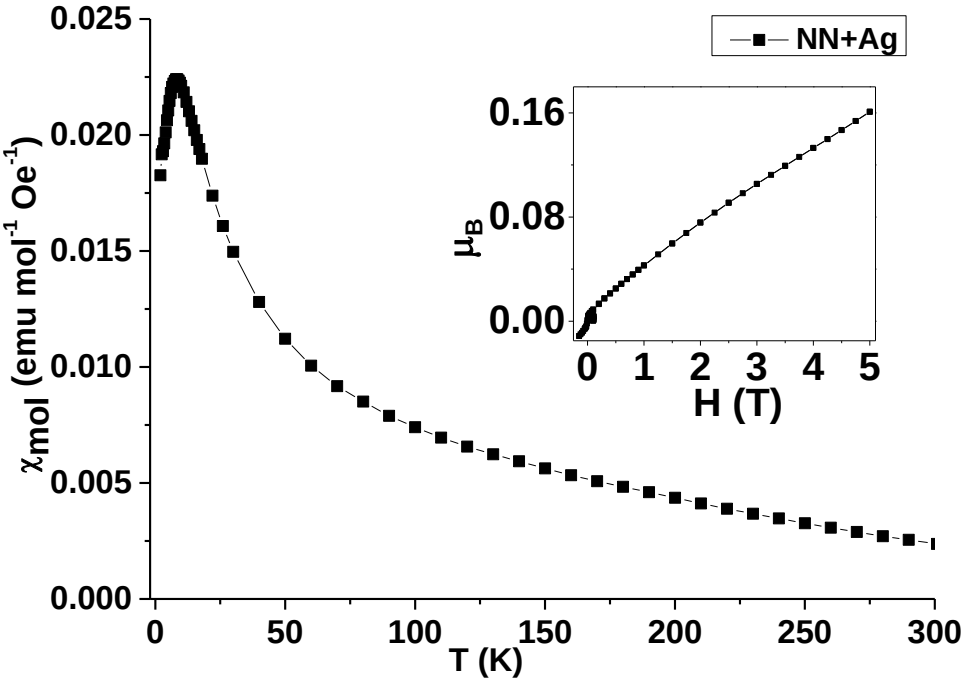

Figure 3.13. Magnetic susceptibility as a function of temperature under magnetic field 0.1 T, Inset: Magnetization as a function of magnetic field at 2 K.

To probe into magnetic properties of metal-complex, magnetic measurements were performed in the temperature range 2 K ≤ T ≤ 300 K. The magnetic susceptibility measurements showed a similar behavior as the functionalized tolane bridged nitronyl nitroxides. Here the transition temperature T_{max} from thermally populated magnetic spin triplet state to a non-magnetic spin singlet ground state is 8 K which in the same range as the T_{max} for **NN1-4** (Figure 3.13). This indicates that the exchange coupling constant J_{intra} is of same order of magnitude as **NN** and other tolane bridged nitronyl nitroxide derivatives. Thus the intra-molecular magnetic exchange interactions are not influenced by complex formation with Ag metal ion.

3.9 Summary

In conclusion we have successfully introduced hydrogen bond donor and acceptor groups at the tolane bridge to obtain functionalized tolane bridged nitronyl nitroxide biradicals. Although the intra-molecular exchange interactions remained similar on functionalizing the tolane bridge, a significant difference in the magnetization was observed upon application of an external magnetic field. Crystal structure analysis revealed that hydrogen bond donor functional groups formed hydrogen bonds directly with the radical moieties and thereby increased the inter-molecular exchange interactions. Thus, by utilizing the crystal engineering approach the tuning of inter-molecular exchange interactions was realized. Furthermore DFT calculations were employed to determine the exchange interactions. The calculated values of intra-molecular coupling constant J_{intra} were well in accordance with the ones obtained from the magnetic susceptibility measurements. Quantitative estimation of inter-molecular exchange interactions requires more sophisticated magnetic measurements. Additionally a metal-organic framework of NN with Ag metal ion was synthesized. Interestingly the intra-molecular magnetic exchange interactions were not influenced by complex formation with silver salt.

3.10 Synthetic details

4-Amino-3-bromo benzaldehyde (1)

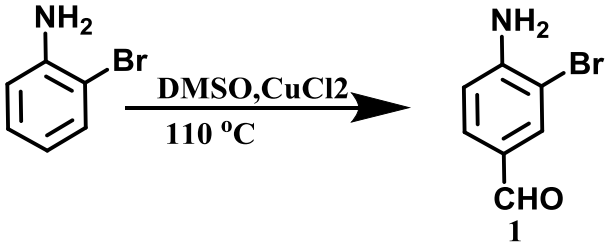

The mixture of 2-bromoaniline (7.0 g, 40 mmol) was dissolved in DMSO (300 ml), concentrated aqueous HCl (30 ml) and $CuCl_2$ (10.7 g, 80 mmol) was added in a 500 ml round bottom flask with reflux condenser was heated at 90 °C for 8 hour. The reaction was quenched with ice-water, the pH of mixture was adjusted to 8 with 10% solution of NaOH and the mixture was extracted with Et_2O (4 X 100 ml). The solvent was evaporated and crude product was purified with column chromatography (9:1, Hexane: Ethyl acetate). The 4-amino-3-bromo benzaldehyde was obtained with 66% yield. M.P. 101 °C. ^{1}H NMR (250 MHz, $CDCl_3$) δ 9.71 (s, 1H), 7.89-7.88 (d, 1H), 7.59-7.55 (dd, 1H), 6.75-6.72 (d, 1H), 4.70 (s, 2H). **MS-FD** (8 kV, CH_2Cl_2) m/z: found 201.1 (100%).

3-Bromo-4-iodobenzaldehyde (2)

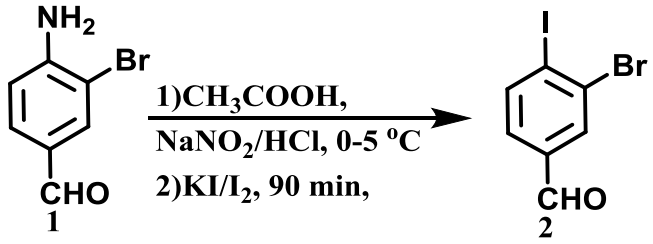

To the solution of 4-amino-3-bromobenzaldehyde (**1**) (3.4 g, 17 mmol) in 70 ml acetic acid, 18 ml HCl (6 molar) was added and the resulting suspension was cooled in ice/salt bath. To this cooled suspension the solution of $NaNO_2$ (1.3 g 19 mmol) in 40 ml H_2O was added slowly maintaining internal temperature of the reaction mixture <5 °C,

the solution was stirred for 30 minutes and then the resulting clear solution was poured into solution of KI (5.6 g, 35 mmol) and iodine (1.14 g, 4.5 mmol) in 40 ml H_2O and the mixture was stirred for 90 minutes at room temperature. 100 ml of water added and the mixture was extracted with DCM (4 × 100 ml). The collected extracts were washed with aqueous $Na_2S_2O_4$ solution (10% w/v, 2 × 100 ml), aqueous NaOH (2.0 M, 100 ml), water (2 × 100 ml) and brine solution (50 ml). The 3-bromo-4-iodobenzaldehyde obtained in 72% yield. M.P. 65 °C. ^{1}H NMR (250 MHz, $CDCl_3$) δ 9.91 (s, 1H), 8.09-8.05 (m, 2H), 7.49-7.45 (dd, 1H). **MS-FD** (8 kV, CH_2Cl_2) m/z: found 311.9 (100%).

2-Amino-5-formylbenzonitrile (3)

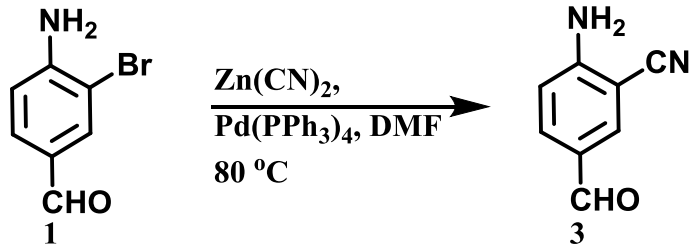

To the deoxygenated solution of 4-amino-3-bromobenzaldehyde (**1**) (4.75 mmol) in 8 ml DMF, $ZnCN_2$ (2.85 mmol) and $Pd(PPh_3)_4$ (6 mol%) were added. The resulting solution was heated at 80 °C for 8 hour under argon. The reaction was mixture was cooled to room temperature, diluted with toluene, followed by washing with 2N NH_4OH (10 ml × 2), brine (10 ml × 1), dried over $MgSO_4$. The collected organic extract was concentrated under vacuum and purified by silica gel column chromatography (100:30, Hexane: Ethyl acetate). Yield 89%. M.P. 166 °C. ^{1}H NMR (300 MHz, DMSO-d_6) δ 9.62 (S, 1H), 8.01-8.00 (d, 1H), 7.77-7.73 (dd, 1H), 7.16(S, 2H), 6.87, 6.84 (d, 1H). ^{13}C NMR (75 MHz, DMSO-d_6) δ 189.03, 155.83, 138.22, 133.15, 125.07, 116.98, 115.34, 92.85. **MS-FD** (8 kV, CH_2Cl_2) m/z: found 145.4 (100%).

5-Formyl-2-iodobenzonitrile (4)

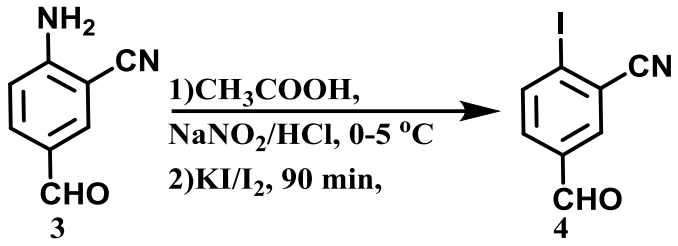

Following the procedure same as for **2**. Crystalline white solid obtained in 71% yield. M.P. 136 °C. ^{1}H NMR (250 MHz, $CDCl_3$) δ 9.98 (S, 1H), 8.18-8.14 (d, 1H), 8.08-8.07 (d, 1H), 7.78-7.74 (dd, 1H). **MS-FD** (8 kV, CH_2Cl_2) m/z: found 256.5 (100%).

4-Iodo-3-methoxybenzaldehyde (5)

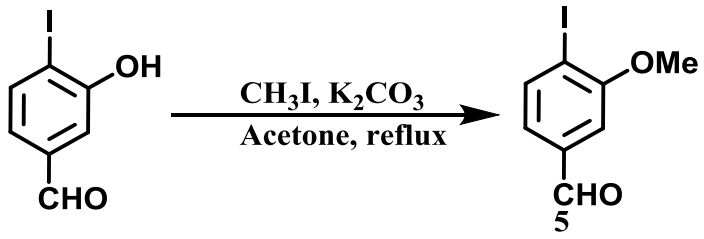

To the solution of 4-iodo-3-hydroxybenzaldehyde (1 mmol) in 10 ml acetone, K_2CO_3 (1.5 mmol) was added and stirred at room temperature for 30 minutes. To the resulting mixture iodomethane was added and heated to reflux for 5 hour. Reaction mixture was cooled to room temperature, volatiles were evaporated under vacuum. Crude product partitioned in DCM/water (50/20 ml), organic layer was separated washed with brine and dried over $MgSO_4$. The solvent was removed under vacuum and crude product was purified by silica gel column chromatography (100:10, Hexane: Ethyl acetate). Yield 97%. M.P. 86 °C. ^{1}H NMR (300 MHz, $CDCl_3$) δ 9.95 (s, 1H), 8.00-7.97 (d, 1H), 7.29 (d, 1H), 7.20-7.17 (dd, 1H), 3.96 (s, 3H). ^{13}C NMR (75 MHz, $CDCl_3$) δ 191.44, 159.00, 140.40, 137.96, 125.10, 108.73, 95.34, 56.71.

3-Bromo-4-((trimethylsilyl)ethynyl)benzaldehyde (6)

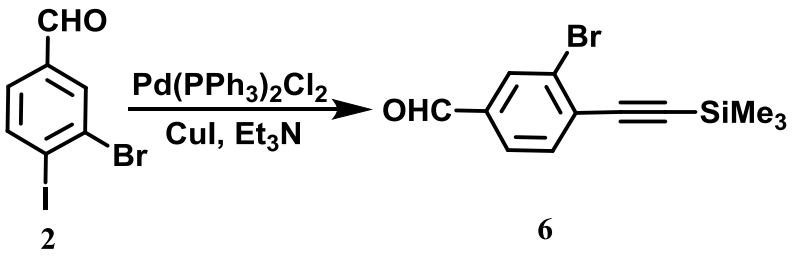

2 6

The mixture of 3-bromo-4-iodobenzaldehyde (**2**) (1 mmol), $Pd(PPh_3)_2Cl_2$ (5 mol%), CuI (10 mol%) in 5 ml Et_3N was deoxygenated by bubbling with argon for 20 mins. To this TMSA (1.1 mmol) was added and solution left stirring at room temperature for overnight. The resulting mixture was filtered and washed with saturated ammoniumchloride solution followed by brine and dried over $MgSO_4$. Solvent was removed under vacuum and the crude product was purified by silica gel column chromatography (100:3, Hexane: Ethyl acetate). 3-bromo-4-((trimethylsilyl)ethynyl) benzaldehyde was obtained with 70% yield as pale yellow oil. ^{1}H NMR (300 MHz, $CDCl_3$) δ 9.94 (s, 1H), 8.07 (d, 1H), 7.76-7.73 (dd, 1H), 7.64-7.61 (d, 1H), 0.29 (s, 9H). ^{13}C NMR (75 MHz, $CDCl_3$) δ 190.15, 136.63, 134.16, 133.39, 131.17, 127.82, 126.65, 104.84, 102.34, −0.20.

3-Bromo-4-ethynylbenzaldehyde (7)

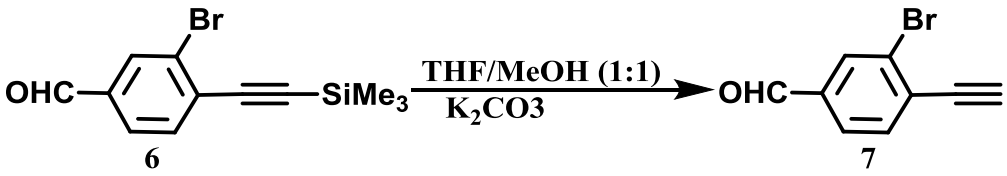

6 7

To the solution of 3-bromo-4-((trimethylsilyl)ethynyl)benzaldehyde (**6**) (1 mmol) in 10 ml 1:1 THF/MeOH, K_2CO_3 was added and mixture allowed to stir at room temperature for overnight. The resulting solution was diluted with DCM and washed with 1N HCl, followed by brine and dried over $MgSO_4$. The solvent was removed under vacuum and crude product was purified by silicagel column chromatography (100:5, Hexane: Ethyl acetate). 3-bromo-4-((trimethylsilyl)ethynyl)benzaldehyde obtained with 90% yield. ^{1}H

NMR (300 MHz, $CDCl_3$) δ 9.95 (s, 1H), 8.08 (d, 1H), 7.79-7.76 (dd, 1H), 7.68-7.65 (d, 1H), 3.60 (s, 1H). ^{13}C NMR (75 MHz, $CDCl_3$) δ 190.04, 137.06, 134.70, 133.41, 130.17, 127.86, 126.56, 85.85, 81.39.

4,4'-(Ethyne-1,2-diyl)bis(3-bromobenzaldehyde) (NN1a)

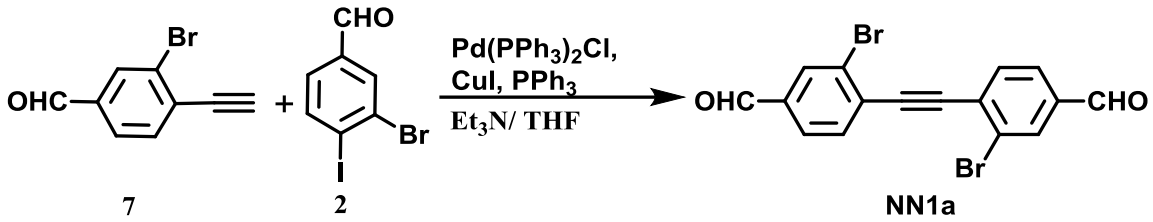

The mixture of 3-bromo-4-iodobenzaldehyde (**2**) (1 mmol), 3-bromo-4-ethynylbenzaldehyde (**7**) (1 mmol), $Pd(PPh_3)_2Cl_2$ (5 mol%), CuI (10 mol%) in 6 ml Et_3N and 4 ml THF was deoxygenated by bubbling with argon for 20 minutes and solution left stirring at room temperature for overnight. The resulting mixture was filtered and washed with saturated ammoniumchloride solution followed by brine and dried over $MgSO_4$. Solvent was removed under vacuum and crude product was purified by silicagel column chromatography (100:15, Hexane: Ethyl acetate). 4,4'-(ethyne-1,2-diyl)bis(3-bromobenzaldehyde) was obtained with 65% yield as pale yellow solid. M.P. 190 °C. ^1H NMR (300 MHz, $CDCl_3$) δ 9.99 (s, 2H), 8.08 (d, 2H), 7.79-7.76 (dd, 2H), 7.73, 7.70 (d, 2H).^{13}C NMR (75 MHz, $CDCl_3$) δ 190.01, 137.25, 134.46, 133.64, 130.36, 128.00, 126.67, 95.16. **MS-FD** (8 kV, CH_2Cl_2) m/z: found 392.1 (100%).

5-Formyl-2-((4-formylphenyl)ethynyl)benzonitrile (NN2a)

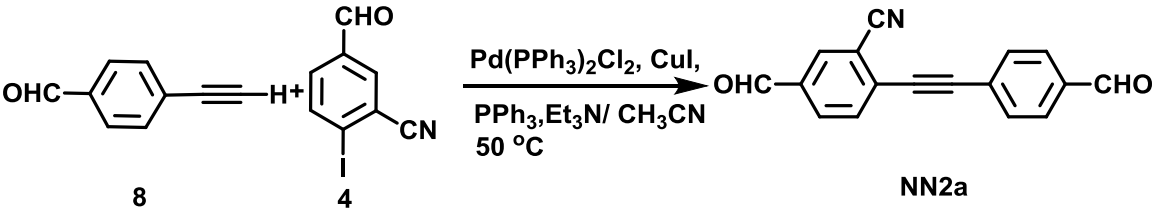

Following the same procedure as for **NN1a**. Yield 83%. M.P. 169 °C. ^1H NMR (300

MHz, $CDCl_3$) δ 9.99 (s, 1H), 9.98 (s, 1H), 8.14-8.13 (d, 1H), 8.05-8.02 (dd, 1H), 7.87-7.84 (m, 2H), 7.78-7.72 (m, 3H). ^{13}C NMR (75 MHz, $CDCl_3$) δ 191.34, 189.18, 136.75, 135.86, 133.84, 133.14, 132.95, 132.77, 131.75, 129.79, 127.39, 116.79, 116.43, 98.69, 88.44. **MS-FD** (8 kV, CH_2Cl_2) m/z: found 258.5 (100%).

3-Bromo-4-((4-formyl-2-methoxyphenyl)ethynyl)benzaldehyde (NN3a)

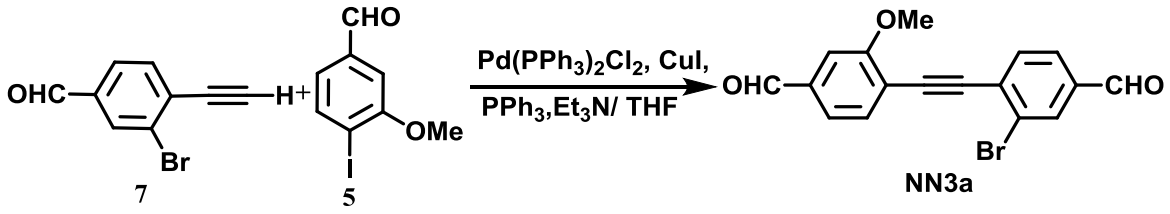

Following the same procedure as for **NN1a**. Yield 86%. ^{1}H NMR (300 MHz, $CDCl_3$) δ 10.00 (s, 1H), 9.97 (s, 1H), 8.13 (d, 1H), 7.83-7.80 (dd, 1H), 7.76-7.71 (m, 2H), 7.49-7.43 (m, 2H), 4.01 (s, 3H).^{13}C NMR (75 MHz, $CDCl_3$) δ 191.43, 190.10, 160.89, 137.94, 136.82, 134.40, 134.06, 133.54, 131.06, 127.97, 126.55, 123.68, 118.12, 109.33, 94.88, 93.61, 56.34.**MS-FD** (8 kV, CH_2Cl_2) m/z: found 343.8 (100%).

4-((4-Formylphenyl)ethynyl)-3-nitrobenzaldehyde (NN4a)

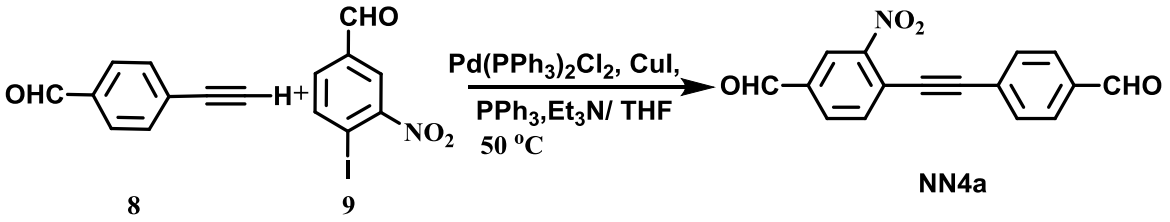

Following the same procedure as for **NN1a**. Yield 43%. M.P. 154 °C. ^{1}H NMR (300 MHz, DMSO-d_6) δ 10.12 (s, 1H), 10.05 (s, 1H), 8.66 (d, 1H), 8.27- 8.24 (dd, 1H), 8.06-8.04 (d, 1H), 7.99-7.96 (d, 2H), 7.81-7.78 (d, 2H). ^{13}C NMR (75 MHz, DMSO-d_6) δ 191.81, 190.47, 149.43, 136.27, 136.22, 135.52, 132.78, 132.33, 129.51, 126.75, 125.54, 121.45, 98.36, 87.41. . **MS-FD** (8 kV, CH_2Cl_2) m/z: found 287.2 (100%).

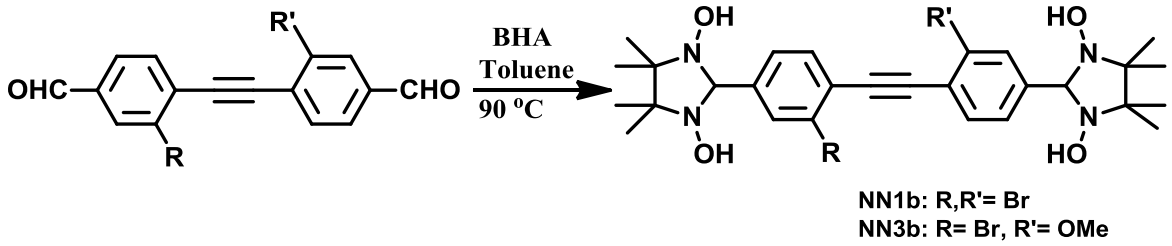

NN1b and NN3b: dialdehyde (1 mmol) and BHA (2.5 mmol) were dissolved in toluene. The resulting solution was degassed with argon bubbling for 20 mins and heated under argon at 90 °C for 2 days. The reaction mixture was cooled to room temperature, the white precipitate was filtered and used as it is for next step.

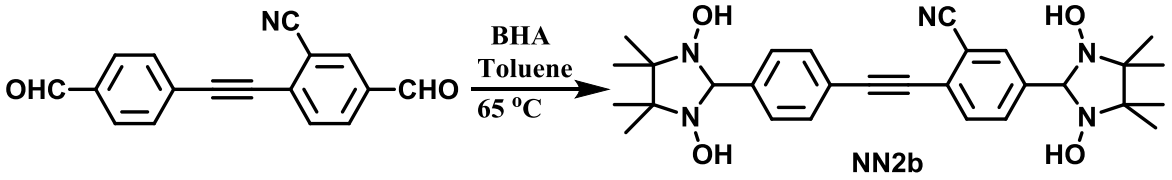

NN2b: Following the same procedure as for **NN1b** except temperature was maintained 65 °C and reaction continued for 5 days.

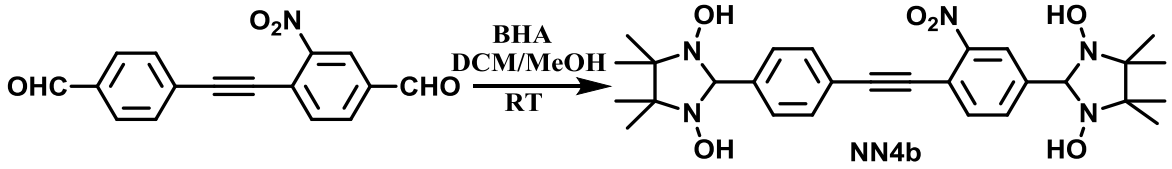

NN4b: Dialdehyde (1 mmol) and BHA (2.5 mmol) were dissolved in DCM:MeOH (1:2). The resulting solution was degassed with argon bubbling for 20 mins and stirred at room temperature under argon for 7 days. The resulting pale yellow precipitate filtered and used as it is for the next step.

General procedure for synthesis of biradicals:

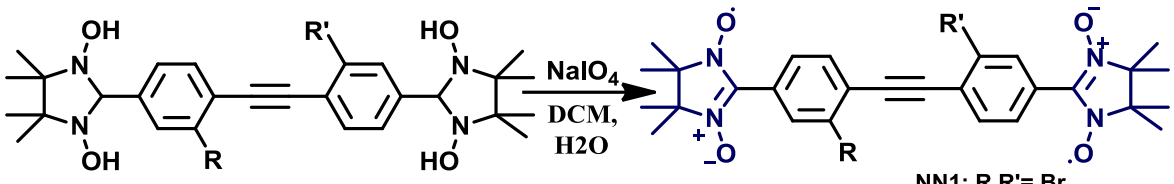

NN1b: R,R'= Br
NN2b: R= H, R'= CN
NN3b: R= Br, R'= OMe
NN4b: R= H, R'= NO_2

NN1: R,R'= Br
NN2: R= H, R'= $CONH_2$
NN3: R= Br, R'= OMe
NN4: R= H, R'= NO_2

To the two phase H_2O/CH_2Cl_2 (1:1) mixture, hydroxyl amines (100 mg, 0.16 mmol) and $NaIO_4$ (0.32 mmol) were suspended. The reaction mixture was stirred in an ice bath. After 45 to 120 minutes (monitoring the reaction with TLC) the dark bluish-green organic phase was separated, washed with water, brine and dried over $MgSO_4$. The aqueous phase was extracted with DCM. Solvent was removed under vacuum, residue was chromatographed over silica gel using hexane: ethylacetate (1:1) as eluent to obtain blue crystalline product. It should be noted that during the oxidation of bishydroxylamine **NN2b** the cyano functional group undergoes oxidation to amide.

NN1: Yield 51%. M.P. 225 °C (decomp.). **EPR** (290 K, 10^{-4} M in toluene): nine lines, g_{iso} = 2.0068, $a_{N1}/2$ = 0.372 mT. **UV-Vis** (Toluene) λ_{max} (n—π*) (ε, $M^{-1}cm^{-1}$): 625 nm (395).

NN2: Yield 43%. M.P. 228 °C (decomp.). **EPR** (290 K, 10^{-4} M in toluene): nine lines, g_{iso} = 2.0067, $a_{N1}/2$ = 0.372 mT. **UV-Vis** (Toluene) λ_{max} (n—π*) (ε, $M^{-1}cm^{-1}$): 622 nm (716).

NN3: Yield 63%. M.P. 220 °C (decomp.). **EPR** (290 K, 10^{-4} M in toluene): nine lines, g_{iso} = 2.0068, $a_{N1}/2$ = 0.372 mT. **UV-Vis** (Toluene) λ_{max} (n—π*) (ε, $M^{-1}cm^{-1}$): 620 nm (540).

NN4: Yield 45%. M.P. >250 °C (decomp.). **EPR** (290 K, 10^{-4} M in toluene): nine lines, g_{iso} = 2.0067, $a_{N1}/2$ = 3.72 mT. **UV-Vis** (Toluene) λ_{max} (n—π*) (ε, $M^{-1}cm^{-1}$): 630 nm (464).

3.11 References

[1] Y. B. Borozdina, E. Mostovich, V. Enkelmann, B. Wolf, P. T. Cong, U. Tutsch, M. Lang, M. Baumgarten, *Journal of Materials Chemistry C, DOI: 10.1039/c4tc00399c,* **2014**.

[2] J. M. Kosterlitz, D. J. Thouless, *Journal of Physics C: Solid State Physics* **1973**, *6*, 1181.

[3] Z. Hadzibabic, P. Kruger, M. Cheneau, B. Battelier, J. Dalibard, *Nature* **2006**, *441*, 1118.

[4] B. Wolf, P. T. Cong, K. Remović-Langer, Y. D. Borozdina, E. Mostovich, M. Baumgarten, M. Lang, *J. Phys.: Conf. Ser.* **2010**, *200*, 012225.

[5] J. H. Osiecki, E. F. Ullman, *J. Amer. Chem. Soc.* **1968**, *90*, 1078.

[6] M. J. Mio, L. C. Kopel, J. B. Braun, T. L. Gadzikwa, K. L. Hull, R. G. Brisbois, C. J. Markworth, P. A. Grieco, *Org. Lett.* **2002**, *4*, 3199.

[7] K. Park, G. Bae, J. Moon, J. Choe, K. H. Song, S. Lee, *J. Org. Chem.* **2010**, *75*, 6244.

[8] B. Liedholm, *J. Chem. Soc., Perkin Trans. 1* **1992**, 2235.

[9] G. Mao, A. Orita, D. Matsuo, T. Hirate, T. Iwanaga, S. Toyota, J. Otera, *Tetrahedron Lett.* **2009**, *50*, 2860.

[10] P. Ravat, Y. Ito, E. Gorelik, V. Enkelmann, M. Baumgarten, *Org. Lett.* **2013**, *15*, 4280.

[11] C. Hirel, K. E. Vostrikova, J. Pécaut, V. I. Ovcharenko, P. Rey, *Chem. Eur. J.* **2001**, *7*, 2007.

[12] M. Tamura, Y. Nakazawa, D. Shiomi, K. Nozawa, Y. Hosokoshi, M. Ishikawa, M. Takahashi, M. Kinoshita, *Chem. Phys. Lett.* **1991**, *186*, 401.

[13] M. Tamura, Y. Hosokoshi, D. Shiomi, M. Kinoshita, Y. Nakasawa, M. Ishikawa, H. Sawa, T. Kitazawa, A. Eguchi, Y. Nishio, K. Kajita, *J. Phys. Soc. Jpn.* **2003**, *72*, 1735.

[14] G. A. Bain, J. F. Berry, *J. Chem. Educ.* **2008**, *85*, 532.

[15] B. Bleaney, K. D. Bowers, *Proc. R. Soc. London A* **1952**, *214*, 451.

[16] W. P. Neumann, A. Penenory, U. Stewen, M. Lehnig, *J. Am. Chem. Soc.* **1989**, *111*,

5845.

[17] G. Zoppellaro, V. Enkelmann, A. Geies, M. Baumgarten, *Org. Lett.* **2004**, *6*, 4929.

[18] L. Noodleman, *J. Chem. Phys.* **1981**, *74*, 5737.

[19] K. Yamaguchi, F. Jensen, A. Dorigo, K. N. Houk, *Chem. Phys. Lett.* **1988**, *149*, 537.

[20] T. Soda, Y. Kitagawa, T. Onishi, Y. Takano, Y. Shigeta, H. Nagao, Y. Yoshioka, K. Yamaguchi, *Chem. Phys. Lett.* **2000**, *319*, 223.

[21] M. Shoji, K. Koizumi, Y. Kitagawa, T. Kawakami, S. Yamanaka, M. Okumura, K. Yamaguchi, *Chem. Phys. Lett.* **2006**, *432*, 343.

[22] G. W. T. M. J. Frisch, H. B. Schlegel, G. E. Scuseria, M. A. Robb, J. R. Cheeseman, G. Scalmani, V. Barone, B. Mennucci, G. A. Petersson, H. Nakatsuji, M. Caricato, X. Li, H. P. Hratchian, A. F. Izmaylov, J. Bloino, G. Zheng, J. L. Sonnenberg, M. Hada, M. Ehara, K. Toyota, R. Fukuda, J. Hasegawa, M. Ishida, T. Nakajima, Y. Honda, O. Kitao, H. Nakai, T. Vreven, J. A. Montgomery, Jr., J. E. Peralta, F. Ogliaro, M. Bearpark, J. J. Heyd, E. Brothers, K. N. Kudin, V. N. Staroverov, R. Kobayashi, J. Normand, K. Raghavachari, A. Rendell, J. C. Burant, S. S. Iyengar, J. Tomasi, M. Cossi, N. Rega, J. M. Millam, M. Klene, J. E. Knox, J. B. Cross, V. Bakken, C. Adamo, J. Jaramillo, R. Gomperts, R. E. Stratmann, O. Yazyev, A. J. Austin, R. Cammi, C. Pomelli, J. W. Ochterski, R. L. Martin, K. Morokuma, V. G. Zakrzewski, G. A. Voth, P. Salvador, J. J. Dannenberg, S. Dapprich, A. D. Daniels, O. Farkas, J. B. Foresman, J. V. Ortiz, J. Cioslowski, and D. J. Fox, in *Gaussian 09*, Gaussian, Inc, Wallingford CT, **2009**.

[23] A. D. Becke, *J. Chem. Phys.* **1993**, *98*, 1372.

[24] C. Lee, W. Yang, R. G. Parr, *Physical Review B* **1988**, *37*, 785.

[25] A. D. Becke, *Phys. Rev. A* **1988**, *38*, 3098.

[26] E. R. Davidson, D. Feller, *Chem. Rev.* **1986**, *86*, 681.

[27] K. C. Ko, D. Cho, J. Y. Lee, *J. Phys. Chem. A* **2013**, *117*, 3561.

[28] B. N. Plakhutin, E. V. Gorelik, N. N. Breslavskaya, M. A. Milov, A. A. Fokeyev, A. V. Novikov, T. E. Prokhorov, N. E. Polygalova, S. P. Dolin, L. I. Trakhtenberg, *J. Struct. Chem.* **2005**, *46*, 195.

[29] H. Oshio, T. Watanabe, A. Ohto, T. Ito, T. Ikoma, S. TeroKubota, *Inorg. Chem.* **1997**, *36*, 3014.

[30] D. Zhang, L. Ding, W. Xu, H. Hu, D. Zhu, Y. Huang, D. Fang, *Chem. Commun.* **2002**,

44.

[31] H. Oshio, T. Watanabe, A. Ohto, T. Ito, U. Nagashima, *Angew. Chem.* **1994**, *33*, 670.

[32] H.-H. Lin, H.-H. Wei, *Inorg. Chem. Commun.* **2004**, *7*, 27.

CHAPTER 4

TUNING THE INTRA-MOLECULAR EXCHANGE INTERACTIONS BY VARYING THE RADICAL MOIETY

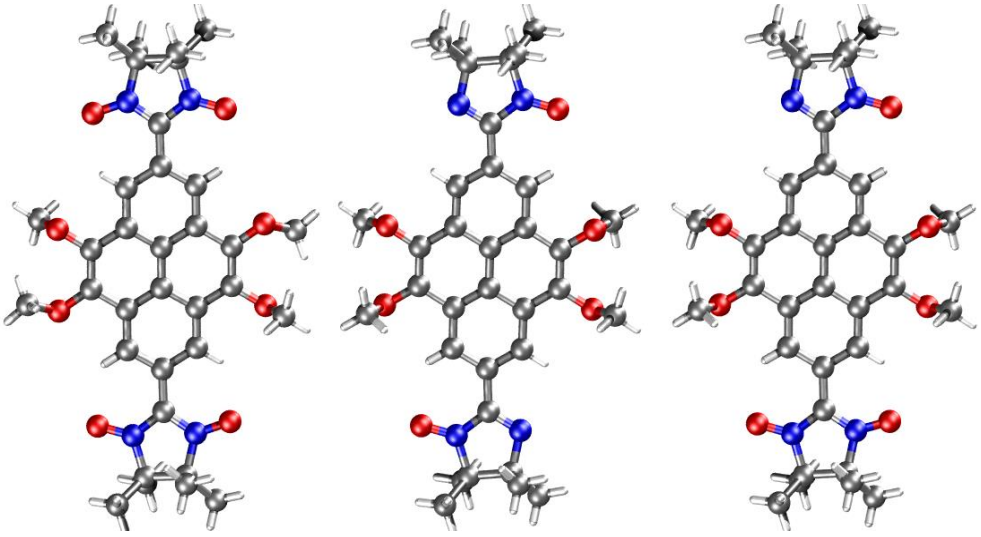

$J/k_B = -14$ K $\quad$ $J/k_B = -4.5$ K $\quad$ $J/k_B = -9.0$ K

2,7-Disubstituted tetramethoxypyrene-based neutral biradical donors are described. The fine tuning of magnetic exchange interactions was achieved by changing the radical moieties. The experimental results were verified by DFT calculations.

Note: Large part of this chapter has been published in Org. Lett. 2013, 15 (17), 4280.

4.1 Introduction

In chapter 1, it was shown how inter-molecular exchange interactions can be tuned by utilizing the approach 1, i.e. by varying the length of π-spacer. But this approach coerces to change the π-spacer which in turn alters the crystal packing. Additionally the change in exchange coupling constant could be large. It is known that the different kind of radical moieties exhibit different exchange interactions. This is mainly due to the difference in spin delocalization from the radical moiety to the π-spacer. Thence it was planned to utilize approach 4, i.e. attachment of different radical moieties while maintaining the same π-spacer to tune intra-molecular exchange interactions.[1]

The functionalization of polyaromatic hydrocarbons with stable radical moieties has attracted great attention because of their potential for applications in organic field effect transistors (OFETs),[2-4] sensors[5], magneto conducting materials,[6] photo excited spin systems,[7-8] quantum magnets,[9] and batteries.[10-11] Pyrene was chosen as a spacer molecule because of its planer structure, ability to act as donor for the synthesis of charge transfer complexes, and possibilities to obtain a high spin state on photo excitation. Moreover to the best of our knowledge, only C1 substituted pyrene based neutral mono radicals are known,[4, 12-14] nonetheless no pyrene based biradical has been reported to the date.

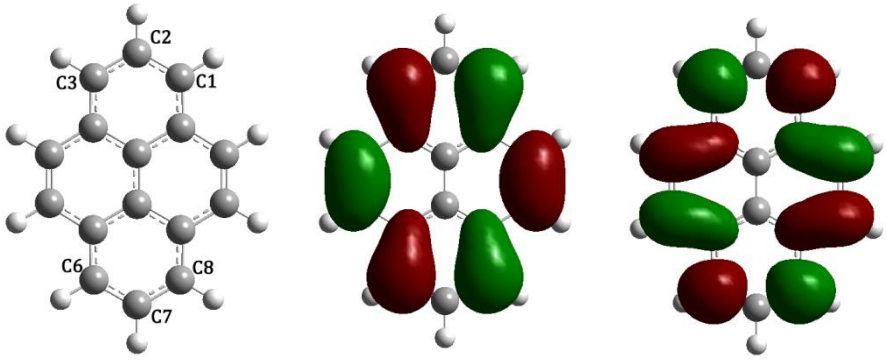

Figure 4.1: Structure of pyrene with its (a) HOMO and (b) LUMO orbitals.

The 2,7-disubstituted bis(nitronyl nitroxide) (NN) biradical (TMPNN), bis(imino

nitroxide) (IN) biradical (TMPIN) and biradical TMPMIX which possesses both NN and IN radical moieties were synthesized and characterized by UV-Vis, EPR, SQUID, cyclic voltammetry (CV), and single crystal X-ray diffraction method. Additionally, the experimental results were verified by DFT calculations.

4.2 Synthesis

The pyrene is a unique example of polyaromatic hydrocarbons with a nodal plane passing through the 2,7-positions (Figure 4.1).[15-17] Attachment of a radical moiety to the 2,7-postions of pyrene involves a synthetic challenge because the negative electron density at these positions does not allow halogenation. Thus, an alternative synthetic route must be followed to functionalize the 2,7-positions of pyrene.

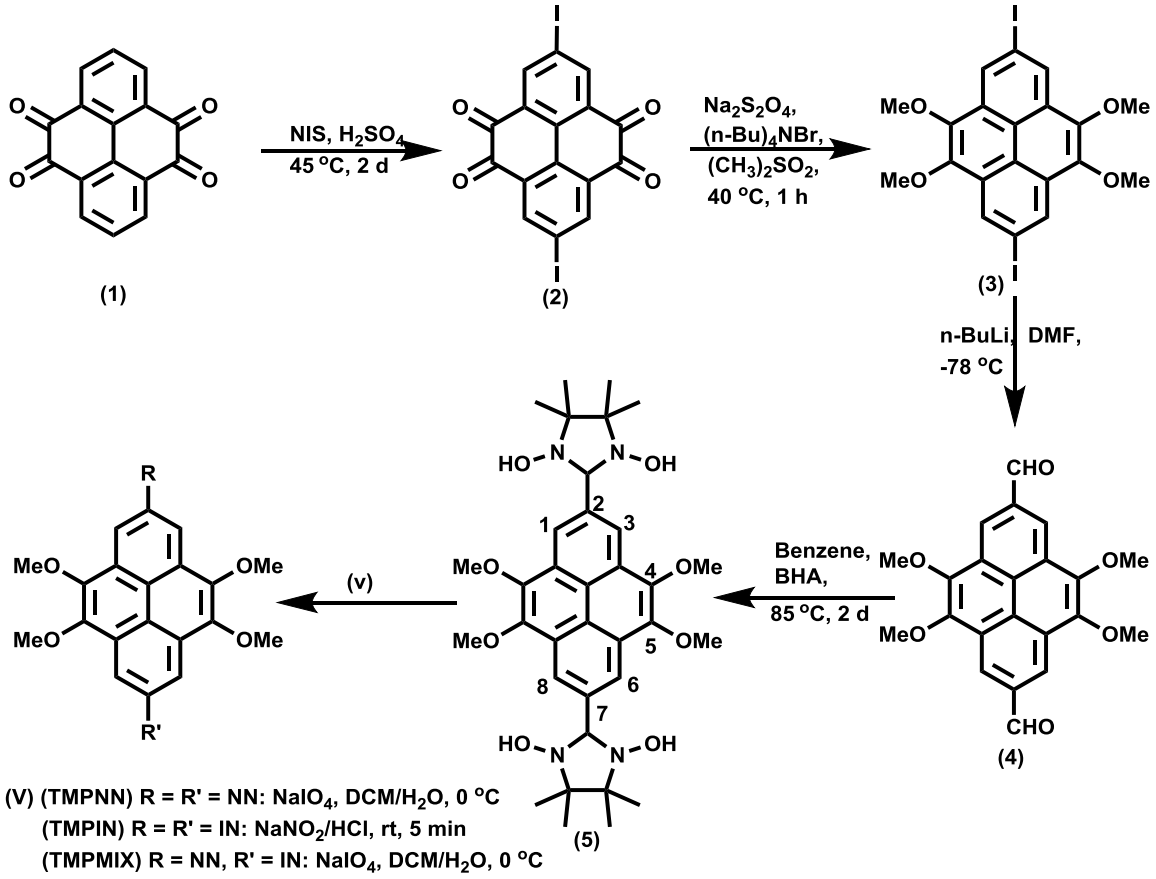

Scheme 4.1: Synthesis of TMPNN, TMPIN, and TMPMIX.

Recently Baumgarten *et al.* reported the new synthetic route for 2,7-halogenation of pyrene.[18] As shown in Scheme 4.1, the 2- and 7- positions of pyrene can be activated by oxidizing pyrene to pyrene-4,5,9,10-tetraone (**1**), which can undergo efficient halogenation at these positions. Further reduction of **2** gave the desired 2,7-diiodotetramethoxy pyrene (**3**).[18] The precursor for the synthesis of nitronyl or imino nitroxide radical is dialdehyde (**4**) which was prepared in 71% yield by lithiation of **3** with *n*-BuLi and subsequent addition of DMF at –78 °C. Condensation of **4** with bis(hydroxylamino)-dimethylbutane (BHA) to obtain **5** was performed in benzene at 85 °C. Depending on the oxidation conditions of **5** the biradicals TMPNN, TMPIN, and TMPMIX were synthesized. Oxidation of **5** with two equivalents $NaIO_4$ in DCM/H_2O two phase mixture in an ice bath for 2.5 hour afforded TMPNN. Under similar reaction condition, with three equivalents of $NaIO_4$, for longer period of time TMPMIX was obtained as major product along with small amount of TMPNN and TMPIN. This reaction was carefully monitored with TLC in order to avoid formation of TMPIN. The biradical TMPIN was prepared by oxidation of **5** with $NaNO_2$/HCl at room temperature.

4.3 Optical Properties

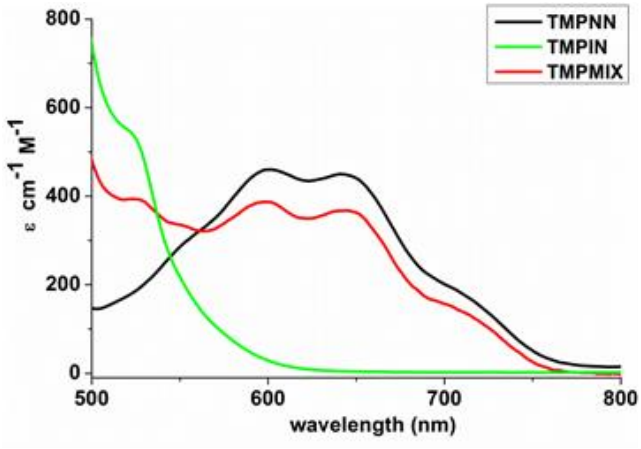

Figure 4.2: Characteristic n—π* transition of biradicals TMPNN, TMPIN, and TMPMIX in toluene (c ~ 10^{-4} M).

The UV-Vis spectrum of neutral radicals gave clear insight of the corresponding

radical moieties. The UV-Vis spectra of the biradicals TMPNN, TMPIN, and TMPMIX measured in toluene showed characteristic λ_{max} due to n—π* transition of the radical moiety in the visible range (Figure 4.2). While the blue color biradical TMPNN carrying two nitronyl nitroxide (NN) moieties absorbed at λ_{max} = 601 nm (ε = 460 cm^{-1} M^{-1}) and λ_{max} = 641 nm (ε = 450 cm^{-1} M^{-1}), the orange color biradical TMPIN carrying two imino nitroxide (IN) moieties absorbed at λ_{max} = 520 nm (ε = 551 cm^{-1} M^{-1}). Moreover, the grey color biradical TMPMIX, which possesses both NN and IN moieties simultaneously showed characteristic absorption at λ_{max} = 599 nm (ε = 389 cm^{-1} M^{-1}) and λ_{max} = 642 nm (ε = 368 cm^{-1} M^{-1}) due to the NN moiety, and λ_{max} = 524 nm (ε = 393 cm^{-1} M^{-1}) stemming from the IN moiety. Therefore, UV-Vis spectra clearly indicated the presence of both radical moieties NN and IN simultaneously in biradical TMPMIX.

4.4 Electrochemical Analysis

The donor ability and electrochemical properties of biradicals were investigated by Cyclic Voltammetry (CV) measurements. The CV experiments were carried out using a three-electrode cell in acetonitrile solution of Bu_4NPF_6 (0.1 M) with a scan rate of 100 mV/s at room temperature. A Pt wire, a silver wire, and a glassy carbon electrode were used as the counter electrode, the reference electrode, and the working electrode, respectively. Ferrocene was used as an internal standard. The CV of TMPNN showed reversible redox waves (Figure 4.3) at $E_{ox(onset)}$ = 0.95 V and $E_{red(onset)}$ = –0.48 V versus Ag/Ag^+, the former can be assigned to resonance delocalization of oxoammonium cation while the latter is due to delocalization of aminoxy anion as shown in Scheme 4.2.[19] The biradical TMPIN showed non-reversible oxidation wave at $E_{ox(onset)}$ = 1.24 V and quasi-reversible reduction wave at $E_{red(onset)}$ = –0.60 V.[20-21] Interestingly biradical TMPMIX displayed similar redox behavior as TMPNN with an additional non-reversible oxidation wave. This non-reversible wave can be assigned to oxidation of the IN radical moiety. The energy level of Singly Occupied Molecular Orbital (SOMO) and Lowest Unoccupied Molecular Orbital (LUMO) were estimated based on the formula,

$$E_{SOMO} = -(E_{ox,onset} - E^{1/2}\ Fc^{+}/Fc + 4.8)\ eV \quad \textbf{4-1}$$

$$E_{LUMO} = -(E_{red,onset} - E^{1/2}\ Fc^{+}/Fc + 4.8)\ eV \quad \textbf{4-2}$$

As shown in Table 4.1 the electrochemical energy gap is in accordance with the optical energy gap. The higher SOMO level of biradicals showed their ability as donor molecule to form charge transfer complexes.

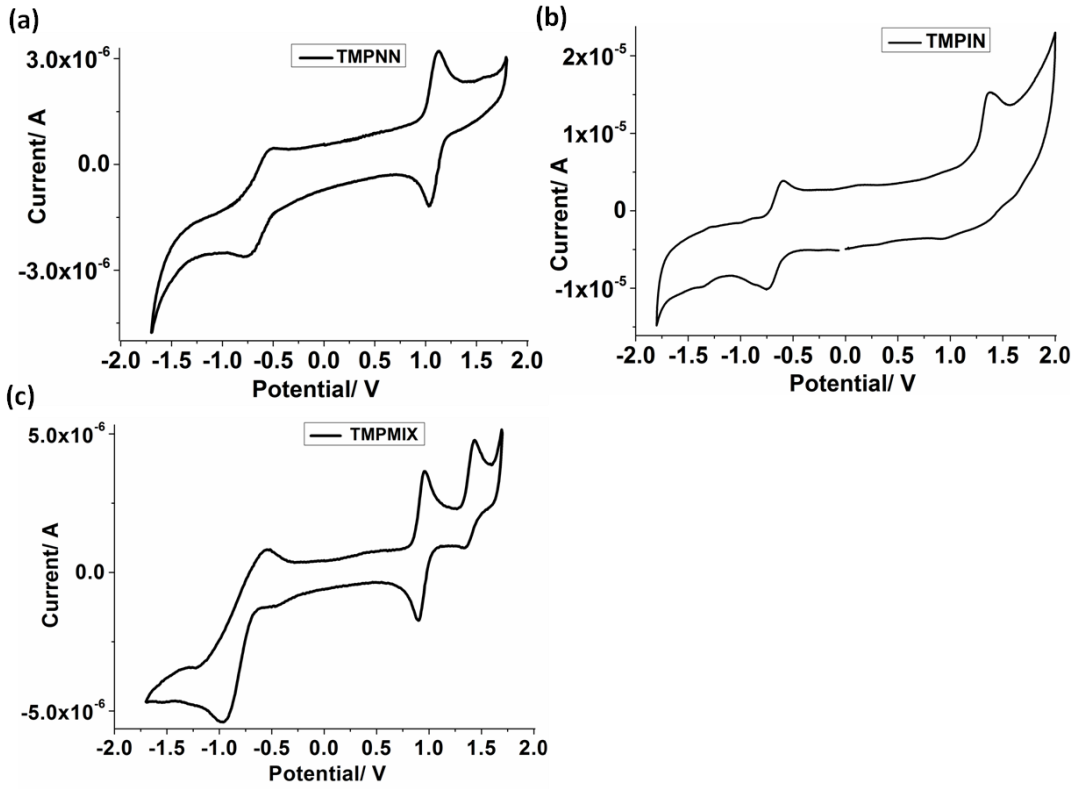

Figure 4.3: Cyclic Voltammetry curve of biradicals TMPNN, TMPIN, and TMPMIX recorded in acetonitrile (Bu_4NPF_6 (0.1 M), scan rate of 100 mV/s).

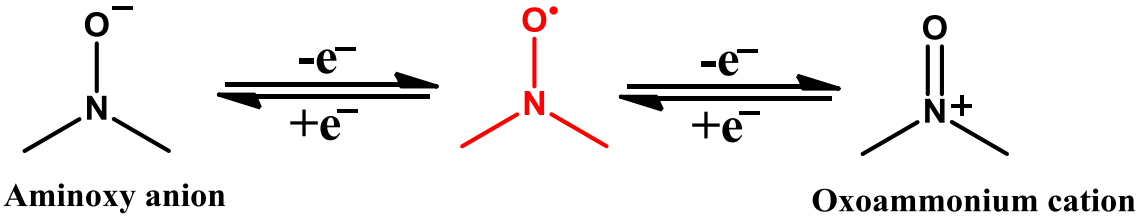

Scheme 4.2: Expected reversible redox mechanism

Table 4.1: Optical and electrochemical properties of biradicals.

	λ_{max} (nm)	ε ($cm^{-1}M^{-1}$)	E_{Ox} (V)[a]	E_{Red} (V)[b]	E_{SOMO} (eV)[c]	E_{LUMO} (eV)[d]	E_g^{EC} (eV)[e]	E_g^{OP} (eV)[f]
TMPNN	604 641	460 450	0.950	–0.485	–5.012	–3.578	1.434	1.614
TMPIN	520	551	1.238	–0..603	–5.600	–3.750	1.850	2.049
TMPMIX	524 599 642	393 389 368	0.786 1.246	–0.705	–5.019	–3.526	1.492	1.624

[a,b]0.1 M of *n*-Bu_4NPF_6, in acetonitrile, Pt electrode, scan rate 100 mVs^{-1}. [c,d] Calculated based on formula $E_{SOMO} = -(E_{ox,onset} - E^{(1/2)}\ Fc^+/Fc + 4.8)$ and $E_{LUMO} = -(E_{red,onset} - E^{(1/2)}\ Fc^+/Fc + 4.8)$ eV. [e]Electrochemical energy gap. [f]Optical energy gap calculated according to the absorption edge.

4.5 Crystal structure analysis

As magnetic interactions depend on the geometry and packing of the molecules in the crystal lattice,[12, 22-23] the single crystals of biradicals TMPNN, TMPIN, and TMPMIX, were obtained. The good quality crystals were grown by slow diffusion of hexane to the solution of biradicals in DCM under ambient conditions. The single crystals were investigated with single crystal X-ray diffraction. Crystal structure analysis revealed that molecules TMPNN, TMPIN, and TMPMIX were crystallized in monoclinic $P2_1/n$ space group with similar unit cell parameters (Appendix-III). Further they also possess similar packing of the molecules in the crystal lattice. Thus, it was considered that these three biradicals are isomorphous. In two dimensions the molecules of biradical arranged in herring-bone fashion (Figure 4.5), utilizing inter- and intra-molecular C—H···O hydrogen bonds. However, interestingly a significant difference was observed in inter-planar spacing. The shortest π-π stacking distance was observed in biradical TMPNN (3.730 Å) followed by biradical TMPMIX (4.258 Å) and TMPIN (4.367 Å) (Figure 4.4). These differences can be attributed to the influence of the radical moiety on the pyrene core.

The torsion angles between the NN moiety and the pyrene ring in TMPNN are 15° (C3-C4-C11-N1) and 14.8° (C5-C4-C11-N2). The IN moiety in TMPIN is nearly coplanar to the pyrene core with smaller torsion angle 3.9° (C3-C4-C11-N1). The intermediate torsion angles are observed in biradical TMPMIX, 5.4° (C3-C4-C9-N1) and 4.7° (C5-C4-C9-N2). Even though the different radical moieties showed different torsion angles with the pyrene core the overall crystal packing was not disturbed, and as discussed earlier the only difference observed, was in the inter-planar spacing.

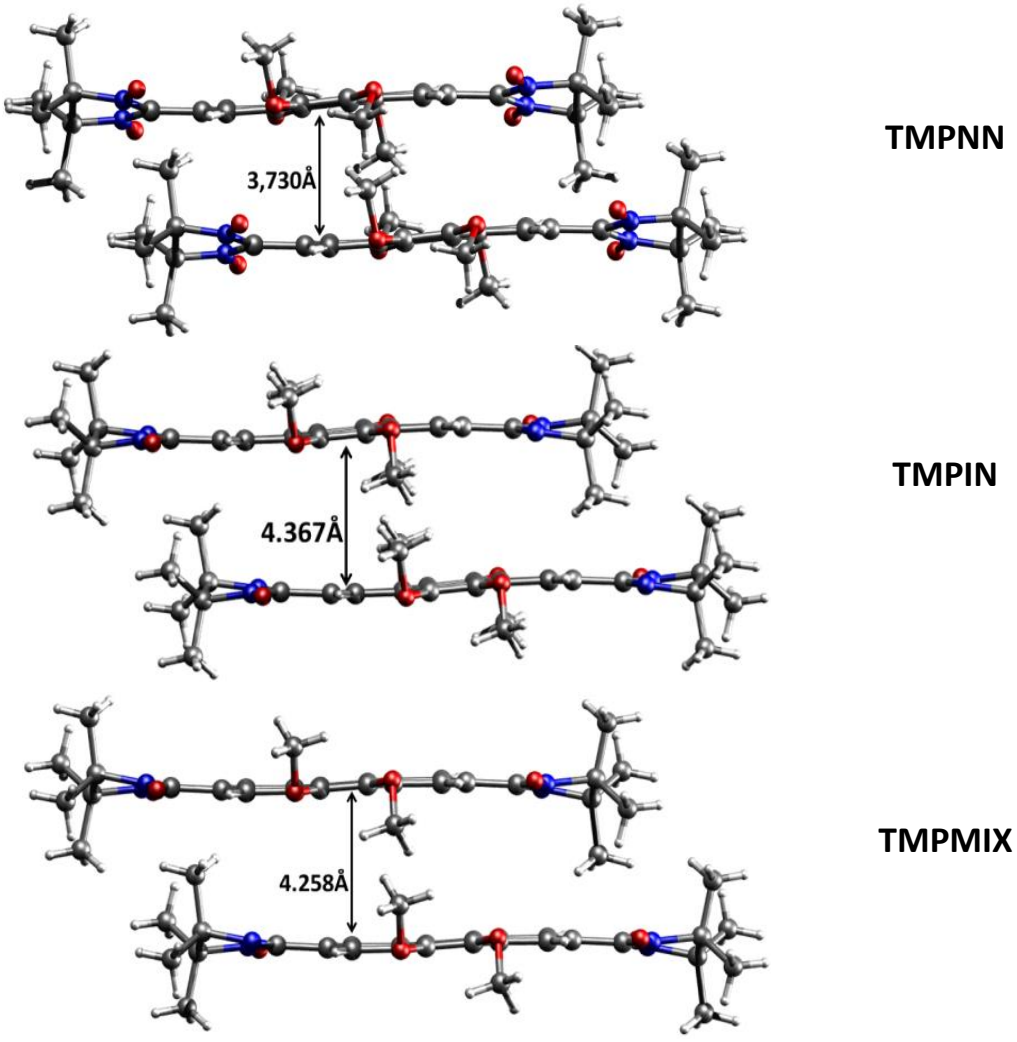

Figure 4.4: π-π stacking of the biradicals.

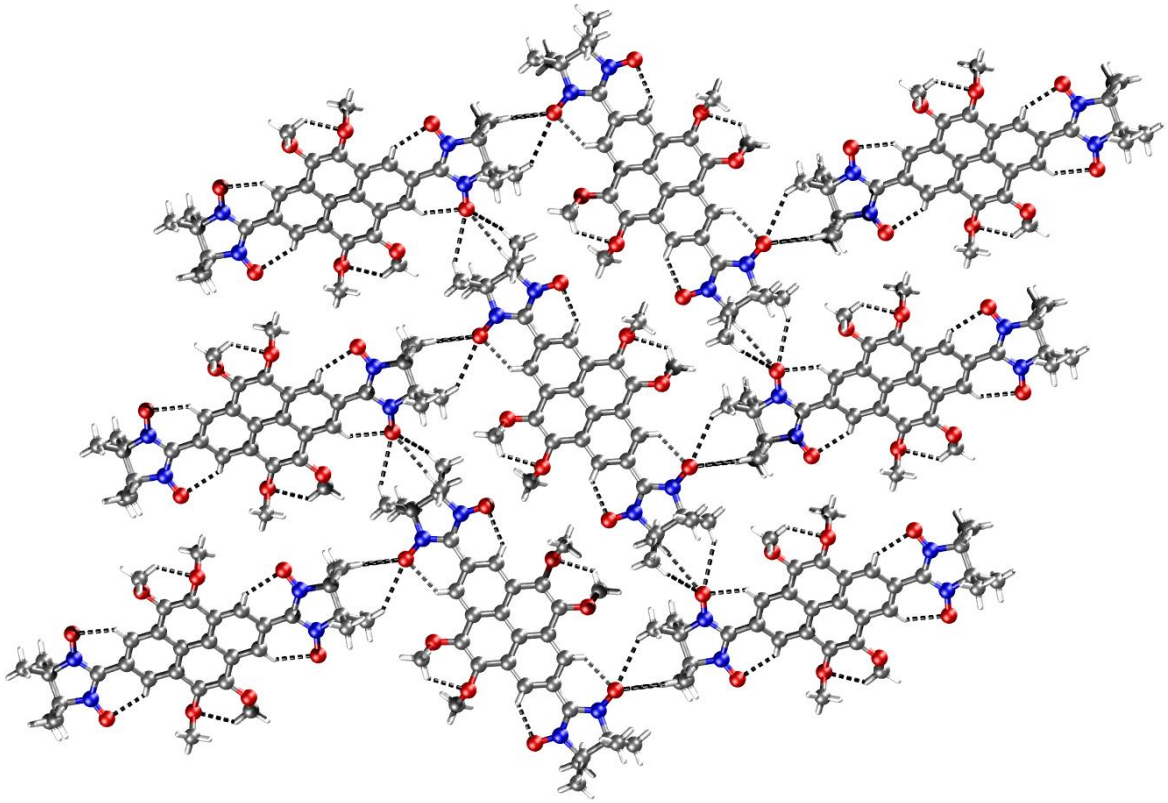

Figure 4.5: Two-dimensional herring-bone arrangement of biradical TMPNN.

4.6 EPR spectra

The X-band EPR spectra were recorded in oxygen free toluene at room temperature (Figure 4.6). The typical EPR spectrum of TMPNN consisted of well resolved nine lines due to hyperfine coupling (*hfc*) of two electron spins with four equivalent nitrogen atoms. The experimental spectrum of TMPNN showed a good agreement with the simulated one considering a nitrogen *hfc* ($a_N/2$) value 0.373 mT (which is half of the *hfc* observed for mono nitronyl nitroxide a_N = 0.748 mT) at g-value 2.0066. The biradical TMPIN with two imino nitroxide moieties contains two pairs of non-equivalent N atoms. Thus following the 2nI+1 rule, 25 line EPR spectrum was expected but due to overlapping of some transitions, a 13 line EPR spectrum was observed with same spectral width as for the mono radical. The 13 line spectrum of biradical TMPIN was reproduced with nitrogen *hfc* values $a_{N1}/2$ = 0.225 and $a_{N2}/2$ = 0.440 at g-value 2.0059. However, the non-symmetric

EPR spectrum of biradical TMPMIX was not simple to fit. This can be accounted by considering the interaction between two different kinds of radical moieties. The spectrum for TMPMIX was simulated by taking into account *hfc* of two similar and two different, in total three, N nuclei. Whereas the N nuclei of NN moiety are equivalent (with *hfc* a_{N1}), the IN moiety possesses two non-equivalent N nuclei (with *hfc* a_{N2} and a_{N3}). The best fitting *hfc* values were $a_{N1}/2$ = 0.374 mT for two equivalent nuclei (corresponds to NN moiety), $a_{N2}/2$ = 0.200 and $a_{N3}/2$ = 0.460 for the other two non-equivalent N nuclei (corresponds to IN moiety) at g-value 2.0062. The EPR spectra for all biradicals demonstrated that the exchange interactions (*J*) between the radical moieties are much larger than the hyperfine coupling ($J >> a_N$).

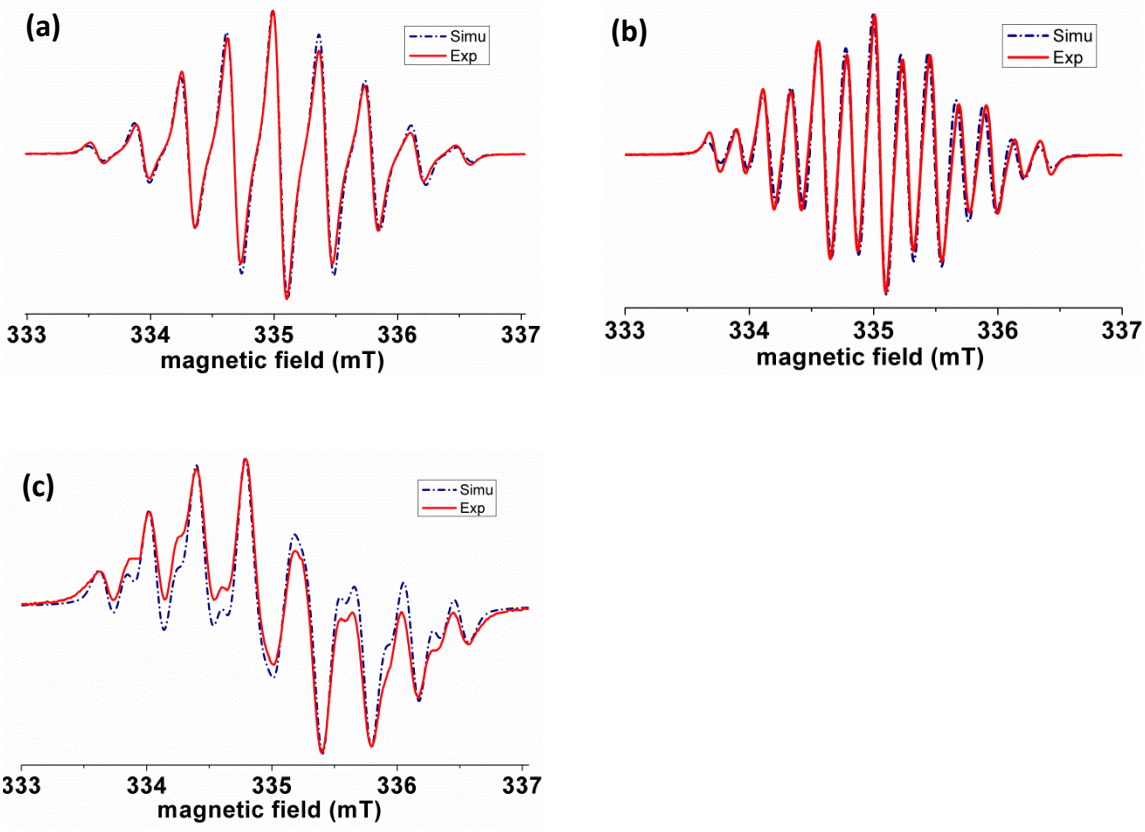

Figure 4.6: X-band EPR spectra of biradical (a) TMPNN, (b) TMPIN, and (c) TMPMIX in toluene (c ~ 10^{-4} M) at room temperature.

4.7 Magnetic measurements

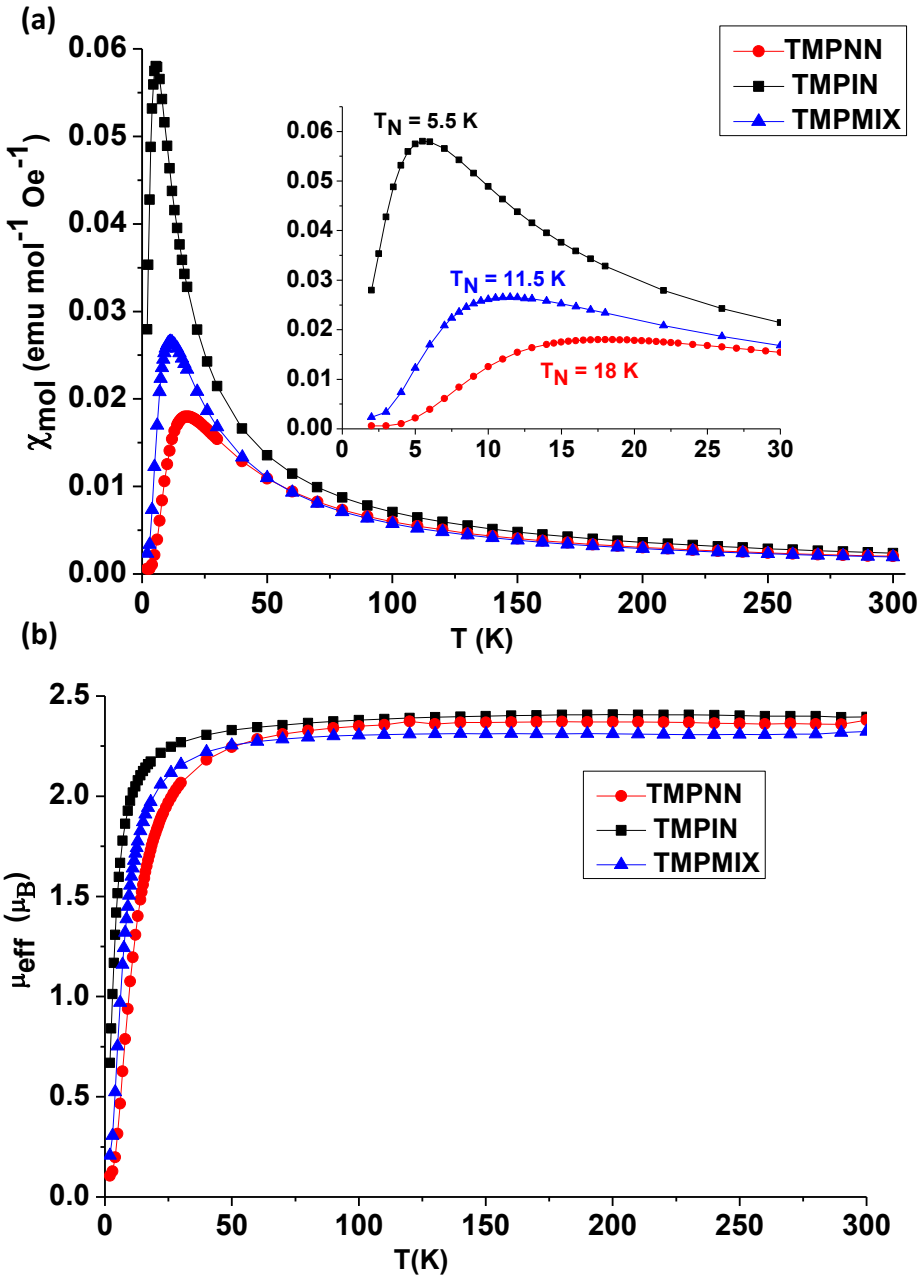

Figure 4.7: (a) Molar magnetic susceptibility, χ_{mol}, (emu mol^{-1} Oe^{-1}) as a function of temperature. (b) effective magnetic moment, μ_{eff}, as a function of temperature under magnetic field 0.1 Tesla.

To get an insight into the magnetic exchange interactions operating in biradicals, magnetic susceptibilities and magnetizations of polycrystalline samples were measured in

the temperature range of 2 K ≤ T ≤ 300 K using SQUID magnetometer. Background signals of sample holder and diamagnetic correction were subtracted.[24] As shown in Figure 4.7a, the molar magnetic susceptibility (χ_{mol}) initially increased with the Curie-Weiss behavior at higher temperature region and decreased at lower temperature with a broad peak mainly caused by intra-molecular antiferromagnetic (AF) interactions. On further lowering the temperature χ_{mol} decreases close to zero at 2 K which means the biradicals switch from a thermally populated magnetic spin triplet state to a non-magnetic spin singlet ground state. The biradical TMPNN showed highest Néel temperature (T_N = 18 K) followed by the biradical TMPMIX (T_N = 11.5 K) and TMPIN (T_N = 5.5 K). The intra-dimer coupling constant J_{intra} of R-Py-R' was then estimated using an isolated dimer model ($H = -2J_{intra}S_R.S_{R'}$).[25] Among the three biradicals strongest intra-molecular exchange interactions thus operate between the NN moieties of biradical TMPNN (J_{intra} = –14.0 K) and weakest between the IN moieties of biradical TMPIN (J_{intra} = –4.5 K). The intermediate magnetic exchange interactions were obtained by replacing one of the NN moieties in biradical TMPNN by IN moiety i.e the biradical TMPMIX (J_{intra} = –9.0 K). Thus fine tuning of magnetic exchange interactions was achieved by utilizing different radical moieties while maintaining the same π-spacer. Moreover, the negative Weiss temperature (Table 4.2) was observed in all biradicals indicating existence of AF intra- and inter-molecular magnetic interactions. The observed effective magnetic moment (μ_{eff}) values for all biradicals were calculated from the temperature dependence of the magnetic susceptibility under 0.1 T (Figure 4.7b). At room the temperature the magnetic moments were close to the theoretical value 2.45 μ_B for magnetically uncorrelated spins of biradicals.[26] μ_{eff} was temperature independent down to 40 K, below which it decreased sharply due to the strong AF inter-dimer interactions.

Moreover, magnetization curves of all biradicals were measured at 2 K (Figure 4.8). Whereas biradicals TMPNN and TMPMIX showed very small applied magnetic field dependence up to 5 T, the biradical TMPIN showed gradual increase in magnetization with applied magnetic field. This means the biradicals TMPNN and TMPMIX demonstrate strong AF intra-molecular coupling, keeping the singlet state at 5 T and only the biradical

TMPIN present a switching from singlet to the triplet spin state with the applied magnetic field owing to the moderate AF interactions.

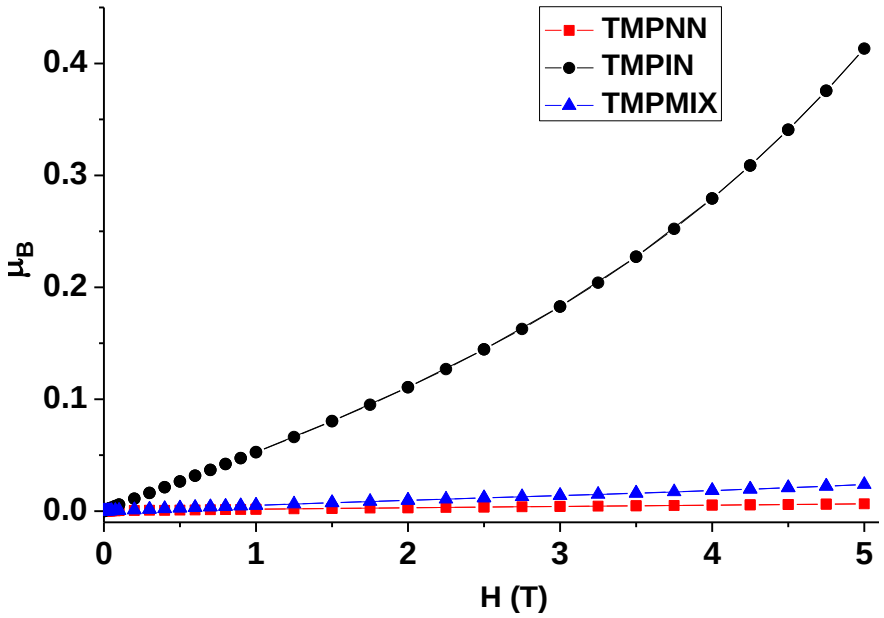

Figure 4.8: Magnetization as a function of magnetic field at 2 K.

Table 4.2: Magnetic properties of biradicals.

Radical	*g-factor*	N nuclei	$a_N/2$ (mT)[a]	T_N (K)[b]	Θ (K)[c]	J_{intra}(K)[d], *calc*	J_{intra}(K)[e], *exp*
TMPNN	2.0066	4	0.373	18.0	–4.3	–14.5	–14.0
TMPIN	2.0059	2 2	0.225 0.440	5.5	–5.7	–3.7	–4.5
TMPMIX	2.0062	2 1 1	0.374 0.200 0.460	11.5	–4.2	–8.0	–9.0

[a]Hyperfine coupling constant values in mT, [b]Néel temperature, [c]Weiss-temperature. [d]Calculated using UBLYP/ 6-31G(d). [e]Calculated by fitting with isolated dimer model (s = 1/2).

4.8 DFT Calculations

The intra-molecular exchange interaction energies of the biradical species were also estimated from the broken-symmetry DFT calculations (Appendix-I).[27] The geometry of biradical was taken from the X-ray diffraction determination without further optimization. The broken-symmetry approach proposed by Noodleman *et al.* was employed to elucidate the magnetic properties of the biradical species under study. The exchange coupling constant (*J*) was calculated by the generalized spin projection method suggested by Yamaguchi *et al*.[28-30] Calculations were performed at UBLYP/6-31G(d) level of theory. The calculated exchange interactions were very close to the same obtained from the magnetic measurements (Table 4.3). Good agreement between the latter estimations and the results of magnetic measurements support the suggested structure of magnetic interactions within the crystalline phase and the experimentally observed trend in the strength of intra-molecular exchange interactions within the biradical family R-Py-R': $-J_{NN\text{-}Py\text{-}NN} > -J_{NN\text{-}Py\text{-}IN} > -J_{IN\text{-}Py\text{-}IN}$.

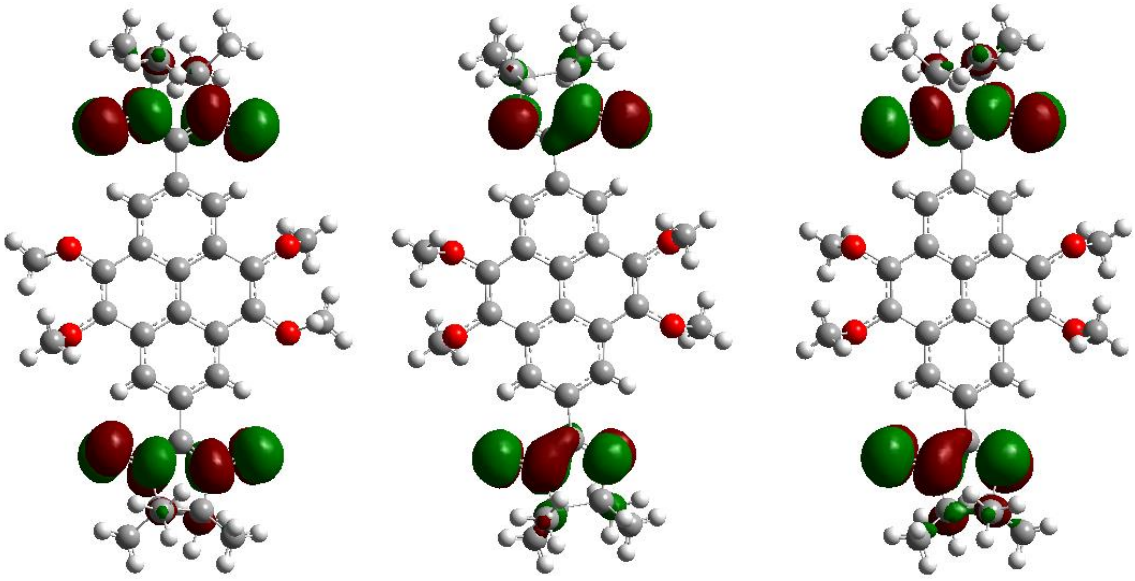

TMPNN **TMPIN** **TMPMIX**

Figure 4.9: SOMO orbital calculated using DFT quantum calculations (UBLYP/6-31G).

4.9 Summary

2,7-Disubstituted tetramethoxypyrene based neutral biradicals possessing NN and IN radical moieties were successfully synthesized. The fine tuning of the physical and magnetic properties was achieved by changing the radical moieties. The TMPMIX is a unique example of biradical with NN and IN radical moieties simultaneously. Furthermore the complex EPR spectrum of TMPMIX could be simulated using suitable parameters. The experimentally obtained intra-molecular exchange coupling constant (J_{intra}) values are well in accordance with the theoretical ones.

4.10 Synthetic Details

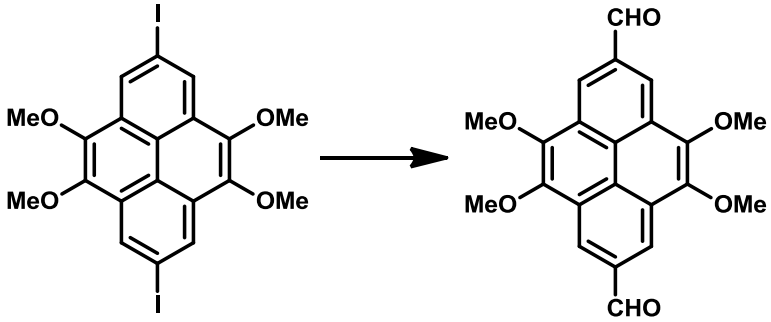

4,5,9,10-Tetramethoxypyrene-2,7-dicarbaldehyde (4)

To the oven dried Schlenk flask 2,7-diiodo-4,5,9,10-tetramethoxypyrene (400 mg, 0.69 mmol) was dissolved in 60 ml THF and cooled to –78 °C. At this temperature 6 ml *n*-BuLi (1.6 M) hexane solution was added drop wise under argon and stirred for 3 hour. Then 10.3 mmol of DMF was added and continued stirring at –78 °C for 2.5 hour. The reaction was mixture warmed to room temperature and hydrolyzed in saturated NH_4Cl solution. The yellow precipitate (192 mg) was collected by vacuum filtration in 71% yield. M.P 323 °C.^{1}H NMR (250 MHz, $CDCl_3$) δ (ppm) 4.19 (s, 12H), 8.89 (s, 4H), 10.43 (s, 2H).^{13}C NMR (75 MHz, CDCl3) δ (ppm) 61.92, 120.70, 123.71, 130.58, 135.21, 146.06, 193.40. **MS-FD** (8 kV, CH_2Cl_2) m/z: found 387.8 (100%). ESI-HRMS: found 401.1005 calculated 401.1001 for C_{22} H_{18} O_6 Na.

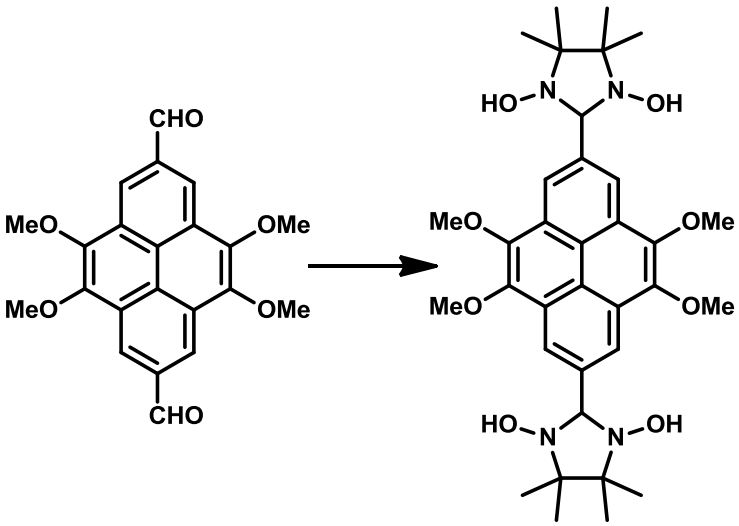

2,2'-(4,5,9,10-Tetramethoxypyrene-2,7-diyl)bis(4,4,5,5-tetramethylimidazolidine-1,3-diol) (5)

The 4,5,9,10-tetramethoxypyrene-2,7-dicarbaldehyde (200 mg, 0.52 mmol) and BHA (390 mg, 2.6 mmol) were suspended in argon bubbled 80 ml benzene in a round bottom flask equipped with a water condenser. The resulting suspension was refluxed under argon for 2 days. The precipitate formed, was filtered and washed with benzene to obtain a pale yellow product (250 mg) in 74% yield, and used as it is without any purification for the next step.

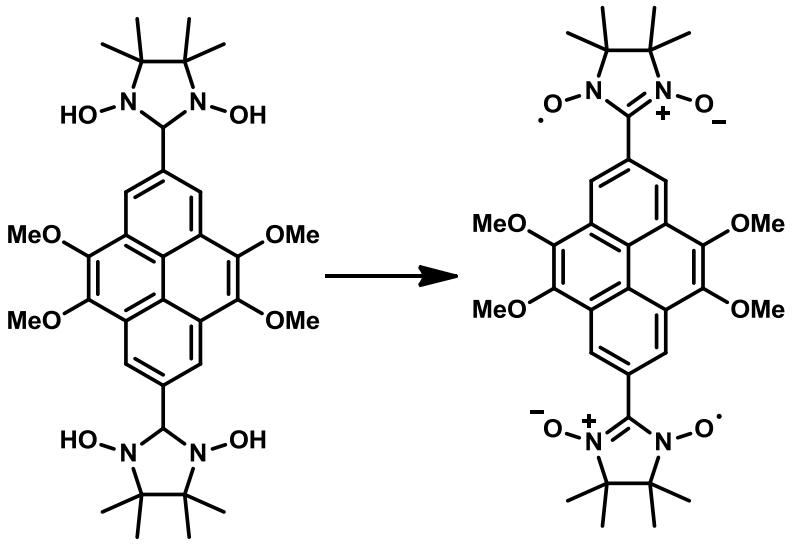

2,2'-(4,5,9,10-Tetramethoxypyrene-2,7-diyl)bis(4,4,5,5-tetramethylimidazo-

lidine-1-oxyl-3-oxo) (TMPNN)

2,2'-(4,5,9,10-Tetramethoxypyrene-2,7-diyl)bis(4,4,5,5-tetramethylimidazolidine-1,3-diol) (100 mg, 0.16 mmol) and $NaIO_4$ (0.32 mmol) were suspended in two phase H_2O/CH_2Cl_2 (1:1) mixture and the reaction mixture stirred in an ice bath. After 2.5 hour the dark bluish-green organic phase was separated, washed with water, brine and dried over $MgSO_4$. The aqueous phase was extracted with DCM. Solvent was removed under vacuum, and the residue was chromatographed over silica gel using hexane: ethylacetate (1:1) as eluent to obtain blue crystalline product (25 mg) in 25% yield. M.P > 300 °C (decomp). **EPR** (298 K, 8×10^{-4} M in toluene): nine lines, g_{iso} = 2.0066, $a_{N1}/2$ = 0.0.373 mT. **UV-Vis** (toluene) λ_{max} (ε, $M^{-1}\,cm^{-1}$): 604 nm (460), 641 nm (450).

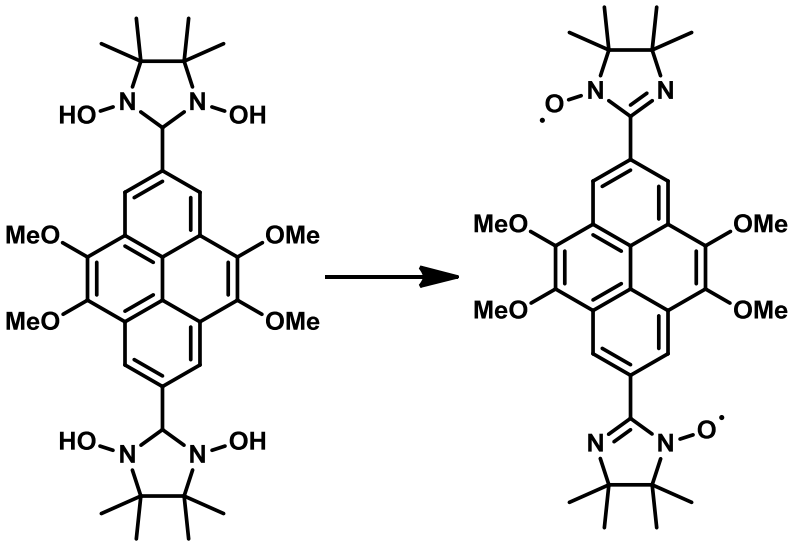

2,2'-(4,5,9,10-tetramethoxypyrene-2,7-diyl)bis(4,4,5,5-tetramethylimidazo-lidine-1-oxyl) (TMPIN)

2,2'-(4,5,9,10-Tetramethoxypyrene-2,7-diyl)bis(4,4,5,5-tetramethylimidazolidine-1,3-diol) (100 mg, 0.16 mmol) was suspended in two phase H_2O/CH_2Cl_2 (1:1) mixture. To the resulting mixture $NaNO_2$/HCl solution (60 mg $NaNO_2$, 6 drops of HCl) in water was added and stirred for 10 mins at room temperature. The orange organic phase was separated and washed with water followed by brine and dried over $MgSO_4$. Solvent was

removed under vacuum, and the residue was chromatographed over silica gel using hexane: ethylacetate (2:1) as eluent to give orange solid (35 mg) in 36% Yield. **EPR** (298 K, 8×10^{-4} M in toluene): thirteen lines, g_{iso} = 2.0059, $a_{N1}/2$ = 0.225 mT and $a_{N2}/2$ = 0.460 mT. **UV-Vis** (Toluene) λ_{max} (ε, M^{-1} cm^{-1}): 520 nm (551).

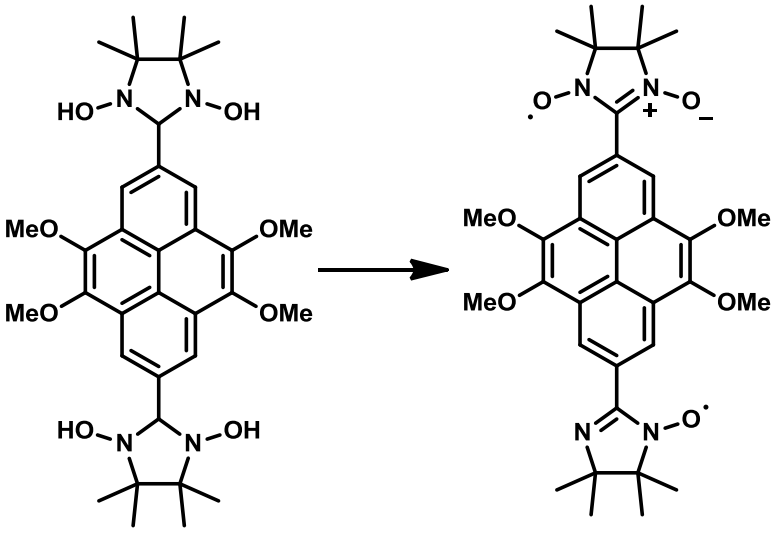

2,2'-(4,5,9,10-tetramethoxypyrene-2,7-diyl)(4,4,5,5-tetramethylimidazolidine-1-oxyl-3-oxo)(4,4,5,5-tetramethylimidazolidine-1-oxyl) (TMPMIX)

2,2'-(4,5,9,10-Tetramethoxypyrene-2,7-diyl)bis(4,4,5,5-tetramethylimidazolidine-1,3-diol) (100 mg, 0.16 mmol) and $NaIO_4$ (0.48 mmol) were suspended in two phase H_2O/CH_2Cl_2 (1:1) mixture. The reaction mixture was stirred in an ice bath (reaction monitored by TLC). After 3 hour the dark grey organic phase was separated, washed with water, brine and dried over $MgSO_4$. The aqueous phase was extracted with DCM. Solvent was removed under vacuum, and the residue was chromatographed over silica gel using hexane: ethylacetate (1:1) as eluent and the desired product obtained as grey powder (18 mg) in 25% yield along with 5 mg of **1** and 6 mg of **2**. M.P > 300 °C (decomp). **EPR** (298 K, 8×10^{-4} M in toluene): g_{iso} = 2.0062, $a_{N1}/2$ = 0.374 mT, $a_{N2}/2$ = 0.200 mT and $a_{N3}/2$ = 0.460 mT. **UV-Vis** (Toluene) λ_{max} (ε, M^{-1} cm^{-1}): 524 nm (393), 599 nm (389), 642 nm (368).

4.11 References

[1] P. Ravat, Y. Ito, E. Gorelik, V. Enkelmann, M. Baumgarten, *Org. Lett.* **2013**, *15*, 4280.

[2] K. Aoki, H. Akutsu, J.-i. Yamada, S. i. Nakatsuji, T. Kojima, Y. Yamashita, *Chem. Lett.* **2009**, *38*, 112.

[3] T. M. Figueira-Duarte, K. Müllen, *Chem. Rev.* **2011**, *111*, 7260.

[4] Y. Wang, H. Wang, Y. Liu, C.-a. Di, Y. Sun, W. Wu, G. Yu, D. Zhang, D. Zhu, *J. Am. Chem. Soc.* **2006**, *128*, 13058.

[5] Y. B. Borozdina, V. Kamm, F. Laquai, M. Baumgarten, *J. Mater. Chem.* **2012**, *22*, 13260.

[6] T. Sugawara, H. Komatsu, K. Suzuki, *Chem. Soc. Rev.* **2011**, *40*, 3105.

[7] R. T. Hayes, C. J. Walsh, M. R. Wasielewski, *J. Phys. Chem. A* **2004**, *108*, 2375.

[8] Y. Teki, S. Miyamoto, K. Iimura, M. Nakatsuji, Y. Miura, *J. Am. Chem. Soc.* **2000**, *122*, 984.

[9] E. A. Mostovich, Y. Borozdina, V. Enkelmann, K. Remović-Langer, B. Wolf, M. Lang, M. Baumgarten, *Cryst. Growth Des.* **2012**, *12*, 54.

[10] Y. Morita, S. Suzuki, K. Sato, T. Takui, *Nat. Chem.* **2011**, *3*, 197.

[11] Y. Morita, S. Nishida, T. Murata, M. Moriguchi, A. Ueda, M. Satoh, K. Arifuku, K. Sato, T. Takui, *Nat. Mater.* **2011**, *10*, 947.

[12] H. Akpinar, J. T. Mague, M. A. Novak, J. R. Friedman, P. M. Lahti, *CrystEngComm* **2012**, *14*, 1515.

[13] Y. Teki, M. Kimura, S. Narimatsu, K. Ohara, K. Mukai, *Bull. Chem. Soc. Jpn.* **2004**, *77*, 95.

[14] Y. Miura, N. Matsuba, R. Tanaka, Y. Teki, T. Takui, *J. Org. Chem.* **2002**, *67*, 8764.

[15] M. Kreyenschmidt, M. Baumgarten, N. Tyutyulkov, K. Mullen, *Angew. Chem. Int. Ed.* **1994**, *33*, 1957.

[16] S. Karabunarliev, M. Baumgarten, *Chem. Phys.* **2000**, *254*, 239.

[17] S. Suzuki, T. Takeda, M. Kuratsu, M. Kozaki, K. Sato, D. Shiomi, T. Takui, K. Okada,

Org. Lett. **2009**, *11*, 2816.

[18] S.-i. Kawano, M. Baumgarten, D. Chercka, V. Enkelmann, K. Müllen, *Chem. Commun.* **2013**, *49*, 5058.

[19] J. Lee, E. Lee, S. Kim, G. S. Bang, D. A. Shultz, R. D. Schmidt, M. D. E. Forbes, H. Lee, *Angew. Chem. Int. Ed.* **2011**, *50*, 4414.

[20] Y. G. Budnikova, T. V. Gryaznova, M. K. Kadirov, E. V. Tret'yakov, K. V. Kholin, V. I. Ovcharenko, R. Z. Sagdeev, O. G. Sinyashin, *Russ. J. Phys. Chem. A* **2009**, *83*, 1976.

[21] M. Kadirov, E. Tretyakov, Y. Budnikova, M. Valitov, K. Holin, T. Gryaznova, V. Ovcharenko, O. Sinyashin, *J. Electroanal. Chem.* **2008**, *624*, 69.

[22] M. Tamura, Y. Nakazawa, D. Shiomi, K. Nozawa, Y. Hosokoshi, M. Ishikawa, M. Takahashi, M. Kinoshita, *Chem. Phys. Lett.* **1991**, *186*, 401.

[23] Y. H. Masafumi Tamura, Daisuke Shiomi, Minoru Kinoshita, Yasuhiro Nakasawa, Masayasu Ishikawa, Hiroshi Sawa, Takafumi Kitazawa, Atsushi Eguchi, Yutaka Nishio and Koji Kajita, *J. Phys. Soc. Jpn* **2003**, *72*, 1735.

[24] G. A. Bain, J. F. Berry, *J. Chem. Educ.* **2008**, *85*, 532.

[25] B. Bleaney, K. D. Bowers, *Proc. R. Soc. London A* **1952**, *214*, 451.

[26] G. Zoppellaro, V. Enkelmann, A. Geies, M. Baumgarten, *Org. Lett.* **2004**, *6*, 4929.

[27] L. Noodleman, *J. Chem. Phys.* **1981**, *74*, 5737.

[28] K. Yamaguchi, F. Jensen, A. Dorigo, K. N. Houk, *Chem. Phys. Lett.* **1988**, *149*, 537.

[29] T. Soda, Y. Kitagawa, T. Onishi, Y. Takano, Y. Shigeta, H. Nagao, Y. Yoshioka, K. Yamaguchi, *Chem. Phys. Lett.* **2000**, *319*, 223.

[30] M. Shoji, K. Koizumi, Y. Kitagawa, T. Kawakami, S. Yamanaka, M. Okumura, K. Yamaguchi, *Chem. Phys. Lett.* **2006**, *432*, 343.

CHAPTER 5

TUNING THE INTRA-MOLECULAR EXCHANGE INTERACTIONS BY SYNTHESIZING THE POSITIONAL ISOMERS OF BIRADICALS

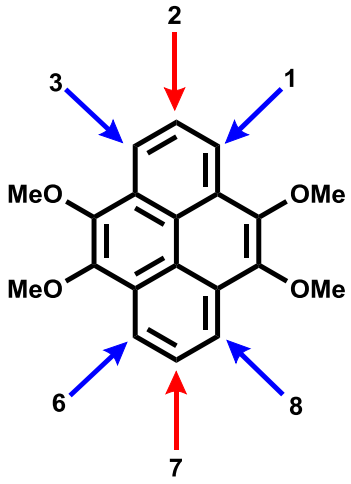

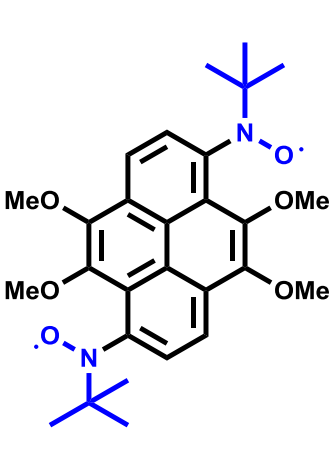

1,6-TMPNO

J/k_B = -122 K

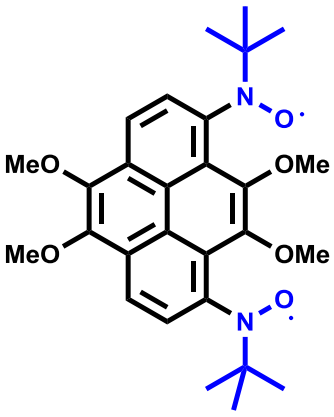

1,8-TMPNO

J/k_B = -108 K

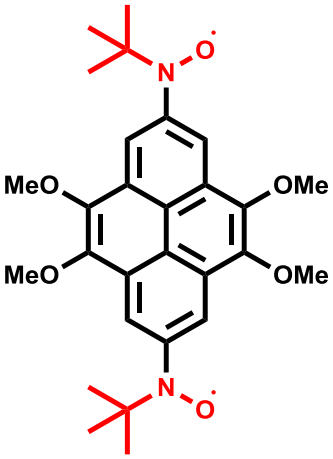

2,7-TMPNO

J/k_B = -1005 K

In this chapter the tuning of intra-molecular exchange interactions by synthesizing the positional isomers of biradical is described utilizing the approach 5. This approach allowed us to tune exchange interactions while maintaining the same π-spacer as well as the radical moieties.

5.1 Introduction

The magnetic exchange interactions in organic biradicals highly depend on the type and position of the radical moiety on the spacer molecule.[1] In previous chapters it was shown how intra-molecular exchange interactions can be tuned either by *changing the radical moiety while maintaining the same π-spacer* (Approach 4, Chapter 4)[2] or *changing the π-spacer while keeping the same radical moiety* (Approach 1, Chapter 1).[3-5] Thus, it was intriguing to design the biradical systems in which the magnetic exchange interactions can be tuned without changing either the radical moiety or a π-system (Approach 5). This approach allows tuning of intra-molecular magnetic exchange interactions while conserving same π-spacer as well as radical moiety. This could be realized by appropriate choice of the spacer unit and the radical moiety. The π-spacer should be chosen such that it can be functionalized at several positions selectively. Thereby synthesizing positional isomers of biradicals it may be possible to tune the exchange interactions.

The 4,5,9,10-tetramethoxy pyrene (TMP)[6] was chosen as a spacer unit as its dihalo-positional isomers can be synthesized which in turn used as precursors for the synthesis of biradicals. The *tert*-butylnitroxide was opted as radical moiety owing to its high stability and ease of synthesis. Thus, we have planned to synthesize following positional biradical isomers of TMP.

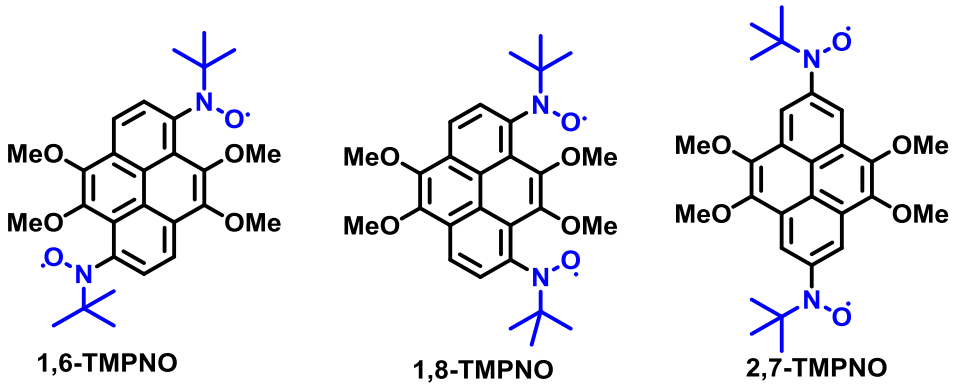

Figure 5.1: 1,6-, 1,8- and 2,7- positional isomers of TMP based biradicals.

The antiferromagnetically coupled 1,6-, 1,8-, and 2,7- positional isomers of TMP based biradicals (Figure 5.1) were synthesized and characterized by FD-Mass, EPR and UV-Vis spectral analysis. The intra-molecular magnetic exchange interactions were investigated using DFT calculations. In the first part of the chapter the structural property relationship was investigated for isomeric mono radicals 1-TMPNO and 2-TMPNO (Figure 5.2), which were obtained as side product during the synthesis of biradicals. Otherwise they can be easily synthesized from 1-bromo-TMP or 2-bromo-TMP. Furthermore synthesis of tri- and tetra-radical (1,3,6-TMPNO and 1,3,6,8-TMPNO) was also attempted to realize high spin system and the obtained results are discussed in details in the following sections (Figure 5.3).

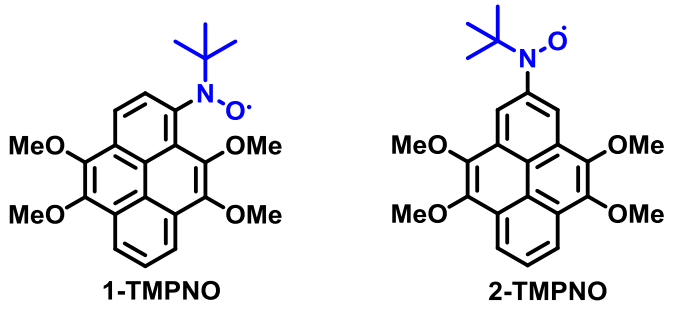

Figure 5.2: Mono radicals 1-TMPNO and 2-TMPNO.

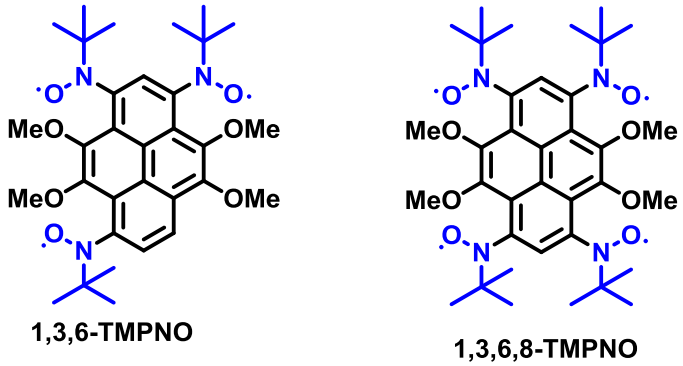

Figure 5.3: Tri- and tetra- radical 1,3,6-TMPNO and 1,3,6,8-TMPNO.

5.2 Mono radicals, 1-TMPNO and 2-TMPNO

The UV-Vis spectra of 1-TMPNO and 2-TMPNO showed distinct features for the pyrene as well as radical absorption pattern (Figure 5.4). While 1-TMPNO showed absorption band for pyrene at 339 and 356 nm, 2-TMPNO displayed the same at 312 and 354 nm with different extinction coefficient as shown in Figure 5.4. Both the radicals exhibited the characteristic n—π* transition for *tert*-butylaminoxyl radical moiety which appeared as a shoulder of pyrene absorption peak in 1-TMPNO and as a distinguished peak in 2-TMPNO. The UV-Vis analysis clearly indicated the influence of position of radical moiety on electronic structure of pyrene core. This was also reflected in EPR measurements.

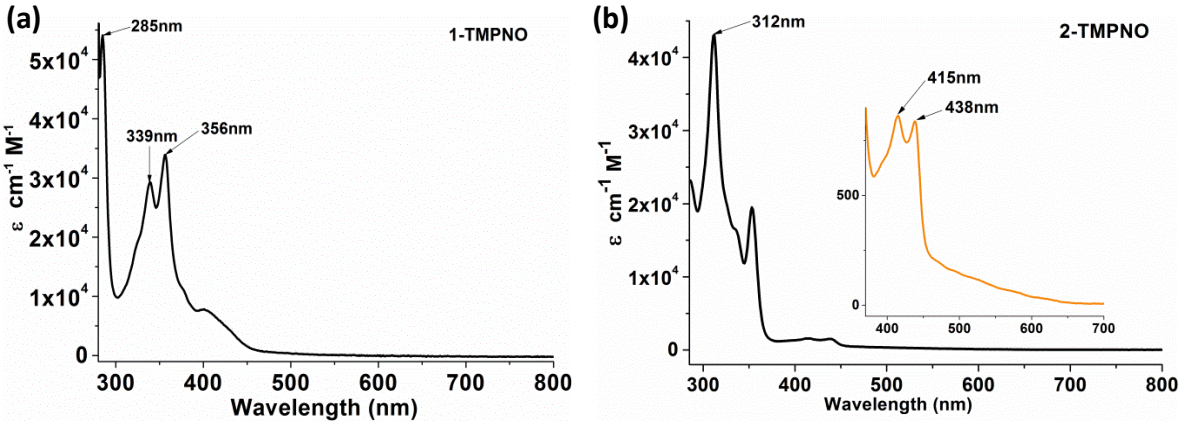

Figure 5.4: UV-Vis spectra of 1-TMPNO and 2-TMPNO.

The room temperature EPR spectrum of 1-TMPNO in toluene consisted of three lines having equal intensity due to hyperfine coupling (*hfc*) with nitrogen (Figure 5.5). The obtained *hfc* constant from the spectral simulation, was a_N = 16 G at g-value 2.0068. Interestingly 2-TMPNO gave an EPR spectrum which comprises of triplet of triplet because of *hfc* with aminoxyl nitrogen and two *ortho* protons (Figure 5.6). The spectral simulation gave the *hfc* constant values a_N = 8 G and a_H = 1.96 G at g-value of 2.0067. Thus the EPR analysis indicated the extent of spin delocalization is higher in case of 2-TMPNO

than in 1-TMPNO.

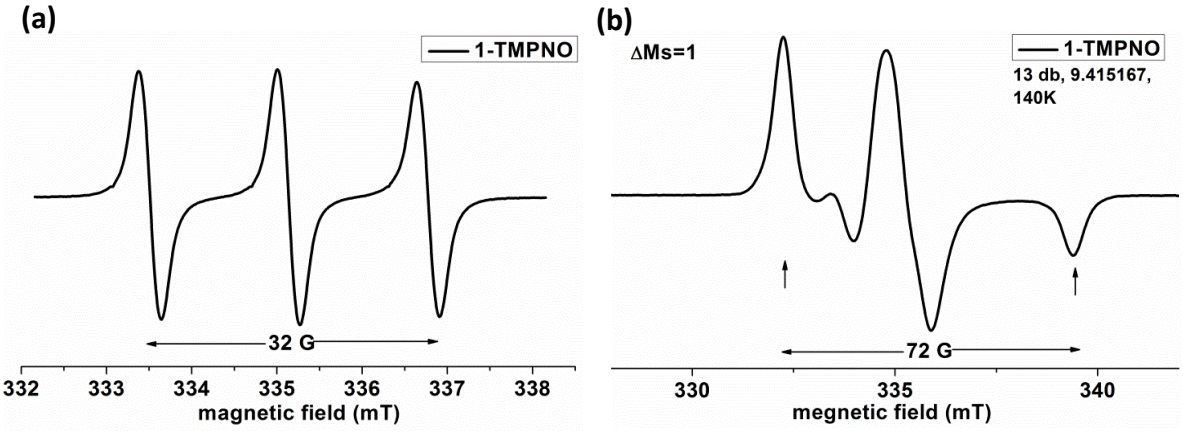

Figure 5.5: EPR spectra of 1-TMPNO in toluene (a) at room temperature and (b) in frozen state at 140 K.

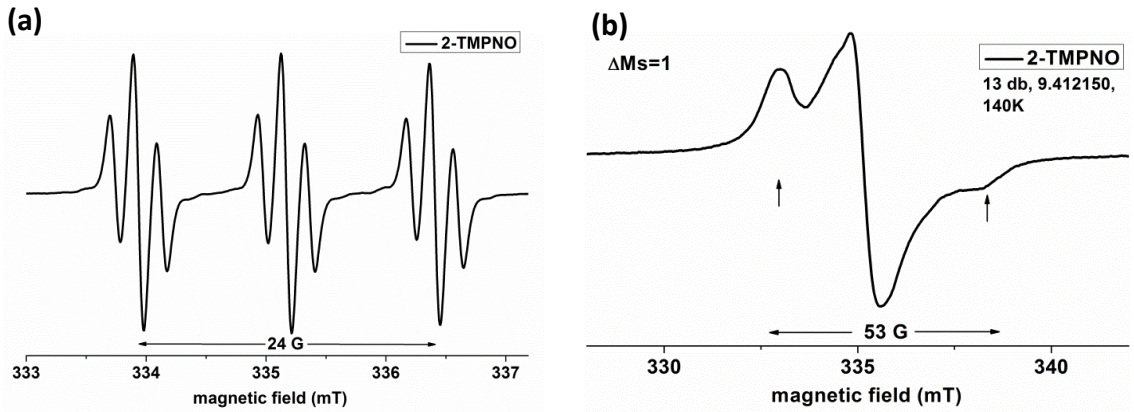

Figure 5.6: EPR spectra of 2-TMPNO in toluene (a) at room temperature and (b) in frozen state at 140 K.

Single crystals of both radicals were successfully obtained. Single crystal X-ray analysis revealed that 1-TMPNO and 2-TMPNO crystallized in triclinic and monoclinic space groups, respectively. The crystal packing analysis indicated no short contacts between radical centers ruling out presence of any substantial inter-molecular magnetic interactions (Figure 5.9). Notably very significant difference was observed in torsion angle of aminoxyl group with pyrene core in isomers. The radical moiety was, in plane with the pyrene core for 2-TMPNO (torsion angle 13°) and out of plane for 1-TMPNO (torsion angle

60°) (Figure 5.7). Using the single crystal geometries the spin densities were calculated with DFT. In concurrence with EPR measurements, the spin density was localized in 1-TMPNO but highly delocalized in 2-TMPNO (Figure 5.8).

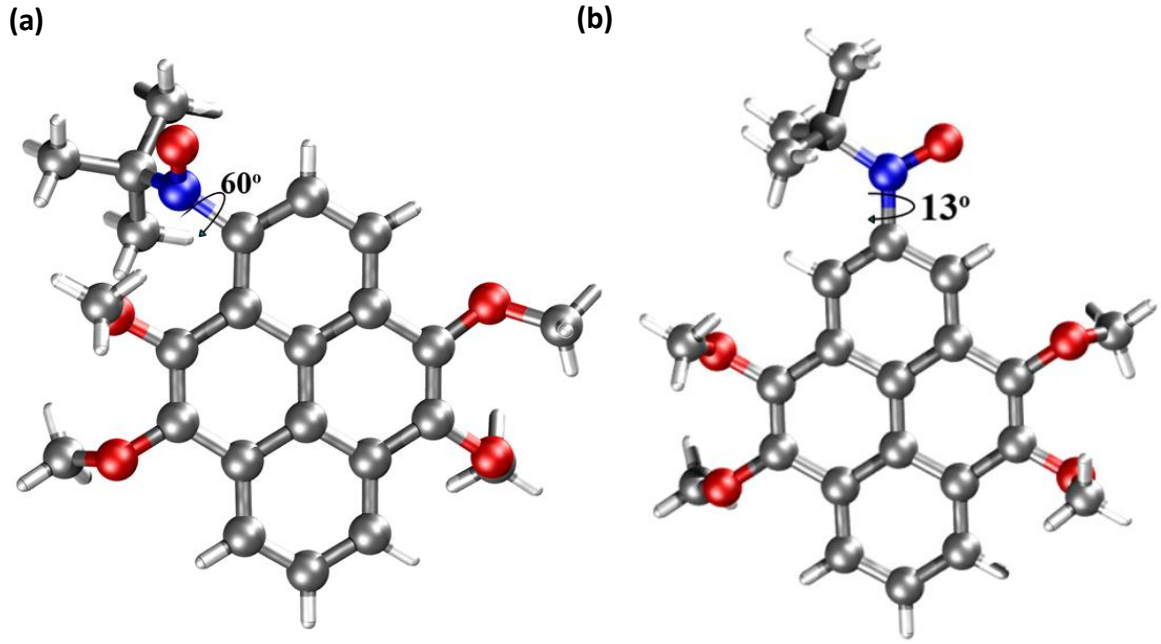

Figure 5.7: Crystal structure of (a) 1-TMPNO and (b) 2-TMPNO.

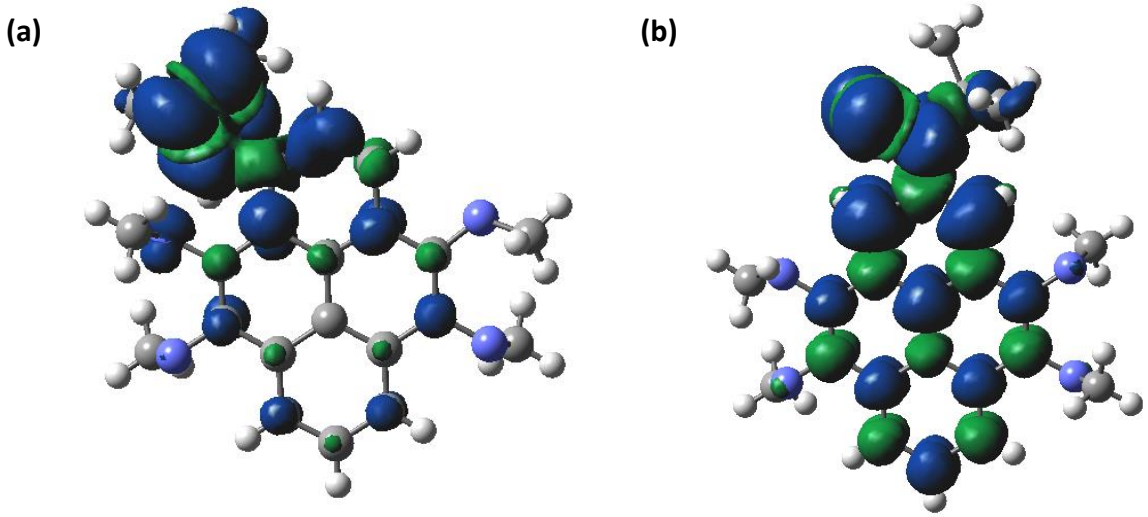

Figure 5.8: Spin density distribution in (a) 1-TMPNO and (b) 2-TMPNO.

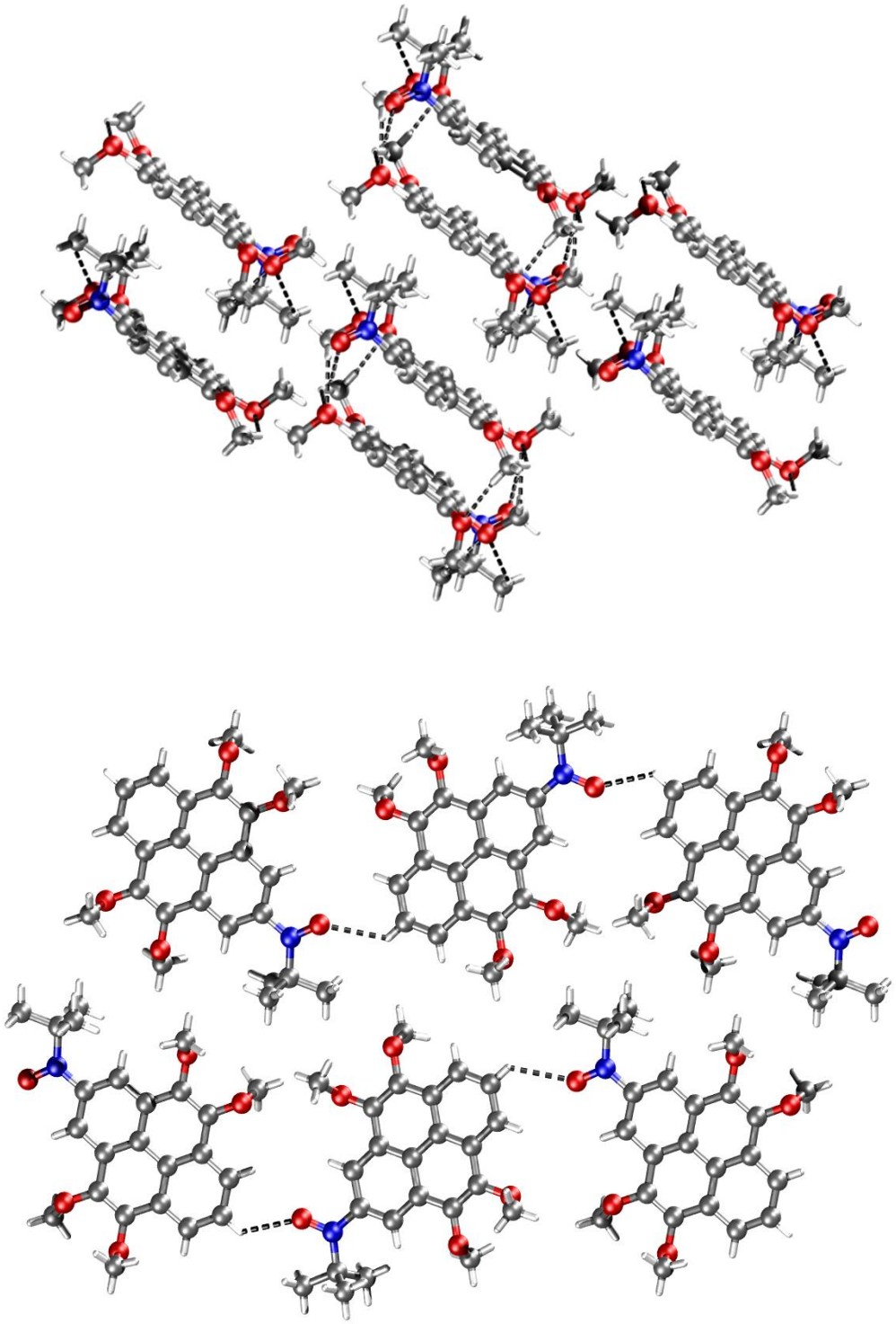

Figure 5.9: Crystal packing and hydrogen bond pattern of (a) 1-TMPNO and (b) 2-TMPNO.

To probe the influence of the position of radical moiety on the electrochemical property of TMPNO, cyclic volatammetry (CV) measurements were carried out. The CV spectra were measured in acetonitrile using ferrocene as an internal standard. Interestingly while 2-TMPNO gave a reversible oxidation ($E^{1/2}$(ox) = 0.94 V) and reduction wave ($E^{1/2}$(red) = −0.91 V), the 1-TMPNO displayed a reversible oxidation ($E^{1/2}$(ox) = 0.79 V) and a non-reversible reduction wave (Figure 5.10). The oxidation peak could be assigned to resonance delocalization of oxoammonium cation while the reduction peak was due to delocalization of aminoxy anion. This indicated the position of the radical moiety not only influences the electronic structure of pyrene but also the affinity of the radical moiety towards oxidation or reduction.

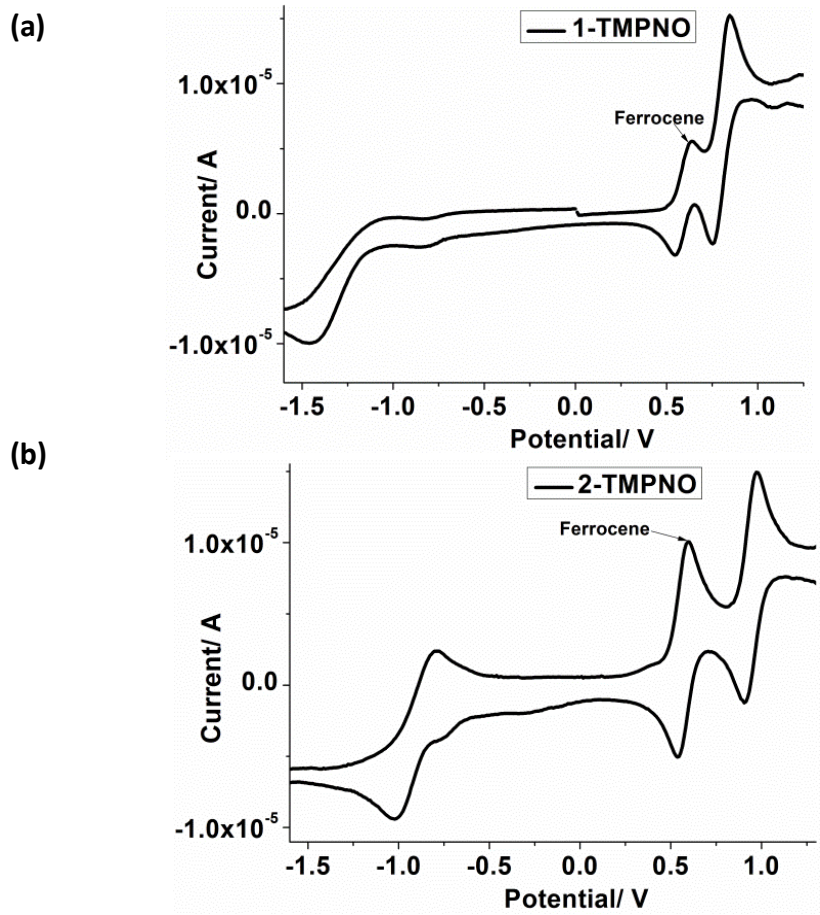

Figure 5.10: Cyclic Voltammetry curve of 1-TMPNO and 2-TMPNO recorded in acetonitrile (Bu_4NPF_6 (0.1 M), scan rate of 100 mV/s).

5.3 Biradicals, 1,6-, 1,8- and 2,7-TMPNO

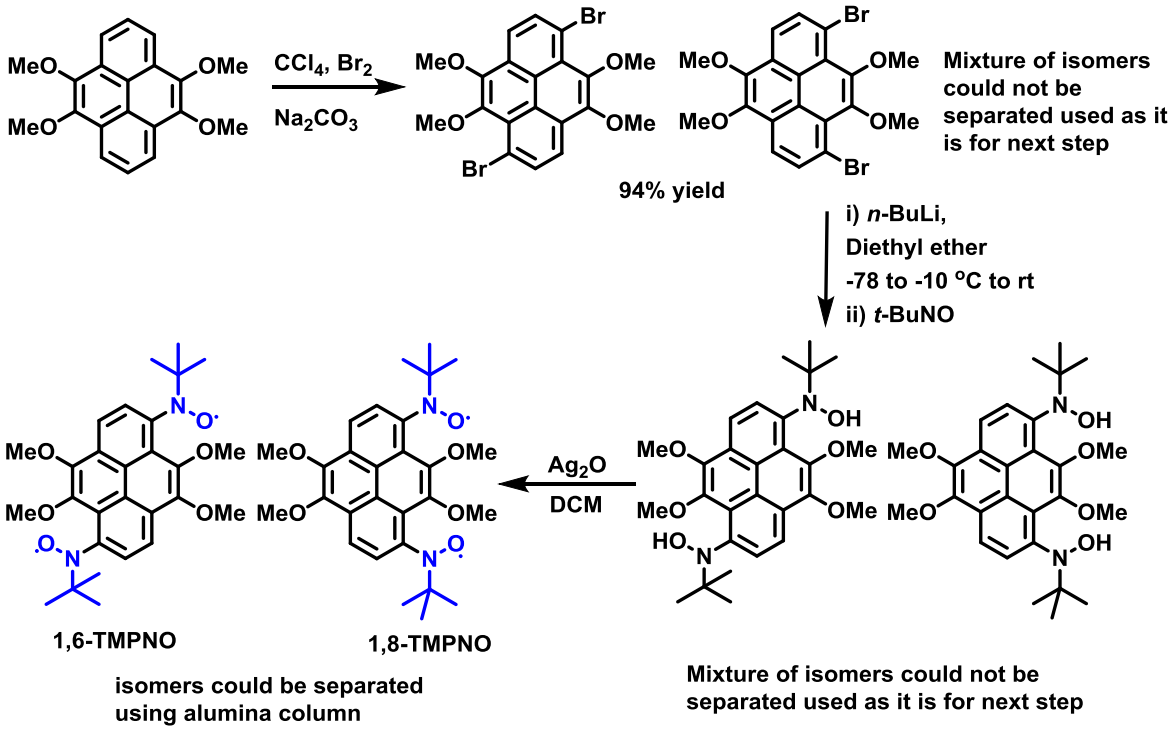

Scheme 5.1: Synthesis of 1,6- and 1,8-TMPNO.

4,5,9,10-Tetramethoxypyrene (TMP) can be efficiently brominated by Br_2 in CCl_4 as a solvent at room temperature . Depending on the equivalence of bromine used and reaction time mono-, di-, tri- or tetra- bromo-4,5,9,10-tetramethoxypyrene can be synthesized. Dibromo-4,5,9,10-tetramethoxypyrene (DBrTMP) was obtained in just 10 min after the addition of 2 M bromine in CCl_4 to the solution of TMP in CCl_4, as an inseparable mixture of 1,6- and 1,8- isomers (Scheme 5.1). These two isomers could not be separated by column chromatography. After the purification by silica gel column isomeric mixture of DBrTMP was used in next step for the synthesis of radicals. Reaction of DBrTMP with *n*-BuLi in diethyl ether and subsequent addition of 2-methyl-2-nitrosopropane gave bishydroxylamine which was also used for further reaction without separating the isomers. Oxidation of bishydroxylamine yielded desired the biradicals. Both isomers showed poor separation as well as stability on silica-gel column but could be well separated over the alumina column. Along with desired biradicals the small amount

(~5%) of monoradical 1-TMPNO was also separated from the column. The limited stability of 1,6- and 1,8- TMPNO allowed their characterization only by FD-Mass, EPR, UV-Vis and DFT calculations. The isomers were distinguished by low temperature EPR measurements in toluene glass matrix.

Synthesis and detailed characterization of 2,7-TMPNO is explained in Chapter 6. 2,7-TMPNO was found to be existing in semi-quinoid form (Scheme 5.2) with very strong intra-molecular exchange interactions (ΔE_{ST} (= $2J/k_B$) = −1185 K).

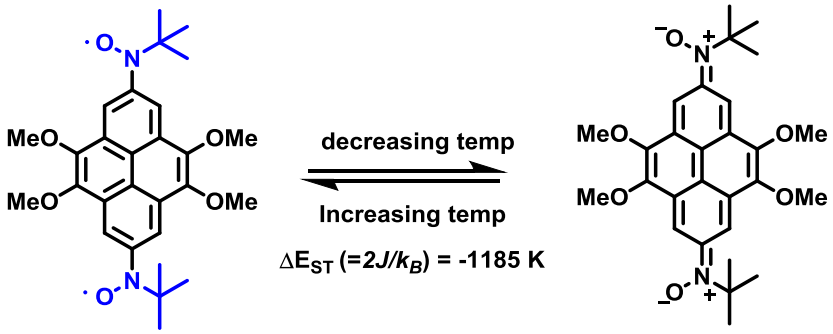

Scheme 5.2: The structural transformation of 2,7-TMPNO with temperature.

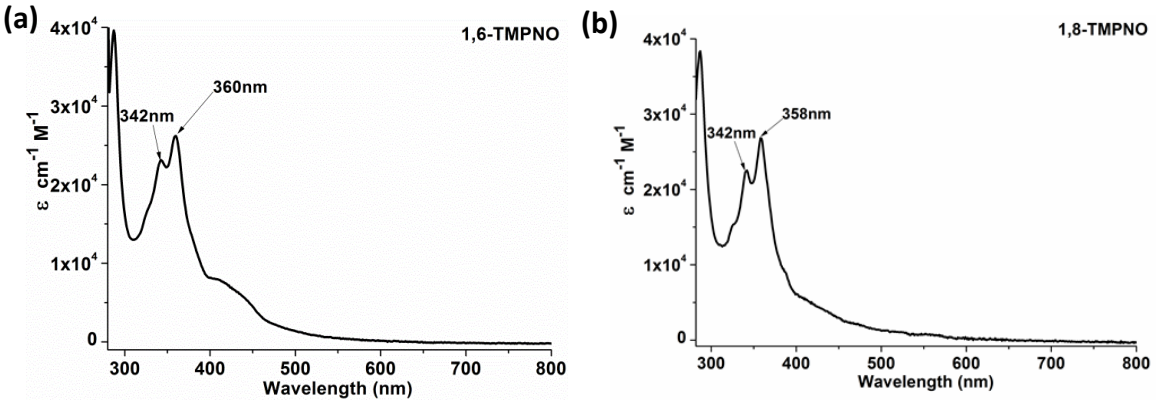

Figure 5.11: UV-Vis specrum of (a) 1,6-TMPNO and (b) 1,8-TMPNO.

1,6-TMPNO and 1,8-TMPNO displayed similar UV-Vis spectra as mono radical 1-TMPNO. While 1,6-TMPNO showed pyrene absorption at 342 and 360 nm, 1,8-TMPNO absorbed at 342 and 358 nm (Figure 5.11). For both biradicals the absorption due to radical moiety appeared as a shoulder to the pyrene absorption. This indicated unlike 2,7-TMPNO, the 1,6-TMPNO and 1,8-TMPNO exist in complete biradicaloid structure.

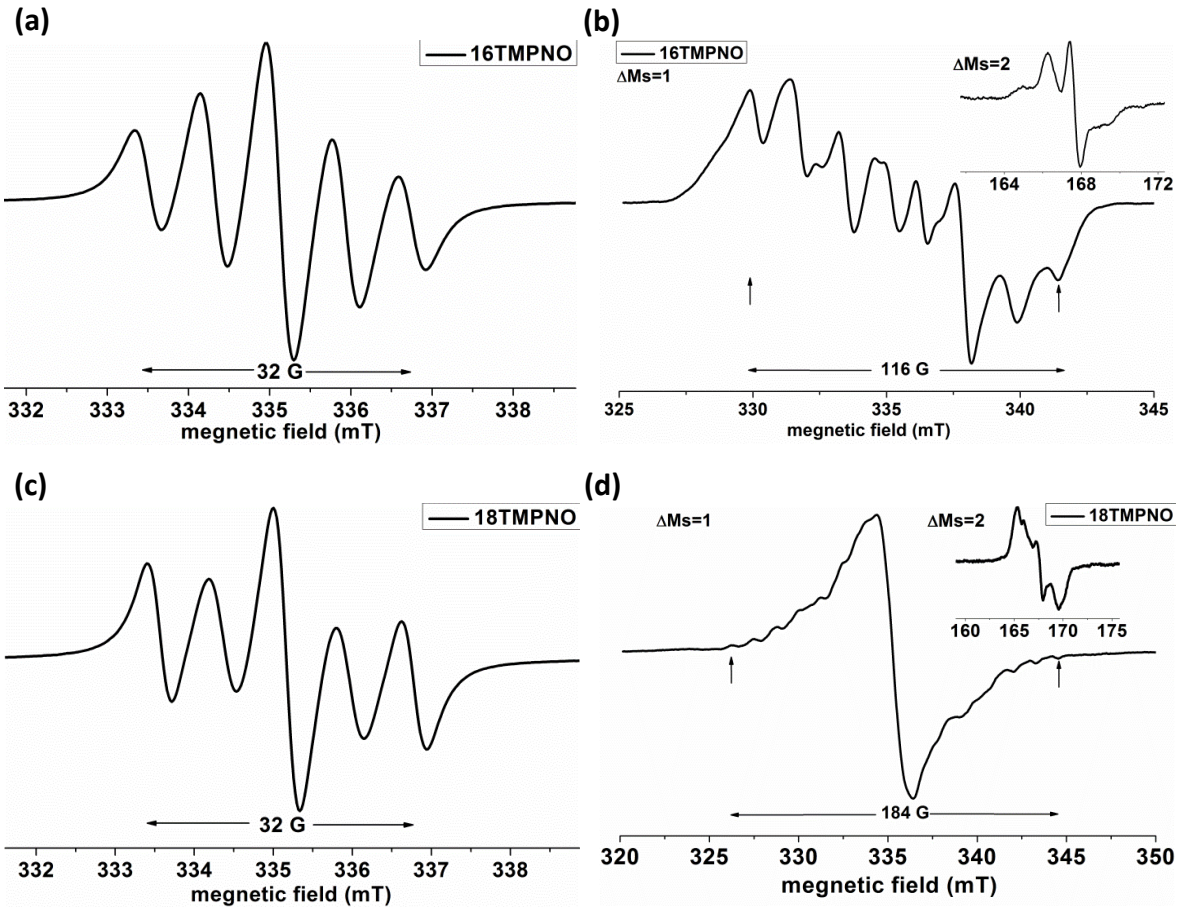

Figure 5.12: EPR spectra of 1,6-TMPNO in toluene (a) at room temperature and (b) in frozen state at 140 K and 1,8-TMPNO in toluene (c) at room temperature and (d) in frozen state at 140 K.

The room temperature EPR spectra of biradicals in toluene consisted of five lines due to hyperfine coupling of two equivalent nitrogen atoms (Figure 5.12). The spectral simulation gave the *hfc* constant $a_N/2$ = 8 G, which was half of the *hfc* constant for the mono radical 1-TMPNO at a g-value of 2.0068. This indicated, $J >> a_N$, the exchange interactions were much larger than the *hfc* constant. The EPR measurement of biradicals in toluene glass matrix at 140 K gave distinct fine structure spectra as shown in Figure 5.12. The zero field splitting was observed due to dipolar (anisotropic) interaction of unpaired electrons in a molecule. For an axial system the magnitude *zfs* parameter *D* is related to intra-radical distance (*d*) by $1/d^3$. The *D* value increases as the distance between the radical center decreases. The average intra radical distance can be obtained

by using the formulae, $d = 0.138/|D|^{1/3}$, *d* and *D* are in nm and cm^{-1} units, respectively (details are given in Chapter 2).

The 1,6- and 1,8- biradical isomers of TMPNO were distinguished from the magnitude of *zfs* parameter *D*. From the point dipole calculations using above formula the *D* value should be larger for 1,8-isomer compared to 1,6-isomer. Thus the EPR spectrum with *D* value 92 G was assigned to 1,8-TMPNO and with *D* value of 58 G assigned to 1,6-TMPNO. The calculated average intra radical distances were 6.74 Å and 7.85 Å for 1,6-TMPNO and 1,8-TMPNO, respectively. Additionally a $\Delta M_S = 2$ transition was also observed for both the radicals supporting the biradical nature of the molecules. The number of lines for the half field $\Delta M_S = 2$ transition are more than one instead of the expected just single line for biradical species. This discrepancy can be accounted for the different orientation of radical moieties in frozen state or the stronger inter molecular interactions.

5.4 Tri and tetra radicals, 1,3,6-TMPNO and 1,3,6,8-TMPNO

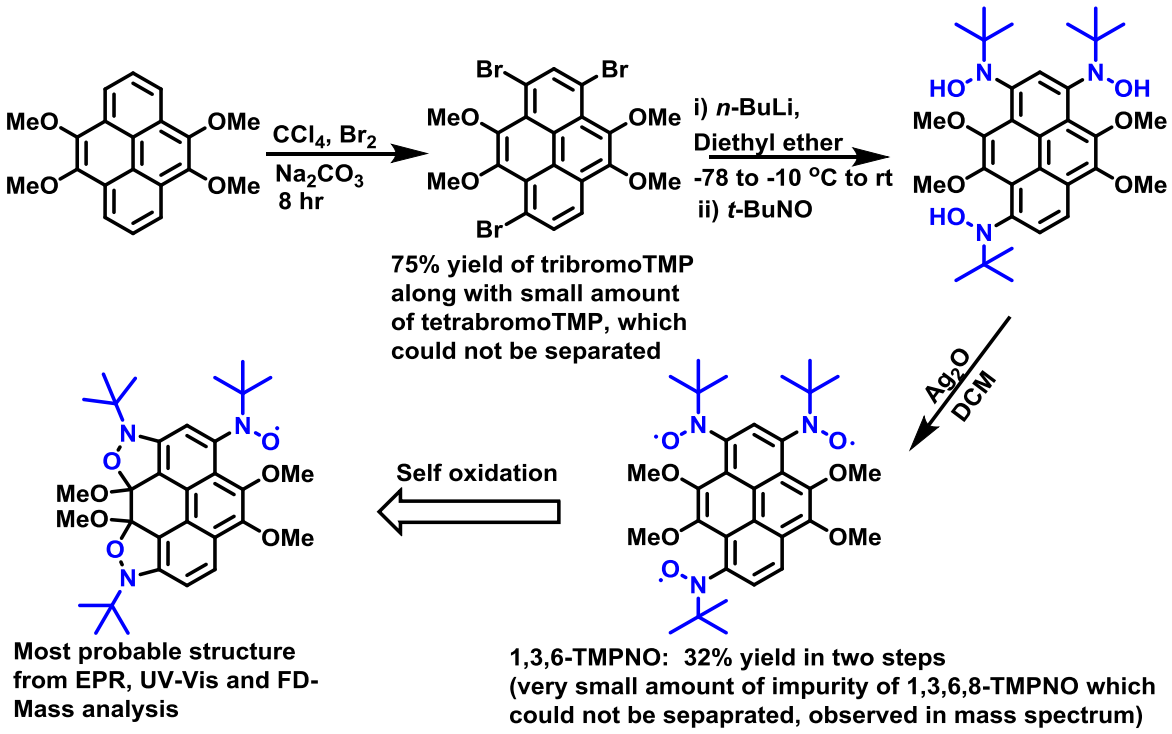

Scheme 5.3: Synthesis of 1,3,6-TMPNO.

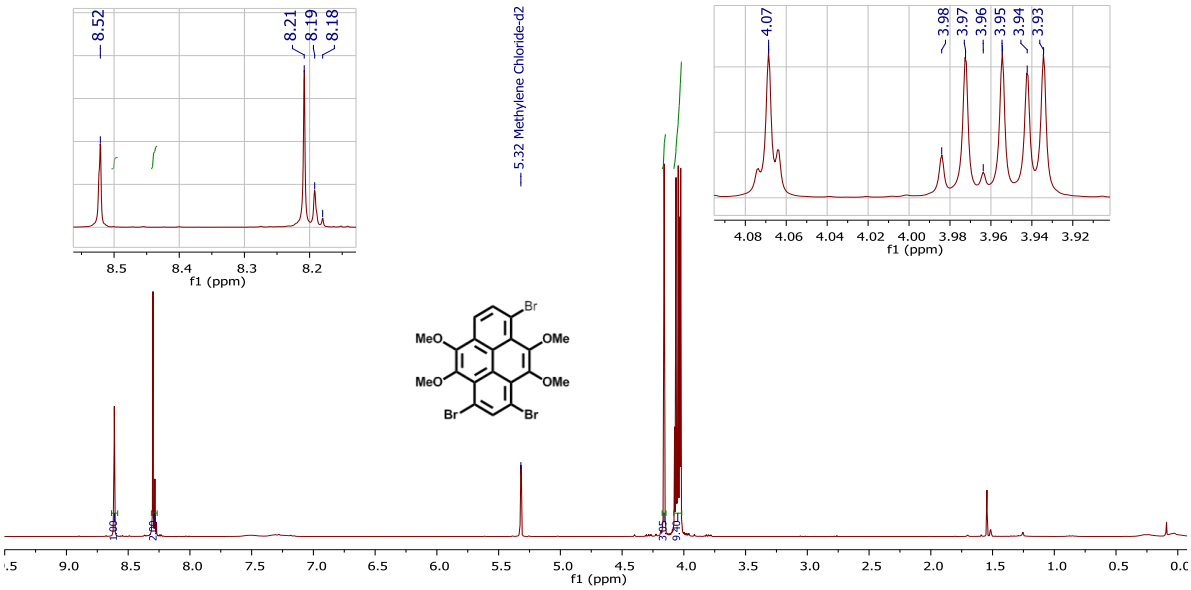

Figure 5.13: NMR spectrum of TBrTMP.

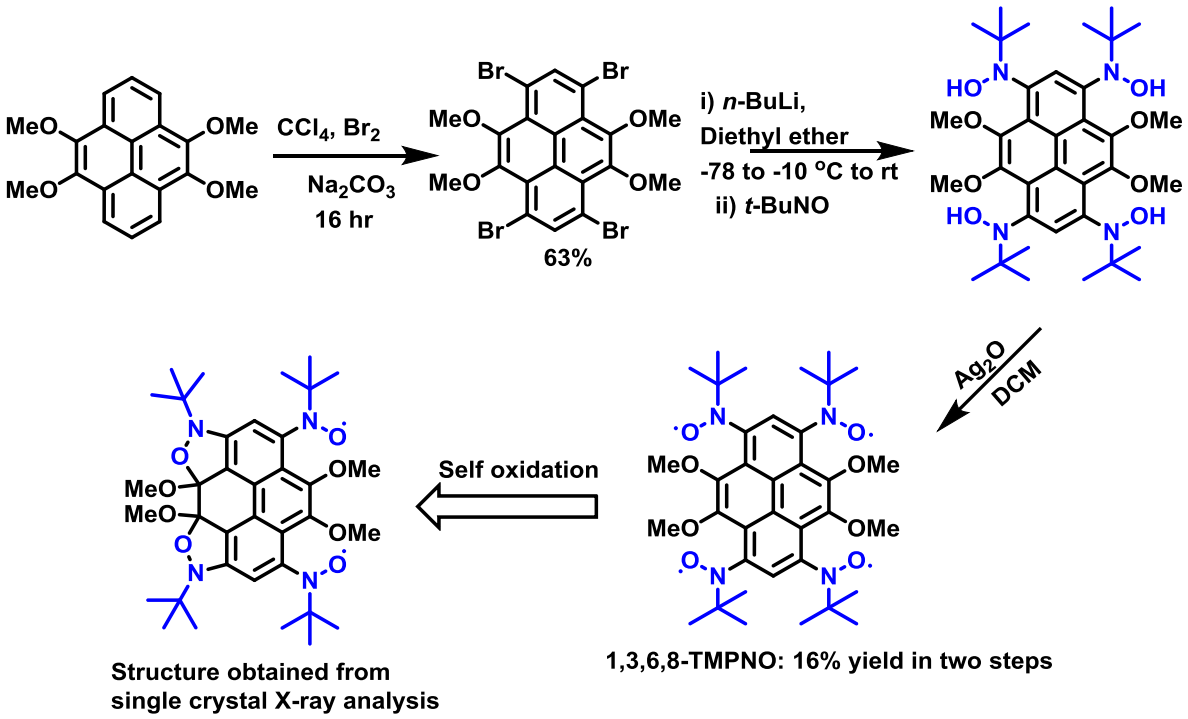

Scheme 5.4: Synthesis of 1,3,6,8-TMPNO.

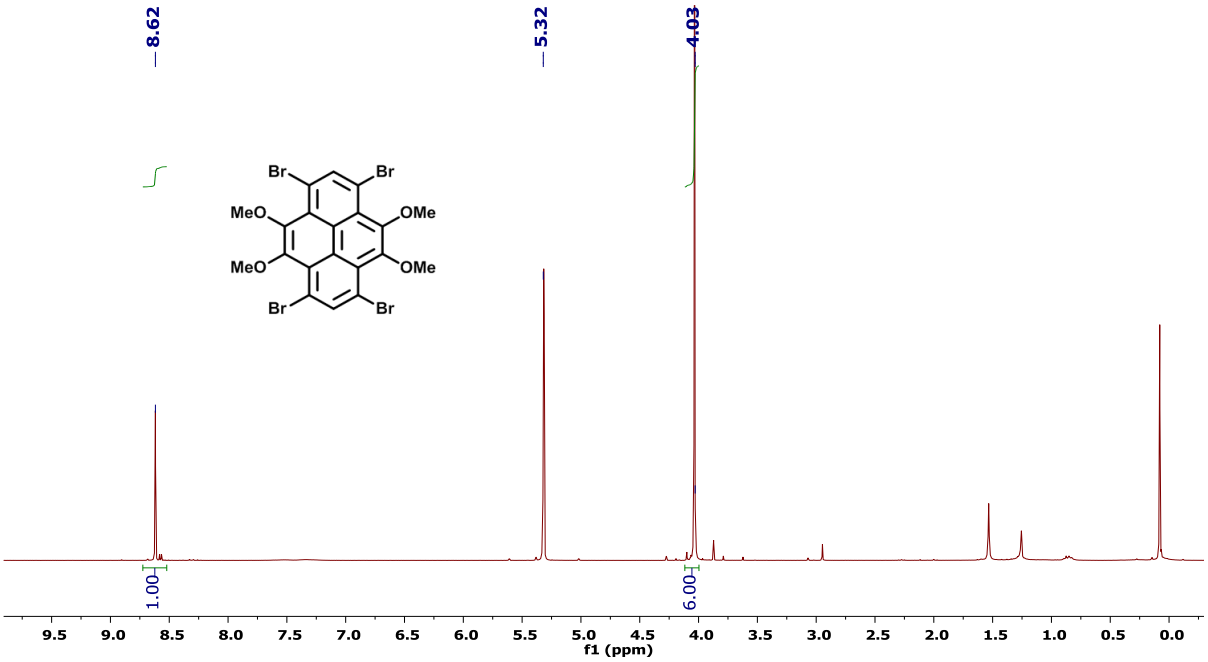

Figure 5.14: NMR spectrum of TetBrTMP.

The 1,3,6-TMPNO and 1,3,6,8-TMPNO were also synthesized like 1,6- or 1,8-TMPNO using the corresponding tribromo and tetrabromo TMP derivatives. 1,3,6-tribormo-4,5,9,10-tetramethoxypyrene (TBrTMP) and 1,3,6,8-tetrabormo-4,5,9,10-tetramethoxypyrene (TetBrTMP) were synthesized from 4,5,9,10-tetramethoxypyrene using similar synthetic procedure as for DBrTMP employing the larger amount of Br_2 and continuing reaction for longer time. TetBrTMP could be obtained in very pure form, TBrTMP contains small amount of impurity of TetBrTMP. The mass spectrum of TBrTMP showed a small peak corresponding to TetBrTMP. This small impurity of TetBrTMP could not be separated by column. Formation of products 1,3,6-TMPNO and 1,3,6,8-TMPNO was confirmed by FD-Mass.

While all the attempts to obtain single crystals of 1,3,6-TMPNO failed, the single crystals of 1,3,6,8-TMPNO were successfully obtained. Surprisingly crystal structure analysis revealed that 1,3,6,8-TMPNO undergoes intra-molecular self-oxidation as shown in Scheme 5.4, via oxidation of the double bond of the pyrene by two nitroxide radical moieties, giving a biradical species (Figure 5.15). The UV-Vis and EPR analysis indicated

1,3,6-TMPNO also undergoes self-oxidation, similar to 1,3,6,8-TMPNO, yielding the corresponding mono radical as shown in Scheme 5.3.

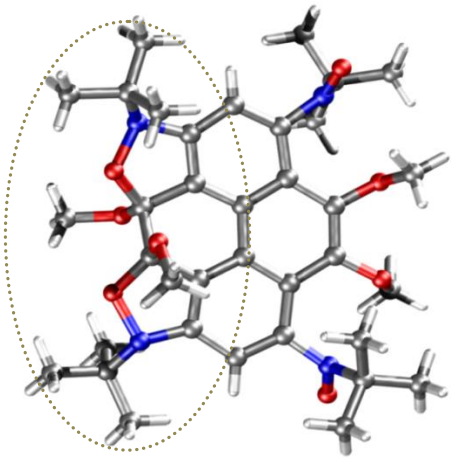

Figure 5.15: Crystal structure of 1,3,6,8-TMPNO.

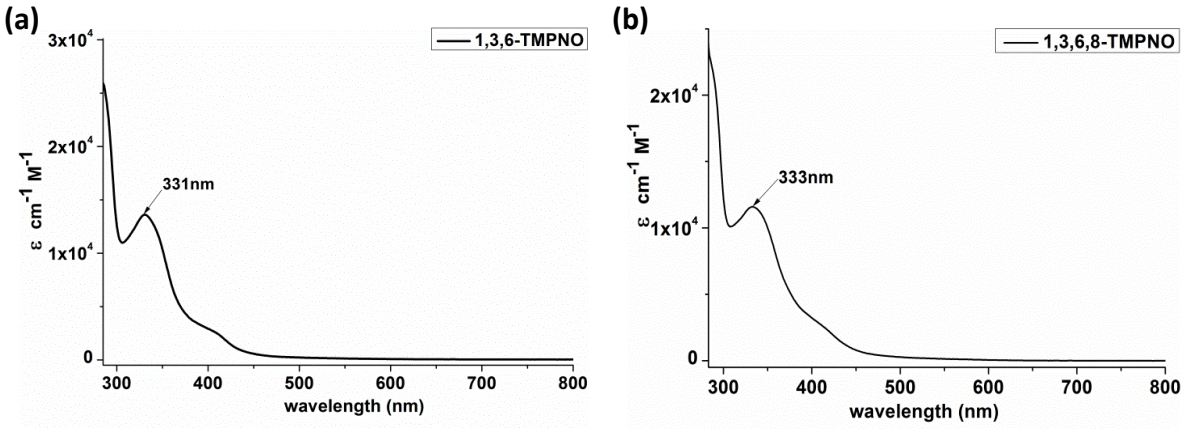

Figure 5.16: UV-Vis specrum of 1,3,6-TMPNO and 1,3,6,8-TMPNO.

As shown in Figure 5.16, the absorption spectra of 1,3,6-TMPNO and 1,3,6,8-TMPNO loses the features originating from the pyrene core. This indicated the destruction of the pyrene core in 1,3,6-TMPNO and 1,3,6,8-TMPNO. Both molecules showed similar absorption pattern with absorption maxima at λ_{max} = 330 nm and a shoulder around 420 nm stemming from the characteristic n—π* transition of the radical moiety.

The 1,3,6-TMPNO gave EPR spectrum alike 1-TMPNO (Figure 5.17a) with same g-

value and *hfc* constant (Table 5.1). Thus 1,3,6-TMPNO possesses only one free aminoxyl radical moiety while two radical moieties were involved in the oxidation of the pyrene core. The 1,3,6,8-TMPNO exhibited the EPR spectrum consist of five lines with two equivalent nitrogen *hfc* constant $a_N/2$ = 8 G at g-factor 2.0068 (Figure 5.17c). This showed the biradical nature of 1,3,6,8-TMPNO. When the EPR spectrum was measured in frozen toluene glass matrix *zfs* was observed with 2*D* = 163 G (Figure 5.17d). Using the formula discussed earlier the obtained distance between two radical moieties, 7.01 Å, was in accordance with the calculated spin-spin distance (7.5 Å) from point dipole calculation. This slight difference can be accounted by the delocalization of spin density into the pyrene. Additionally a forbidden ΔM_S = 2 transition at half field was also observed at 140 K for 1,3,6,8-TMPNO owing to thermally accessible triplet state.

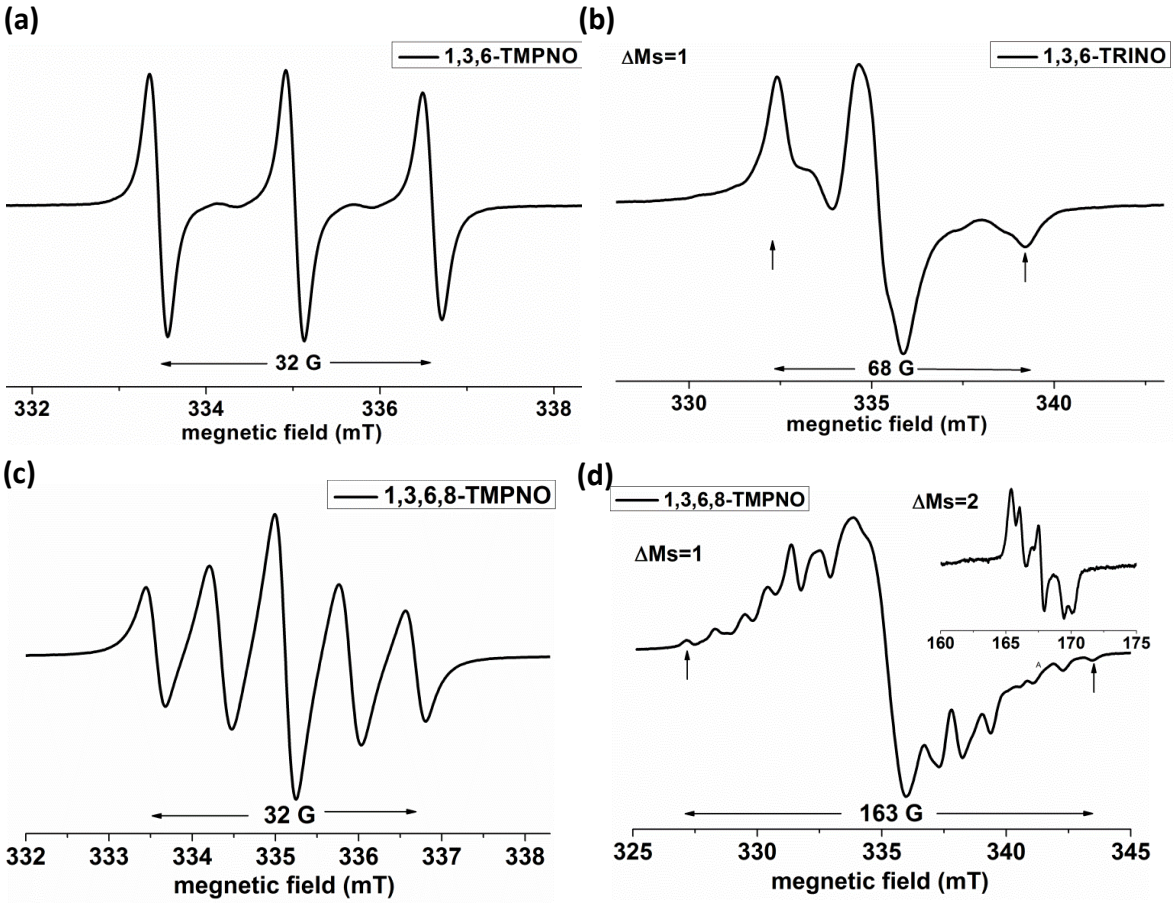

Figure 5.17: EPR spectra of 1,3,6-TMPNO in toluene (a) room temperature (b) 140 K and 1,3,6,8-TMPNO in toluene (c) room temperature (d) 140 K.

5.5 Biradical 1,3-PyNO with triplet ground state

Calder *et. al* reported the *meta* coupled biradical, *N,N'*-di-*tert*-butyl-*m*-phenylenebinitroxide (1,3-PhNO, Figure 5.18) which exist in triplet ground state.[7] The polyaromatic compound with triplet ground state is of special interest to obtain magneto conducting material. Thus keeping structure of 1,3-PhNO in mind we planned to synthesize pyrene based biradical 1,3-PyNO presuming to have triplet ground state.

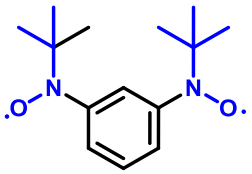

1,3-PhNO

Figure 5.18: Structure of 1,3-PhNO

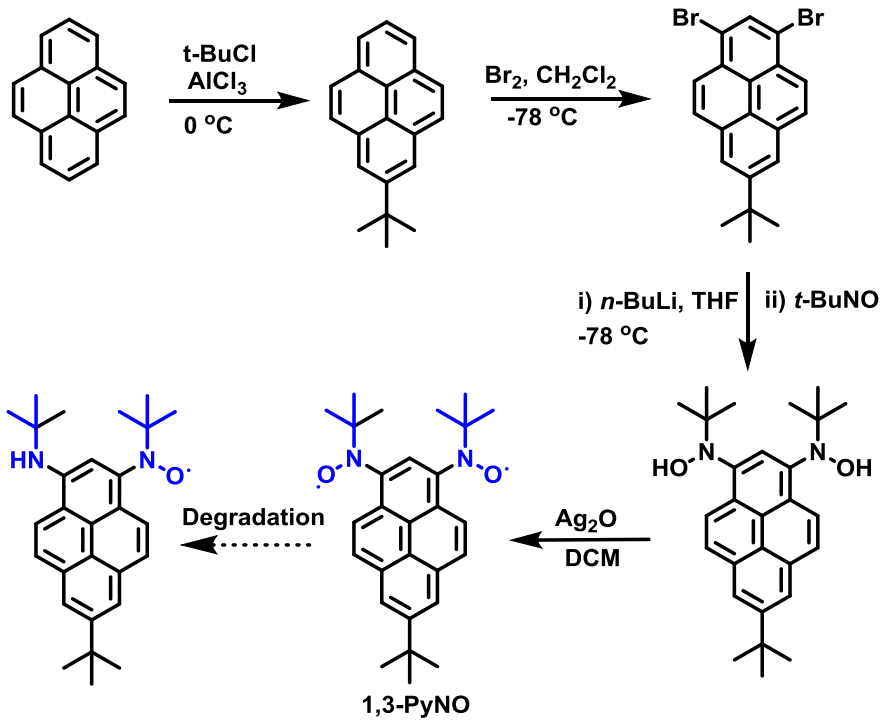

Scheme 5.5: Synthesis of 1,3-PyNO.

The 1,3- positions of pyrene can be brominated selectively by first introducing *tert*-butyl group at 2-position. The 2-*tert*-butylpyrene undergoes efficient bromination at 6,8-positions as shown in Scheme 5.5.[8-9] The bromination was carried out at −78 °C using Br_2 in dichloromethane. The *tert*-butyl nitroxide radical moieties were substituted in similar way as 1,6/1,8-TMPNO to obtain desired product 1,3-PyNO. The biradical 1,3-PyNO was unstable in solution as well as in solid state. It undergoes decomposition to monoradical (Scheme 5.5) and several other unidentified products. The poor stability of 1,3-PyNO allowed its characterization only by mass and EPR analysis.

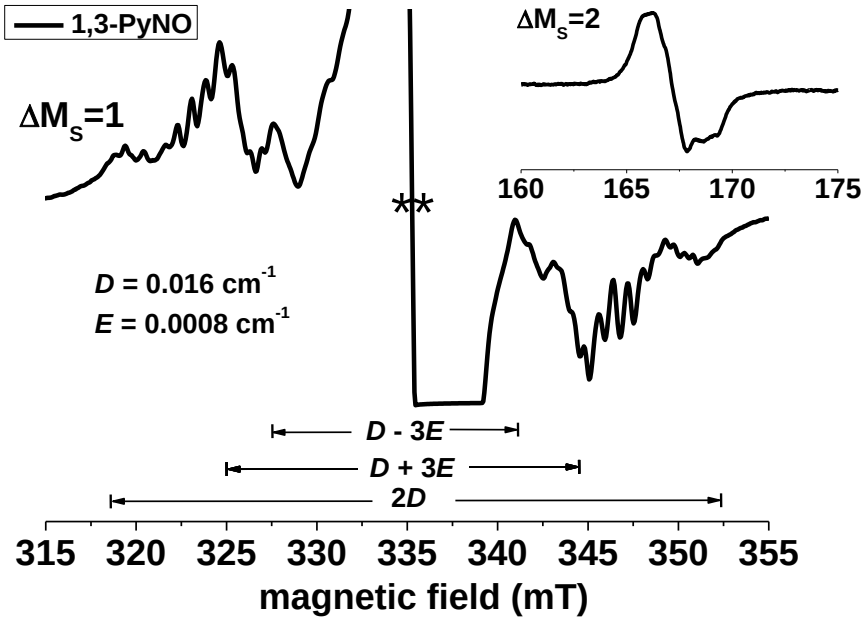

Figure 5.19: EPR spectrum of 1,3-PyNO measured in toluene glass matrix at 140 K (inset $\Delta M_S = 2$ transition).

The EPR spectrum of 1,3-PyNO measured in toluene glass matrix at 140 K is shown in Figure 5.19. The central peak marked by ** corresponds to mono radical impurity. The obtained spectrum was typical of randomly oriented triplet state for a rhombic system ($E \neq 0$).[7, 10] The spectrum was little complex as it can be originated from the superimposed spectra of the conformational isomers of 1,3-PyNO as shown in Scheme 5.6. Additionally

a half field transition was also observed with intensity much lower than the $\Delta M_S = 1$ transition. This was because of the much smaller value of *D* than the Zeeman splitting. The separation between extreme pair of lines gave *2D* while separation between inner pair was *D − 3E* and the remaining pair *D + 3E*. The estimated *zfs* parameters were *D/hc* = 0.016 cm^{-1} and *E/hc* = 0.008 cm^{-1}. The figured average inter spin distance, 5.53 Å, using *zfs* parameter *D*, was quite larger than the distance between two N centers of the molecule (4.9 Å) from the point dipole calculation.

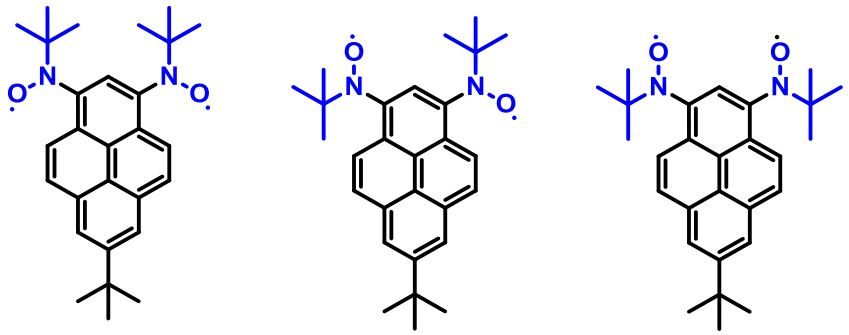

Scheme 5.6: Conformational isomers of 1,3-PyNO.

Table 5.1: Summary of EPR parameters.

Radical	Spectral width (G)	*hfc* (G)	g ($\Delta M_S = 1$) 290 K	g ($\Delta M_S = 2$) 140 K	2D, (G) 140 K	d, (Å)
1-TMPNO	32	16 (a_N)	2.0068	-	-	-
2-TMPNO	24	12.3(a_N), 1.96(a_H)	2.0067	-	-	-
1,6-TMPNO	32	8(a_N/2)	2.0068	4.012	116	7.85
1,8-TMPNO	32	8(a_N/2)	2.0068	4.012	184	6.74
1,3-PyNO	28	7(a_N/2)	2.0068	4.022	334	5.53
1,3,6-TMPNO	32	16(a_N)	2.0068	-	-	-
1,3,6,8-TMPNO	32	8(a_N/2)	2.0068	4.011	164	7.01

5.6 Calculation of intra-molecular magnetic exchange interactions in biradicals using DFT

The DFT calculations were performed to get an insight into magnetic exchange interactions operating between radical moieties in biradicals 1,6-, 1,8-, 2,7-, and 1,3,6,8-TMPNO. The DFT calculations were executed with the Gaussian 09 program package[11] employing the unrestricted BLYP functional[12] and the 6-31G(d) basis set.[13] The geometry of biradical 2,7-TMPNO and 1,3,6,8-TMPNO was taken from X-ray diffraction determinations without further optimization. The X-ray structure geometry of monoradical 1-TMPNO was used for 1,6-TMPNO and 1,8-TMPNO by including one more radical moiety with same bond lengths and torsion angles at desired positions. All the attempts to optimize geometry for these two biradicals failed. Geometry optimization always led to distortion of the pyrene core for 1,6-TMPNO and 1,8-TMPNO.

While the biradicals 1,6-TMPNO and 1,8-TMPNO showed similar triplet state spin density distribution, they showed large difference compared to the other two biradicals 2,7-TMPNO and 1,3,6,8-TMPNO (Figure 5.20). The biradical 2,7-TMPNO which exist in semi-quinoid form showed larger spin density distribution along the nodal plane of pyrene giving rise to extremely strong antiferromagnetic intra-molecular exchange interaction, exchange coupling constant J_{intra} = −1005 K. The biradicals 1,6-TMPNO and 1,8-TMPNO displayed spin density distribution along the periphery of pyrene core while nearly no spin density in the central part. The moderate exchange coupling constant (J_{intra}) values −121.6 K and −108.1 K were obtained for 1,6-TMPNO and 1,8-TMPNO, respectively. The spin density was more localized around the radical moiety and conjugated part of 1,3,6,8-TMPNO, with nearly no spin density around the oxidized part of the molecule. Surprisingly although the distance between two radical moieties in 1,3,6,8-TMPNO was the same as for 1,8-TMPNO, the J_{intra} for former was very small −0.41 K. This was probably due to localization of spin density because of the destruction of the pyrene core. It should be noted although the distance between two radical moieties is in the order 2,7-TMPNO > 1,6-TMPNO > 1,3,6,8-TMPNO > 1,8-TMPNO, the calculated J_{intra}

follows the order 2,7-TMPNO >> 1,6-TMPNO > 1,8-TMPNO >> 1,3,6,8-TMPNO (Table 5.2). This was highly in contradiction to approach 1, which says that exchange interactions decrease as spin centers move away from each other. The only logical reason again came from spin density distribution. These findings showed that in these biradical systems the exchange interaction operated more through bond than space and highly depend on the position of the radical moiety on pyrene core and the spin density distribution along the π-spacer.

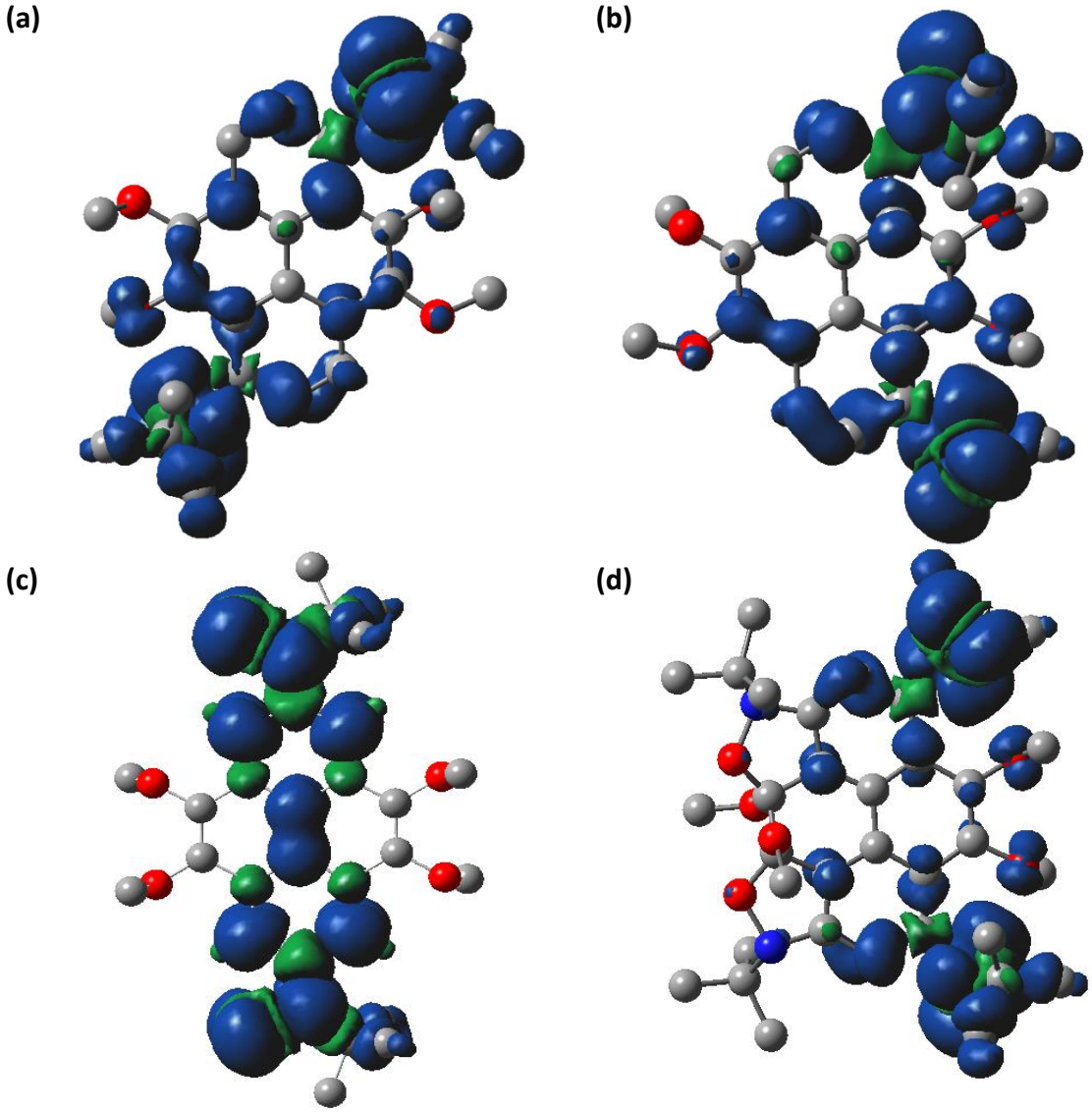

Figure 5.20: Spin density distribution of triplet state of (a) 1,6-, (b) 1,8-, (c) 2,7- and (d) 1,3,6,8- TMPNO calculated at UBLYP/6-31G(d) level of theory. Hydrogen atoms are omitted for clarity.

The exchange coupling constant was also calculated for 1,3-PyNO with the optimized geometry at unrestricted B3LYP/6-31g level of theory. The exchange interactions were calculated using the method described before. The earlier theoretical and experimental analysis showed the intra-molecular exchange interactions in *meta* coupled nitroxide biradical, 1,3-PhNO, were ferromagnetic with singlet-triplet energy gap $2J/k_B \geq 300$ K.[14-16] Interestingly the calculated intra-molecular exchange interactions in 1,3-PyNO were also ferromagnetic but with much lower singlet-triplet energy gap $2J/k_B$ = 96.8 K. This aberrant behavior can be attributed to extent of delocalization of spin density. In case of 1,3-PhNO the spin density was delocalized on the phenyl ring, while in 1,3-PyNO the spin delocalization was not only limited to the aromatic ring connecting both the radical moiety but also extended throughout the pyrene core. This extended delocalization of spin reduces the exchange interaction and thereby the singlet-triplet energy gap decreases. This behavior was in concomitance with EPR measurements where the *zfs* was smaller than expected from the point dipole calculations.

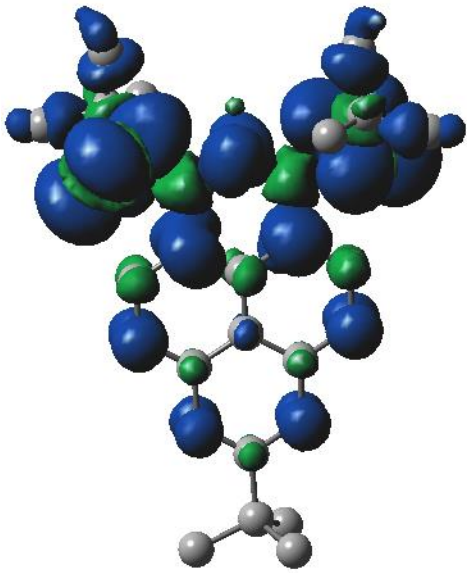

Figure 5.21: Spin density distribution in triplet state of 1,3-PyNO calculated at UBLYP/6-31G(d) level of theory. Hydrogen atoms omitted for clarity.

Table 5.2: Energy of BS and triplet states.

Molecule	E, eV (BS), ($<S^2>$)	E, eV (triplet), ($<S^2>$)	J_{intra}, (K)	ΔE_{ST}, (K)[a]	d_{rr}, (Å)[b]
1,6-TMPNO	-44806.60482 (0.99)	-44806.59434 (2.00)	-121.6	-243	8.6
1,8-TMPNO	-44808.97459 (0.99)	-44808.96528 (2.00)	-108.1	-216	7.2
2,7-TMPNO	-44813.72592 (0.82)	-44813.62375 (2.00)	-1005	-2010	9.8
1,3,6,8-TMPNO	-60429.26894 (1.00)	-60429.26891 (2.00)	-0.41	-0.82	7.4
1,3-PyNO	-36645.39117 (1.00)	-36645.39534 (2.01)	48.4	96.8	4.9

[a]Singlet-triplet energy gap = $2J/k_B$, [b]distance between two N-center of biradical.

5.7 Summary

- The structure-property analysis of isomeric mono radicals 1-TMPNO and 2-TMPNO showed that position of radical moiety highly influences the electronic structure of the aromatic core.
- The 1,6-, 1,8-, and 2,7- positional isomers of TMP based antiferromagnetically coupled biradicals have been successfully synthesized.
- The 1,6- and 1,8- isomers could be separated in the final step of synthesis. The isomers 1,6-TMPNO and 1,8-TMPNO were distinguished from the magnitude of *zfs* parameter *D*.
- While the biradical 2,7-TMPNO exist in semi-quinoid structure, the biradical 1,6-TMPNO and 1,8-TMPNO exist in biradicaloid form.
- The synthesis of tri- and tera- radicals 1,3,6-TMPNO and 1,3,6,8-TMPNO were also attempted but due to excessive spin density two of the radical moiety oxidizes one double bond of pyrene to give corresponding mono and biradical species, respectively.
- The ferromagnetically coupled biradical 1,3-PyNO was also synthesized and found

to exist in triplet state. This biradical showed poor stability in solution and solid state thus it was characterized only by EPR and FD-Mass.

- DFT calculations were performed to get an insight into intra-molecular magnetic exchange interactions.
- The calculated exchange coupling constant J_{intra} follows the order 2,7-TMPNO >> 1,6-TMPNO > 1,8-TMPNO >> 1,3,6,8-TMPNO. Theoretical analysis showed that the exchange interactions highly depend on distribution of spin density.
- Tuning of exchange interactions was achieved in positional isomers maintaining the same radical moiety and π-spacer.

5.8 Synthetic details

4,5,9,10-Tetramethoxypyrene and *tert*-BuNO were synthesized according to literature procedures.[6, 17-18]

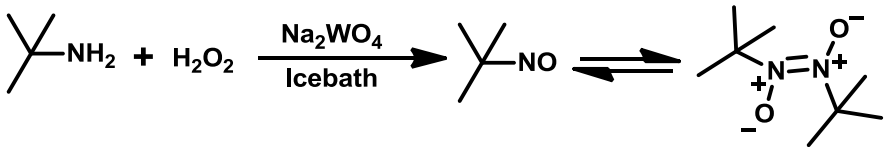

2-Methyl-2-nitrosopropane (*t*-BuNO)

To the solution of sodium tungstate ($Na_2WO_4{\cdot}2H_2O$, 1.04 g) in water, *tert*-butylamine (19 g) was added and cooled in ice bath. To this H_2O_2 solution (27 ml of 30% H_2O_2 in 13 ml H_2O) was added drop wise over 1.5 hr while maintaining the temperature of reaction bath below 10 °C. The stirring was continued for an additional 1 hr. Then NaCl was added to break the emulsion. The blue organic layer was separated and purified by distillation to give 2.5 g (28% yield) of 2-methyl-2-nitrosopropane as blue liquid, which dimerizes giving white needles upon cooling.

1,6(/1,8)-Dibromo-4,5,9,10-tetramethoxypyrene

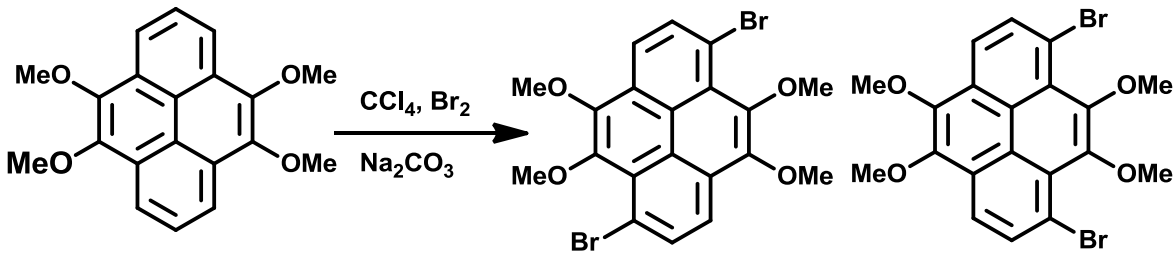

To the round bottom flask containing 4,5,9,10-tetrameythoxypyrene (1 g, 3.1 mmol), and Na_2CO_3 (150 mg) in 50 ml CCl_4, 12 ml 2 M Br_2 in CCl_4 was added drop wise over 10 min. The reaction mixture was stirred for 20 min at room temperature. The resulting solution was poured into saturated $Na_2S_2O_3$ to remove unreacted Br_2. Organic layer was separated washed with water, brine and dried over $MgSO_4$. The solvent was

removed under vacuum and the residue chromatographed over silica gel using hexane: ethyl acetate (100:5) as eluent. The 1,6 and 1,8-dibromo isomers were obtained as inseparable mixture in 94% yield (1.4 g). (MS-FD= 479.9 (100%)).

N,N'-(4,5,9,10-tetramethoxypyrene-1,6-diyl)bis(N-oxy-*tert*-butylamine) and N,N'-(4,5,9,10-tetramethoxypyrene-1,8-diyl)bis(N-oxy-*tert*-butylamine)

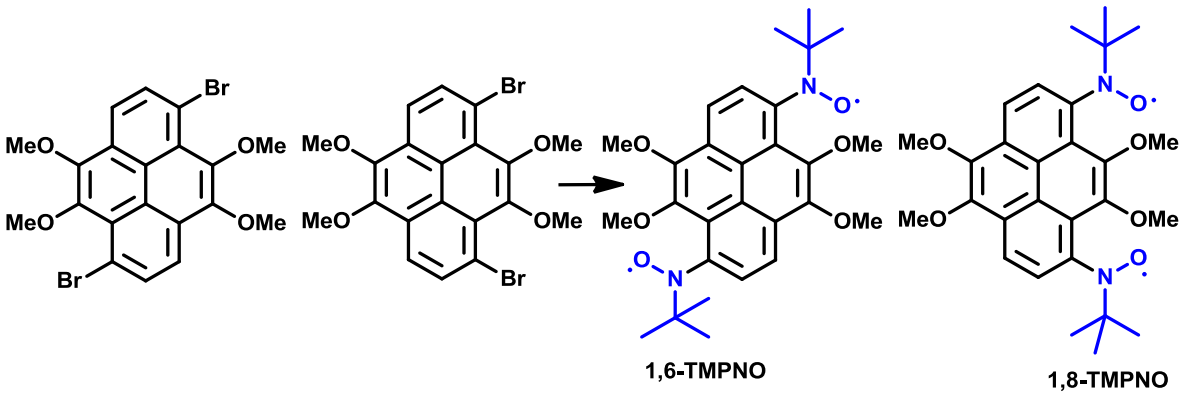

To a solution of 1,6(/1,8)-dibromo-4,5,9,10-tetramethoxypyrene (400 mg, 0.84 mmol) in 65 ml diethyl ether, 2.6 ml (5 equivalents) 1.6 M *n*-BuLi hexane solution was added drop wise at −78 °C and stirred for 1 hour at same temperature. The mixture was gradually warmed to −10 to −5 °C and further stirred for 1.5 hour. To the resulting mixture was added the solution of *t*-BuNO dimer (5 equivalents) in 8 ml diethyl ether drop wise at −78 °C, and stirred for 1 hour and warmed to room temperature. The mixture was hydrolyzed with aqueous ammonium chloride. Organic layer was separated, washed with water and brine, and dried over $MgSO_4$. Solvent was removed under vacuum and the residue used as it is for next step without any purification. To the slurry of crude product in 30 ml chloroform 200 mg of Ag_2O was added and stirred for 2 hour. The mixture was filtered through celite and solvent evaporated, the residue purified by alumina preparative TLC using hexane:ethylacetate (100:5) as eluent. At this stage both isomers can be separated. Yield 1,6-TMPNO 60 mg, 1,8-TMPNO 50 mg (26% in two steps). **1,6-TMPNO**: (MS-FD= 494.1(100%)), UV-Vis (Toluene) $\boldsymbol{\lambda_{max}}$ (ε, $M^{-1}\,cm^{-1}$) 287 (3.9 X 10^4), 342 (2.3 X 10^4), 360 (2.6 X 10^4), **EPR** (298 K, 10^{-4} M in toluene): five lines, g_{iso} = 2.0068,

a_N/2 = 8 G. **1,8-TMPNO**: (MS-FD= 494.5 (100%), UV-Vis (Toluene) $\boldsymbol{\lambda_{max}}$ (ε, M^{-1} cm^{-1}) 287 (3.8 X 10^4), 342 (2.25 X 10^4), 358 (2.6 X 10^4), **EPR** (298 K, 10^{-4} M in toluene): five lines, g_{iso} = 2.0068, a_N/2 = 8 G.

1,3,6-Tribromo-4,5,9,10-tetramethoxypyrene

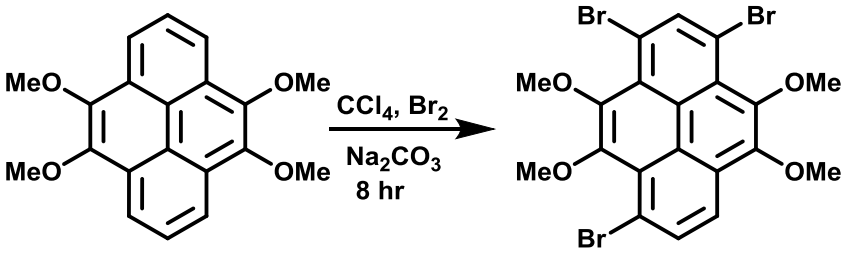

To a round bottom flask containing 4,5,9,10-tetrameythoxypyrene (500 mg), Na_2CO_3 (85 mg) in 25 ml CCl_4 , Br_2 in CCl_4 (10 ml, 2 M) was added drop wise (in 3 portions in the time interval of 2 hour each). The reaction mixture was stirred for 8 hour at room temperature. The resulting solution was poured into saturated $Na_2S_2O_3$ to remove unreacted Br_2. Organic layer was separated washed with water, brine and dried over $MgSO_4$. The solvent was removed under vacuum and residue chromatographed over silica gel using hexane: ethyl acetate (100:5) as eluent. 1,3,6-tribromo-4,5,9,10-tetramethoxypyrene was obtained in 75% yield along with small amount of 1,3,6,8-tetrabromo-4,5,9,10-tetramethoxypyrene. ^{1}H NMR (300 MHz, CD_2Cl_2) δ 8.52 (s, 1H), 8.18-8.21 (m, 2H), 4.07 (bs, 3H), 3.98, 3.97, 3.96, 3.95, 3.94, 3.93 (m, 9H). MS-FD= 559.7 (100%).

1,3,6,8-tetrabromo-4,5,9,10-tetramethoxypyrene

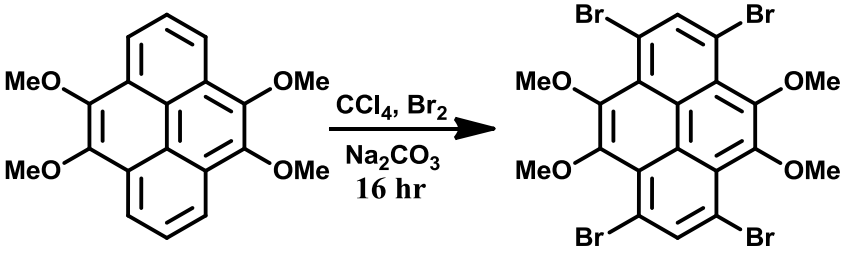

To a round bottom flask containing 4,5,9,10-tetrameythoxypyrene (400 mg) and Na_2CO_3 (160 mg) in 25 ml CCl_4, the 24 ml 2 M Br_2 in CCl_4 was added drop wise (in 4 portions in the time interval of 2 hour each). The reaction mixture was stirred for overnight at room temperature. The resulting solution poured into saturated $Na_2S_2O_3$ to remove unreacted Br_2. The organic layer was separated, washed with water, brine and dried over $MgSO_4$. The solvent was removed under vacuum and residue chromatographed over silica gel using hexane: ethyl acetate (100:5) as eluent. 1,3,6,8-tetrabromo-4,5,9,10-tetramethoxypyrene was obtained in 63% Yield. ^{1}H NMR (300 MHz, CD_2Cl2) δ 8.62 (s, 2H), 4.03 (s, 12H). ^{13}C NMR (75 MHz, CD_2Cl_2) δ 147.66, 141.87, 126.24, 124.00, 113.96, 61.53.MS-FD= 637(100%).

N,N',N''-(4,5,9,10-Tetramethoxypyrene-1,3,6-triyl)tris(N-oxy-*tert*-butylamine)

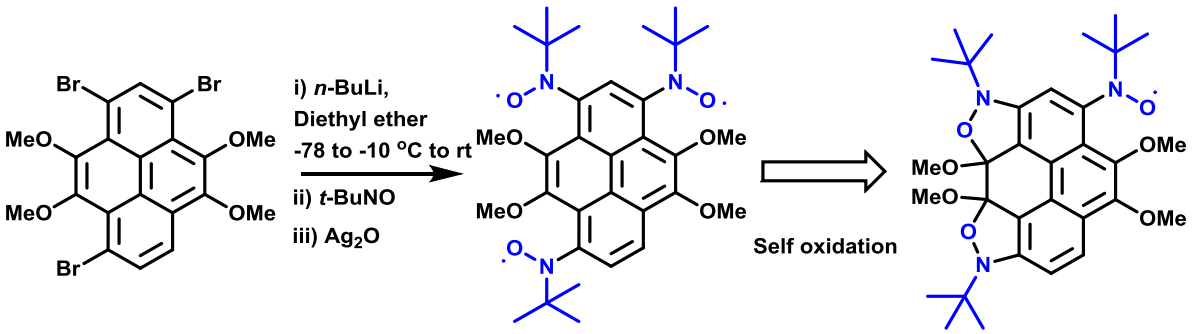

Following the same procedure as for 1,6-TMPNO, instead of dibromoTMP, tribromoTMP was used.16% Yield. MS-FD= 580.7 (100%). UV-Vis (Toluene) $\boldsymbol{\lambda_{max}}$ (ε, $M^{-1}\,cm^{-1}$) 331 (1.4 X 10^4), **EPR** (298 K, 10^{-4} M in toluene): three lines, g_{iso} = 2.0068, a_N = 16 G.

N,N',N'',N'''-(4,5,9,10-Tetramethoxypyrene-1,3,6,8-tetrayl)tetrakis(N-oxy-*tert*-butylamine)

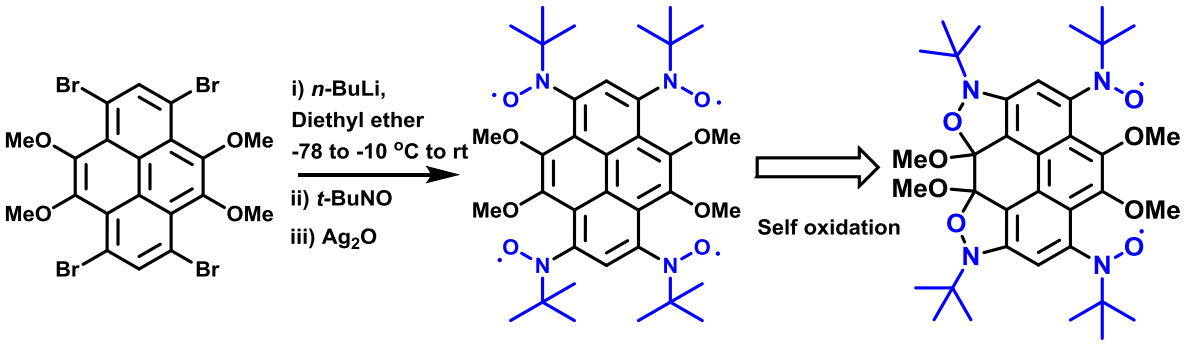

Following the same procedure as for 1,6-TMPNO, instead of dibromoTMP, tetrabromoTMP was used. 32% Yield. MS-FD= 666.8 (100%). UV-Vis (Toluene) $\boldsymbol{\lambda_{max}}$ (ε, M^{-1} cm^{-1}) 333 (1.2 X 10^4), **EPR** (298 K, 10^{-4} M in toluene): five lines, g_{iso} = 2.0068, $a_{N/2}$ = 8 G.

N,N'-(7-(*Tert*-butyl)pyrene-1,3-diyl)bis(N-oxy-*tert*-butylamine)

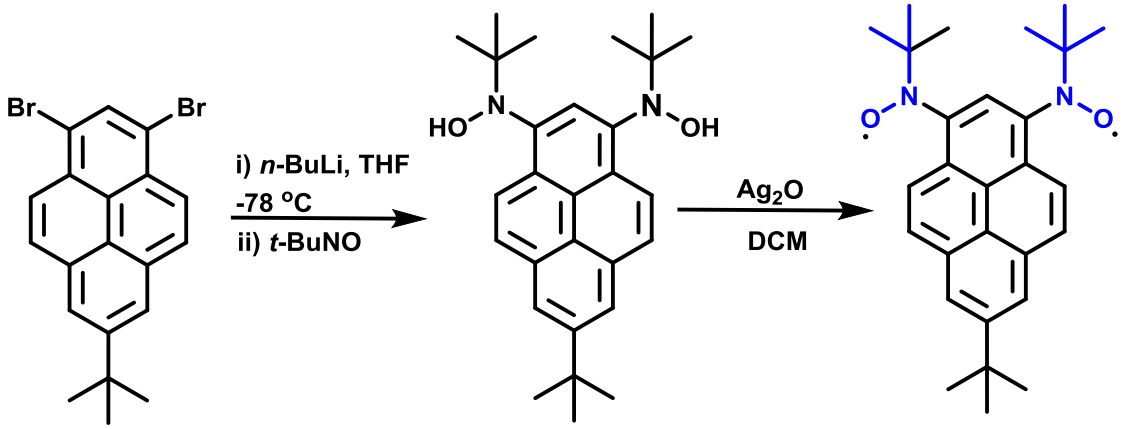

Following the same procedure as for 1,6-TMPNO, instead of dibromoTMP, 1,3-dibromo-7-(*tert*-butyl)pyrene was used. 1,3-PyNO: < 5% Yield. MS-FD= 430.6 (100%).

5.9 References

[1] T. Mitsumori, K. Inoue, N. Koga, H. Iwamura, *J. Am. Chem. Soc.* **1995**, *117*, 2467.

[2] P. Ravat, Y. Ito, E. Gorelik, V. Enkelmann, M. Baumgarten, *Org. Lett.* **2013**, *15*, 4280.

[3] M. Shinomiya, K. Higashiguchi, K. Matsuda, *J. Org. Chem.* **2013**, *78*, 9282.

[4] E. A. Mostovich, Y. Borozdina, V. Enkelmann, K. Remović-Langer, B. Wolf, M. Lang, M. Baumgarten, *Cryst. Growth Des.* **2012**, *12*, 54.

[5] B. Wolf, P. T. Cong, K. Remović-Langer, Y. D. Borozdina, E. Mostovich, M. Baumgarten, M. Lang, *J. Phys.: Conf. Ser.* **2010**, *200*, 012225.

[6] S.-i. Kawano, M. Baumgarten, D. Chercka, V. Enkelmann, K. Müllen, *Chem. Commun.* **2013**, *49*, 5058.

[7] A. Calder, A. R. Forrester, P. G. James, G. R. Luckhurst, *J. Am. Chem. Soc.* **1969**, *91*, 3724.

[8] T. M. Figueira-Duarte, P. G. Del Rosso, R. Trattnig, S. Sax, E. J. W. List, K. Müllen, *Adv. Mater.* **2010**, *22*, 990.

[9] T. M. Figueira-Duarte, S. C. Simon, M. Wagner, S. I. Druzhinin, K. A. Zachariasse, K. Müllen, *Angew. Chem. Int. Ed.* **2008**, *47*, 10175.

[10] E. Wasserman, L. C. Snyder, W. A. Yager, *J. Chem. Phys.* **1964**, *41*, 1763.

[11] G. W. T. M. J. Frisch, H. B. Schlegel, G. E. Scuseria, M. A. Robb, J. R. Cheeseman, G. Scalmani, V. Barone, B. Mennucci, G. A. Petersson, H. Nakatsuji, M. Caricato, X. Li, H. P. Hratchian, A. F. Izmaylov, J. Bloino, G. Zheng, J. L. Sonnenberg, M. H A. F. Izmaylov, J. Bloino, G. Zheng, J. L. Sonnenberg, M. Hada,M. Ehara, K. Toyota, R. Fukuda, J. Hasegawa, M. Ishida, T. Nakajima, Y. Honda, O. Kitao, H. Nakai, T. Vreven, J. A. Montgomery, Jr., J. E. Peralta, F. Ogliaro, M. Bearpark, J. J. Heyd, E. Brothers, K. N. Kudin, V. N. Staroverov, R. Kobayashi, J. Normand, K. Raghavachari, A. Rendell, J. C. Burant, S. S. Iyengar, J. Tomasi, M. Cossi, N. Rega, J. M. Millam, M. Klene, J. E. Knox, J. B. Cross, V. Bakken, C. Adamo, J. Jaramillo, R. Gomperts, R. E. Stratmann, O. Yazyev, A. J. Austin, R. Cammi, C. Pomelli, J. W. Ochterski, R. L. Martin, K. Morokuma, V. G. Zakrzewski, G. A. Voth, P. Salvador, J. J. Dannenberg, S. Dapprich, A. D. Daniels, O. Farkas, J. B. Foresman, J. V. Ortiz, J. Cioslowski, and D. J. Fox., in *Gaussian 09*, Gaussian, Inc, Wallingford CT, **2009**.

[12] A. D. Becke, *J. Chem. Phys.* **1993**, *98*, 1372.

[13] E. R. Davidson, D. Feller, *Chem. Rev.* **1986**, *86*, 681.

[14] R. Chiarelli, S. Gambarelli, A. Rassat, *Molecular Crystals and Liquid Crystals Science and Technology. Section A. Molecular Crystals and Liquid Crystals* **1997**, *305*, 455.

[15] C. Calzado, C. Angeli, C. Graaf, R. Caballol, *Theor. Chem. Acc.* **2011**, *128*, 505.

[16] T. Sadhukhan, S. Hansda, I. A. Latif, S. N. Datta, *J. Phys. Chem. A* **2013**, *117*, 13151.

[17] J. C. Stowell, *J. Org. Chem.* **1971**, *36*, 3055.

[18] R. J. Smith, R. M. Pagni, *J. Org. Chem.* **1981**, *46*, 4307.

CHAPTER 6

PHOTO-EXCITED HIGH-SPIN STATE OF 2,7-TMPNO

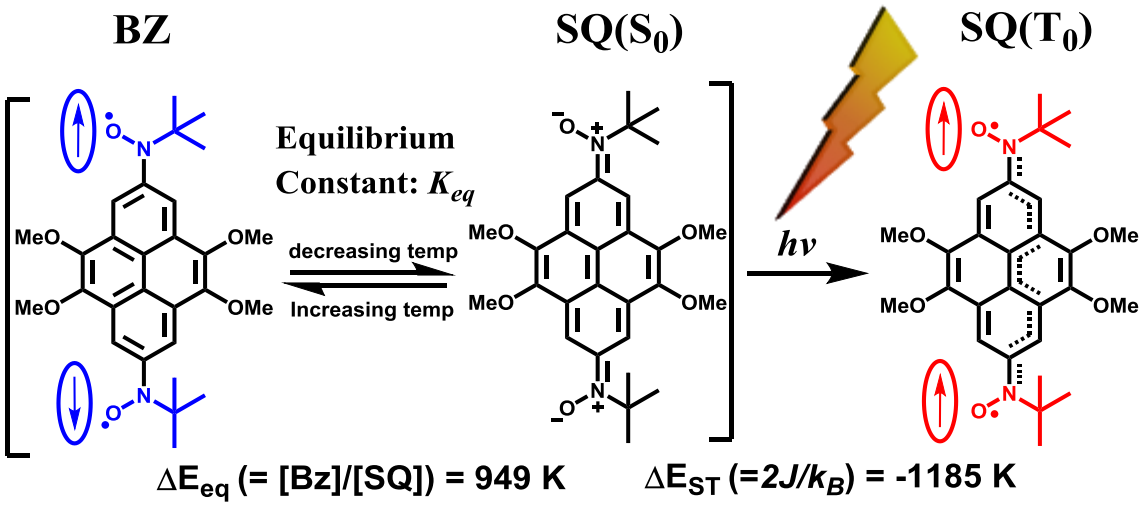

2,7-TMPNO (4,5,9,10-tetramethoxypyrene-2,7-bis(tert-butylnitroxide)) was found to exist in semi-quinoid form with an unprecedented strong intra-molecular magnetic exchange interaction of $2J/k_B$ = –1185 K operating over a distance of 10 Å. Structural transformations were observed by varying the temperature, from more quinoid structure at low temperature to more benzenoid structure at higher temperature. Moreover, this molecule undergoes a spin transition from singlet to spin polarized triplet state upon photo-excitation revealed by TREPR spectroscopy. The spin Hamiltonian parameters were determined to be S = 1, g = 2.0065, D = –0.0112 cm^{-1}, and E = –0.0014 cm^{-1} by spectral simulation with the hybrid Eigenfield/ exact diagonalization method.

Note: Large part of this chapter has been published in Chem. Eur. J, 2014, 2014, 20, 12041-12045

6.1 Introduction

Tuning of magnetic properties by external stimuli has attracted much attention because of applicability of such materials in future molecular memory and switching devices.[1] External perturbations like temperature, pressure, electrochemical redox reactions, and chemical treatments are widely used to control magnetic properties. Recently photo induced magnetization has attained a great interest and photo induced spin transitions, valance tautomerisms and photo magnets have been reported.[2-3] In purely organic based materials photo induced magnetization is of special interest because such materials can be designed precisely by proper choice of the aromatic core and the radical moiety.[4-7]

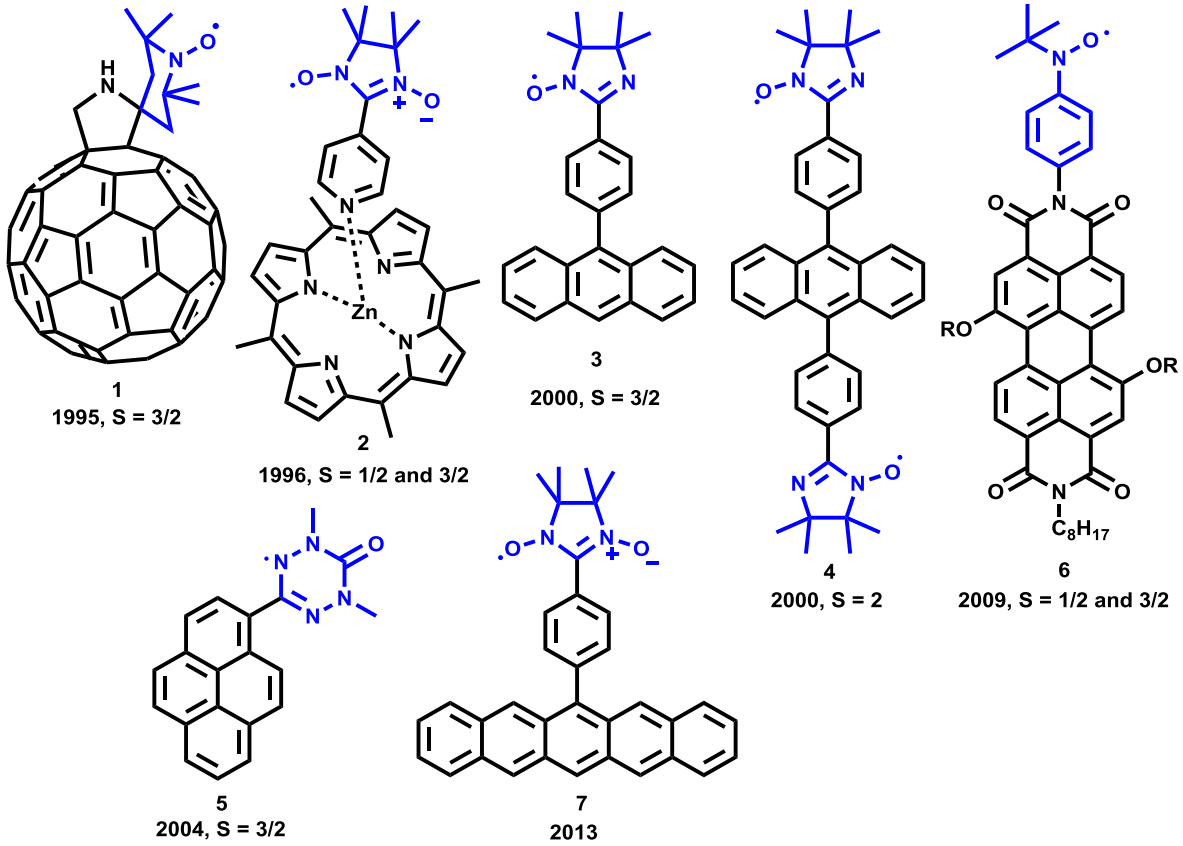

Figure 6.1: Representative examples of organic photo-excited high spin molecules.

Even though the very first example purely organic based photo-excited high spin system through radical-triplet pair mechanism in fullerene linked nitroxide (**1**) was reported in 1995 by Corvaja *et al.*, there are only a limited number of new systems explored up to date.[8] Some of which include tetraphenylporphinatozinc(II) (ZnTPP) co-ordinated with *p*-pyridylnitronylnitroxide (**2**) (1996)[9] by Yamauchi *et. al*, phenyl anthracene and diphenyl anthracene covalently bonded to imino nitroxide (3 and 4) (2000 and 2001)[10-11] or verdazyl (2002),[12] verdazyl attached to pyrene (**5**) (2004)[13] by Teki *et al.* and perylenediimides linked to *tert*-butyl nitroxide and TEMPO (**6**) (2009 and 2010)[14-15] by Wasielewski *et at.* (Figure 6.1). In most of the cases photo-excited high spin states were observed because of dynamic electron spin polarization (DEP) which was induced by enhanced anisotropic intersystem crossing.[16-17] It was found that the spin state highly depends on the type of the radical moiety and its position at the π-conjugated system.[18-20] Moreover recently Teki *et al.* have shown utilization of stable radicals to protect pentacene derivative (**7**) from photo degradation. The life time of pentacene increased significantly by attachment of nitronyl nitroxide or verdazyl radical moiety at 6-position of pentacene.[21] Here they utilized the property of organic radicals to scavenge energy of photo-excited state which leads to enhanced stability.

The photochemical properties of pyrene makes it an interesting building block for the detection of high spin excited systems.[22] Its potential for this application, however, has not been explored in detail decently, since only one report so far was published.[13] In this regard and to satisfy our quest to explore the photo-excited high spin state of pyrene based biradical system, molecule 2,7-TMPNO (4,5,9,10-tetramethoxypyrene-2,7-bis(*tert*-butylnitroxide)) was designed. The *tert*-butylnitroxide radical moiety was chosen as a spin source because of its good stability and ability to delocalize over π-spacer. The radical moieties were attached to the nodal plane of pyrene. The molecule was characterized by EPR, UV-Vis, SQUID and single crystal X-ray diffraction. The time resolved electron paramagnetic resonance (TREPR) spectroscopy and picoseconds transient absorption (TA) spectroscopy were used to probe the excited state dynamics.

Astonishingly structural analysis by UV-Vis, EPR and X-ray suggested that 2,7-TMPNO possesses semi-quinoid structure in solution as well as in the solid state.[23] The experimentally estimated singlet-triplet energy gap, ΔE_{ST} (= $2J/k_B$) = –1185 K, was well supported by theoretical investigation which showed that the ground state is spin paired singlet with a very large singlet-triplet energy gap –1415 K or –2010 K determined using B3LYP/6-31G* or BLYP/6-31G* level of theory, respectively. The TREPR analysis revealed that upon photo-excitation the triplet state was stimulated.

6.2 Synthesis

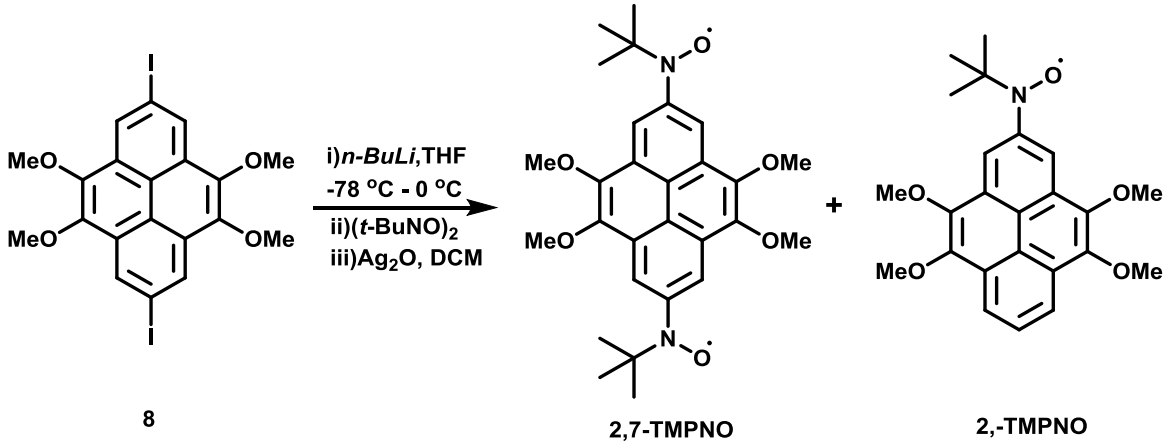

Scheme 6.1: Synthesis of 2,7-TMPNO.

2,7-TMPNO was synthesized as shown in Scheme 6.1. Lithiation of 2,7-diiodo-(4,5,9,10)-tetramethoxypyrene (**8**)[24] with *n*-BuLi followed by subsequent addition of 2-methyl-2-nitrosopropane gave bishydroxylamine. It was separated as white powder and used as it is for next step without any purification. The product formation was confirmed by FD-Mass. The oxidation of bishydroxylamine with Ag_2O in DCM yielded the desired product 2,7-TMPNO (45%) along with small amount (~5%) of monoradical 2-TMPNO. Both radicals could be separated using silica-gel column chromatography in a very pure form using hexane/ethyl acetate as eluent.

6.3 UV-Vis Analysis

The UV-Vis spectra of 2-TMPNO and 2,7-TMPNO were recorded in toluene at room temperature. The UV-Vis spectra of both radicals depicted large differences. The monoradical 2-TMPNO showed weak absorptions at λ_{max} = 415 nm and 438 nm (ε = 862 and 838 cm^{-1} M^{-1}, Figure 6.2a) which was characteristic for the n—π* transition of *tert*-butylaminoxyl radical moiety. The 2,7-TMPNO showed very strong absorption at λ_{max} = 472 nm (ε = 1.6 × 10^4 cm^{-1} M^{-1}) along with weak absorption at higher wavelength λ_{max} = 608 nm (ε = 1280 cm^{-1} M^{-1}, Figure 6.2b). Following the literature by Iwamura *et al.* the strong absorption at 472 nm can be attributed to a partial quinoid structure.[25] In order to visualize any structural transformation with temperature (quinoid to benzenoid), the 2,7-TMPNO in toluene was subjected to variable temperature UV-Vis measurements from 293 K to 353 K. Interestingly upon increasing the temperature a gradual decrease in molar absorptivity occurred at λ_{max} = 472 nm and λ_{max} = 608 nm (Figure 6.4). This indicated that the weak absorption at 608 nm is also related to the quinoid structure and as the intensity of absorption at λ_{max} = 472 nm decreases with temperature the structural transformation from quinoid to benzenoid is expected.

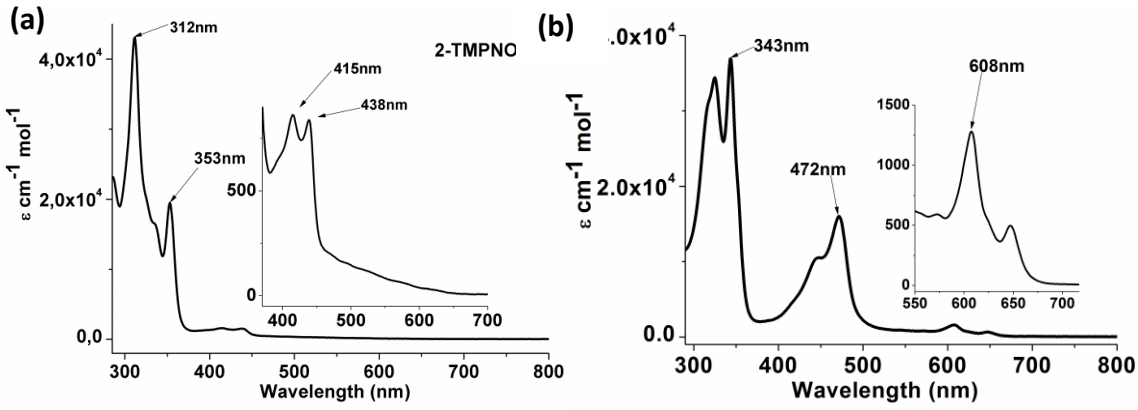

Figure 6.2: Uv-Vis spectra of (a) 2-TMPNO (b) 2,7-TMPNO in toluene at room temperatures.

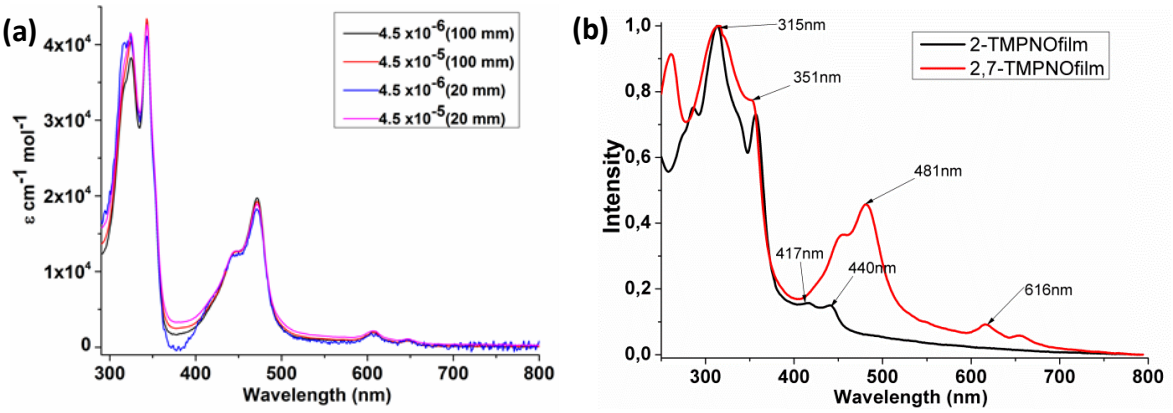

Figure 6.3: Uv-Vis spectra of (a) 2,7-TMPNO in toluene with different concentration (c.a. 4.5 x 10^{-5} and 4.5 x 10^{-6}) and different path length of cell (c.a. 20 mm and 100 mm (b) 2-TMPNO (black) and 2,7-TMPNO (red) film on quartz slide.

No significant change in absorptivity or peak position was observed when UV-Vis spectra of 2,7-TMPNO measured either by varying the concentration or using different optical path length of the cell. This suggests that the UV-Vis spectral change with temperature can only be attributed to structural change and not because of the aggregation (Figure 6.3a). Moreover the UV-Vis spectra of thin film of 2,7-TMPNO showed similar features as in solution with a tiny red shift of peaks by 8-9 nm which proves that 2,7-TMPNO in solution retains a similar structure as in the solid state (Figure 6.3b).

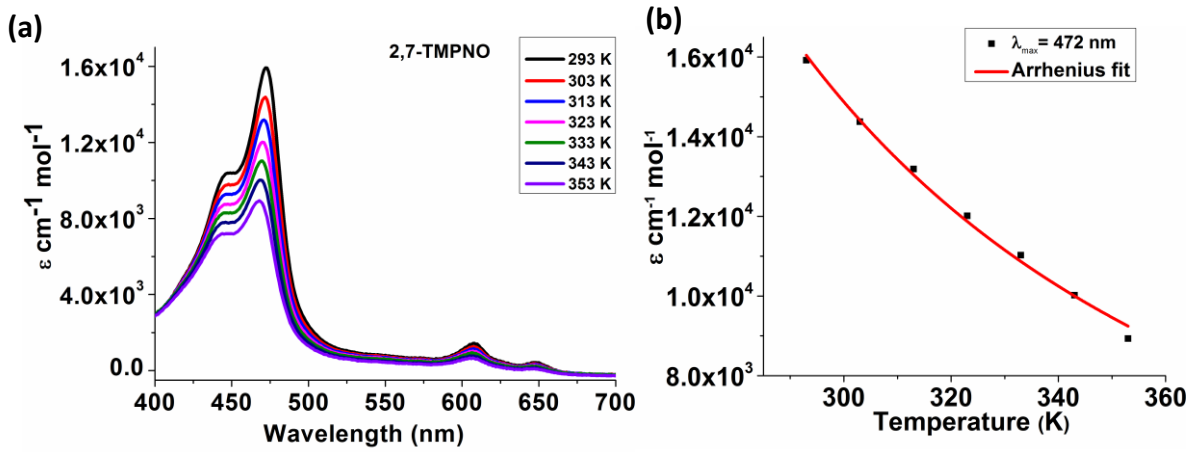

Figure 6.4: Uv-Vis spectra of 2,7-TMPNO (a) at different temperatures in toluene (b) decrease in signal intensity at λ_{max} = 472 nm with temperature (black dot) and Arrhenius fit (red line).

The temperature dependence of absorption maxima at 472 nm stemming from the quinoid structure was analyzed using Arrhenius equation as shown below. The activation energy from the Arrhenius fit was determined to be 949 K.

$$Arrhenius\ Equation, \qquad k_{eq} = \mathrm{A}\exp\left(-\frac{\Delta E_{eq}}{k_B T}\right) \qquad \textbf{6-1}$$

Here, K_{eq} and ΔE_{eq} are the equilibrium constant and the energy gap between the spin singlet semi-quinoid (SQ) structure and the benzenoid (BZ) structure as shown in Scheme 6.2.

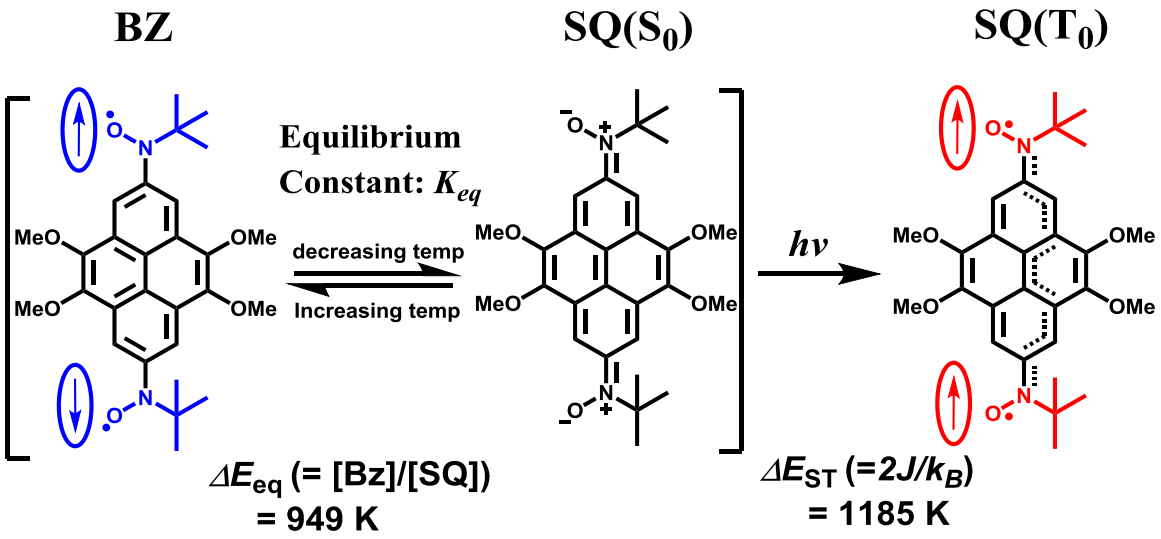

Scheme 6.2: Structural equilibrium of semi-quinoid structure (left) and transformation into biradical upon photo-excitation (right).

6.4 EPR analysis

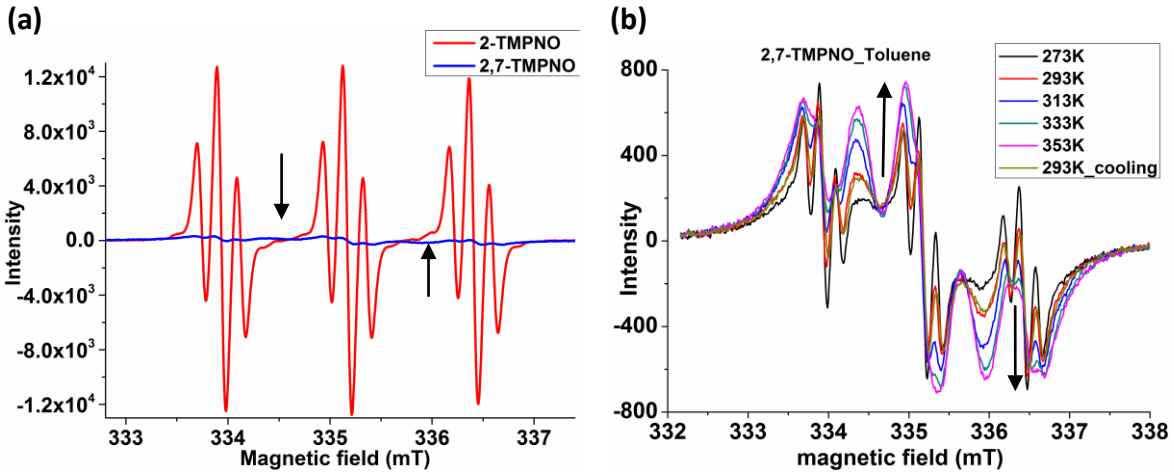

Figure 6.5: (a) EPR spectra 2-TMPNO (red), 2,7-TMPNO (blue) in toluene at room temperature (b) temperature dependent EPR spectra of 2,7-TMPNO in toluene

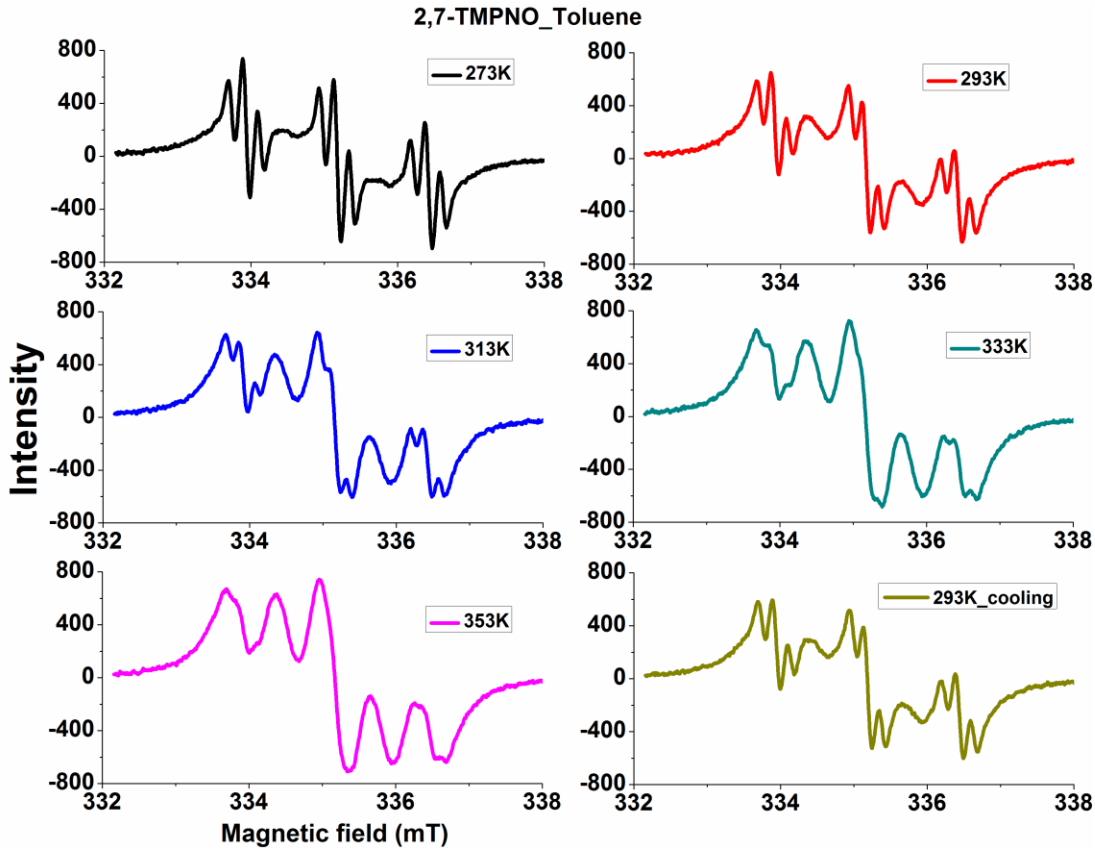

Figure 6.5: (c) individual EPR spectra of 2,7-TMPNO in toluene at different temperature.

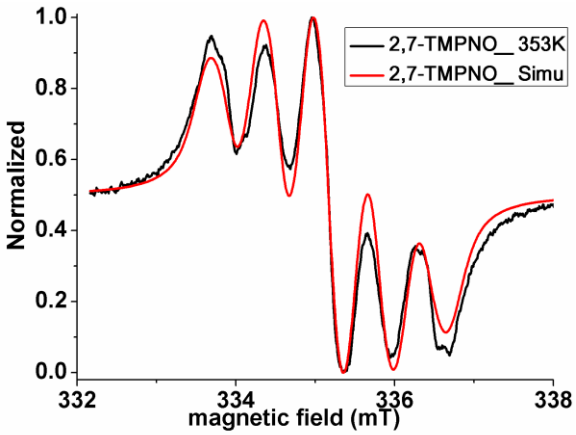

Figure 6.6: EPR spectra of 2,7-TMPNO in toluene at 353 K (black) and simulated spectrum (red).

The EPR spectrum of 2-TMPNO consisted of triplet of triplets due to hyperfine interactions of the unpaired electron of one NO· moiety with two ortho hydrogen atoms of pyrene. Surprisingly, freshly prepared solution of 2,7-TMPNO at 293 K did not show the expected five line EPR spectrum for a strongly coupled biradical with integrated signal intensity double that of a monoradical 2-TMPNO but a very low signal intensity spectrum was observed with tiny shoulders in between the triplets (Same concentration and EPR experimental parameters used to record spectra of 2-TMPNO and 2,7-TMPNO, Figure 6.5a).[26-28] Upon increasing the temperature these tiny shoulders became more predominant and at 353 K the five line pattern for biradical was observed (Figure 6.5b). The observed spectrum at 353 K could be reproduced by spectral simulation considering two equivalent nitrogen *hfc* ($a_N/2$) value 6.25 G at g = 2.0067 (Figure 6.6). Thus the initially observed spectrum at low temperature could originate from a trace amount of mono radical impurity, which may have masked very low intensity five line spectrum for the biradical. The sample for variable temperature EPR measurement was prepared by dissolving few crystals in toluene in order to achieve very high purity.

Moreover, single crystals of 2,7-TMPNO were EPR active, demonstrating that the sample is indeed paramagnetic and does not possess a complete singlet quinoid form in the solid state. A single crystal of 2,7-TMPNO was subjected to variable temperature EPR

measurements. Notably, significant increase in EPR signal intensity was observed upon raising the temperature from 273 K to 353 K (Figure 6.7a) reflecting inverse Curie like behavior, thus enhancing the paramagnetic content. These results were in concomitance with observations from the variable temperature UV-Vis measurement, where the absorption peaks due to quinoid structure, decreased upon increasing temperature. Thus increase of the EPR signal intensity with temperature can be imputed to enhanced population of triplet state following the structural transformation from more quinoid structure at low temperature to more biradicaloid at higher temperature. Additionally the single crystal of 2,7-TMPNO showed angular dependence (anisotropy of g-factor). As shown in Figure 6.7b, the significant shift of g-factor was observed upon rotating the crystal by 90°. The temperature dependent EPR spectra of randomly oriented multiple crystals of 2,7-TMPNO is shown in Figure 6.8. Due to anisotropy of g-factor the averaged 3 line spectrum was observed which also displayed the similar temperature dependent behavior as for the one single crystal.

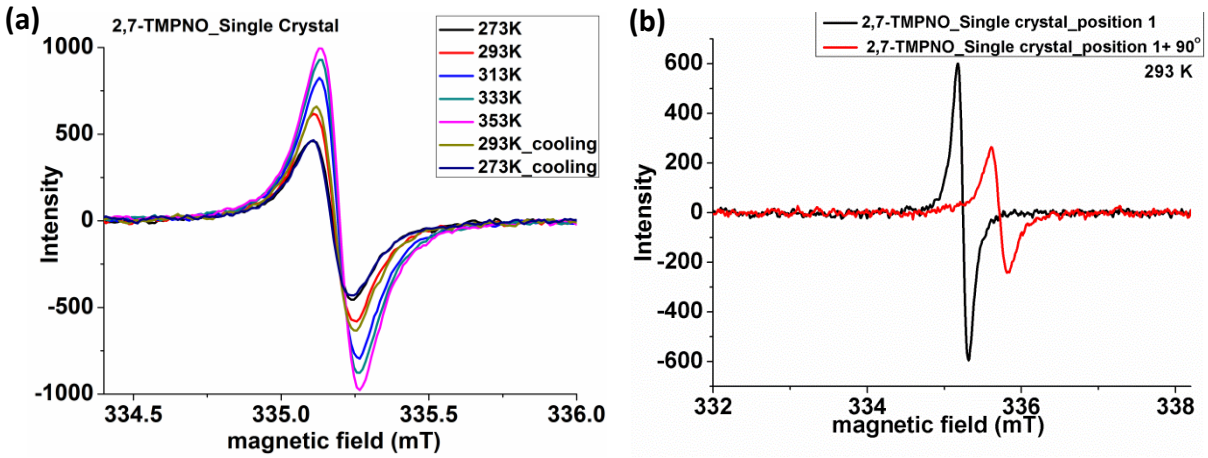

Figure 6.7: (a) Variable temperature EPR spectra of single crystals of 2,7-TMPNO and (b) angular dependence of 2,7-TMPNO single crystal.

The temperature dependence of EPR signal of 2,7-TMPNO crystallites (Figure 6.9) was well analyzed by the singlet-triplet energy gap of ΔE_{ST} = –1185 K applying the singlet-triplet activation for the intensity using Bleaney and Bowers equation 6-2.[29-30] This activation energy can be taken as lower limit if some uncoupled spins are still present.

$$I = 3(C/T)\exp(-\frac{\Delta E_{ST}}{k_B T})/(1 + 3\exp\left(-\frac{\Delta E_{ST}}{k_B T}\right)) \quad \textbf{6-2}$$

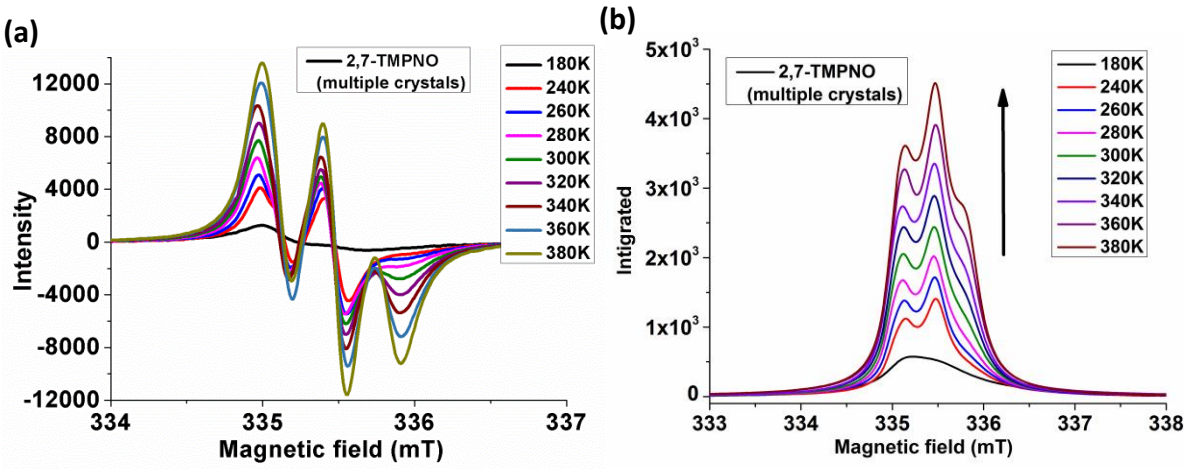

Figure 6.8: (a) Variable temperature (VT) EPR spectra and (b) integrated VT EPR spectra of multiple crystals of 2,7-TMPNO.

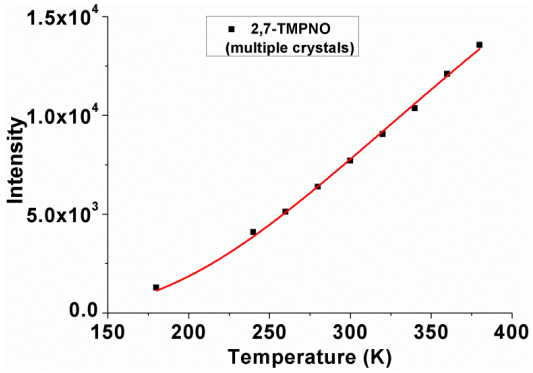

Figure 6.9: Intensity change of EPR spectral maxima of 2,7-TMPNO with temperature (black dot) and Bleanley and Bower's fit (red line).

In solution, the absorption change as shown in Figure 6.4a and their Arrhenius fit indicate the equilibrium on the structural transformation from more SQ structure at low temperature to more BZ structure with weakly-coupled biradical character at higher temperature as shown in Scheme 6.2. The activation energy of ΔE_{eq} = 949 K is smaller than the singlet-triplet activation energy gap of ΔE_{ST} = −1185 K and it seems that the open-shell form of T_0 in SQ is an intermediate structure between S_0 of SQ and BZ structure. Therefore, the T_0 state in SQ might play the role of the intermediate state of the structure transformation (Scheme 6.3).

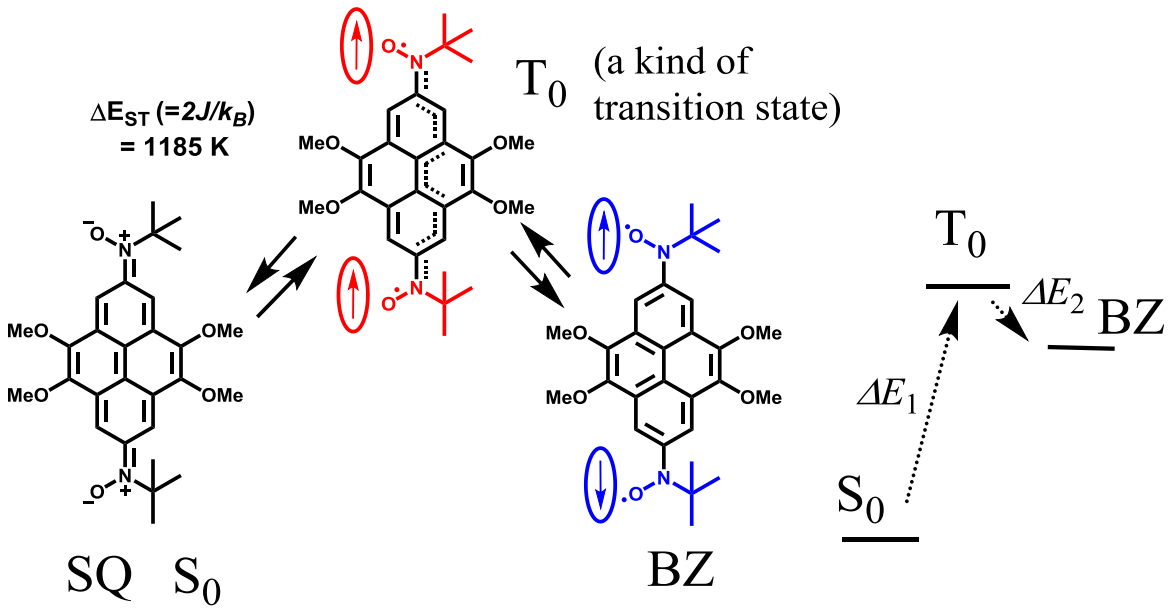

Scheme 6.3: Plausible explanation between the equilibrium and the energy locations among T_0 and S_0 of SQ structure and BZ structure.

Furthermore the variable temperature EPR spectra were also measured for 2-TMPNO (Figure 6.10). Unlike 2,7-TMPNO, 2-TMPNO showed Curie like behavior, with increasing the temperature the EPR signal intensity decreases. This demonstrated that the EPR activity of 2,7-TMPNO is not because of impurity of mono radical as both the sample displayed different temperature dependent behavior.

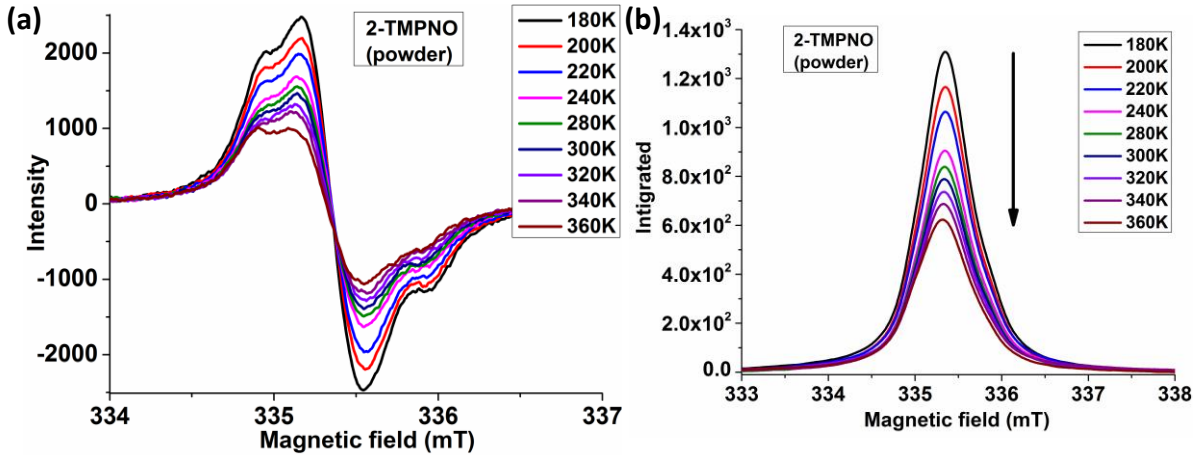

Figure 6.10: (a) Variable temperature (VT) EPR spectra and (b) integrated VT EPR spectra of 2-TMPNO.

6.5 Single Crystal Analysis

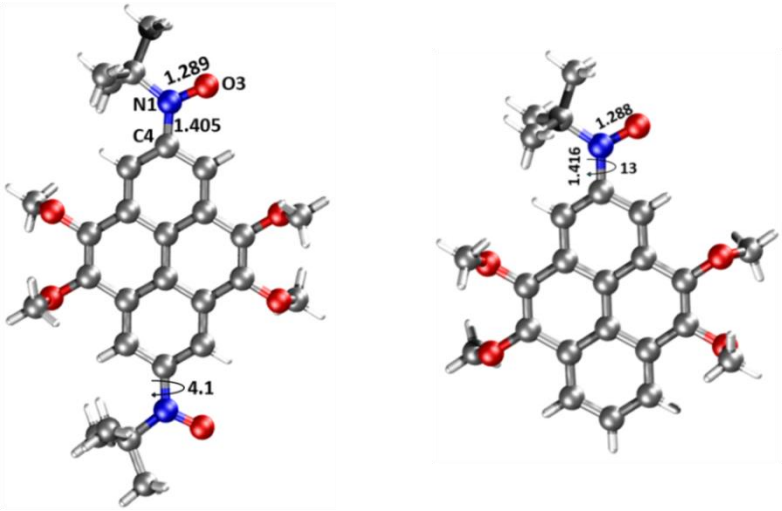

Figure 6.11: Crystal structure of 2,7-TMPNO and 2-TMPNO.

To get an insight into the structure of the radicals good quality single crystals were grown from DCM/hexane solution of 2,7-TMPNO and 2-TMPNO. The single crystal X-ray analysis revealed that monoradical 2-TMPNO crystallizes in P21/c space group. As the case for majority of phenylaaminoxyls radicals, *tert*-butylaminoxyl groups in 2-TMPNO is slightly out of the plane of pyrene (torsion angle 13°).

The biradical 2,7-TMPNO crystallized in monoclinic C2/c space group. Two *tert*-butylaminoxyl groups adopt *syn* configuration which are nearly coplanar with the pyrene ring (torsion angle 4.1°). The elongation of N(1)–O(3) bond lengths (1.289 Å) and shortening of C(4)–N(1) bond lengths (1.405 Å) was observed in comparison with typical N–O (1.27 Å) and C–N (1.41 Å) bond lengths in phenylaminoxyls,[31-32] while a tiny change in alternating C–C bonds was detected (Figure 6.11). The co-planarity of the aminoxyl group with pyrene induces better overlap of π-orbitals of the radicals and pyrene favoring the quinoid structure. The molecules of 2,7-TMPNO recognizes each other through C—H···O hydrogen bond forming a planar self-assembled hexagonal host-guest structure in two-dimensions (Figure 6.12). This planar assembly further extends through π–π stacking forming a sheet structure in three-dimensions. No close contacts between

aminoxyl groups are found pointing to the absence of significant inter-molecular spin exchange in crystal lattice. The UV-Vis, EPR and crystal structure analysis led to the inference that 2,7-TMPNO possesses semi-quinoid structure in solution as well as in solid state. Moreover with increasing temperature the molecule approaches a more benzenoid form.

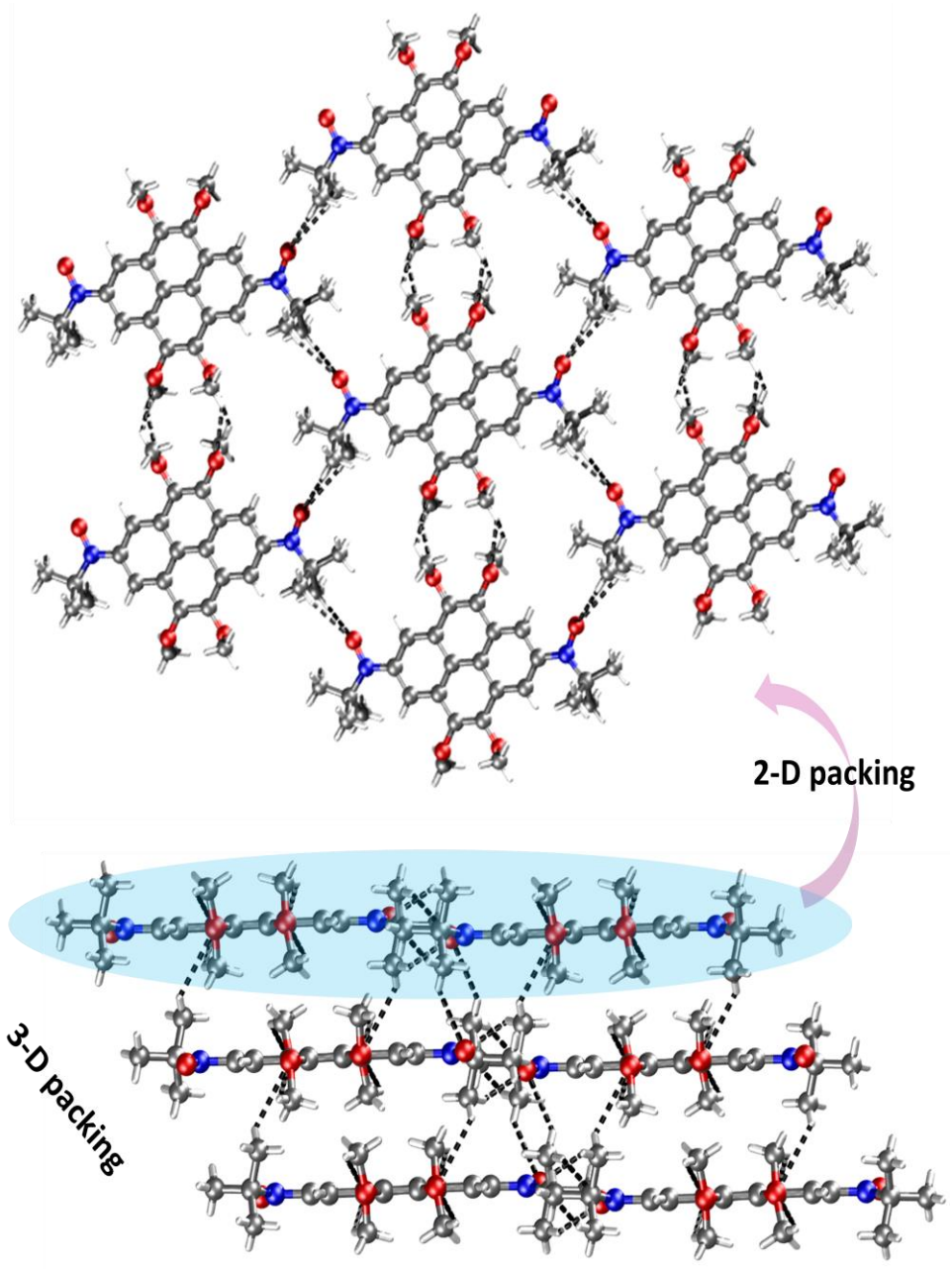

Figure 6.12: 2 and 3-dimensional arrangement of molecules in crystal lattice of 2,7-TMPNO.

6.6 Magnetic measurement & DFT calculations

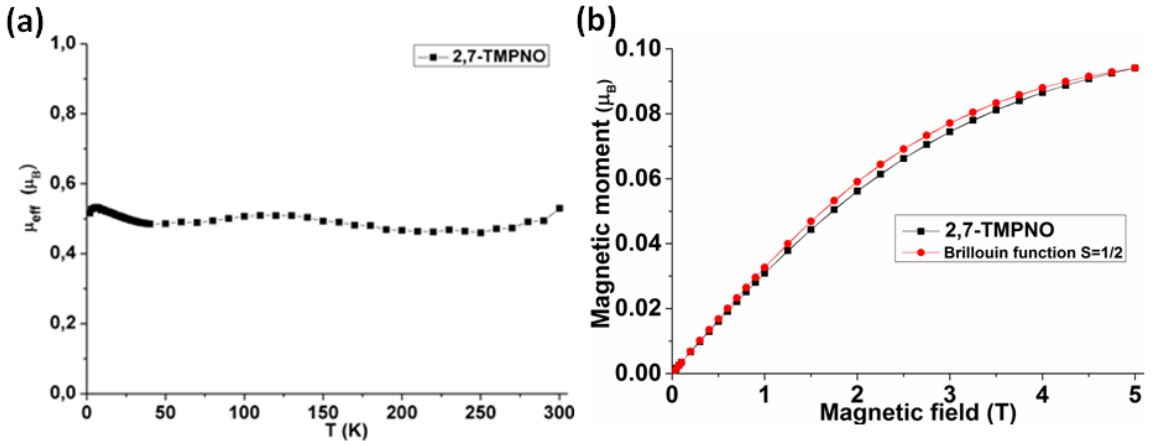

Figure 6.13: (a) Effective magnetic moment of 2,7-TMPNO as a function of temperature under magnetic field 0.1 T (b) Magnetization as a function of magnetic field at 2 K.

The magnetic susceptibility of polycrystalline sample of 2,7-TMPNO was measured as a function of temperature in the temperature range 2 to 300 K. The magnetic susceptibility measurement revealed that the effective magnetic moment (μ_{eff}) between temperature 2 K to 300 K was nearly constant of 0.53 Bohr magneton (μ_B), which was much lower than the expected value of 2.45 μ_B for a magnetically uncorrelated biradical system,[33] suggesting very large antiferromagnetic exchange interactions in solid state (Figure 6.13a). This result was a little contrary to variable temperature EPR measurements where the increase in signal intensity was observed with temperature. The reason why only EPR can detect the increase was ascribed to the detection sensitivity of radicals between EPR and SQUID. EPR can detect very small amount of radicals whereas SQUID cannot. Moreover, the increase at higher temperature can be lower than the detection limit of SQUID due to very small increase of paramagnetic species. Furthermore the effective Bohr magneton of 0.5 means that the spin value is ca. 0.08 per molecule. As the strong antiferromagnetic interaction suppresses the magnetic moment below the Néel temperature (i.e. no significant population of triplet state), the origin of 0.08 spin per molecule should be imputed weakly coupled biradical and monoradical impurity.

Moreover, the magnetization curve, which demonstrated only a paramagnetic component below the Neel temperature, at 2 K also shows 0.09 spin per molecule estimated from the Brillouin function (S = 1/2) (Figure 6.13b). This is a quantitative agreement. Thus, the ground state of 2,7-TMPNO is spin-paired singlet due to partial quinoid structure. The singlet ground state of 2,7-TMPNO due to SQ structure was supported by DFT calculations with the broken symmetry solution providing the estimated singlet (S_0)-triplet (T_0) energy gaps, ΔE_{ST} (= $2J/k_B$) = −1415 K or −2010 K applying B3LYP/6-31G* or BLYP/6-31G* level of theory, respectively (with the Heisenberg type Hamiltonian; $H = -2J\boldsymbol{S}_1\boldsymbol{\bullet}\boldsymbol{S}_2$). The preference of the open-shell singlet was supported by the $<S^2>$ values which are closer to 1 than for a closed shell solution $<S^2> = 0$ (Table 6.1). While for weakly coupled biradicals the BLYP method usually provides better agreement with experiments than the B3LYP method (with its Hartree Fock contamination), this comparison seems to be reverted here for the strongly coupled biradical. This very strong magnetic exchange interaction can be attributed to the SQ structure and the co-planarity of the aminoxyl group and the pyrene spacer. Because of such large exchange interaction small thermal population of the triplet spin state occurs at room temperature, which explains the weak intensity EPR signals at room temperature. Upon increasing the temperature, the population of triplet state enhanced corroborating the increase in EPR signal intensity and decrease in λ_{max} for quinoid structure observed at higher temperatures.

Table 6.1: Energy of BS and triplet states of 2,7-TMPNO

Method	E, eV (BS),(<S**2>)	E, eV (triplet), (<S**2>)	*J*, eV	*J*, K	ΔE_{ST}, K
B3LYP	−44832.6550, (1.01)	−44832.5941, (2.10)	−0.0609	−707.3	−1415
BLYP	−44813.72592, (0.82)	−44813.62375, (2.00)	−0.0866	−1004.8	−2010

6.7 TREPR spectroscopy

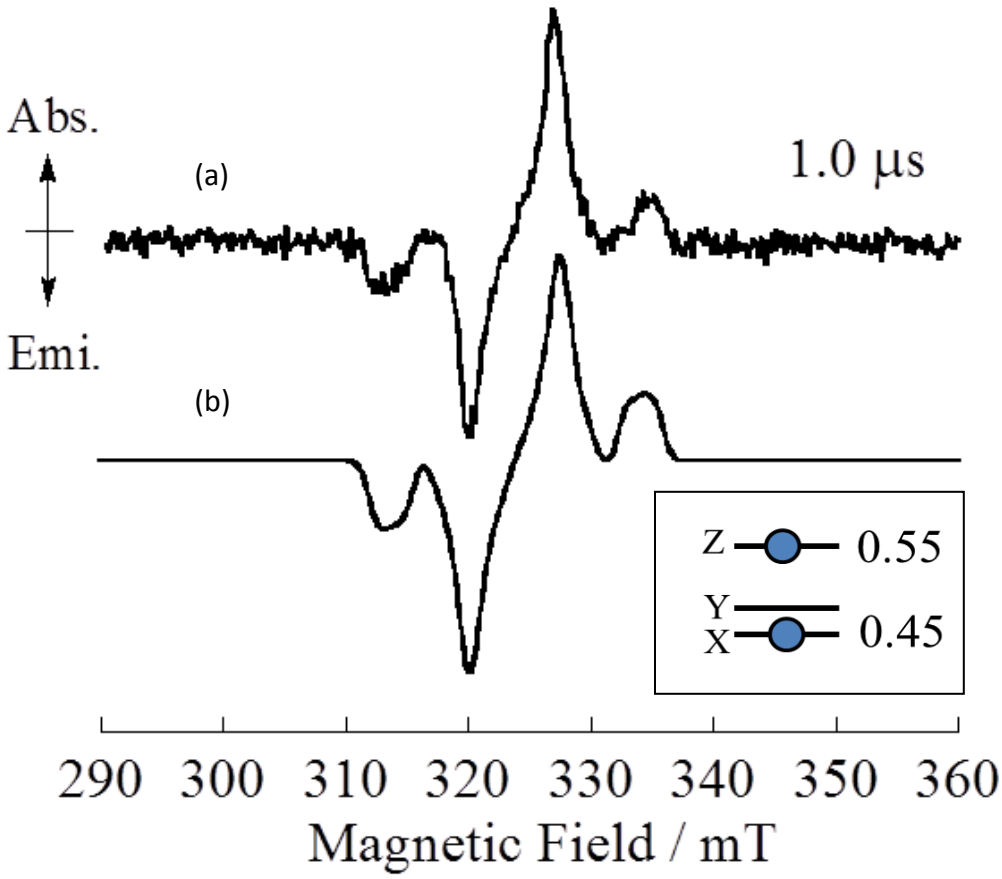

Figure 6.14: Typical TREPR spectrum of 2,7-TMPNO at 30 K at 1.0 μs after photo-excitation. (a) Observed spectrum of 2,7-TMPNO. The upper (down) direction is absorption (emission) of microwave. (b) Simulation of 2,7-TMPNO. In the inset, the phenomenological relative populations in the zero-field spin-sublevels are shown which gave the simulated spectrum.

To clarify what happens upon photo-excitation, the time-resolved EPR (TREPR) spectra were measured using nano-second (ns) pulsed YAG laser excitation. The TREPR measurement and analysis was performed by Prof. Yoshio Teki at Osaka City University Japan. Figure 6.14a shows a typical TREPR spectrum of 2,7-TMPNO observed at 1.0 μs after laser excitation of the pyrene absorption band (λ = 355 nm). The spin Hamiltonian parameters of 2,7-TMPNO were determined to be S = 1, g = 2.0065, D = –0.0112 cm^{-1},

and E = –0.0014 cm^{-1} by spectral simulation (Figure 6.14b), with the hybrid Eigenfield/exact diagonalization method taking dynamic electron spin polarization (DEP) into account.[11, 34-35] The minus sign of D was estimated from the point dipole calculation of biradical form depicted in Scheme 6.2 (breaking quinoid structure). The magnitude of D value was, however, much larger than that of the point dipole calculation obtained using the averaged distance (R = 0.986 nm) between two radical moieties. Applying the formulae ($R = 0.138/ |D (cm^{-1})|^{1/3}$) with the experimental D value of 0.0112 cm^{-1} the averaged distance between two unpaired spins was estimated to be 0.62 nm. This distance was much smaller than the distance between both N-centers of the radical units indicating large delocalization of unpaired spin density into the tetramethoxypyrene. The delocalization of unpaired electrons through a quinoid structure was supported by DFT calculations, since their SOMOs (Figure 6.19a) and the spin densities of the biradical triplet state (Figure 6.19b) were delocalized into the pyrene core. In the inset of Figure 6.14b, the relative populations in the zero-field spin-sublevels are shown which gave the simulated spectrum. However, it should be noted that these populations were phenomenological ones which were assumed to give the spectral simulation at that time. As shown in Figure 6.15, at the earlier time at 0.2 μs the populations of X, Y and Z spin-sublevels were 0, 0.7 and 0.3, respectively. They have changed to 0.45, 0 and 0.55 at 1.0 μs, which indicated the Y spin-sublevels being more allowed to the S_0 state. The simulation of the time dependence can be done by necessarily taking the spin-lattice relaxation between triplet spin-sublevels, the anisotropic relaxation (a kind of intersystem crossing between T_0 and S_0), the external magnetic field, and the stimulated transition induced by the resonance microwave into account.

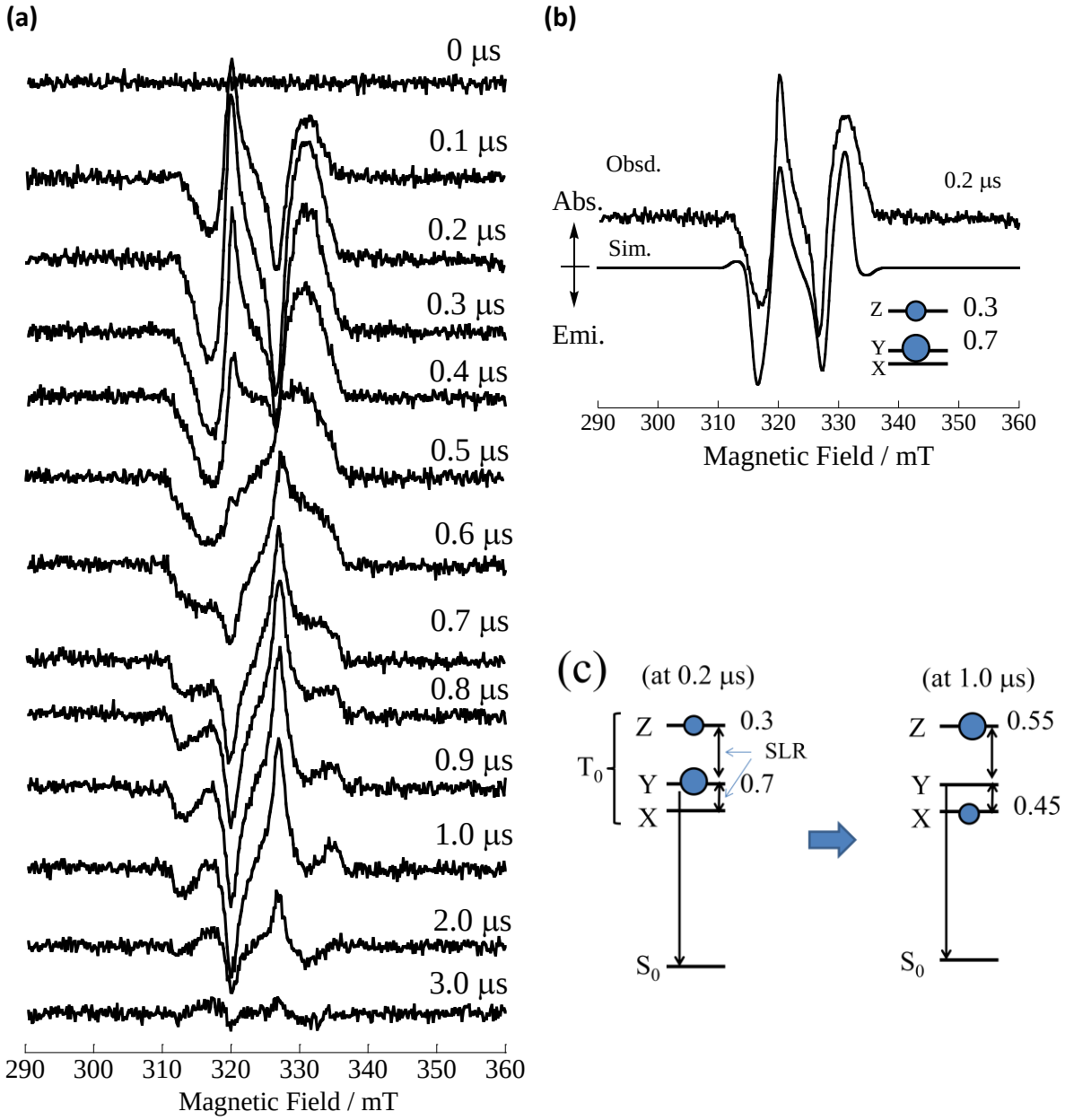

Figure 6.15: (a) Time dependence of TREPR spectra of 2,7-TMPNO (b) observed and simulated TREPR spectra at 30 K on 0.2 μs after photo-excitation, (c) relative population change. The relative populations to give the spectral simulation have changed to 0.45, 0 and 0.55 at 1.0 μs, which indicates the Y spin-sublevels being more allowed to the S_0 state.

The plausible mechanism of the dynamic electron spin polarization through photo-excited multiplet state is shown in Figure 6.16. The low-lying triplet state (T_0) above the singlet ground state (S_0) can be populated through photo-excited (S_1, T_1, T_2, Qu_1) states that were generated by the exchange coupling between photo-excited triplet state of the pyrene moiety and two connecting NO radicals. The transition from T_1 and T_2 to T_0 was allowed since the total spins were the same (S = 1). The similar phenomena, that the electron spin polarization of the low-lying triplet state (T_0) was enhanced through photo-excited multiplet states, was reported in an exchange coupled phthalocyanine-bis(radical) system.[34-35]

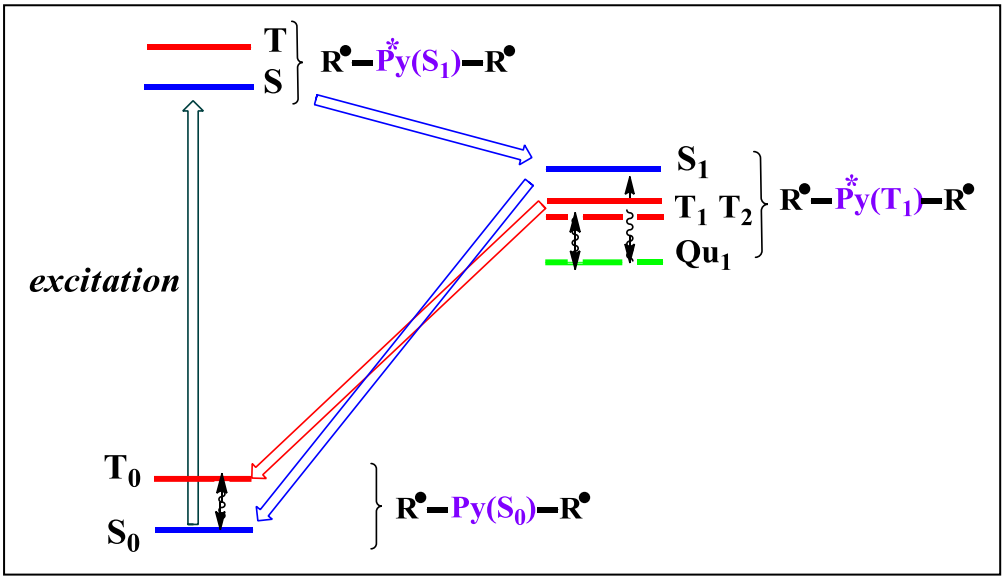

Figure 6.16: Generation of electron spin polarization in the low-lying triplet state (T_0) and spin dynamics through photo-excited multiplet states. According to the spin density distribution of the triplet state of pyrene, the ferromagnetic coupling between the pyrene and two radical moieties is expected on the photo-excited state due to the topological rule. Therefore, the energy ordering of $S_1 > T_1, T_2 > Qu_1$ is depicted in this figure.

In order to confirm this mechanism we measured TREPR spectra of 2,7-TMPNN ((4,5,9,10-tetramethoxypyrene-2,7-bis(nitronyl nitroxide)).[36] The polarized triplet state (T_0) was also observed in 2,7-TMPNN (Figure 6.17). In this case, the fine-structure splitting was much smaller than that of 2,7-TMPNO, which was comparable with the line-width.

This small magnitude of the fine structure splitting was consistent with the long distance of 10.93 Å between two nitronyl nitroxide (NN) moieties and the localized spin-structure. The DFT calculation of the ground state supported this localized spin structure (Figure 6.20). In addition, the T_0 and S_0 states were expected to be almost degenerate because the two radical moieties were connected to each other in disjoint configuration through the pyrene as spin coupler.[37] In contrast, two radical spins in 2,7-TMPNO were strongly exchange-coupled in the ground state through quinoid structure proven by the magnetic susceptibility measurement as mentioned above.

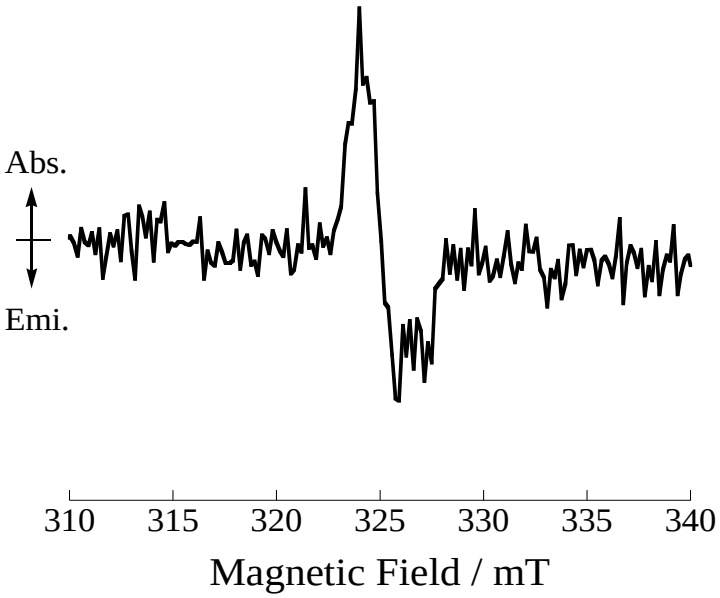

Figure 6.17: Observed TREPR spectrum of 2,7-TMPNN at 0.8 μs

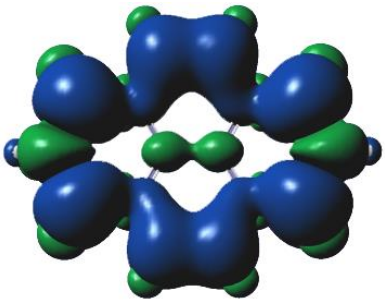

Figure 6.18: Spin density distribution of the triplet state of pyrene calculated by using DFT quantum mechanical calculations (UB3LYP/6-31G(d,p)).

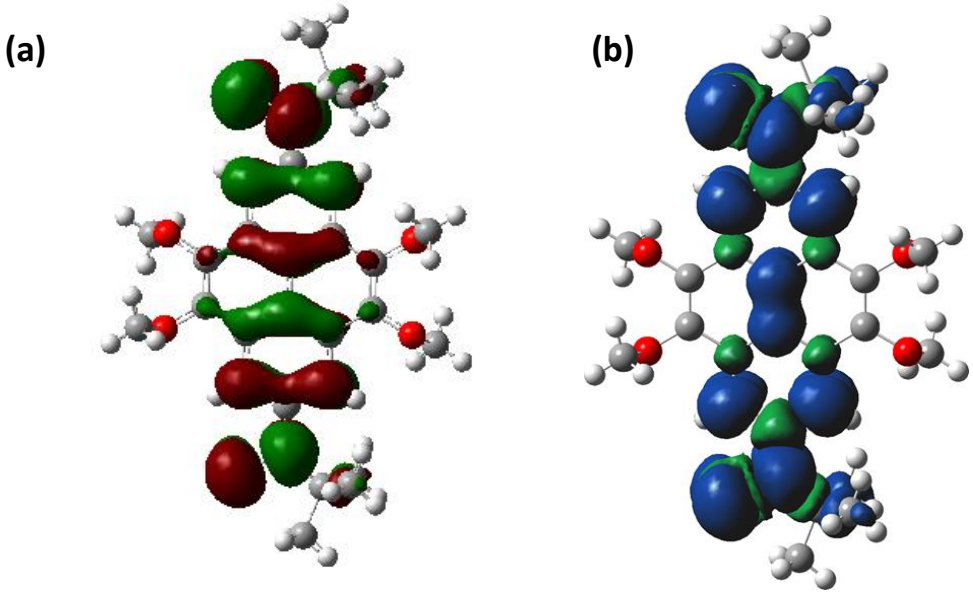

Figure 6.19: (a) SOMO-1 and (b) spin density distribution of the biradical triplet state of 2,7-TMPNO calculated by using DFT quantum mechanical calculations (UBLYP/6-31G(d)).

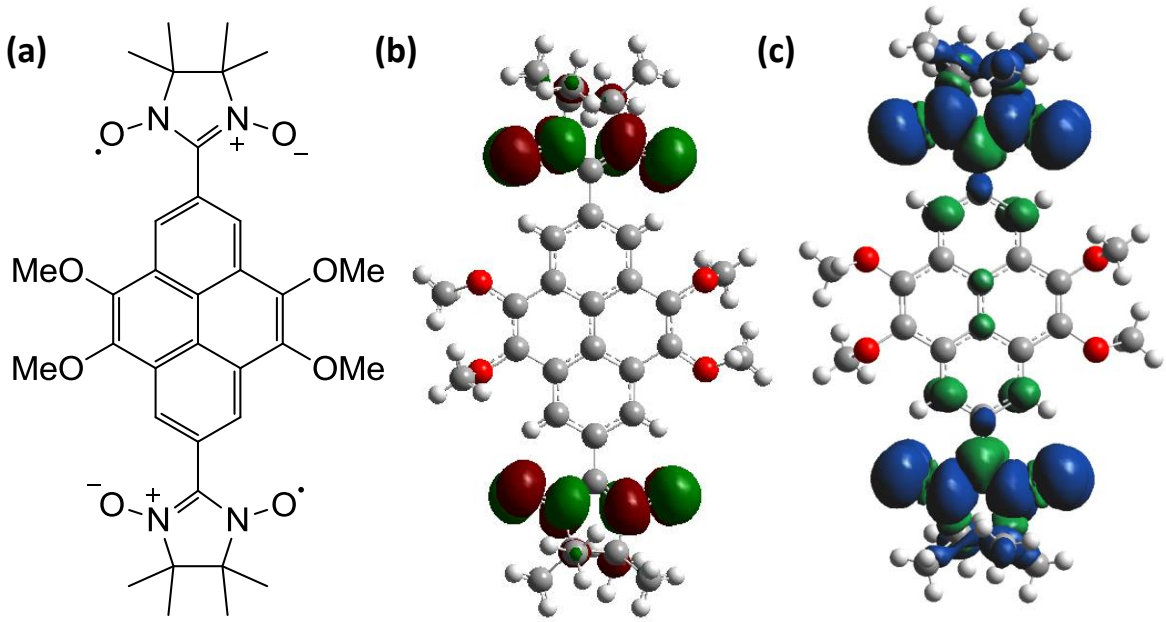

Figure 6.20: (a) structure (b) SOMO orbital (c) spin density distribution of 2,7-TMPNN calculated by using DFT quantum mechanical calculations (UBLYP/6-31G(d)).

6.8 Theoretical investigation of *zfs* parameters

The obtained zero field splitting (*zfs*) parameters from TREPR measurements were verified by DFT calculations. *zfs* parameters (*D* and *E*) were determined using restricted open shell DFT calculations with the BLYP functional and 6-31g(d) basis set using ORCA-software. The calculations using ORCA-software were done by Dr. Elena Gorelik. Good agreement of the calculated zero field splitting with experiment, ascertained for the biradicals 2,7-TMPNO and 2,7-TMPNN. This also reflects the large difference in spin density distribution. The calculated *zfs* parameters are,

2,7-TMPNO: D = –0.00921 cm^{-1}; E = –0.00094 cm^{-1}

2,7-TMPNN: D = –0.00155 cm^{-1}; E = –0.00004 cm^{-1}

Individual contributions to *zfs* (cm^{-1})				
	2,7-TMPNO		**2,7-TMPNN**	
	D	**E**	**D**	**E**
SPIN-SPIN	–0.00921	–0.00094	–0.00155	-0.00004
Exchange *vs* Coulomb				
Coulomb	0.11183	0.07535	0.13046	0.04030
Exchange	–0.12104	–0.07629	–0.13201	-0.04034
One through four center contributions				
1-center	–0.000	0.000	–0.000	0.000
2-center-Coulomb	–0.013	–0.001	–0.003	-0.000
2-center-Exchange	0.000	–0.000	–0.000	0.000
2-center-Hybrid	–0.000	–0.000	0.000	0.000
3-center-Coulomb	0.005	0.000	0.002	0.000
3-center-Exchange	–0.001	–0.000	–0.000	–0.000
4-center	–0.000	–0.000	–0.000	–0.000

6.9 Excited state dynamics through transient absorption spectroscopy

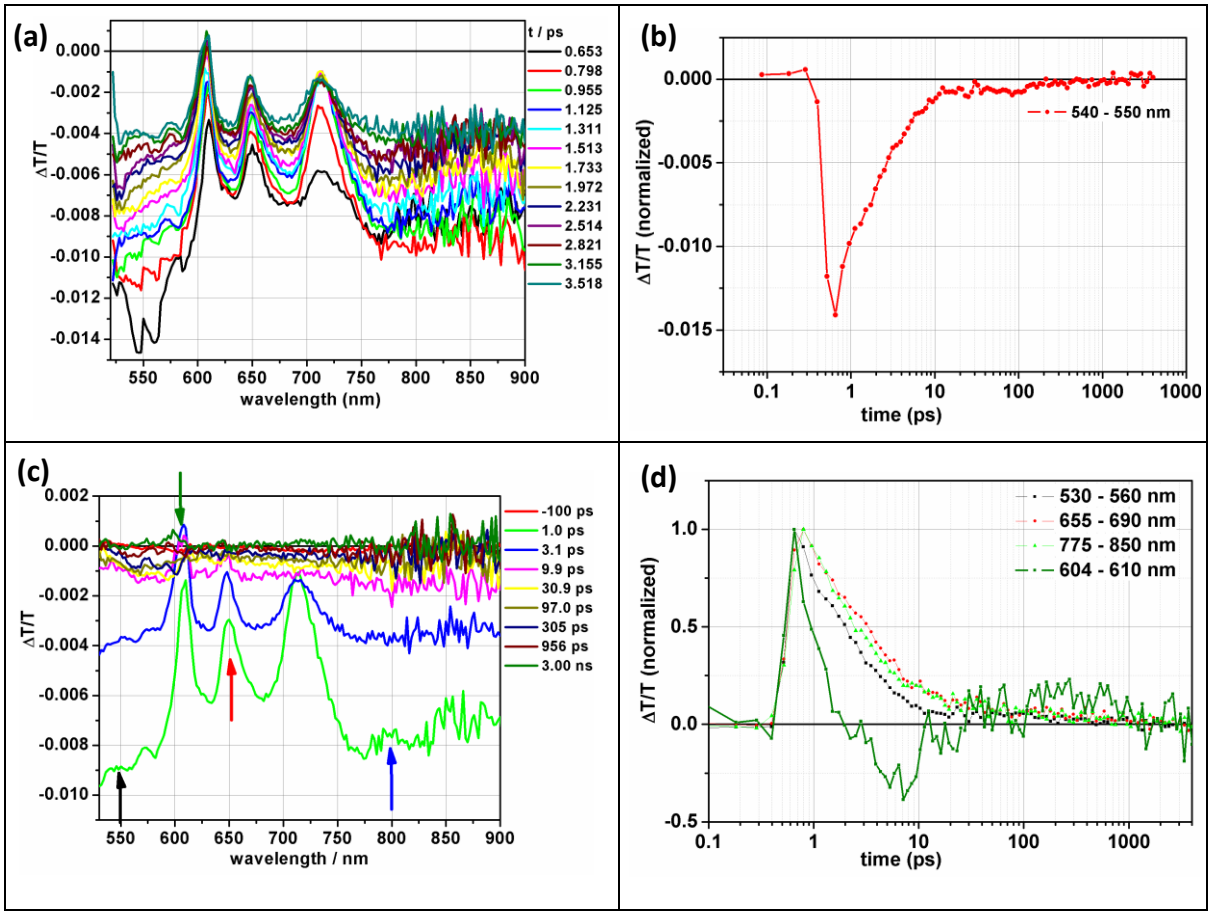

Figure 6.21: Picosecond transient absorption spectra and decay profile of 2,7-TMPNO in toluene at room temperature after excitation at 470 nm.

To probe excited state dynamics, picosecond transient absorption (TA) spectra of 2,7-TMPNO were measured. The TA measurements were performed by Mr. Dominik Gehrig, PhD student with Dr. Frédéric Laquai, at MPIP. We intended to observe the change absorption spectra when pyrene core is excited with a laser as in the case of TREPR measurements. Due to experimental limitations of TA set up measurement at 355 nm laser excitement was not possible, as the optical element like corner tube, λ/2 plates, mirrors etc. absorbs significant amount of UV light. So TA measurements were done with 470 nm laser excitation where the quinoid form of 2,7-TMPNO showed strong absorption.

It is known that the photo induced absorption (PIA) for pyrene can be seen at 520-530 nm.[38] Here this dynamics was red shifted by 20 nm around 540-550 nm (Figure 6.21a). Notably the PIA of pyrene decay faster than the rest of PIA within the first 3 ps indicating ultrafast relaxation/quenching of excited pyrene moiety. As shown in Figure 6.21c ground state bleach of absorption at 600-650 nm was observed. This indicated the structural transformation on photo-excitation, as this signal is also associated with quinoid form of 2,7-TMPNO. Additionally the decay behavior seems to be similar over the whole wavelength range except at 600-610 nm (Figure 6.21d).

6.10 Summary

In summary, the biradical 2,7-TMPNO exist in singlet semi-quinoid structure revealed by variable temperature EPR, UV-Vis and single crystal X-ray diffraction measurements and DFT calculations. This led to extremely strong intra-molecular exchange coupling $2J/k_B$ = –1185 K. Upon photo-excitation, the breaking of semi-quinoid structure was observed due to dynamic electron spin polarization leading to a spin polarized triplet state. The observed relatively large zero field splitting can be attributed to delocalization of spin density of biradical triplet into the pyrene core. Dynamic molecules like 2,7-TMPNO are of special interest not only for the fundamental study but also for their applications in future spintronic devices.

6.11 Synthetic details

2,7-Diiodo-4,5,9,10-tetramethoxypyrene and *t*-BuNO were synthesized according to literature procedures.[24, 39-40]

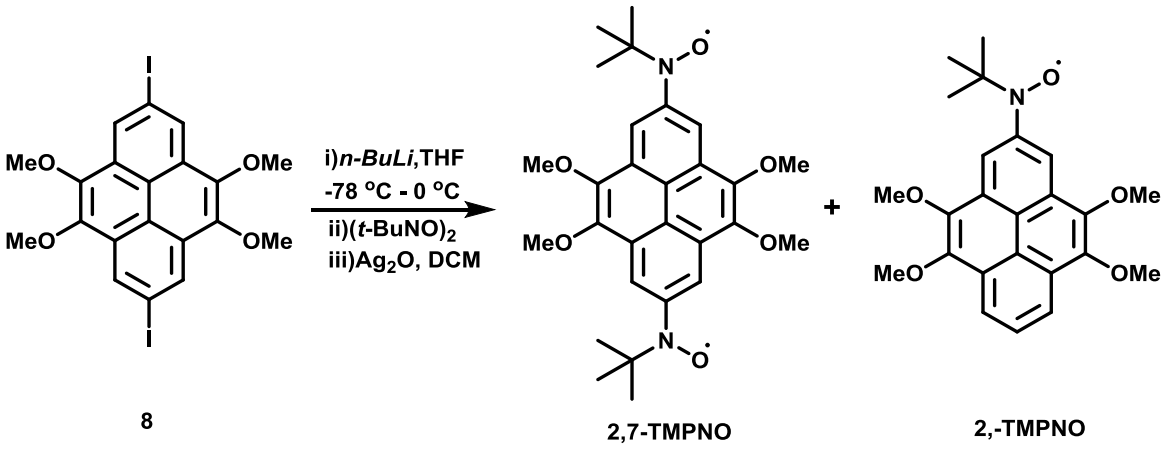

8 2,7-TMPNO 2,-TMPNO

N,N'-(4,5,9,10-Tetramethoxypyrene-2,7-diyl)bis(N-oxy-tert-butylamine)

To a solution of 2,7-diiodo-4,5,9,10-tetramethoxypyrene (**8**) (100 mg, 0.17 mmol) in 10 ml THF, 0.5 ml (5 equivalents) of 1.6 M *n*-BuLi hexane solution was added drop wise at –78 °C and stirred for 1 hour at the same temperature. The mixture was gradually warmed to 0 °C and further stirred for 2 hour. To the resulting mixture, solution of *t*-BuNO dimer (5 equivalents) in 2 ml THF was added drop wise at –78 °C the, stirred for 1 hour at the same temperature and warmed to room temperature. The mixture was hydrolyzed with saturated aqueous ammonium chloride solution. The white precipitate, which was almost insoluble in DCM, filtered and used for next step without further purification. To the slurry of crude product in 15 ml chloroform 100 mg of Ag_2O was added and stirred for 4 hour. The mixture was filtered through celite and the solvent was evaporated. The residue was purified by silica gel chromatography using hexane:ethylacetate (100:15) as eluant. 40 mg (46% yield in two steps) of biradical (2,7-TMPNO) was obtained along with 4 mg (5%) of monoradical (2-TMPNO) which were separated on silica gel column. **2,7-TMPNO:** (MS-FD = 494.2(100%)) HRMS (ESI): 494.2409 (calc. 494.2417), MP; 176 °C, UV-Vis (Toluene) λ_{max} (ε, $cm^{-1}\,M^{-1}$) : 472 nm (1.6×10^4) 608

nm (1280). **2-TMPNO:** (MS-FD = 408.0 (100%)), UV-Vis (Toluene) λ_{max} (ε, cm^{-1} M^{-1}): λ_{max} = 415 nm and 438 nm (862 and 838), MP; 106 °C.

6.12 References

[1] O. Sato, J. Tao, Y.-Z. Zhang, *Angew. Chem. Int. Ed.* **2007**, *46*, 2152.

[2] F. Renz, H. Oshio, V. Ksenofontov, M. Waldeck, H. Spiering, P. Gütlich, *Angew. Chem. Int. Ed.* **2000**, *39*, 3699.

[3] O. Sato, *Journal of Photochemistry and Photobiology C: Photochemistry Reviews* **2004**, *5*, 203.

[4] J. Wang, L. Hou, W. R. Browne, B. L. Feringa, *J. Am. Chem. Soc.* **2011**, *133*, 8162.

[5] S. i. Nakatsuji, *Chem. Soc. Rev.* **2004**, *33*, 348.

[6] Y. Teki, H. Tamekuni, J. Takeuchi, Y. Miura, *Angew. Chem. Int. Ed.* **2006**, *45*, 4666.

[7] S. Suzuki, A. Nagata, M. Kuratsu, M. Kozaki, R. Tanaka, D. Shiomi, K. Sugisaki, K. Toyota, K. Sato, T. Takui, K. Okada, *Angew. Chem. Int. Ed.* **2012**, *51*, 3193.

[8] C. Corvaja, M. Maggini, M. Prato, G. Scorrano, M. Venzin, *J. Am. Chem. Soc.* **1995**, *117*, 8857.

[9] K. Ishii, J.-i. Fujisawa, Y. Ohba, S. Yamauchi, *J. Am. Chem. Soc.* **1996**, *118*, 13079.

[10] Y. Teki, S. Miyamoto, K. Iimura, M. Nakatsuji, Y. Miura, *J. Am. Chem. Soc.* **2000**, *122*, 984.

[11] Y. Teki, S. Miyamoto, M. Nakatsuji, Y. Miura, *J. Am. Chem. Soc.* **2001**, *123*, 294.

[12] Y. Teki, M. Nakatsuji, Y. Miura, *Mol. Phys.* **2002**, *100*, 1385.

[13] Y. Teki, M. Kimura, S. Narimatsu, K. Ohara, K. Mukai, *Bull. Chem. Soc. Jpn.* **2004**, *77*, 95.

[14] E. M. Giacobbe, Q. Mi, M. T. Colvin, B. Cohen, C. Ramanan, A. M. Scott, S. Yeganeh, T. J. Marks, M. A. Ratner, M. R. Wasielewski, *J. Am. Chem. Soc.* **2009**, *131*, 3700.

[15] M. T. Colvin, E. M. Giacobbe, B. Cohen, T. Miura, A. M. Scott, M. R. Wasielewski, *J. Phys. Chem. A* **2010**, *114*, 1741.

[16] F. Adrian, *Reviews of Chemical Intermediates* **1979**, *3*, 3.

[17] A. Kawai, K. Obi, *The Journal of Physical Chemistry* **1992**, *96*, 52.

[18] Y. Teki, T. Toichi, S. Nakajima, *Chem. Eur. J.* **2006**, *12*, 2329.

[19] Y. Teki, *Polyhedron* **2005**, *24*, 2299.

[20] M. Baumgarten, High Spin Molecules Directed Towards Molecular Magnets. In *EPR of Free Radicals in Solids II*, A. Lund, M. Shiotani, Eds. Springer Netherlands: 2012; Vol. 25, pp 205.

[21] Y. Kawanaka, A. Shimizu, T. Shinada, R. Tanaka, Y. Teki, *Angew. Chem. Int. Ed.* **2013**, *52*, 6643.

[22] A. Saha, I. A. Latif, S. N. Datta, *J. Phys. Chem. A* **2011**, *115*, 1371.

[23] H. Kurata, Y. Takehara, T. Kawase, M. Oda, *Chem. Lett.* **2003**, *32*, 538.

[24] S.-i. Kawano, M. Baumgarten, D. Chercka, V. Enkelmann, K. Müllen, *Chem. Commun.* **2013**, *49*, 5058.

[25] S. Nakazono, S. Karasawa, N. Koga, H. Iwamura, *Angew. Chem. Int. Ed.* **1998**, *37*, 1550.

[26] Y. Kanzaki, D. Shiomi, K. Sato, T. Takui, *J. Phys. Chem. B* **2012**, *116*, 1053.

[27] E. Dormann, M. J. Nowak, K. A. Williams, R. O. Angus, F. Wudl, *J. Am. Chem. Soc.* **1987**, *109*, 2594.

[28] R. M. Dupeyre, A. Rassat, J. Ronzaud, *J. Am. Chem. Soc.* **1974**, *96*, 6559.

[29] U. Müller, M. Baumgarten, *J. Am. Chem. Soc.* **1995**, *117*, 5840.

[30] B. Bleaney, K. D. Bowers, *Proc. R. Soc. London A* **1952**, *214*, 451.

[31] K. Inoue, H. Iwamura, *Angew. Chem. Int. Ed.* **1995**, *34*, 927.

[32] J. Ohshita, T. Iida, N. Ohta, K. Komaguchi, M. Shiotani, A. Kunai, *Org. Lett.* **2002**, *4*, 403.

[33] G. Zoppellaro, V. Enkelmann, A. Geies, M. Baumgarten, *Org. Lett.* **2004**, *6*, 4929.

[34] K. Ishii, Y. Hirose, H. Fujitsuka, O. Ito, N. Kobayashi, *J. Am. Chem. Soc.* **2001**, *123*, 702.

[35] K. Ishii, Y. Hirose, N. Kobayashi, *J. Am. Chem. Soc.* **1998**, *120*, 10551.

[36] P. Ravat, Y. Ito, E. Gorelik, V. Enkelmann, M. Baumgarten, *Org. Lett.* **2013**, *15*, 4280.

[37] W. T. Borden, E. R. Davidson, *J. Am. Chem. Soc.* **1977**, *99*, 4587.

[38] Y. B. Borozdina, V. Kamm, F. Laquai, M. Baumgarten, *J. Mater. Chem.* **2012**, *22*, 13260.

[39] J. C. Stowell, *J. Org. Chem.* **1971**, *36*, 3055.

[40] R. J. Smith, R. M. Pagni, *J. Org. Chem.* **1981**, *46*, 4307.

CHAPTER 7

"TSCHITSCHIBABIN TYPE BIRADICALS": BENZENOID OR QUINOID?

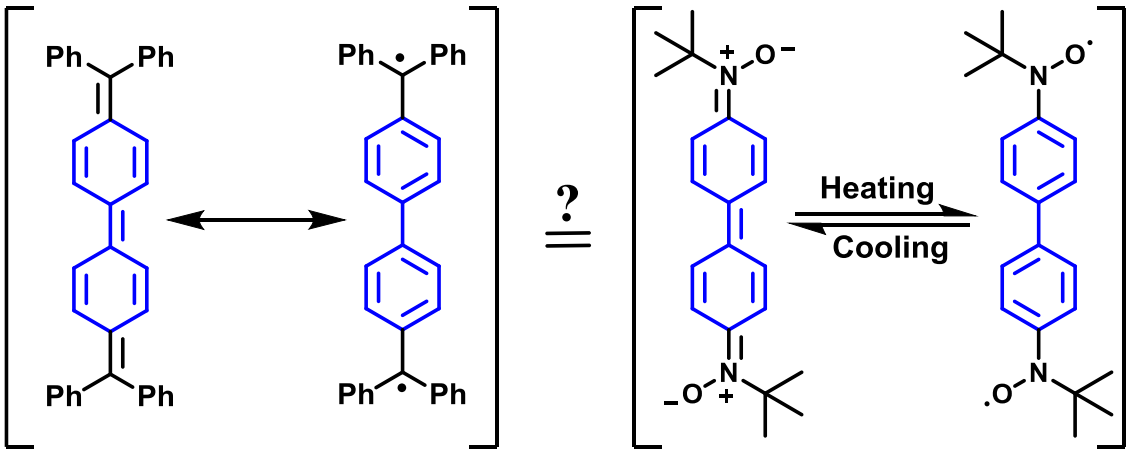

Tschitschibabin's HC
(ΔE_{ST} = ($2J/k_B$) = -8.1 kcal/mol)

BPNO, Semi-Quinoid
(ΔE_{ST} = ($2J/k_B$) = -5.1 kcal/mol)

Our findings in this chapter provides a better understanding of the discrepancies related to the discussion in the literature on the ground state of Tschitschibabin's hydrocarbon. The simple theoretical and experimental methodologies have been developed and utilized to understand the singlet biradicaloids which exist in semi-quinoid form and exhibits characteristics of biradicaloid and quinoid form simultaneously.

Note: Large part of this chapter has been submitted to PCCP, 2014.

7.1 Introduction

Shortly after the discovery of the first stable organic radical, namely triphenylmethyl by Gomberg,[1] Tschitschibabin reported the synthesis of the first biradical linked through biphenyl bridge in 1907, now more commonly known as Tschitschibabin's hydrocarbon (HC) or biradical.[2] Recently there is a considerable amount of interest of various research groups in synthesizing Kekulé open shell polyaromatic hydrocarbons owing to their application in designing spintronic and energy storage devices.[3-6] In most of the cases the molecular structural design of Kekulé open shell polyaromatic hydrocarbons relied on the bases of Tschitschibabin's HC, and the biradicaloid nature of HC appeared as a consequence of loss of quinoidal form upon extending conjugation thereby gaining the aromaticity.[7-10] As the Tschitschibabin's HC is a fundamental building block in designing the majority of Kekulé open shell polyaromatic HCs, it has been studied most extensively by various EPR spectroscopic techniques and theoretical calculations.[11] While Thiele's HC was well accepted as quinoid singlet, there are different opinions on the ground state of Tschitschibabin's HC, whether it is open shell or closed shell (Figure 7.1).[12] In principle the EPR spectroscopy should be able to resolve this problem simply but the analysis of this molecule is severely affected by paradox, disputation and repugnancies.[12-16] Firstly Reitz and Weissman investigated Tschitschibabin's HC, labeled at exocyclic carbon atom with ^{13}C.[11] They obtained EPR spectra corresponding to two non interacting triphenyl methyl moieties with $J < 10^8$ Hz.[16] This result showed the divergence with the initial theoretical study which predicted the $J > 10^{13}$ Hz.[17-18] This discrepancy often alluded as "biradical paradox".[13, 19-20] Later several theories have been proposed relating to the biradical paradox of this molecule. In subsequent years the studies by Brauer *et al*.,[19, 21] van der Hart, and Oosterhoff[22] suggested that the biradical paradox is not real and the observed EPR spectra, alike the doublet species, is due to impurities owing to high reactivity of Tschitschibabin's HC. Brauer *et al.* did extensive ENDOR studies and suggested that the spectrum originated from a monoradical impurity with structural formula shown in Figure 7.2a.[19, 21] Along

with this van der Hart and Oosterhoff suggested dimers of the biradicals as shown in Figure 7.2b, responsible for the observed EPR spectrum.[22] Thus, the reported EPR spectrum with vanishing exchange interactions ($J < 10^8$ Hz) could be imputed to impurities thereby solving the biradical paradox. This problem seemed to be completely resolved when Brauer *et al.* reported the triplet resonance signal for the polycrystalline sample of Tschitschibabin's HC.[14-15] But the discrepancies were triggered back when Montgomery *et al.* successfully obtained the single crystal of Tschitschibabin's HC, which provided doublet EPR spectrum alike all previous studies of the same.[12] Since then no clear explanation has been given to such conflicting observations which were supposedly caused by the possibility of the paramagnetic impurities.

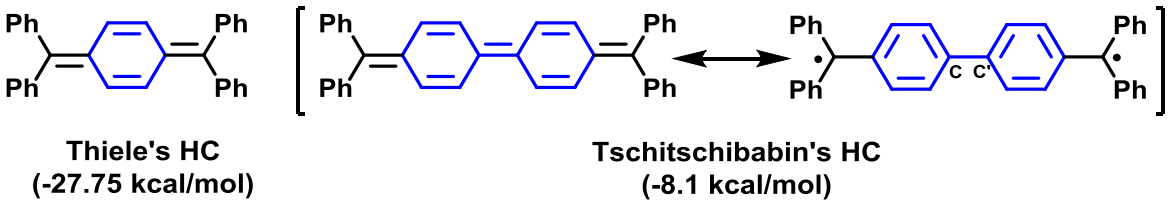

Figure 7.1: Thiele's and Tschitschibabin's hydrocarbon and calculated singlet-triplet energy gap.

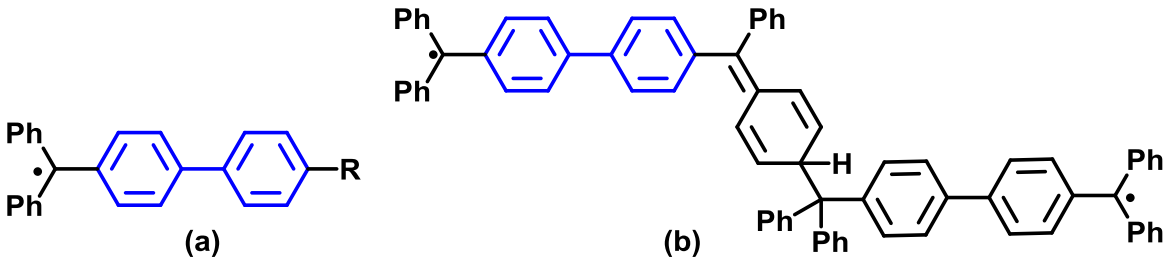

Figure 7.2: (a) Structural formula of monoradical impurity proposed by Brauer *et al*. (b) structural formula of dimer impurity proposed by van der Hart and Oosterhoff.

Serendipitously during the course of our study on the tuning of intra- and inter-molecular exchange interactions in antiferromagnetically coupled biradicals, described in previous chapters, we found the molecule BPNO which exist in semi-quinoid form (Figure 7.3).[23-26] At room temperature BPNO showed doublet EPR spectrum. Even after several

purifications by column followed by repetitive crystallization no improvement in EPR spectrum was observed. Thus, this molecule was studied in depth by variable temperature EPR, UV-Vis spectroscopy and DFT calculation. All the analysis led to inference that the molecule BPNO exist in semi-quinoid form with very large singlet-triplet energy gap of –5.1 kcal/mol. A similar semi-quinoid structure was also found for the 2,7-disubstituted tetramethoxypyrene based biradical system described in chapter 6.[27] The initially observed monoradical like spectrum at room temperature was caused by the trace amount of monoradical impurity and the very weak intensity biradical spectrum due to low population of triplet state at given temperature was suppressed under the monoradical impurity spectrum. At the elevated temperature clear five line EPR spectrum for biradical was observed. These observations reminded us the very well known Tschitschibabin's HC which also suffered from the absence of triplet EPR spectrum in solution as discussed above. So we planned to revisit the discrepancy of ground state of Tschitschibabin's HC. Alike in Tschitschibabin's HC, the two spin centers in BPNO are separated by the same spacer molecule. The BPNO can serve as a stable heteroatom analogue of Tschitschibabin's HC.

I reanalyzed the crystal structures of Thiele's and Tschitschibabin's HC reported by Montgomery *et al.* with DFT calculations.[12] While the Thiele's HC showed bond alterations in phenylene ring indicating quinoid form, the Tschitschibabin's HC did not show significant difference in alternating bonds of the biphenyl. Most importantly the C—C′ bond (1.448 Å) between the phenylene rings was 0.1 Å longer than the typical double bond average, but still shorter than the typical aryl-aryl single bond distance (1.493 Å) in biphenyls. The crystal structure data for Tschitschibabin's HC recorded at three different temperatures did not show systematic change in bond lengths and dihedral angles. The DFT calculations were performed with the geometry of single crystal structure to obtain the singlet-triplet energy gap and to compare the spin density distribution. The estimated antiferromagnetic singlet-triplet energy gap for Thiele's and Tschitschibabin's HC were –27.7 and –8.1 kcal/mol, respectively, using unrestricted

broken symmetry B3LYP/6-31g(d) level of theory. Interestingly, while the Eigen function (S^2) for broken symmetry state of Thiele's HC converged to zero, it was close to 1 for Tschitschibabin's HC (S^2 = 0.77). This clearly indicated the ground state of Thiele's and Tschitschibabin's HC are closed shell singlet and open shell singlet, respectively. The singlet-triplet energy gap for Tschitschibabin's HC was nearly double than that of BPNO, which suggested alike BPNO, Tschitschibabin's HC may also exist in semi-quinoid form. Therefore considering the very strong antiferromagnetic exchange interactions no significant population of triplet state occurs at room temperature or lower temperatures. So the triplet EPR spectrum of Tschitschibabin's HC was masked under the monoradical impurities. If this hypothesis is true then all the historical discrepancies related to EPR spectra of Tschitschibabin's HC can be well accounted for.

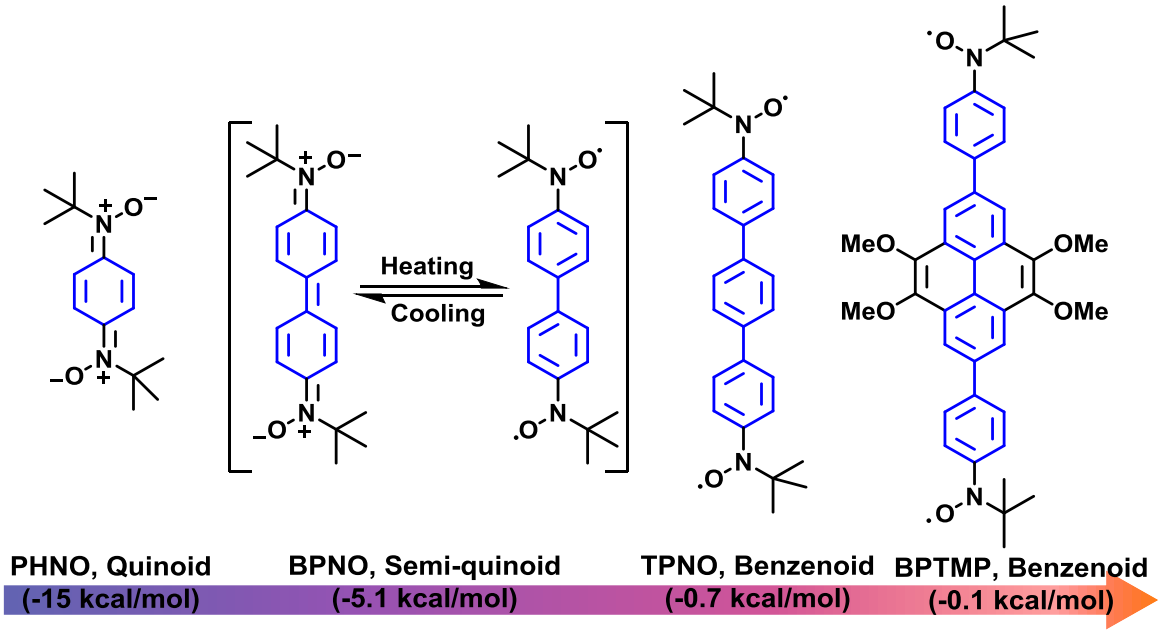

Figure 7.3: The structures of molecules under investigation and the energy gap between singlet and triplet states.

Thus to confirm our hypothesis, we designed and studied a series of phenylene bridged bisnitroxide molecules (Figure 7.3) experimentally as well as theoretically. The structure of PHNO was comparable to Thiele's HC, both of which exist in a complete quinoid form. On further extending the π-bridge from monophenylene to biphenylene

and terphenylene, the molecules showed the transition from complete quinoid to complete biradicaloid form via semi-quinoid structure. Unlike Tschitschibabin's HC, the excellent stability of BPNO allowed its analysis under very harsh condition. In BPTMP the spacer molecule biphenyl tetramethoxypyrene can be considered as a tetraphenylene in which two central phenyl rings are locked from the rotation.

7.2 Synthesis

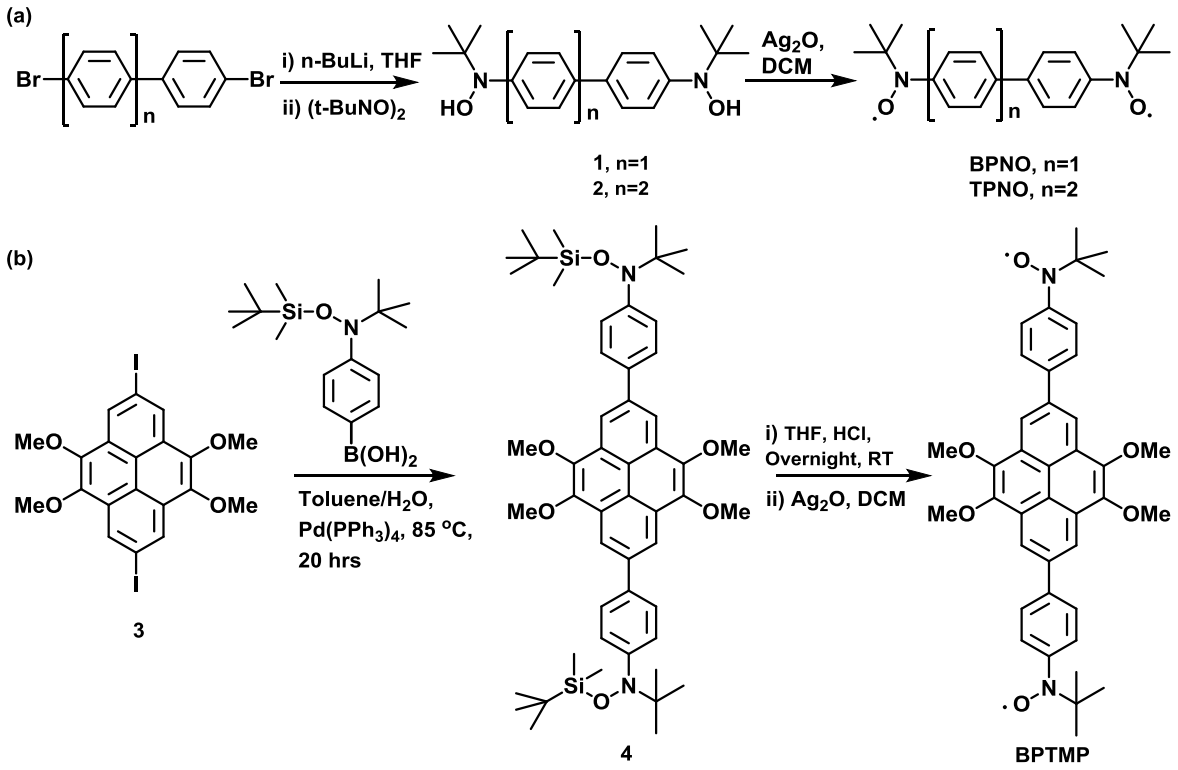

Scheme 7.1: Synthesis of (a) BPNO and TPNO, and (b) BPTMP.

In 1998 Iwamura *et al.* reported the synthesis and characterization of p-phenylenebis(N-*tert*-butylaminoxyl) (PHNO).[28] The PHNO was analyzed by NMR, EPR, UV-Vis and single crystal X-ray analysis. Single crystal structure analysis revealed that PHNO exist in quinoid form which was supported by its EPR silence and clear NMR spectrum with two sharp singlets at 7.40 and 1.68 ppm. The UV-Vis spectrum of PHNO in DCM showed the broad absorption at 403 nm due to quinoid form. The BPNO and TPNO were synthesized in two steps from corresponding 4,4'-dibromobiphenyl and 4,4'-

dibromoterphenyl, respectively. As shown in Scheme 1a in the first step the dibromo derivatives were lithiated with *n*-BuLi at –78 °C followed by addition of 2-methyl-2-nitrosopropane (*t*-BuNO) dimer, which gave bishydroxylamine (**1** or **2**). In second step oxidation of bishydroxylamine with Ag_2O in DCM afforded the desired product BPNO or TPNO. The Suzuki coupling reaction of 2,7-diiodo-4,5,9,10-tetramethoxypyrene (**3**) and 4-(*tert*-butyl(*tert*-butyldimethylsilyloxy)-amino)phenyl-boronicacid (4PBA) gave the *tert*-butyldimethylsilyl protected bis(N-(*tert*-butyl)-N-phenylhydroxylamine) (**4**). The deprotection of the silyl group and subsequent oxidation of the obtained bishydroxylamine yielded BPTMP.[29-31]

7.3 Optical Properties

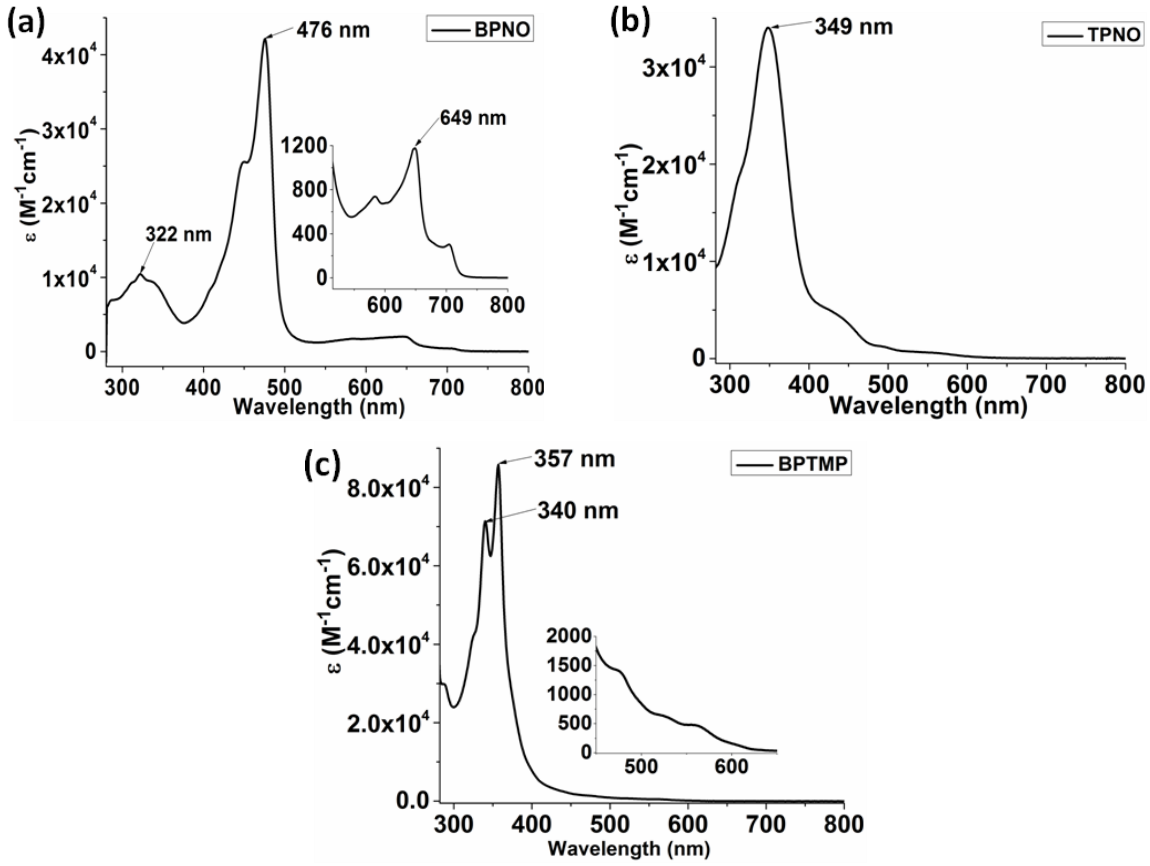

Figure 7.4: UV-Vis spectra of (a) BPNO (b) TPNO, and (c) BPTMP at room temperature in toluene.

The UV-Vis spectra of BPNO and TPNO recorded in toluene at room temperature were completely different (Figure 7.4). While the TPNO showed typical polyphenylene absorption at 349 nm with shoulder at 430 nm due to n—π* transition of *tert*-butylaminoxyl radical moiety, the BPNO displayed biphenyl absorption at 322 nm along with additional very strong absorption at 476 nm and weak absorption at 649 nm. As it has been found in previous studies[27] the two additional absorption peaks in BPNO at 476 nm and 649 nm which were completely absent in TPNO can be assigned to the presence of partial quinoid form. The BPTMP exhibited the pyrene absorption peak at 357 nm and low intensity broad absorption shoulder due to n—π* transition of radical moiety between 450 nm to 650 nm. To probe into structural change with temperature, the BPNO in toluene was subjected to variable temperature (VT) UV-Vis measurements. Interestingly upon increasing the temperature the absorption peaks at 476 nm and 649 nm due to quinoid form were decreased and the absorption peak at 322 nm corresponding to benzenoid biphenyl core increased (Figure 7.5).

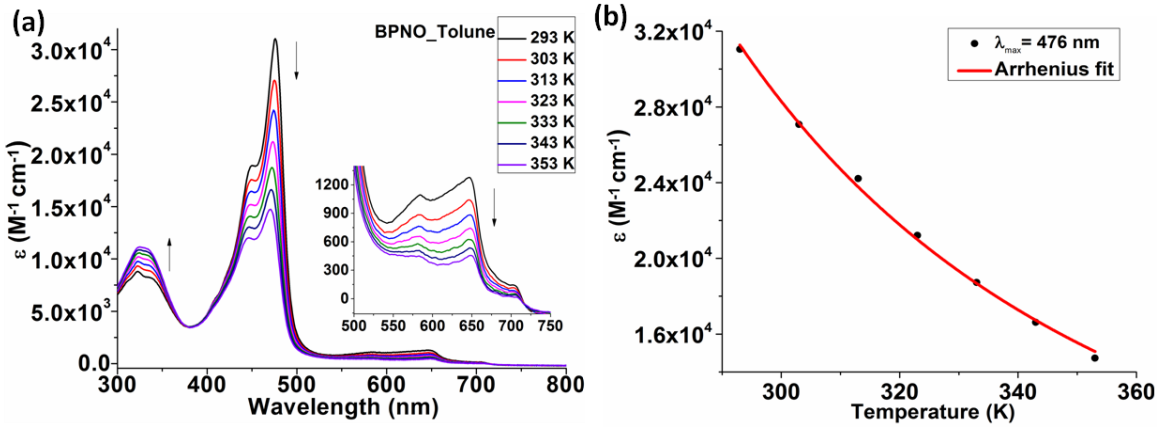

Figure 7.5: (a) Variable temperature UV-Vis spectra of BPNO in toluene, (b) change in absorption maxima (black dot) at 476 nm and Arrhenius fit (red line).

The hyperchromic shift of absorption band at 476 nm with temperature was analyzed applying the Arrhenius equation.

$$Arrhenius\ Equation, \qquad k_{eq} = \mathrm{A}\exp\left(-\frac{\Delta E_a}{k_B T}\right) \qquad \textbf{7-1}$$

Where k_{eq} is the equilibrium constant, ΔE_a is the energy gap between quinoid structure and benzenoid structure, and k_B is the Boltzmann constant. The best Arrhenius fit gave the activation energy of 2.5 kcal/mol for the structural transformation from benzenoid to semi-quinoid form (and vice-versa, Scheme 7.2).

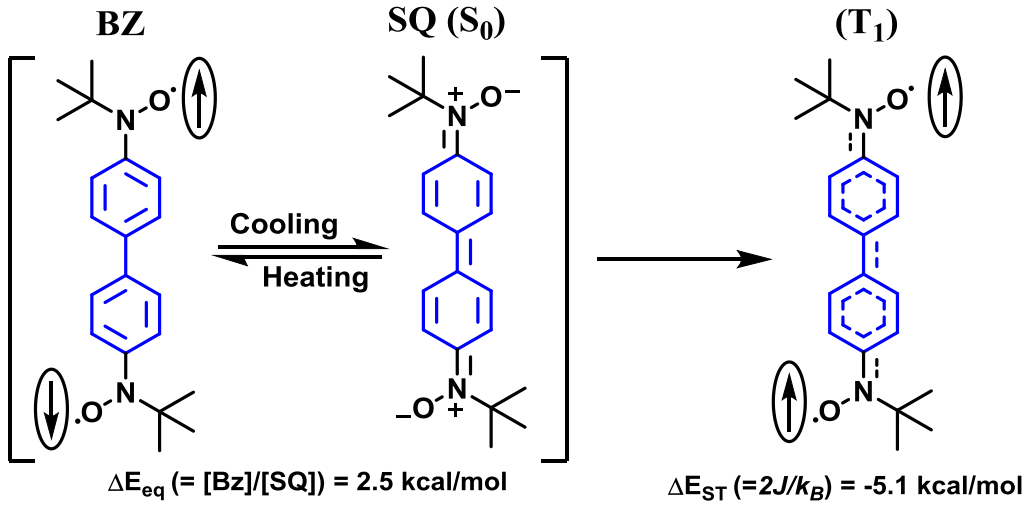

Scheme 7.2: Structural transformation with temperature.

7.4 EPR spectroscopy

The TPNO and BPTMP in toluene at room temperature gave typical five line EPR spectra for the biradical possessing two aminoxyl radical moieties (Figure 7.6a & 7.6b). The EPR spectra can be reproduced by spectral simulation considering two equivalent nitrogen hyperfine coupling constants $a_N/2$ = 6.225 G at g = 2.0065 for TPNO and $a_N/2$ = 5.948 G at g = 2.0058 for BPTMP. This demonstrates the exchange interaction between radical moieties are much larger than the hyperfine coupling $J >> a_N$.[32] In contradiction to this, the room temperature (293 K) EPR spectrum of BPNO in toluene appeared more alike mono radical species consisting of low intensity three lines with tiny shoulders in

between as shown in Figure 7.6c. When this toluene solution of BPNO was subjected to VT EPR measurement these tiny shoulders became more predominant with increasing the temperature. Notably at 333 K clear five line spectrum for biradical was observed which became more prominent at 353 K. The detected spectrum at 353 K was recreated with spectral simulation taking two equivalent nitrogen hyperfine coupling constant $a_N/2$ = 6.250 G at g = 2.0067 (Figure 7.6d). The temperature dependent process was reversible as upon cooling the sample to 293 K the spectrum reached back to its previous position. The initially observed three line low intensity spectrum at room temperature may arise from the trace amount of mono radical impurity.

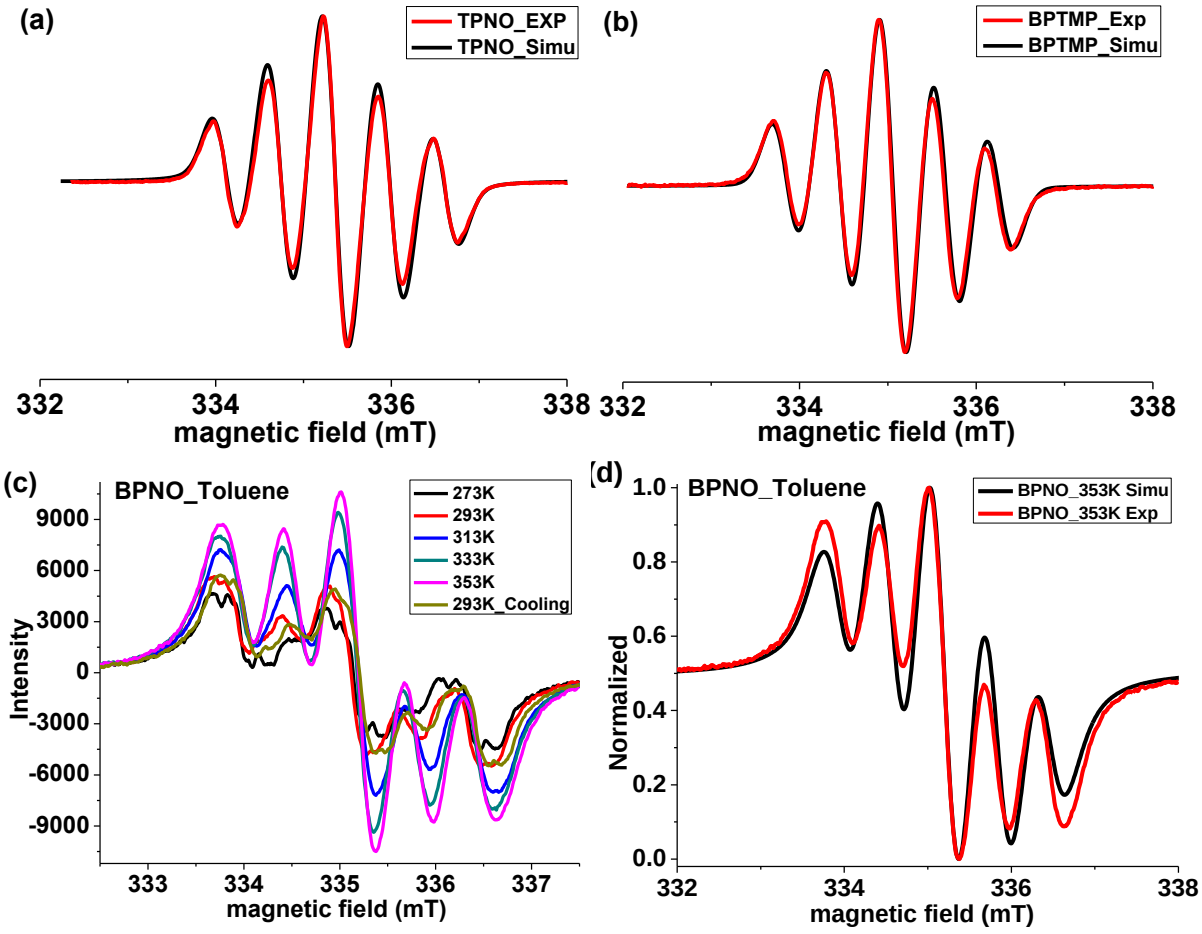

Figure 7.6: Experimental and simulated EPR spectra of (a) TPNO and (b) BPTMP in toluene at room temperature. (c) Variable temperature EPR spectra of BPNO in toluene. (d) Experimental and simulated EPR spectra of BPNO at 353 K in toluene.

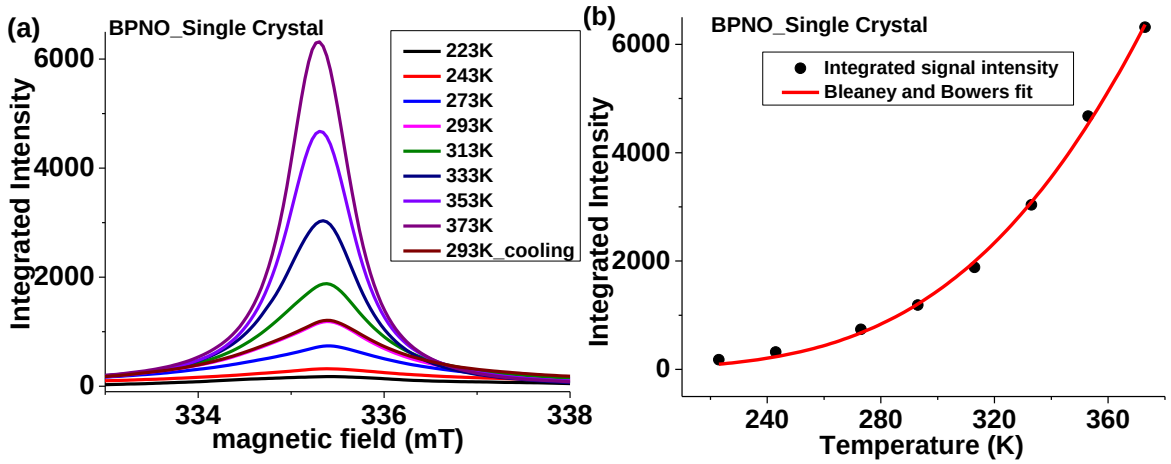

Figure 7.7: (a) Integrated EPR spectra of single crystalline BPNO at different temperature and (b) change in integrated signal intensity with temperature (black dot) and Bleaney and Bowers fit (red line).

Furthermore a single crystal of BPNO was EPR active indicating that the sample is not in complete quinoid form in solid state (Figure 7.7a). Notably with raising the temperature the signal intensity increased significantly showing inverse Curie like behavior thereby enhancing the paramagnetic content. The increased signal intensity with temperature can be imputed to enhanced population of the triplet state. This is in accordance with the VT EPR and UV-Vis measurements in toluene which showed the increase in biradical nature of BPNO with raising the temperature. The temperature dependence of EPR signal intensity was analyzed using the Bleaney and Bowers equation 7-2,[33]

$$I = 3(C/T)exp(-\frac{\Delta E_{ST}}{k_B T})/(1 + 3exp\left(-\frac{\Delta E_{ST}}{k_B T}\right)) \qquad \textbf{7-2}$$

The estimated singlet-triplet energy gap was as large as –5.1 kcal/mol. Therefore very strong antiferromagnetic exchange interactions are operating between two radical moieties in BPNO. Because of the large singlet-triplet energy gap very small population of triplet state occurs at room temperature which is in concomitance with the low intensity EPR spectrum in toluene at room temperature. All these experimental results led to the

inference that BPNO exist in semi-quinoid form and exhibits structural transformation with temperature. While at low temperature it shows more quinoid character at higher temperature it stabilizes in biradicaloid form (Scheme 7.2). To collect more information about the structure of these molecules the single crystals were obtained and their structures compared.

7.5 Crystal structure analysis

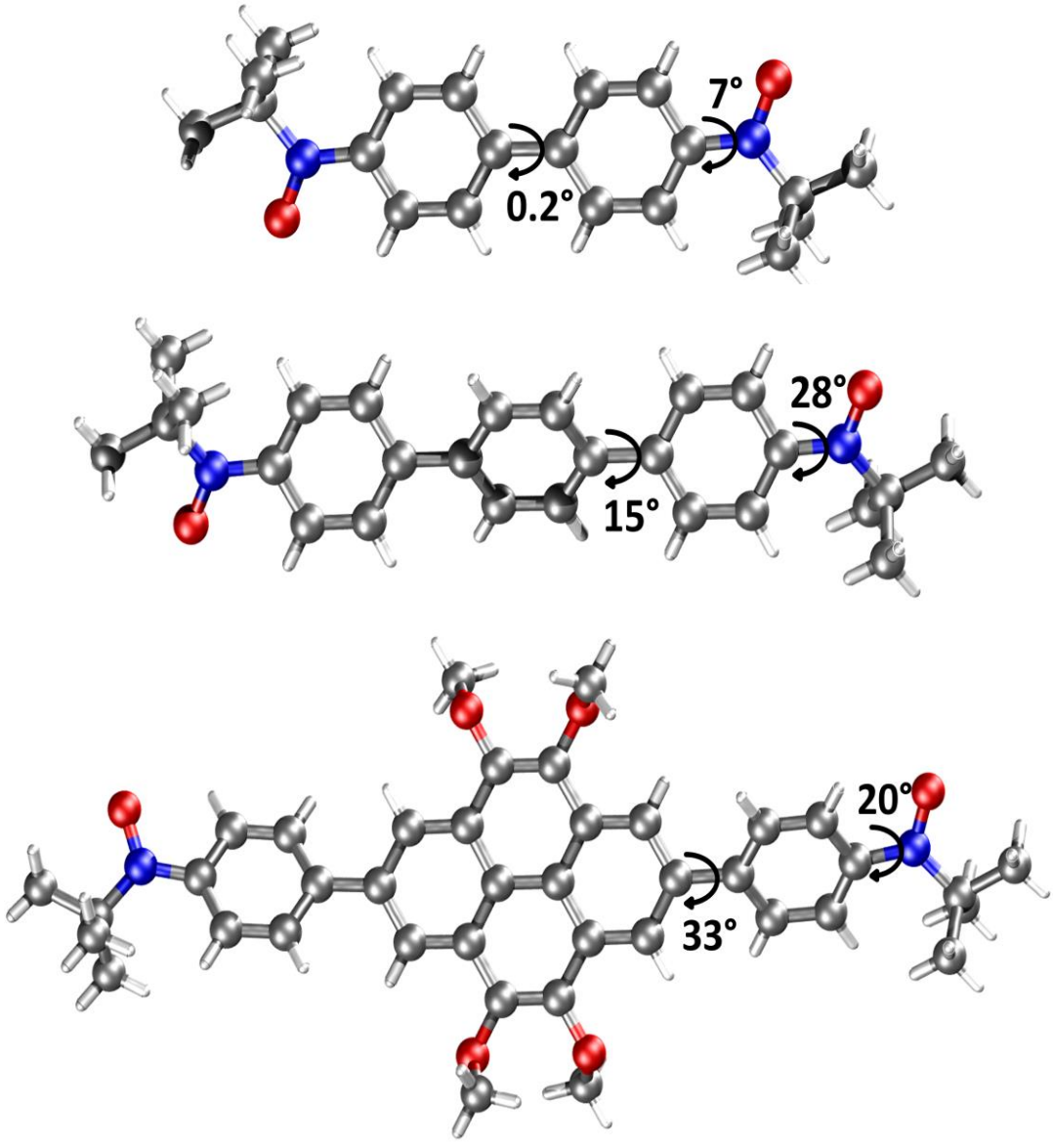

Figure 7.8: Single crystal structure of (a) BPNO (b) TPNO, and (c) BPTMP.

The crystal structure analysis is a vital requirement to get an insight into structure of molecules under study. Good quality crystals were grown by slow diffusion of hexane to the solution of samples in DCM. Single crystals were analyzed using single crystal X-ray diffraction method. For comparison purpose the single crystal structure for PHNO was obtained from CCDC on request. Crystal structure analysis of PHNO indicated the presence of two independent molecules (PHNO1 and PHNO2) in an asymmetric unit. Although the bond lengths and dihedral angles differ slightly, both the molecules showed alternating C—C bond lengths where the aminoxyl group was in plane with the benzene ring. The N—O bond was slightly elongated and C—N bond was shortened (Table 7.1) in comparison with typical C—N (1.41 Å) and N—O (1.27 Å) bond lengths in phenyl aminoxyls. Thus, the structure of PHNO was concluded as the one of the quinoid form. So far the UV-Vis and EPR analysis indicated that while TPNO and BPTMP are in complete biradicaloid form, the BPNO exist in semi-quinoid form. Thus, it was intriguing to compare the crystal structure of BPNO with completely quinoid form PHNO and wholly biradicaloid form TPNO (or BPTMP). Crystal structure analysis of TPNO and BPTMP revealed that the C—N bond length was larger (distinctive of C—N single bond) in comparison to PHNO. The C—C bond lengths were of the order of typical C—C bond of phenylenes. The aminoxyl radical moiety formed dihedral angle of 28° and 20° with respect to the phenyl ring in TPNO and BPTMP, respectively (Figure 7.8). The dihedral angle between central and terminal phenyl rings of TPNO was 15°. Crystal structure analysis of BPNO indicated that the two phenyl rings were nearly co-planar with each other (dihedral angle 0.2°) and the aminoxyl group was slightly deviated from the plane of phenyl ring with dihedral angle of 7°. The C—N bond length in BPNO was larger than the PHNO but comparable to TPNO and BPTMP. The C—C bond length (1.458 Å) between two phenyl ring of BPNO was comparable to Tschitschibabin's HC (1.448 Å) but slightly shorter in comparison with TPNO (1.481 Å). Further the major difference in the structure of BPNO and TPNO came from the planarity of phenyl ring with respect to each other and the planarity of aminoxyl group with respect to the phenyl ring. The planarity of phenyl rings and aminoxyl group in BPNO gives better overlap of π-orbitals in comparison to TPNO. Thus even though the

bond lengths are comparable in BPNO and TPNO, the BPNO exist in semi-quinoid form owing to the exceptional planarity.

Table 7.1: Selected bond lengths and bond angles.

	PHNO1	PHNO2	BPNO	TPNO	BPTMP
bond lengths (Å)					
N1—O1	1.291	1.287	1.284	1.290	1.272
N1—C1	1.354	1.362	1.411	1.413	1.422
C1—C2	1.423	1.417	1.406	1.401	1.399
C2—C3	1.362	1.358	1.380	1.387	1.399
dihedral angle (°)					
O1—N1—C1—C2	1.2	3.4	7.0	28.0	20.3

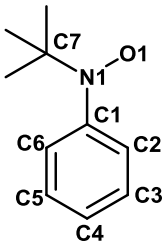

7.6 DFT Calculations

To examine the biradical character of ground state (S_0) of molecules HF and DFT calculations were performed using the crystal structure geometries.[34] Initially the degree of biradical character (y) was predicted by simple two-electron two-orbital model using the occupation numbers of the unrestricted non-bonding orbitals (UNOs) of UHF/6-31g(d, p) as proposed by Kamada *et al*.[35-36] The biradical character y obtained from these calculations has value between 0 and 1, which corresponds to closed shell and pure biradical system, respectively.

$$y = 1 - \frac{4\,(\sigma_{HOMO} - \sigma_{LUMO})}{4 + (\sigma_{HOMO} - \sigma_{LUMO})^2} \qquad \textbf{7-2}$$

The theoretical value of y can be calculated from the occupation numbers of frontier orbitals, σ_{HOMO} and σ_{LUMO}, using the equation shown above. The estimated values of degree of biradical character, y, for Thiele's and Tschitschibabin's HC are 0.31 and 0.72, respectively, which clearly indicates that while the former has closed shell structure the latter has more biradicaloid structure but relatively lower than the ideal biradical

system. In a similar way the degree of biradical character increases on moving from PHNO to TPNO (Table 7.2). TPNO which showed the clear biradical EPR spectrum at room temperature has biradical character (0.99) close to the theoretical value (1.00) of pure biradical system. This also shows the precision of this method for calculating the biradical character. Notably, although having a similar axial spin distance, the Tschitschibabin's HC possesses the lower degree of biradical character compared to BPNO.

The broken symmetry DFT approach proposed by Noodleman *et al.* was employed to evaluate the energy difference between ground state (S_0) and triplet state (T_1).[37] The singlet-triplet energy gap was calculated with the generalized spin projection method suggested by Yamaguchi *et al*.[38-40],

$$\Delta E_{ST} = \frac{\left(E(BS) - E(T)\right)}{\left(S^2(T) - S^2(BS)\right)} * 2 \qquad \textbf{7-3}$$

where E(BS) and E(T) are the energies of the broken symmetry singlet and triplet state, respectively, and S^2 are the Eigenvalues of the spin operator for these states. As shown in Table 2 the triplet T_1 state is always higher in energy than the singlet S_0 state. The S^2-values of BS calculation converge to zero for the closed shell structures Thiele's HC and PHNO. Interestingly, the S^2-values of BS-solution for pure biradicals TPNO and BPTMP are 0.98 and 1.00, respectively, as anticipated for singlet ground state biradicals, and do not converge to zero but close to one for Tschitschibabin's HC (S^2 = 0.81) and BPNO (S^2 = 0.76). This designates the S_0 state of Tschitschibabin's HC and BPNO as open shell singlet. The singlet-triplet energy difference decreases rapidly with increasing the length of the π-spacer. The calculated singlet-triplet energy gap for BPNO using BS-DFT calculations (–4.9 kcal/mol) is well in accordance with the estimated value (–5.1 kcal/mol) from the VT EPR measurement. The T_1 state population obtained using Boltzmann distribution and the energy gaps are 0.06% and 0.0004% for BPNO and Tschitschibabin's HC, respectively.

Table 7.2: Summary of DFT calculations.

Molecule	E, eV (Triplet)	S^2 (triplet)	E, eV (BS-Singlet)	S^2 (BS)	ΔE_{ST}, kcal/mol	Biradical character (y)[c]
Thiele's HC	–3566.36324	2.023	–33567.5810	0.00	–27.75[a]	0.31
Tschitschibabin's HC	–39836.20305	2.039	–39836.41784	0.81	–8.11[a]	0.72
PHNO1	–21927.01325	2.003	–21927.67049	0.00	–15.16[b]	0.60
PHNO2	–21928.54546	2.000	–21929.24631	0.00	–16.16[b]	0.57
BPNO	–28209.51581	2.006	–28209.6485	0.76	–4.91[b]	0.85
TPNO	–34494.35992	2.008	–34494.37674	0.98	–0.75[b]	0.99
BPTMP	–57379.63065	2.008	–57379.63317	1.00	–0.12[b]	-

[a]calculated at UB3LYP/6-31g(d) level, [b]calculated at UBLYP/6-31g(d) level, [c]calculated at UHF/6-31g(d, p) level.

To get an additional insight into the nature of open shell compounds, the frontier molecular orbitals were investigated. As shown in Figure 7.9 the singly occupied molecular orbitals calculated at BS-UB3LYP/6-31g(d) level for Tschitschibabin's HC and BS-UBLYP/6-31g(d) level for BPNO, TPNO, and BPTMP.[41-42] For the pure biradical system TPNO and BPTMP the SOMOs are confined on either half of the molecule with nearly no overlap between them. As the two unpaired electrons in two SOMOs reside on different part of the molecule, TPNO and BPTMP can be classified as singlet disjoint biradicals.[43-44] In contrast, the SOMOs of Tschitschibabin's HC and BPNO are no longer confined separately but overlap at the center of the molecules which takes them little away from the class of the disjoint singlet biradicals. Interestingly while the spin density of triplet state is highly delocalized in Tschitschibabin's HC and BPNO, it is more located on the radical moiety than the phenyl rings in TPNO. In case of BPTMP the triplet spin density is more localized on terminal phenyl ring and radical moiety, with only minor contribution at the pyrene core.

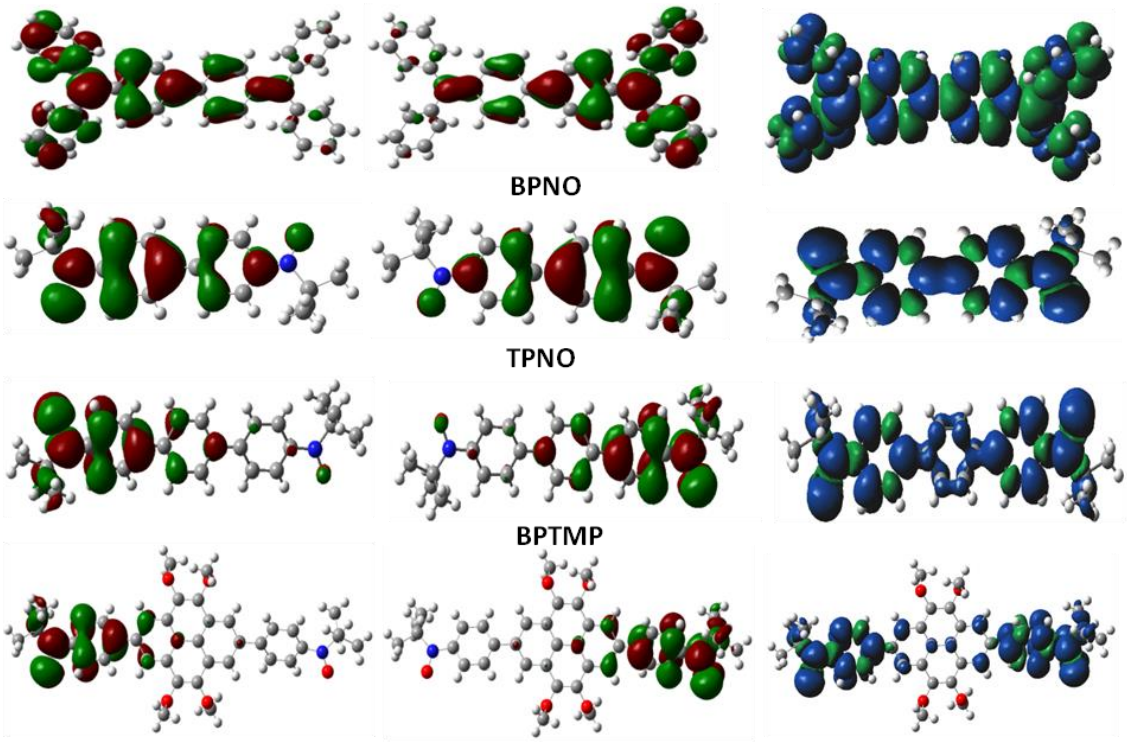

Figure 7.9: Calculated SOMOs of BS singlet and spin density distribution of triplet state.

7.7 Summary

In summary the serendipitous synthesis of BPNO, the open shell singlet semi-quinoid molecule, led us to dig the discrepancies related to Tschitschibabin's HC. For the better understanding of the transition from the purely quinoid to pure biradicaloid structure *via* the semi-quinoid form a series of molecules with extended π-bridge are compared and analyzed. While the longer extended molecules TPNO ($r_{N\text{-}N}$ = 1.43 nm) and BPTMP ($r_{N\text{-}N}$ = 1.84 nm) showed clear biradical features at room temperature with 5 line EPR spectra where $J >> a_N$, the BPNO ($r_{N\text{-}N}$ = 1.0 nm) is a borderline case best described as semi-quinoid. Combining all the theoretical and experimental results led to the inference that like BPNO the Tschitschibabin's HC also possess the semi-quinoid structure with very

strong antiferromagnetic exchange interactions. Because of this very small population of triplet state (< 0.1%) occurs leading to weak intensity triplet EPR spectrum which can be masked under even ~ 0.1% impurity of monoradical species thereby giving doublet like spectrum at room temperature. Furthermore the poor stability of Tschitschibabin's HC under ambient conditions may not allow its unquestionable spectroscopic analysis at elevated temperature as there is possibility of thermal decomposition. The exceptional stability of BPNO permitted its analysis by UV-Vis and EPR at higher temperatures. The VT EPR measurements clearly showed that the small population of triplet state becomes significant at higher temperature. Therefore, in conclusion alike BPNO the Tschitschibabin's HC can also be classified as the new class of molecules which exist in semi-quinoid form and exhibit the property of biradical and quinoid form simultaneously. Moreover these analyses can help in the better understanding of the biradical character of recently pushed search for singlet open shell polyaromatic HCs.

7.8 Synthetic Details

N-(4-Bromophenyl)-N-(*tert*-butyl)-O-(*tert*-butyldimethylsilyl)hydroxylamine

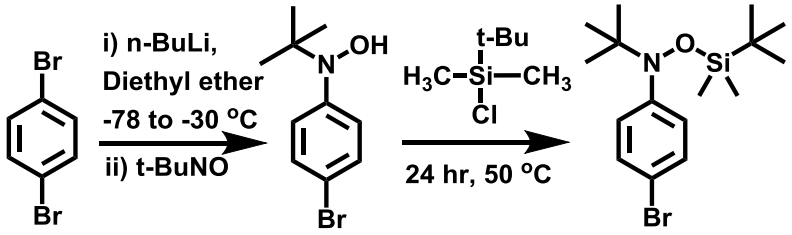

To a solution of 1,4-dibromobenzene (500 mg) in 5 ml diethyl ether, 1.3 ml 1.6 M *n*-BuLi hexane solution was added drop wise at –78 °C and stirred for 2 hour at same temperature. The mixture was gradually warmed to –30 °C and further stirred for 1.5 hour. To the resulting mixture was added the solution of 277 mg *tert*-BuNO dimer in 3 ml diethyl ether drop wise at –78 °C, stirred for 2 hour and warmed to room temperature. The mixture was hydrolyzed with aqueous ammonium chloride. Organic layer was separated washed with water and brine and dried over $MgSO_4$. Solvent was removed under vacuum and residue used as it is for next step without any purification. To the dried round bottom flask containing *tert*-butyldimethylchlorosilane and imidazole, solution of hydroxyl amine in 2.5 ml dry DMF added and mixture heated at 50 °C for 24 hour under argon atmosphere. After completion of reaction the resulting product was poured into water and extracted with hexane. The crude product was purified on silica gel column using hexane as eluent. Yield 73% in two steps. MS-FD= 479.9 (100%).^{1}H NMR (250 MHz, $CDCl_3$) δ 7.36, 7.32, 7.26, 7.14, 7.11, 1.05, 0.88, 0.01.

(4-(*Tert*-butyl((2,3,3-trimethylbutan-2-yl)oxy)amino)phenyl)boronic acid (4PBA)

0.9 ml (1.1 equivalent) 1.6 M solution of *n*-BuLi in hexane was added drop wise to the solution of N-(4-bromophenyl)-N-(*tert*-butyl)-O-(*tert*-butyldimethylsilyl)hydroxyl-amine (450 mg) in 8 ml THF under argon at –78 °C. Reaction mixture was stirred for 3

hour at same temperature and then 0.36 ml triisopropyl borate was added, stirring continued overnight and allowed to warm to room temperature. To the resulting product aqueous ammonium chloride solution was added and stirred further for 1 hour. Organic layer was separated and aqueous portion extracted with diethyl ether. Combined organic layer was washed with brine dried over $MgSO_4$. Crude product was purified by column chromatography over silica gel using hexane: ethyl acetate (100:20) as eluent. Product slowly converts to its trimer as shown in scheme below. The mixture of trimer and monomer used for Suzuki coupling reaction. Yield 76%. MS-FD= 915.6 (100%) (Trimer).

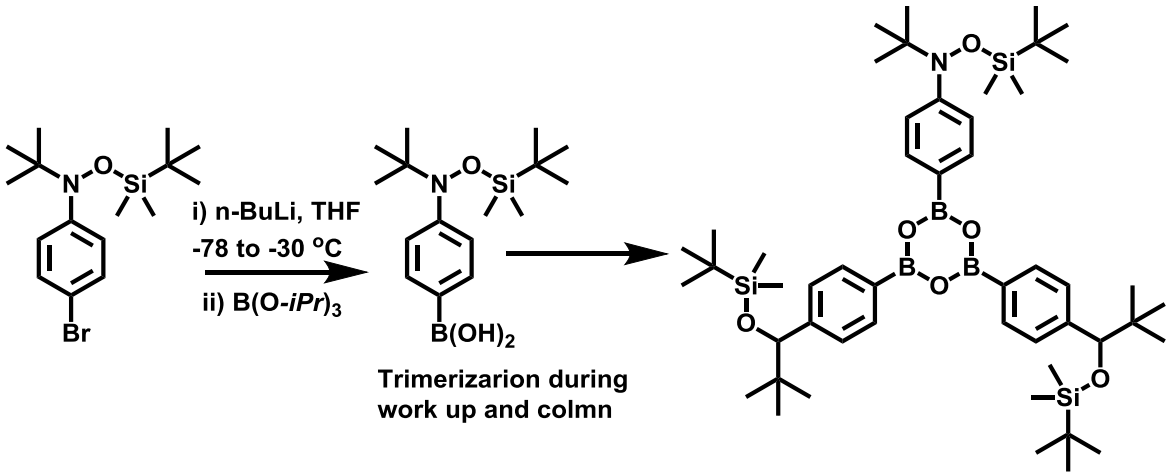

N,N'-([1,1'-Biphenyl]-4,4'-diyl)bis(N-oxy-*tert*-butylamine) (BPNO)

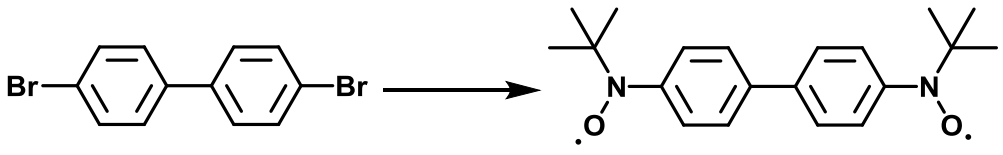

BPNO

To a solution of 4,4'-dibromo-1,1'-biphenyl (200 mg, 0.64 mmol) in 5 ml THF, 2.2 equivalent 1.6 M *n*-BuLi hexane solution was added drop wise at −78 °C and stirred for 1 hour at the same temperature. The mixture was gradually warmed to room temperature over the period of 2 hour and further stirred for 30 min. To the resulting mixture, the

solution of 2-methyl-2-nitrosopropane (*t*-BuNO) dimer (3 equivalents) in 2 ml THF was added drop wise at –78 °C, continued stirring for 2 hour and warmed to room temperature. The reaction mixture was hydrolyzed with aqueous ammonium chloride. Organic layer was separated washed with water and brine and dried over $MgSO_4$. Solvent was removed under vacuum and residue was used as it is for the next step without any purification. To the slurry of crude product in 20 ml DCM, 300 mg of Ag_2O was added and stirred for 3 hour under argon. The reaction mixture was filtered through celite and the solvent was evaporated, the residue was purified by alumina column using hexane:ethylacetate (100:10) as eluent. Yield 60 mg of BPNO (29% in two steps). MS-FD= 325.9 (100%), λ_{max} (ε, M^{-1} cm^{-1}) 322 (1.04 X 10^4), 476 (4.2 X 10^4), 649 (1171). **EPR** (353 K, 10^{-4} M in toluene): five lines, g_{iso} = 2.0067, $a_N/2$ = 6.250 G.

N,N'-([1,1':4',1''-Terphenyl]-4,4''-diyl)bis(N-oxy-*tert*-butylamine) (TPNO)

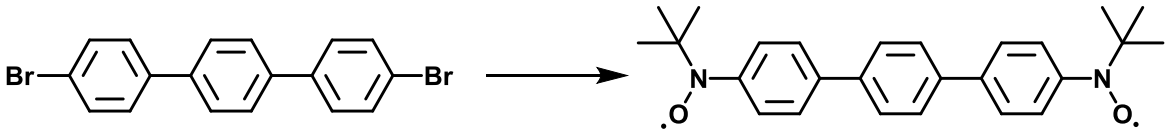

TPNO

To a solution of 4,4''-dibromo-1,1':4',1''-terphenyl (100 mg, 0.26 mmol) in 40 ml THF, 2.2 equivalent 1.6 M *n*-BuLi hexane solution was added drop wise at –78 °C and stirred for 1 hour at same temperature. The mixture was gradually warmed to room temperature over the period of 2 hour and further stirred for 30 min. To the resulting mixture the solution of 2-methyl-2-nitrosopropane (*t*-BuNO) dimer (3 equivalent) in 2 ml THF was added drop wise at –78 °C, continued stirring for 2 hour and warmed to room temperature. The reaction mixture was hydrolyzed with aqueous ammonium chloride. Organic layer was separated, washed with water and brine and dried over $MgSO_4$. Solvent was removed under vacuum and residue used as it is for next step without any purification. To the slurry of crude product in 40 ml DCM, 200 mg of Ag_2O was added and stirred for 3 hour under argon. The mixture was filtered through celite and solvent

evaporated, the residue was purified by alumina column using hexane:ethylacetate (100:25) as eluent. Yield 25 mg of TPNO (24% in two steps). MS-FD= 402.4 (100%). $\boldsymbol{\lambda_{max}}$ (ε, M^{-1} cm^{-1}) 349 (3.4 X 10^4). **EPR** (298 K, 10^{-4} M in toluene): five lines, g_{iso} = 2.0065, $a_N/2$ = 6.225 G.

N,N'-((4,5,9,10-Tetramethoxypyrene-2,7-diyl)bis(4,1-phenylene))bis(N-oxy-*tert*-butylamine) (BPTMP)

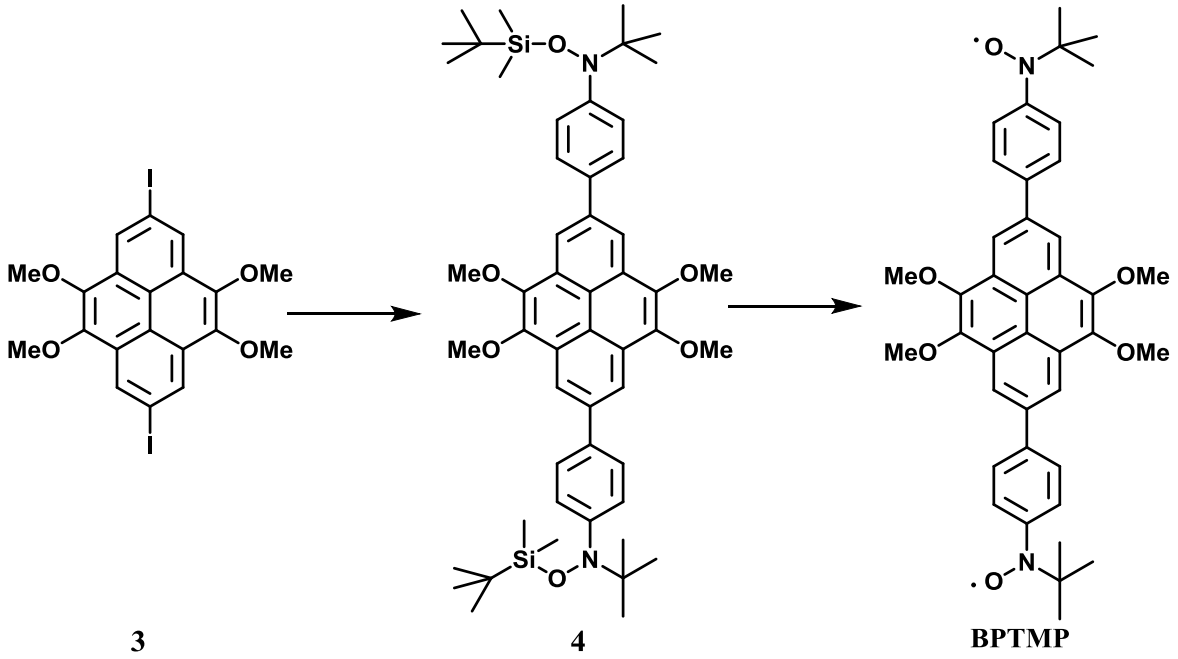

To the oven dried Schlenk flask 2,7-diiodo-4,5,9,10-tetramethoxypyrene (100 mg, 0.17 mmol) and 4-(*tert*-butyl(*tert*-butyldimethylsilyloxy)-amino)phenylboronic acid (140 mg, 2.5 equivalent) were dissolved in 16 ml toluene. To the resulting mixture aqueous solution of Na_2CO_3 (83 mg in 6 ml H_2O) added and mixture was bubbled with argon for 30 min, then 5 mol% $Pd(PPh_3)_4$ was added and the resulting solution heated at 83 °C for 20 hour. The reaction mixture was cooled to room temperature and washed with water. The organic layer was separated, and solvent was removed under vacuum. The crude intermediate product **4** was obtained in quantitative yield characterized by FD mass and used as it is for next step. **MS-FD** (8 kV, CH_2Cl_2) m/z: found 877.3 (100%).

The crude product **4** was dissolved in 15 ml THF. The conc. HCl (1.2 ml) was added and the reaction mixture stirred at room temperature for overnight under argon. The reaction mixture was poured into 10 ml H_20 and the precipitate formed were filtered, dried and used immediately for next step. The precipitate and excess of Ag_2O (200 mg) were dispersed in 30 ml DCM and stirred at room temperature for 3 hour under argon. The solution passed through celite, and the solvent was removed under vacuum. The crude product was purified by column chromatography using 1:1 (hexane:DCM) as eluent. Yield 40 mg (39% in three steps). **MS-FD** (8 kV, CH_2Cl_2) m/z: found 646.6 (100%). $\boldsymbol{\lambda_{max}}$ (ε, $M^{-1}\,cm^{-1}$) 357 (8.6 X 10^4). **EPR** (298 K, 10^{-4} M in toluene): five lines, g_{iso} = 2.0058, $a_N/2$ = 5.948 G.

7.9 References

[1] M. Gomberg, *J. Am. Chem. Soc.* **1900**, *22*, 757.

[2] A. E. Tschitschibabin, *Chem. Ber.* **1907**, *40*, 1810.

[3] T. Sugawara, M. M. Matsushita, *J. Mater. Chem.* **2009**, *19*, 1738.

[4] S. A. Wolf, D. D. Awschalom, R. A. Buhrman, J. M. Daughton, S. von Molnár, M. L. Roukes, A. Y. Chtchelkanova, D. M. Treger, *Science* **2001**, *294*, 1488.

[5] Y. Morita, S. Suzuki, K. Sato, T. Takui, *Nat. Chem.* **2011**, *3*, 197.

[6] Z. Sun, Z. Zeng, J. Wu, *Chem. Asian J.* **2013**, *8*, 2894.

[7] A. Shimizu, T. Kubo, M. Uruichi, K. Yakushi, M. Nakano, D. Shiomi, K. Sato, T. Takui, Y. Hirao, K. Matsumoto, H. Kurata, Y. Morita, K. Nakasuji, *J. Am. Chem. Soc.* **2010**, *132*, 14421.

[8] Z. Zeng, Y. M. Sung, N. Bao, D. Tan, R. Lee, J. L. Zafra, B. S. Lee, M. Ishida, J. Ding, J. T. López Navarrete, Y. Li, W. Zeng, D. Kim, K.-W. Huang, R. D. Webster, J. Casado, J. Wu, *J. Am. Chem. Soc.* **2012**, *134*, 14513.

[9] X. Zheng, X. Wang, Y. Qiu, Y. Li, C. Zhou, Y. Sui, Y. Li, J. Ma, X. Wang, *J. Am. Chem. Soc.* **2013**.

[10] A. Konishi, Y. Hirao, M. Nakano, A. Shimizu, E. Botek, B. Champagne, D. Shiomi, K. Sato, T. Takui, K. Matsumoto, H. Kurata, T. Kubo, *J. Am. Chem. Soc.* **2010**, *132*,

11021.

[11] D. C. Reitz, S. I. Weissman, *J. Chem. Phys.* **1960**, *33*, 700.

[12] L. K. Montgomery, J. C. Huffman, E. A. Jurczak, M. P. Grendze, *J. Am. Chem. Soc.* **1986**, *108*, 6004.

[13] H. M. McConnell, *J. Chem. Phys.* **1960**, *33*, 1868.

[14] H. Hartmann, H. D. Brauer, H. Schafer, *Zeitschrift Fur Physikalische Chemie-Frankfurt* **1968**, *61*, 119.

[15] H. D. Brauer, H. Stieger, H. Hartmann, *Zeitschrift Fur Physikalische Chemie-Frankfurt* **1969**, *63*, 50.

[16] F. Popp, F. Bickelhaupt, C. Maclean, *Chem. Phys. Lett.* **1978**, *55*, 327.

[17] H. M. McConnell, *J. Chem. Phys.* **1960**, *33*, 115.

[18] C. A. Hutchison, A. Kowalsky, R. C. Pastor, G. W. Wheland, *J. Chem. Phys.* **1952**, *20*, 1485.

[19] H. Stieger, H. D. Brauer, *Chem. Ber. Recl.* **1970**, *103*, 3799.

[20] Y. Kanzaki, D. Shiomi, K. Sato, T. Takui, *J. Phys. Chem. B* **2012**, *116*, 1053.

[21] H. D. Brauer, H. Stieger, J. S. Hyde, L. D. Kispert, Luckhurs.Gr, *Mol. Phys.* **1969**, *17*, 457.

[22] W. J. van der Hart, L. J. Oosterhoff, *Mol. Phys.* **1970**, *18*, 281.

[23] P. Ravat, Y. Ito, E. Gorelik, V. Enkelmann, M. Baumgarten, *Org. Lett.* **2013**, *15*, 4280.

[24] E. A. Mostovich, Y. Borozdina, V. Enkelmann, K. Remović-Langer, B. Wolf, M. Lang, M. Baumgarten, *Cryst. Growth Des.* **2012**, *12*, 54.

[25] B. Wolf, P. T. Cong, K. Remović-Langer, Y. D. Borozdina, E. Mostovich, M. Baumgarten, M. Lang, *J. Phys.: Conf. Ser.* **2010**, *200*, 012225.

[26] Y. B. Borozdina, E. Mostovich, V. Enkelmann, B. Wolf, P. T. Cong, U. Tutsch, M. Lang, M. Baumgarten, *J. Mater. Chem. C* **2014**, *2*, 6618.

[27] P. Ravat, Y. Teki, Y. Ito, E. Gorelik, M. Baumgarten, *Chem. Eur. J* **2014**, DOI: 10.1002/chem.201403338.

[28] S. Nakazono, S. Karasawa, N. Koga, H. Iwamura, *Angew. Chem. Int. Ed.* **1998**, *37*, 1550.

[29] S.-i. Kawano, M. Baumgarten, D. Chercka, V. Enkelmann, K. Müllen, *Chem. Commun.* **2013**, *49*, 5058.

[30] J. C. Stowell, *J. Org. Chem.* **1971**, *36*, 3055.

[31] R. J. Smith, R. M. Pagni, *J. Org. Chem.* **1981**, *46*, 4307.

[32] M. Shinomiya, K. Higashiguchi, K. Matsuda, *J. Org. Chem.* **2013**, *78*, 9282.

[33] B. Bleaney, K. D. Bowers, *Proc. R. Soc. London A* **1952**, *214*, 451.

[34] G. W. T. M. J. Frisch, H. B. Schlegel, G. E. Scuseria, M. A. Robb, J. R. Cheeseman, G. Scalmani, V. Barone, B. Mennucci, G. A. Petersson, H. Nakatsuji, M. Caricato, X. Li, H. P. Hratchian, A. F. Izmaylov, J. Bloino, G. Zheng, J. L. Sonnenberg, M. H A. F. Izmaylov, J. Bloino, G. Zheng, J. L. Sonnenberg, M. Hada,M. Ehara, K. Toyota, R. Fukuda, J. Hasegawa, M. Ishida, T. Nakajima, Y. Honda, O. Kitao, H. Nakai, T. Vreven, J. A. Montgomery, Jr., J. E. Peralta, F. Ogliaro, M. Bearpark, J. J. Heyd, E. Brothers, K. N. Kudin, V. N. Staroverov, R. Kobayashi, J. Normand, K. Raghavachari, A. Rendell, J. C. Burant, S. S. Iyengar, J. Tomasi, M. Cossi, N. Rega, J. M. Millam, M. Klene, J. E. Knox, J. B. Cross, V. Bakken, C. Adamo, J. Jaramillo, R. Gomperts, R. E. Stratmann, O. Yazyev, A. J. Austin, R. Cammi, C. Pomelli, J. W. Ochterski, R. L. Martin, K. Morokuma, V. G. Zakrzewski, G. A. Voth, P. Salvador, J. J. Dannenberg, S. Dapprich, A. D. Daniels, O. Farkas, J. B. Foresman, J. V. Ortiz, J. Cioslowski, and D. J. Fox., in *Gaussian 09*, Gaussian, Inc, Wallingford CT, **2009**.

[35] K. Kamada, K. Ohta, A. Shimizu, T. Kubo, R. Kishi, H. Takahashi, E. Botek, B. Champagne, M. Nakano, *J.Phys.Chem.Lett.* **2010**, *1*, 937.

[36] P. O. Dral, T. Clark, *J. Phys. Chem. A* **2011**, *115*, 11303.

[37] L. Noodleman, *J. Chem. Phys.* **1981**, *74*, 5737.

[38] K. Yamaguchi, F. Jensen, A. Dorigo, K. N. Houk, *Chem. Phys. Lett.* **1988**, *149*, 537.

[39] T. Soda, Y. Kitagawa, T. Onishi, Y. Takano, Y. Shigeta, H. Nagao, Y. Yoshioka, K. Yamaguchi, *Chem. Phys. Lett.* **2000**, *319*, 223.

[40] M. Shoji, K. Koizumi, Y. Kitagawa, T. Kawakami, S. Yamanaka, M. Okumura, K. Yamaguchi, *Chem. Phys. Lett.* **2006**, *432*, 343.

[41] A. D. Becke, *J. Chem. Phys.* **1993**, *98*, 1372.

[42] E. R. Davidson, D. Feller, *Chem. Rev.* **1986**, *86*, 681.

[43] W. T. Borden, H. Iwamura, J. A. Berson, *Acc. Chem. Res.* **1994**, *27*, 109.

[44] W. T. Borden, E. R. Davidson, *J. Am. Chem. Soc.* **1977**, *99*, 4587.

CHAPTER 8

POSITIVE MAGNETO-LC EFFECT IN CONJUGATED SPIN-BEARING HEXABENZOCORONENE

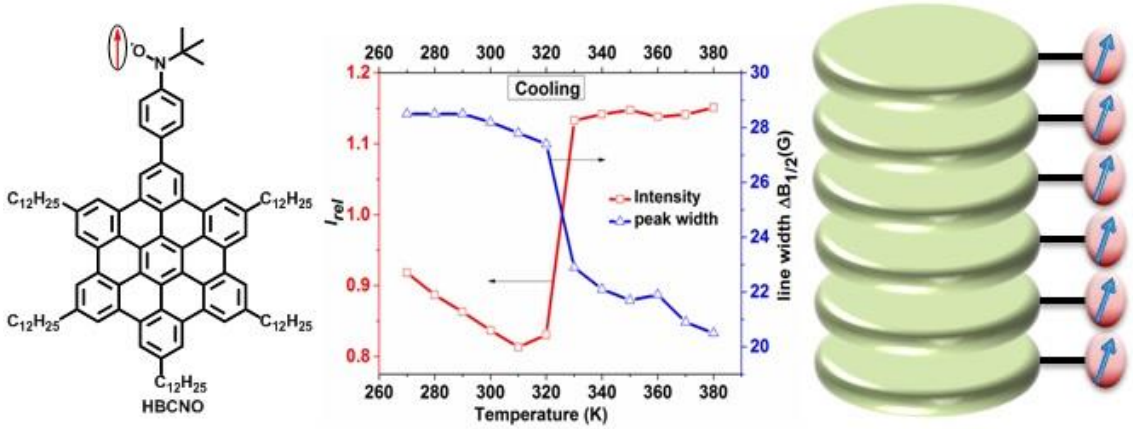

*The first neutral paramagnetic **HBC** derivative was synthesized and characterized. The phenyl nitroxide substituted **HBC** derivative with five alkyl chains was found to exhibit a positive magneto-LC effect in columnar hexagonal liquid crystalline phase, probed with EPR spectroscopy. At 140 K the $\Delta M_S = 2$ transition could be observed indicating the thermally accessible triplet state between the neighboring molecules in the columnar arrangements.*

Note: Large part of this chapter has been published in J. Am. Chem. Soc. 2014, 136, 12860-12863.

8.1 Introduction

Among the various discotics bearing large aromatic cores, hexa-*peri*-hexabenzocoronenes (**HBCs**), are extensively studied because of their assembly into stable columnar structures and promising electronic properties.[1] HBCs have been functionalized with various substituents in order to steer their electronic properties and device applications.[2-5] Earlier studies have shown that **HBCs** or arylamine substituted **HBCs** can be reduced or oxidized to their corresponding radical anions and cations respectively.[6-7] These radicals, however, could not be isolated as material in pure form owing to their limited stability and were only characterized by in-situ analysis with EPR and/or UV-Vis spectroscopy. The peculiar ability of **HBCs** to arrange into columnar superstructures may allow one-dimensional magnetic ordering. Therefore, it was intriguing to design a spin-bearing HBC derivative and study its magnetic behavior in different crystalline phases. Moreover higher conductivity through the columns could be expected in spin-bearing **HBCs** in comparison to their closed shell analogue because of the relatively high lying SOMO (singly occupied molecular orbital) and its delocalization into the aromatic core.[8-9] The recent study by Cammidge *et al*. showed that spin bearing discotic liquid crystalline materials can be used as the spin probe in the analysis of different phases of comparable discotics by EPR spectroscopy.[10]

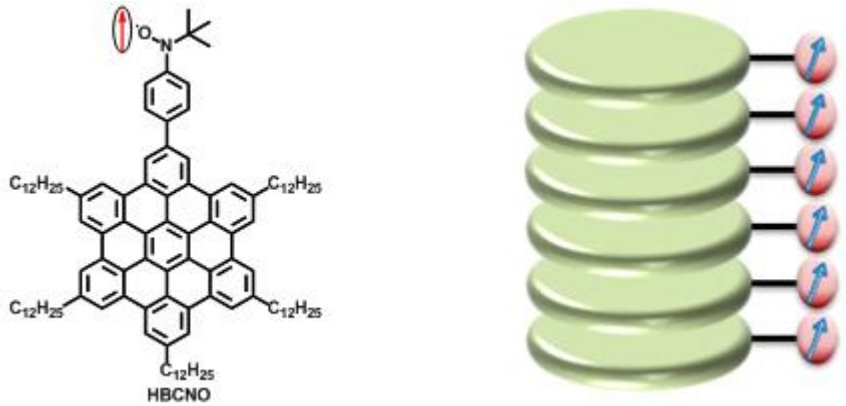

Figure 8.1: Structure of **HBCNO** (left) and schematic (right) representation of supposed arrangement of **HBCNO** molecule in columnar phase.

To synthesize the neutral paramagnetic HBC, the monoradical **HBCNO** (Figure 8.1) was designed. The *tert*-butyl nitroxide radical moiety was chosen as spin source because of its high stability and ability to delocalize SOMO over the poly aromatic core.

8.2 Synthesis of HBCNO

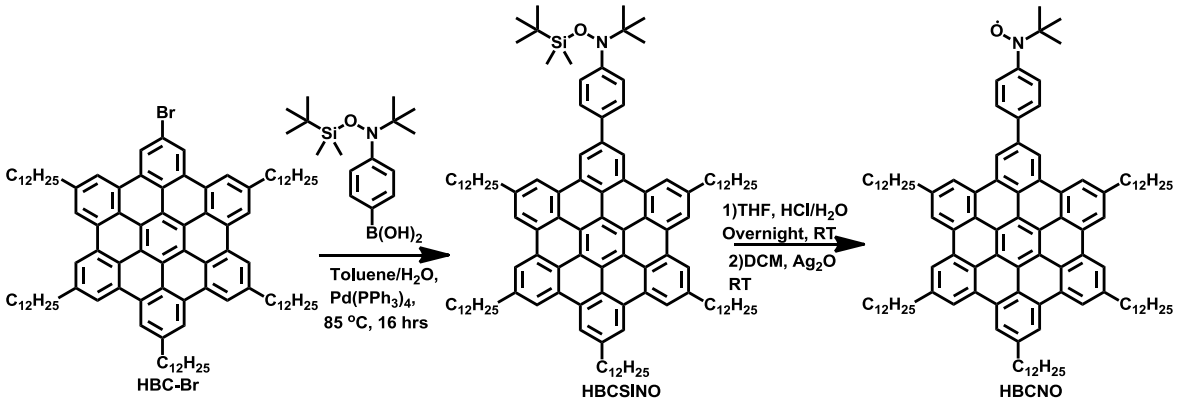

Scheme 8.1: Synthesis of **HBCNO**.

The starting material **HBC-Br** (2-bromo-5,8,11,14,17-pentadodecylhexabenzo-coronene) was synthesized according to literature procedures.[11-12] The *tert*-butyldimethylsilyl protected N-(*tert*-butyl)-N-phenylhydroxylamine was attached to **HBC** by Suzuki coupling reaction of **HBC-Br** with **4PBA** (4-(*tert*-butyl(*tert*-butyldimethylsilyloxy)amino)phenylboronic acid) giving **HBCSINO** in 70% yield. The deprotection of *tert*-butyldimethylsillyl with aqueous HCl gave hydroxyl amine in quantitative yield. Upon oxidation of hydroxyl amine with silver oxide the desired molecule **HBCNO** was obtained in 20% yield in two steps. **HBCNO** was purified using silica gel flash column chromatography using DCM:Hexane (1:1) as eluent. Slight decomposition of HBCNO was observed on silica gel so column should be performed quickly. The synthesized paramagnetic **HBCNO** was analyzed by mass, DSC, CV and UV-Vis absorption/emission spectroscopy. The magnetic behavior was monitored by EPR spectroscopy.

8.3 Thermotropic properties

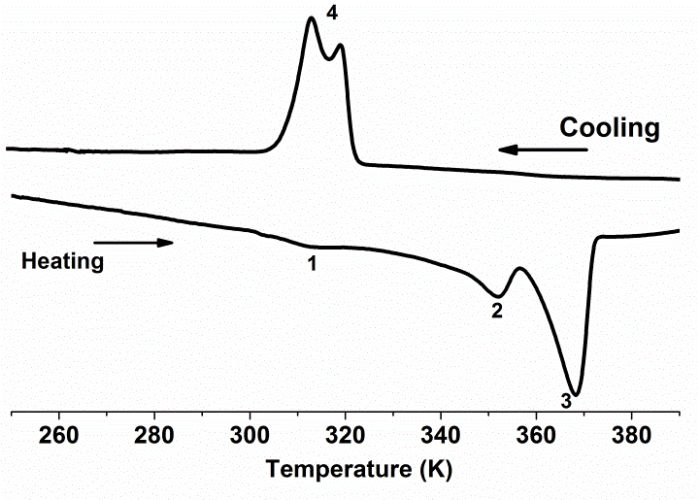

Figure 8.2: DSC plot of **HBCNO** (cooling and heating from 250 K to 390 K) at a rate of 5 K min^{-1}.

The phase transitions were identified by using differential scanning calorimetry (DSC) which exhibited three endothermic peaks during heating (Figure 8.2). The main peak (3) at 368 K is related to the transition from a well-ordered helical columnar to the liquid crystalline phase. The detailed phase assignment is based on the structural analysis below. The minor peak (2) at 352 K prior the phase transition could stem from a cold crystallization. The small and broad transition (1) at 314 K is due to the reorganization of the side chains during heating. Upon cooling, the phase transition back to the ordered helical phase was expressed as a broad double peak at 312 K. The broad peak during heating and cooling process indicates the extensive molecular rearrangement taking place during the conversion from one phase to another.

To precisely assign the phases of **HBCNO** obtained during the DSC scans, the organization in bulk was studied by two-dimensional wide-angle X-ray scattering (2DWAXS) (Figure 8.3a). The 2DWAXS measurements were performed by Dr. Tomasz Marszalek at MPIP. The structural investigation of the bulk supramolecular organization was performed on macroscopically aligned fibers prepared by mechanical extrusion. For

the measurements, the fibers were mounted vertically toward the two-dimensional detector which collected the scattered reflections. In our previous studies on discotic liquid crystals, this technique provided valuable information about the molecular arrangement and order within such superstructures.[13] The pattern of **HBCNO** recorded for the liquid crystalline phase at elevated temperatures exhibited a typical hexagonal columnar organization with non-tilted discs (Figure 8.3). In the small-angle region, three sharp equatorial reflections were observed which correspond to the Miller indices of *100*, *110*, and *200* for a hexagonal unit cell. The positions of the reflections are in the ratio of 1:√3:2 confirmed the hexagonal lattice with an inter-columnar parameter of a_{hex} = 2.95 nm (Figure 8.3b). Wide-angle reflections in the meridional plane were attributed to the non-tilted intra-columnar packing of the molecules from which a π-stacking distance of 0.35 nm for **HBCNO** was determined.

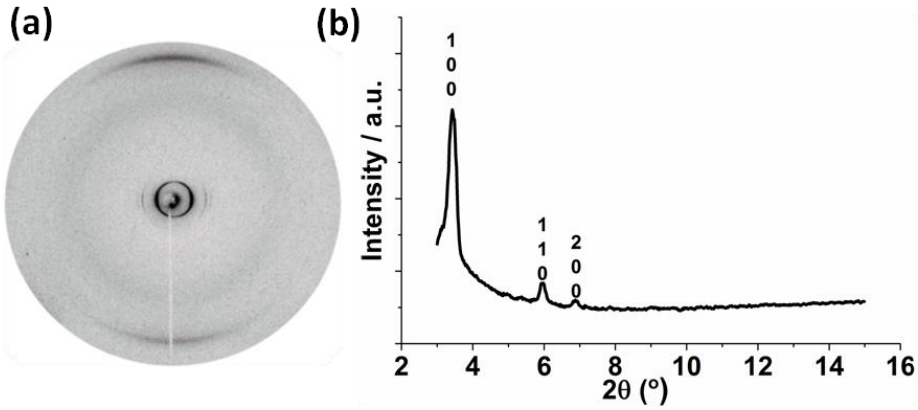

Figure 8.3: (a) 2DWAXS pattern of **HBCNO** (at 393 K) recorded in the liquid crystalline phase and (b) equatorial integration for **HBCNO** (reflections are assigned by Miller indices).

Upon cooling the compound back to the low temperature phase (255 K), the supramolecular ordering significantly changed as evident from a high number of new and distinct reflections indicating a highly ordered phase (Figure 8.4a). In this phase the hexagonal lattice was maintained, but the unit cell parameter decreased to a_{hex} = 2.55 nm. At the same time, the π-stacking distance of the discs increased to 0.37 nm as

determined from the most intensive wide-angle meridional reflection. Interestingly, additional meridional reflections in the wide–angle domain corresponding to d-spacings of 0.34 nm and 0.41 nm could be an evidence for a helical organization. From the even distribution of these meridional four reflections, a helical structure of 8 molecules was concluded, whereby the **HBCNO** molecules should be rotated by 45° towards each other (Figure 8.4c). Further reflections within the middle-range region related to the helical packing were missing. Cerius^2 simulations[14] in which a HBC core was applied, confirm the described model yielding an X-ray pattern with the three characteristic reflections on the wide-angle meridional plane (Figure 8.4b). The disordered alkyl chains and the phenyl nitroxide are neglected in this model for simplicity. The simulated pattern also verified that off-meridional reflections in the middle-range region were missing, which otherwise would be typical for helical columnar structures. Most probably the phenyl nitroxide group was tilted with respect to the plane of the HBC core inducing a rotation of neighbouring **HBCNO** discs and finally a helical arrangement within the columnar stack.

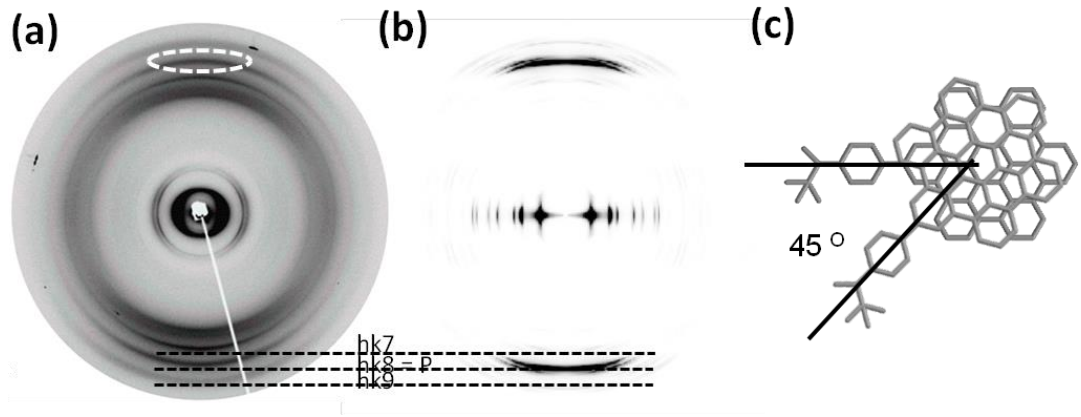

Figure 8.4: (a) 2DWAXS pattern of **HBCNO** recorded at 255 K in the low temperature state after annealing in the LC phase. The scattering lines are assigned by Miller indices (hkl for l = 7, 8, 9) and indicate a characteristic helical intra-columnar organization. The hkl is a periodic reflection (P) assigned to π-stacking interaction indicated by dashed circle. (b) Cerius^2 simulation for a model based on helically packed non-tilted HBC discs rotated by 45° towards each other leading to a helical repetition of 8 molecules, (c) schematic illustration in top view of non-tilted and 45° rotated **HBCNO** molecules.

Thus, the 2DWAXS measurements gave important information about the molecular arrangement in the low and higher temperature phases. While at higher temperature the typical columnar hexagonal liquid crystalline (Col_h) phase was observed, in the lower temperature range the HBCNO molecules preferred to arrange in helical hexagonal crystalline (Hel_h) phase.

8.4 EPR spectroscopic analysis

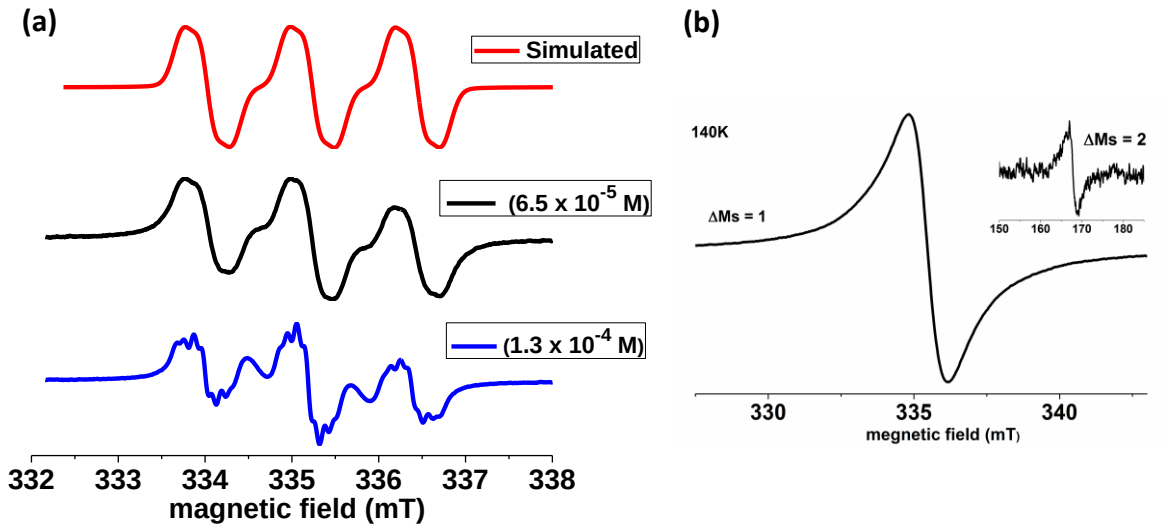

Figure 8.5: EPR spectra of **HBCNO** (a) at room temperature in toluene at different concentrations and the simulated spectrum, and (b) in solid state, $\Delta M_S = 1$ and $\Delta M_S = 2$ transitions at 140 K.

The solution EPR spectra of **HBCNO** were measured at room temperature in toluene at different concentrations. The diluted solution of **HBCNO** in toluene ($c \sim 10^{-5}$ M) yielded an EPR spectrum consisting of equally spaced 3 lines. The observed spectrum can be reproduced by spectral simulation considering *hfc* for one nitrogen a_N = 12.1 G and two equivalent protons a_H = 2 G at g-value 2.0068. Notably, at slightly higher concentration ($c \sim 10^{-4}$ M) the EPR spectrum was quite different and little alike a biradical species (Figure 8.5a). This spectral change was due to the dimerization/aggregation of **HBCNO** molecules even at concentrations as low as 10^{-4} M. When the EPR spectrum of a powder sample was measured at 140 K, a broad resonance band was observed for ΔM_S =

1 transition with no fine structure splitting. Interestingly, along with a $\Delta M_S = 1$ transition, at half field a forbidden $\Delta M_S = 2$ transition was also observed at a g-value 4.013 indicating the thermally accessible triplet state (Figure 8.5b).

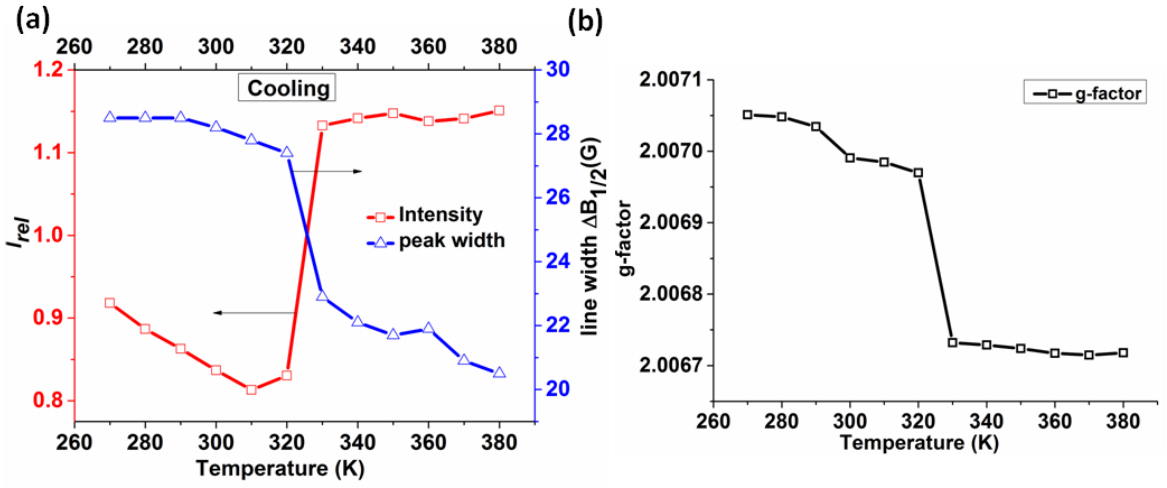

Figure 8.6: (a) Relative signal intensities and line widths, and (b) g-factor during the cooling process as a function of temperature between 270 K and 380 K.

Moreover EPR spectroscopy was found to be an excellent tool for probing the phase transition in spin bearing liquid crystals.[15-17] To obtain an insight into the change in magnetic interaction during phase transition, variable temperature (VT) EPR spectra of a powder sample were measured during the cooling process in the temperature range 380 K (Col_h phase) to 270 K (Hel_h phase) and the variation of g-value, line intensity and line width were plotted as a function of temperature. Very small changes in g-values from 2.0067 to 2.0070 were observed, indicating a minor variation in the orientation of the molecules during the transition from Col_h to Hel_h phase (Figure 8.6b). While the relative intensity and line width ($\Delta B_{1/2}$) remained nearly constant in the temperature range 380 K to 330 K, a sudden significant change of both parameters was observed at 320 K, i.e. at the onset of the phase transition (Figure 8.6a). A higher EPR signal intensity was detected in the Col_h phase as compared to the Hel_h phase indicating a positive magneto-LC effect ($J > 0$) in the Col_h phase. This was supported by 2DWAXS measurements which showed an enhanced π-stacking distance of the discs and the rotation of the **HBCNO** molecules

during the phase transition from Col_h to Hel_h. In the temperature range from 310 K to 270 K (Hel_h phase) the Curie law was obeyed, following the increase in intensity with decreasing temperature. The line width increased upon the phase transition from Col_h to Hel_h owing to the decrease in spin relaxation time. The increase of the line width in the Hel_h phase is attributed to a loss of the intra-columnar spin-spin exchange interaction during the transition from Col_h to Hel_h and can be corroborated with the positive magneto-LC effect in the Col_h phase. Such positive magneto-LC effect was also observed by Uchida *et al.* in chiral rod-like liquid crystalline nitroxide radical compounds.[16-17] To the best of our knowledge this is the first example of spin bearing discotics exhibiting a positive magneto-LC effect.

8.5 Optical and electrochemical properties of HBCNO

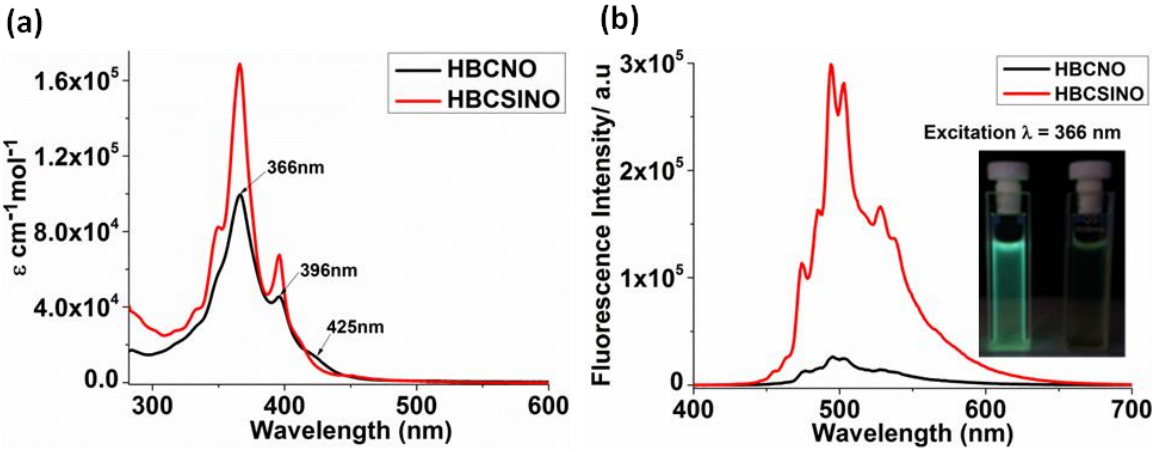

Figure 8.7: UV-Vis spectrum of **HBCSINO** and **HBCNO** at room teperature in toluene (a) absorption (b) emission with excitation at 366 nm (inset: disappearance of fluroscence on conversion from **HBCSINO** (left fluorescent) to **HBCNO**(right non-fluorescent)).

The optical measurements of **HBCNO** and precursor **HBCSINO** were performed in toluene (C ~ 10^{-5} M) at room temperature. Interestingly few notable changes were observed in UV-Vis spectra of **HBCNO** in comparison with precursor **HBCSINO**. The β *and* p-band of HBC were 1.5 times lower in intensity without any shift of λ_{max} (Figure 8.7a). Additionally the weak intensity characteristic absorption due to n—π* transition of

radical moiety appeared as a shoulder of p-band at 425 nm As anticipated for radical substituted aromatic compounds a dramatic quenching of the fluorescence was observed in **HBCNO**.[18] This suggests the effective energy or electron transfer on excitation of **HBCNO**.[19]

Electrochemical properties of **HBCNO** were investigated by CV measurements. The CV measurements were carried out using a three-electrode cell in DCM solution of Bu_4NPF_6 (0.1 M) with a scan rate of 100 mV/s at room temperature. A Pt wire, a silver wire, and a glassy carbon electrode were used as the counter electrode, the reference electrode, and the working electrode, respectively. Ferrocene was used as an internal standard. CV spectra of HBCNO displayed a reversible oxidation and a non-reversible reduction wave (Figure 8.8). The reversible oxidation at 0.269 V vs Fc/Fc^+ can be assigned to oxidation of the nitroxide moiety which is in accordance with the literature value for nitroxides.[20]

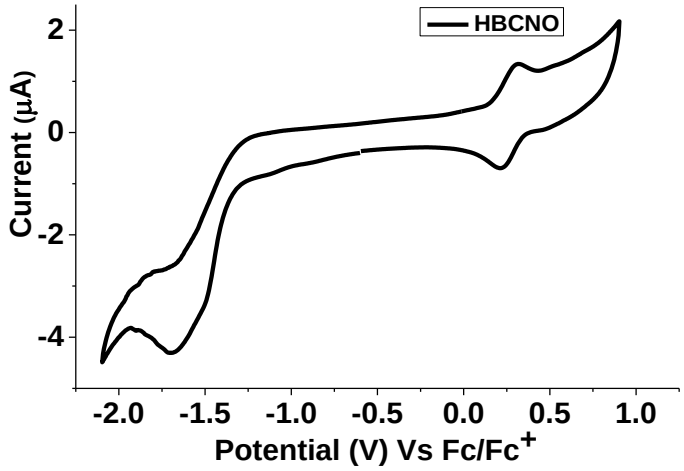

Figure 8.8: Cyclic Voltammetry curve of **HBCNO** measured in DCM vs FC/FC^+ (Bu_4NPF_6 (0.1 M), scan rate of 100 mV/s).

The DFT calculations were performed to visualize the distribution of SOMO orbital, where the unpaired electron usually resides. The geometry was optimized with UB3LYP/ 6-31Gd level of theory. Interestingly as shown in Figure 8.9 the SOMO orbital does not reside only on *tert*-butyl nitroxide radical moiety, but is highly delocalized over the HBC

core. The calculated E_{SOMO}, E_{LUMO} and energy gap between SOMO and LUMO, are well in accordance with estimates from the optical and electrochemical measurements (Table 8.1). The dipole moment of **HBCNO** was found to be 2.99 D.

Table 8.1: Optical and electrochemical properties of HBCNO.

λ_{max} (nm)	ε ($cm^{-1}M^{-1}$)	E_g^{OP} (eV)[a]	$E_{Ox}^{(1/2)}$ (V)[b]	E_{SOMO} (eV)[c]	E_{LUMO} (eV)[d]	E_{SOMO}^{cal} (eV)[e]	E_{LUMO}^{cal} (eV)[e]	E_g^{cal} (eV)[e]	D Debye[e]
366	9.95X 10^4	2.75	0.27	–5.069	2.319	–4.925	–2.122	2.80	2.999

[a]Optical energy gap calculated according to the absorption edge. [b]0.1 M of *n*-Bu_4NPF_6, in DCM, Pt electrode vs Fc/Fc^+, scan rate 100 mV s^{-1}. [c,d]Calculated based on formula $E_{SOMO} = -(E_{ox}^{(1/2)} + 4.8)$ eV and $E_{LUMO} = -(E_g^{OP} - E_{SOMO})$ eV. [e]Obtained using DFT quantum mechanical calculations UB3LYP/ 6 –31G.

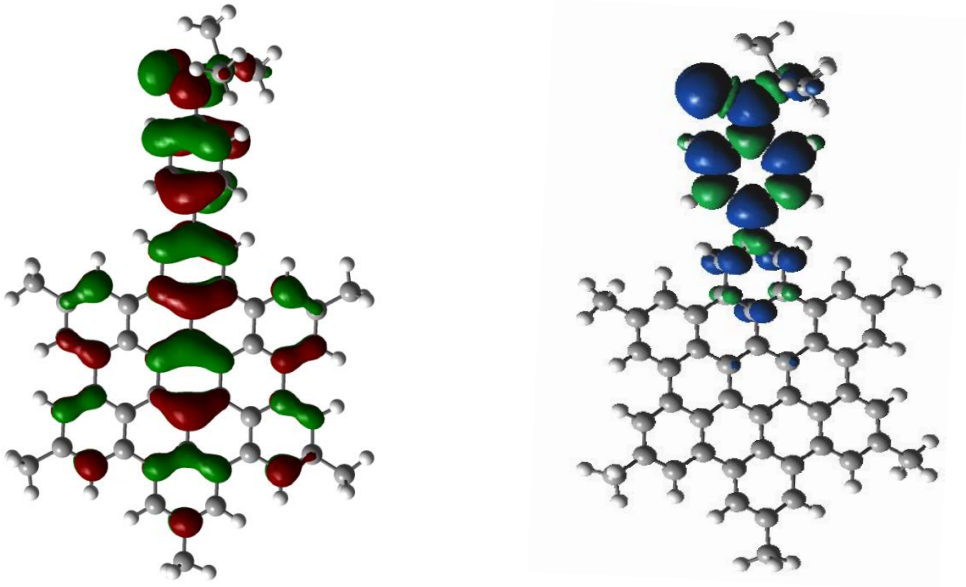

Figure 8.9: SOMO orbital and spin density distribution of **HBCNO** calculated using quantum mechanical calculation DFT-UB3LYP/6-31g.

8.6 Summary

In summary, we have successfully synthesized the first neutral paramagnetic HBC derivative possessing a *tert*-butyl nitroxide radical moiety. The adequate stability of **HBCNO** allowed us to investigate its thermal, optical, electrochemical, and magnetic properties. **HBCNO** was found to exist in a helical hexagonal phase at low temperature and a columnar hexagonal phase at higher temperatures. Notably, closer π-stacking of discs in the Col_h phase allowed stronger intra-columnar magnetic interactions. **HBCNO** exhibited a positive magneto-LC effect in columnar hexagonal liquid crystalline phase as probed by DSC and EPR spectroscopy. The paramagnetic **HBCNO** retains the absorption features of its diamagnetic precursor **HBCSINO**, but a significant quenching of fluorescence indicated extensive energy or electron transfer on excitation of **HBCNO**. All these properties make **HBCNO** an ideal candidate for designing spintronic devices.[21-22]

8.7 Synthetic details

The HBC-Br was synthesized according to literature procedures as shown in scheme below.[11-12]

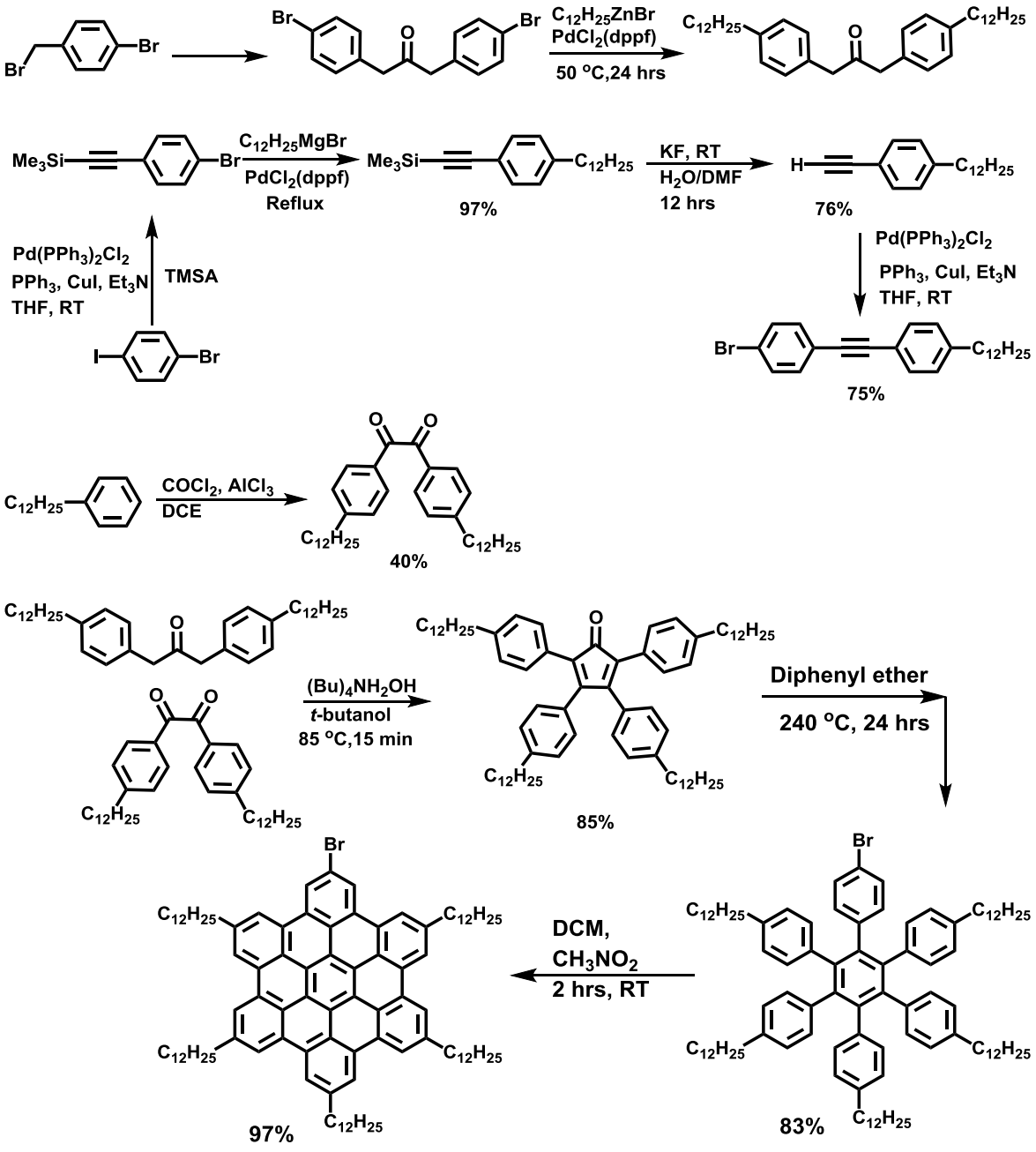

HBCSINO:

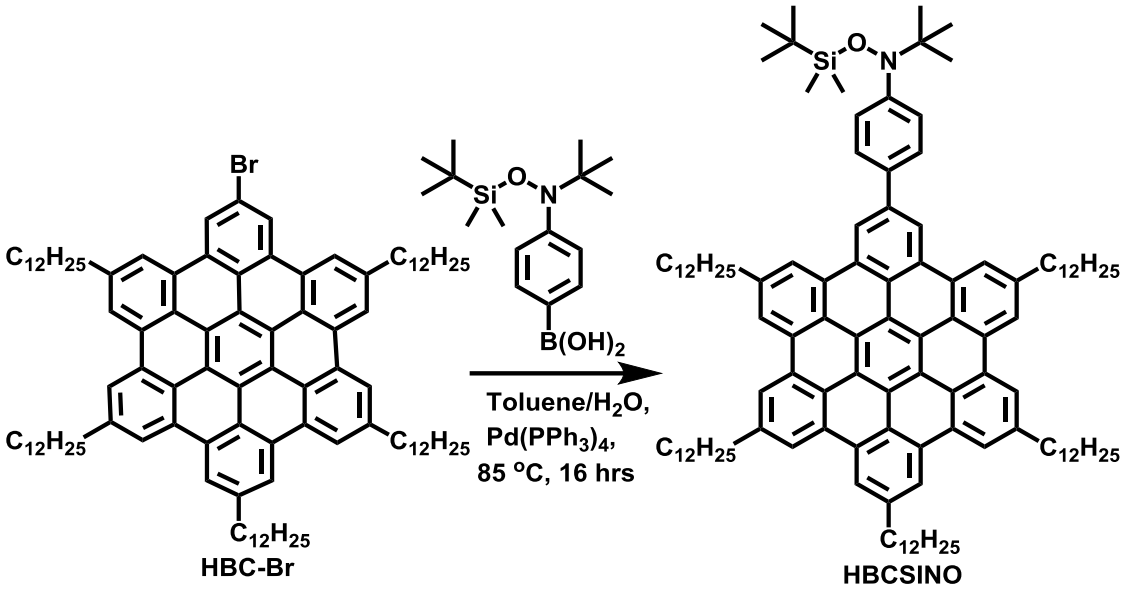

2-Bromo-5,8,11,14,17-pentadodecylhexabenzocoronene (200 mg) and (4-(*tert*-butyl(*tert*-butyldimethylsilyloxy)amino)phenylboronic acid were dissolved in 40 ml toluene in a Schlenk flask. To this mixture an aqueous solution of Na_2CO_3 (144 mg in 10 ml H_2O) was added and combined solution bubbled with argon for 30 min, then 5 mol% $Pd(PPh_3)_4$ were added and the reaction mixture heated at 80 °C for 20 hour. The reaction mixture was cooled to room temperature and washed with water. The organic layer was separated and the solvent removed under vacuum. The crude product was purified by silica gel column chromatography using 4:1 (hexane:DCM) as eluent. Yield 160 mg (70%). **MS-FD** (8 kV, CH_2Cl_2) m/z: found 1640.5 (100%). ESI-MS: found 1641.67 calculated 1641.66 (M). ^{1}H NMR (300 MHz, CD_2Cl_2) δ 8.54 (s, 2H), 8.20-8.09 (m, 10H), 7.94-7.91 (d, 2H), 7.68-7.65 (d, 2H), 3.00 (bs, 9H), 2.00 (bs, 9H), 1.59-0.89 (s, 125H), 0.21 (s, 6H) (Figure 8.10).

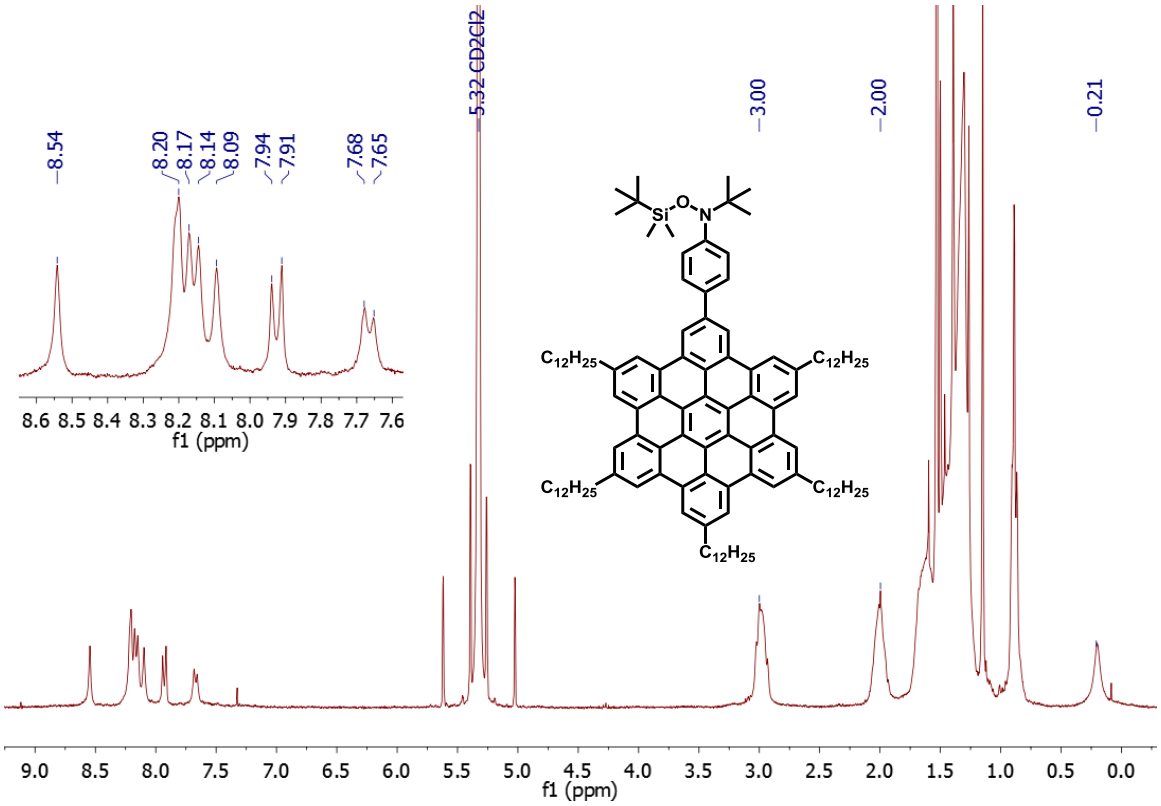

Figure 8.10: NMR spectrum of HBCSINO (C ~ 10^{-4} M).

HBCNO:

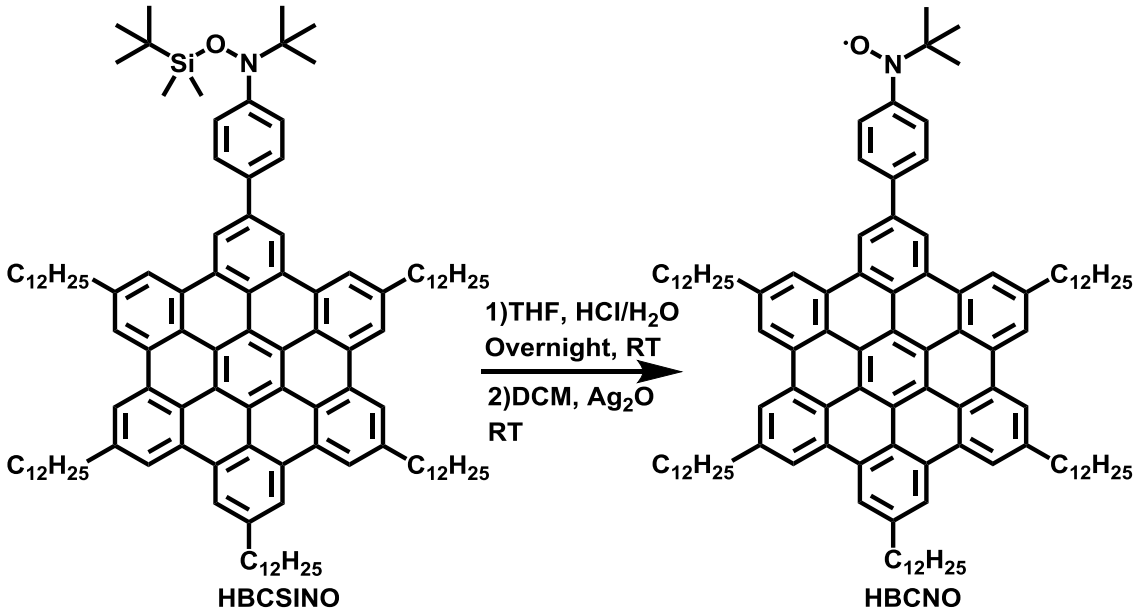

HBCSINO (100 mg) was dissolved in THF. Then conc. HCl was added and reaction mixture stirred at room temperature for overnight under argon. The reaction mixture was poured into H_2O and the formed precipitate was filtered, dried and used immediately for next step. The precipitate and excess of Ag_2O (200 mg) were dispersed in 40 ml dry DCM and stirred at room temperature for 3 hour under argon. The resulting solution passed through celite and the solvent was removed under vacuum. The crude product was purified by silica gel column chromatography using 1:1 (hexane:DCM) as eluent (Yield 22 mg , 20%). **MS-FD** (8 kV, CH_2Cl_2) m/z: found 1524.8 (90%), 1510.9 (100%). ESI-MS: found 1525.15 calculated 1525.17 (M), 1526.16 calculated 1526.17 (M+1). **UV-Vis** (Toluene) λ_{max} (ε, M^{-1} cm^{-1}): 366 nm (9.95 X 10^4). **EPR** (298 K, ~ 10^{-5} M in toluene): three lines, g_{iso} = 2.0068, a_N = 12.1 G a_H = 2 G.

8.7 References

[1] L. Schmidt-Mende, A. Fechtenkötter, K. Müllen, E. Moons, R. H. Friend, J. D. MacKenzie, *Science* **2001**, *293*, 1119.

[2] L. F. Dössel, V. Kamm, I. A. Howard, F. Laquai, W. Pisula, X. Feng, C. Li, M. Takase, T. Kudernac, S. De Feyter, K. Müllen, *J. Am. Chem. Soc.* **2012**, *134*, 5876.

[3] L. Chen, X. Dou, W. Pisula, X. Yang, D. Wu, G. Floudas, X. Feng, K. Müllen, *Chem. Commun.* **2012**, *48*, 702.

[4] W. W. H. Wong, T. B. Singh, D. Vak, W. Pisula, C. Yan, X. Feng, E. L. Williams, K. L. Chan, Q. Mao, D. J. Jones, C.-Q. Ma, K. Müllen, P. Bäuerle, A. B. Holmes, *Adv. Funct. Mater.* **2010**, *20*, 927.

[5] N. T. Lucas, H. M. Zareie, A. M. McDonagh, *ACS Nano* **2007**, *1*, 348.

[6] J. S. Wu, M. Baumgarten, M. G. Debije, J. M. Warman, K. Müllen, *Angew. Chem. Int. Ed.* **2004**, *43*, 5331.

[7] L. Gherghel, J. D. Brand, M. Baumgarten, K. Müllen, *J. Am. Chem. Soc.* **1999**, *121*, 8104.

[8] A. Jankowiak, D. Pociecha, J. Szczytko, H. Monobe, P. Kaszyński, *J. Am. Chem. Soc.*

2012, *134*, 2465.

[9] A. Jankowiak, D. Pociecha, H. Monobe, J. Szczytko, P. Kaszynski, *Chem. Commun.* **2012**, *48*, 7064.

[10] H. Gopee, A. N. Cammidge, V. S. Oganesyan, *Angew. Chem. Int. Ed.* **2013**, n/a.

[11] S. Ito, M. Wehmeier, J. D. Brand, C. Kübel, R. Epsch, J. P. Rabe, K. Müllen, *Chem. Eur. J.* **2000**, *6*, 4327.

[12] A. Fechtenkötter, N. Tchebotareva, M. Watson, K. Müllen, *Tetrahedron* **2001**, *57*, 3769.

[13] C. Grigoriadis, N. Haase, H.-J. Butt, K. Müllen, G. Floudas, *Soft Matter* **2011**, *7*, 4680.

[14] S. D. Cerius2 calculation (Accelrys, CA, USA).

[15] S. Castellanos, F. López-Calahorra, E. Brillas, L. Juliá, D. Velasco, *Angew. Chem. Int. Ed.* **2009**, *48*, 6516.

[16] K. Suzuki, Y. Uchida, R. Tamura, S. Shimono, J. Yamauchi, *J. Mater. Chem.* **2012**, *22*, 6799.

[17] Y. Uchida, K. Suzuki, R. Tamura, N. Ikuma, S. Shimono, Y. Noda, J. Yamauchi, *J. Am. Chem. Soc.* **2010**, *132*, 9746.

[18] Y. B. Borozdina, V. Kamm, F. Laquai, M. Baumgarten, *J. Mater. Chem.* **2012**, *22*, 13260.

[19] A. Ito, A. Shimizu, N. Kishida, Y. Kawanaka, D. Kosumi, H. Hashimoto, Y. Teki, *Angew. Chem. Int. Ed.* **2014**, n/a.

[20] M. Kadirov, E. Tretyakov, Y. Budnikova, M. Valitov, K. Holin, T. Gryaznova, V. Ovcharenko, O. Sinyashin, *J. Electroanal. Chem.* **2008**, *624*, 69.

[21] M. Misiorny, M. Hell, M. R. Wegewijs, *Nat. Phys.* **2013**, *9*, 801.

[22] T. Sugawara, M. M. Matsushita, *J. Mater. Chem.* **2009**, *19*, 1738.

Appendix-I

Analytical Techniques

CW-EPR spectroscopy

ESR spectra were recorded in diluted and oxygen-free solution of toluene with the concentration of 10^{-4} molar unless otherwise stated by using a using a Bruker X-band spectrometer ESP300 E, equipped with an NMR gauss meter (Bruker ER035), a frequency counter (Bruker ER041XK) and a variable temperature control continuous flow N_2 cryostat (Bruker B-VT 2000). The g-factor corrections were obtained by using DPPH (g = 2.0037) as standard. The spectral simulations were carried out using WINEPR SimFonia software.

Time-Resolved EPR spectroscopy

The TREPR measurements were performed at Division of Molecular Material Science, Graduate School of Science, Osaka City University, Japan by Prof Yoshio Teki. In the TREPR experiments, an X-band EPR spectrometer (JEOL TE300) equipped with a variable temperature control continuous flow liq. He cryostat (Oxford EPR910) was used. The measurements were recorded typically at 30 K. Excitations at 532 nm and at 355 nm were carried out by 2^{nd} and 3^{rd} harmonics of the ns pulsed YAG laser (Continuum Surelite II), respectively. Sample was diluted in BuCN (glass matrix) degassed by repeated freeze–pump–thaw cycles.

Magnetic measurement

The SQUID measurements were carried out by colleague Dr. Yoshikazu Ito. Magnetic susceptibility and magnetization were measured using Quantum Design MPMS-XL SQUID magnetometer up to a field of 5 T in the temperature range between 2 to 300 K, at Physics Department, Johannes-Gutenberg-University of Mainz. Background signals of sample holder and diamagnetic correction were subtracted as explained in Appendix-V.

NMR spectroscopy

Proton nuclear magnetic resonance (^{1}H NMR) spectra and carbon nuclear magnetic resonance (^{13}C NMR) spectra were recorded on a Bruker AMX 300 NMR instrument (300 and 75 MHz, respectively) or on a Bruker AMX 250 NMR instrument (250 and 62.5 MHz, respectively). The deuterated solvent was used as an internal standard.

Single crystal X-ray measurements

The single crystal X-ray data collection and structure solution was performed by Dr. Volker Enkelmann at MPIP, Mainz. The single crystal X-ray crystallographic data were collected on Nonius Kappa CCD (Mo-Kα) diffractometer equipped with graphite monochromator. The structures were solved by direct method (SHELXS) and refined by a full-matrix least-squares procedure.

Melting point

Melting points were measured on Büchi B-545 apparatus (uncorrected) by using open ended capillaries.

Mass spectrometry

The field desorption mass spectra were obtained on FD-MS, VG Instruments ZAB 2-SE-FDP using 8 kV accelerating voltage. The high-resolution electron spray ionization mass spectrometry (HR-ESI-MS) was performed at the Institute for Organic Chemistry, Johannes-Gutenberg-University of Mainz, on an ESI-Q-TOF system (maXis, Bruker Daltonics, Germany).

UV–Vis absorption spectroscopy

UV-Vis spectra were recorded in toluene with Perkin Elmer Spectrometer (UV/Vis/NIR Lambda 900) by using 1 cm optical-path quartz cell at room temperature. The baseline was corrected by subtracting a measurement of the cuvette filled with pure

solvent used for the measurement. The optical energy gap was calculated based on the onset absorption band.

Cyclic voltammetry

CV measurements were carried out on a computer-controlled GSTAT12 in a three-electrode cell in a DCM or acetonitrile solution of Bu_4NPF_6 (0.1 M) with a scan rate of 100 mV/s at room temperature. A Pt wire, silver wire, and glassy carbon electrode were used as the counter electrode, the reference electrode, and the working electrode, respectively.

Photoluminescence spectroscopy

PL measurements on performed on a SPEX-FluorologII (F212) steady-state fluorometer in toluene at room temperature.

Column chromatography

The column chromatography was performed using either silica gel (60–120, 100–200 and 230–400 mesh) or neutral aluminium oxide. For thin layer chromatography, aluminium sheets pre-coated with silica gel (Merck, Kieselgel 60, F_{254}) were employed.

Chemical structure & graphics

The chemical structure and reaction scheme were drawn using ChemBioDraw Ultra 12.0. Molecular packing was analyzed by Mercury 3.1 software. The crystal packing diagram and high quality graphics were generated from Diamond and Pov-ray software using cif files.

DFT calculations

The DFT calculations were performed using either Gaussian 09[1] or ORCA[2] software.

Calculating exchange interactions (*J*)

The broken-symmetry approach proposed by Noodleman *et al.* was employed to elucidate the magnetic properties of the biradical species under study.[3] The exchange coupling constant (*J*) was calculated by the generalized spin projection method suggested by Yamaguchi *et al*.[4-6] For the molecule with two exchange coupled unpaired electrons, the Heisenberg-Dirac-van Vleck (HDVV) Hamiltonian,

$$H = -2J_{12}S_1S_{2,} \quad \textbf{1}$$

S_1 and S_2 are the spin angular momentum operators.

$$Exchange\ interaction, \qquad J = \frac{(E(BS) - E(T))}{(S^2(T) - S^2(BS))} \quad \textbf{2}$$

where, E(BS) is the energy of the broken-symmetry (BS) solution, a mixture of singlet and triplet states with $S_Z = 0$ and S^2(BS) close to 1, E(T) is the energy of the triplet state with S^2(T) close to 2, and S^2 are the eigen values of the spin operator for these states.

Thus the direct exchange yields, $J \approx E(BS) - E(T)$ **3**

Calculating biradical character (*y*)

The degree of biradical character (y) can be calculated by simple two-electron two-orbital model using the occupation numbers of the unrestricted non-bonding orbitals (UNOs) of UHF/6-31g(d, p) as proposed by Kamada *et al*.[7-8] The biradical character y obtained from these calculations has value between 0 and 1, which corresponds to closed

shell and pure biradical system, respectively.

$$y = 1 - \frac{4\,(\sigma_{HOMO} - \sigma_{LUMO})}{4 + (\sigma_{HOMO} - \sigma_{LUMO})^2} \qquad \textbf{4}$$

The theoretical value of y can be obtained from the occupation numbers of frontier orbitals, σ_{HOMO} and σ_{LUMO}, using the equation shown above.

References:

[1] G. W. T. M. J. Frisch, H. B. Schlegel, G. E. Scuseria, M. A. Robb, J. R. Cheeseman, G. Scalmani, V. Barone, B. Mennucci, G. A. Petersson, H. Nakatsuji, M. Caricato, X. Li, H. P. Hratchian, A. F. Izmaylov, J. Bloino, G. Zheng, J. L. Sonnenberg, M. H A. F. Izmaylov, J. Bloino, G. Zheng, J. L. Sonnenberg, M. Hada,M. Ehara, K. Toyota, R. Fukuda, J. Hasegawa, M. Ishida, T. Nakajima, Y. Honda, O. Kitao, H. Nakai, T. Vreven, J. A. Montgomery, Jr., J. E. Peralta, F. Ogliaro, M. Bearpark, J. J. Heyd, E. Brothers, K. N. Kudin, V. N. Staroverov, R. Kobayashi, J. Normand, K. Raghavachari, A. Rendell, J. C. Burant, S. S. Iyengar, J. Tomasi, M. Cossi, N. Rega, J. M. Millam, M. Klene, J. E. Knox, J. B. Cross, V. Bakken, C. Adamo, J. Jaramillo, R. Gomperts, R. E. Stratmann, O. Yazyev, A. J. Austin, R. Cammi, C. Pomelli, J. W. Ochterski, R. L. Martin, K. Morokuma, V. G. Zakrzewski, G. A. Voth, P. Salvador, J. J. Dannenberg, S. Dapprich, A. D. Daniels, O. Farkas, J. B. Foresman, J. V. Ortiz, J. Cioslowski, and D. J. Fox., in *Gaussian 09*, Gaussian, Inc, Wallingford CT, **2009**.

[2] F. Neese et al, ORCA - An Ab Initio, DFT and Semiempirical electronic structure package, Program Version 2.9.1 ed., **2012**.

[3] L. Noodleman, *J. Chem. Phys.* **1981**, *74*, 5737.

[4] K. Yamaguchi, F. Jensen, A. Dorigo, K. N. Houk, *Chem. Phys. Lett.* **1988**, *149*, 537.

[5] T. Soda, Y. Kitagawa, T. Onishi, Y. Takano, Y. Shigeta, H. Nagao, Y. Yoshioka, K. Yamaguchi, *Chem. Phys. Lett.* **2000**, *319*, 223.

[6] M. Shoji, K. Koizumi, Y. Kitagawa, T. Kawakami, S. Yamanaka, M. Okumura, K. Yamaguchi, *Chem. Phys. Lett.* **2006**, *432*, 343.

[7] K. Kamada, K. Ohta, A. Shimizu, T. Kubo, R. Kishi, H. Takahashi, E. Botek, B. Champagne, M. Nakano, *The Journal of Physical Chemistry Letters* **2010**, *1*, 937.

[8] P. O. Dral, T. Clark, *J. Phys. Chem. A* **2011**, *115*, 11303.

Appendix-II

Conversion Tables

Energy Conversion Table								
	hartree	**eV**	**cm^{-1}**	**kcal/mol**	**kJ/mol**	**K**	**J**	**Hz**
hartree	1	27.2107	219 474.63	627.503	2 625.5	315 777.	43.60×10^{-19}	$6.57966 \times 10^{+15}$
eV	0.0367502	1	8 065.73	23.060 9	96.486 9	11 604.9	$1.602\ 10 \times 10^{-19}$	$2.418\ 04 \times 10^{+14}$
cm^{-1}	$4.556\ 33 \times 10^{-6}$	$1.239\ 81 \times 10^{-4}$	1	0.002 859 11	0.011962 7	1.428 79	$1.986\ 30 \times 10^{-23}$	$2.997\ 93 \times 10^{+10}$
kcal/mol	0.001 593 62	0.043 363 4	349.757	1	4.18400	503.228	6.95×10^{-21}	$1.048\ 54 \times 10^{+13}$
kJ/mol	0.000 380 88	0.010 364 10	83.593	0.239001	1	120.274	1.66×10^{-21}	$2.506\ 07 \times 10^{+12}$
K	0.000 003 166 78	0.000 086 170 5	0.695 028	0.001 987 17	0.008314 35	1	$1.380\ 54 \times 10^{-23}$	$2.083\ 64 \times 10^{+10}$
J	$2.294 \times 10^{+17}$	$6.241\ 81 \times 10^{+18}$	$5.034\ 45 \times 10^{+22}$	$1.44 \times 10^{+20}$	$6.02 \times 10^{+20}$	$7.243\ 54 \times 10^{+22}$	1	$1.509\ 30 \times 10^{+33}$
Hz	$1.519\ 83 \times 10^{-16}$	$4.135\ 58 \times 10^{-15}$	$3.335\ 65 \times 10^{-11}$	$9.537\ 02 \times 10^{-14}$		$4.799\ 30 \times 10^{-11}$	$6.625\ 61 \times 10^{-34}$	1

Fundamental Physical Constants from NIST. Most of these numbers have been taken from an old book by Karplus and Porter.

http://physics.nist.gov/cuu/Constants/index.html

Conversion Table (EPR)

dB	µWatt	√ µWatt	dB	µWatt	√ µWatt
40	20.1	4.4833	23	1010	**31.7805**
39	25.3	5.02991	22	1270	**35.63706**
38	31.9	5.64801	21	1600	**40**
37	40	6.32456	20	2000	**44.72136**
36	50.4	7.0993	19	2530	**50.29911**
35	63.6	7.97496	18	3180	**56.39149**
34	80	8.94427	17	4000	**63.24555**
33	101	10.04988	16	5040	**70.99296**
32	127	11.26943	15	6350	**79.68689**
31	160	12.64911	14	8010	**89.4986**
30	201	14.17745	13	10100	**100.49876**
29	250	15.81139	12	1270	**35.63706**
28	320	17.88854	11	16000	**126.49111**
27	400	20	10	20100	**141.77447**
26	510	22.58318	9	25300	**159.05974**
25	640	25.29822	8	31800	**178.32555**
24	800	28.28427	7	40100	**200.24984**
		--	6	50400	**224.49944**
dB	**µWatt**	**√ µWatt**	**dB**	**µWatt**	**√ µWatt**

1 hartree (h) = 27.2114 eV

$1cm^{-1} = 1.07 \times 10^{3}$ mT = 1.07×10^{4} Gauss

1 Gauss ~ 2.8 MHz = 1.39967 x g

To convert D, E from Gauss to cm^{-1} multiply by $4.6686 \cdot 10^{-5} \cdot$ 2.0023 cm^{-1}

$1cm^{-1}$ = 29979.25 MHz = 10697.5 G for g=2.0023

Free electron g value: $g_e = 2.0023193$

Boltzmann Constant: $k_B = 0.69504\ cm^{-1}$

Calculating the g value from the frequency and magnetic field:

$g = (h/\mu_B)\ \gamma / B = 714.4775\ \gamma[GHz] / B[G]$

Appendix-III

Crystallographic table

Radical	DBrNN	MAMNN	OMeBrNN
CCDC Number	972701	972702	972703
Formula	C_{14} H_{15} Br_1 N_2 O_2	C_{29} H_{33} N_5 O_5	C_{29} H_{33} Br_1 N_4 O_5
Formula Weight	323.19	531.61	597.51
Crystal System	Monoclinic	Monoclinic	Tetragonal
Space group	P21 (No. 4)	Pc (No. 7)	I 41/a
a,b,c [Å]	10.931 (2), 11.353 (3), 11.195 (2)	10.120 (3), 9.714 (2), 14.629 (5)	28.762(10), 28.762(10), 13.444(5)
α,β,γ [°]	90, 105.20(13), 90	90 105.34(12), 90	90
V [$Å^3$]	1340.88(5)	1387.00(7)	11121.6(7)
Z	4	2	2
D(calc) [g/cm^3]	1.601	1.273	1.427
Mu(MoKa)[mm^{-1}]	3.065	0.089	1.524
F(000)	656	564	4960
Crystal Size [mm]	0.11 x 0.16 x 0.40	0.13 x 0.16 x 0.41	0.11 x0.15 x0.41
Temp. (K)	120	120	120
Radiation [Å,MoKa]	0.71073	0.71073	0.71073
Theta Min-Max [°]	1.9, 30.2	2.1, 30.5	2.969, 27.522
Dataset	-15: 15 ; -15: 14 ; -15: 15	-14: 13 ; 0: 13 ; 0: 20	
Tot., Uniq. Data, R(int)	17180, 7134, 0.089	21433, 4184 0.059	34330, 6296
Observed data [I > 2.0 sigma(I)]	6065	3740	4454
Nref, Npar	6065, 344	3740 352	4454, 352
R, wR2, S	0.0443, 0.0536, 1.09	0.0617, 0.0103, 0.75	0.0587, 0.0666, 0.9840
Min. and Max. Resd. Dens. [$eAng^{-3}$]	-0.92, 0.72	-0.46, 0.46	-0.60, 0.44

Radical	TMPNN	TMPIN	TMPMIX
CCDC No.	915927	915929	915928
Formula	$C_{34}H_{40}N_4O_8$	$C_{34}H_{40}N_4O_6$	$C_{34}H_{40}N_4O_7$
Formula Weight	632.71	600.71	616.71
Crystal System	Monoclinic	Monoclinic	Monoclinic
Space group	P21/n (No. 14)	P21/n (No. 14)	P21/n (No. 14)
a,b,c [Å]	6.288(2), 11.494 (6), 21.064 (9)	6.352 (2), 11.265 (3), 21.231 (5)	6.3490(1), 11.321(2), 21.3030(5)
α,β,γ [°]	90, 90.135(3),90	90, 90.2971(17), 90	90, 90.0050(12), 90
V [$Å^3$]	1522.50(11)	1519.30(7)	1531.20(5)
Z	2	2	2
D(calc) [g/cm^3]	1.380	1.313	1.338
Mu(MoKα) [mm^{-1}]	0.099	0.091	0.094
F(000)	672	640	656
Crystal Size [mm]	0.13 x 0.19 x 0.41	0.14 x 0.19 x 0.44	0.00 x 0.00 x 0.00
Temperature (K)	120	120	293
Radiation [Å,MoKα]	0.71073	0.71073	0.71073
Theta Min-Max [°]	1.9 30.1	3.3 30.0	1.9 31.0
Dataset	-8: 8 ; -14: 16 ; -29: 29	-8: 8 ; -15: 15 ; -27: 29	-9: 9 ; -16: 16 ; -30: 30
Tot., Uniq. Data, R(int)	16332,4167,0.000	15742 4401 0.074	21866 4880 0.000
Observed data [I > 2.0 sigma(I)]	2783	2960	3954
Nref, Npar	2783, 209	2960, 199	3954, 209
R, wR2, S	0.0578, 0.0789, 1.05	0.0428, 0.0535, 1.08	0.0499, 0.0646, 1.08
Min. and Max. Resd. Dens. [e $Å^{-3}$]	-0.36, 0.26	-0.22, 0.41	-0.20, 0.22

Radical	2,7-TMPNO(125K)	2,7-TMPNO(320K)	2-TMPNO
CCDC No.	950752		
Formula	C14 H17 N1 O3	C14 H17 N1 O3	C24 H26 N1 O5
Formula Weight	247.29	247.29	408.47
Crystal System	Monoclinic	Monoclinic	Monoclinic
Space group	C2/c, (No. 15)	C2/c, (No. 15)	P21/c, (No. 14)
a,b,c [Å]	23.1335(9), 10.9524(5), 10.8030(7)	23.4318(8), 11.1815(4), 10.8961(3)	8.1986(2), 21.6402(9,) 11.6933(5)
α,β,γ [°]	90, 106.950(3), 90	90, 108.856(2), 90	90, 100.589(2), 90
V [$Å^3$]	2618.2(2)	2701.60(16)	2039.29(13)
Z	8	8	4
D(calc) [g/cm^3]	1.255	1.216	1.330
Mu(MoKα) [mm^{-1}]	0.088	0.085	0.093
F(000)	1056	1056	868
Crystal Size [mm]	0.13 x 0.17 x 0.44	0.13 x 0.17 x 0.44	0.13 x 0.17 x 0.41
Temperature (K)	120	320	120
Radiation [Å,MoKα]	0.71073	0.71073	0.71073
Theta Min-Max [°]	2.1, 29.5	3.6, 28.6	3.0, 29.6
Dataset	-31: 30 ; -14: 15 ; -13: 14	-31: 31 ; -14: 15 ; -12: 14	-11: 11 ; -29: 30 ; -15: 16
Tot., Uniq. Data, R(int)	9725, 3637, 0.087	9034, 3454, 0.047	23348, 5658, 0.075
Observed data [I > 2.0 sigma(I)]	2211	1797	4319
Nref, Npar	2211, 163	1797, 163	3952, 271
R, wR2, S	0.0497, 0.0640, 1.09	0.0492, 0.0684, 1.07	0.0671, 0.0808, 1.03
Min. and Max. Resd. Dens. [e $Å^{-3}$]	-0.25, 0.35	-0.13, 0.21	-0.36, 0.40

Radical	1-TMPNO	1,3,6,8-TMPNO	NN+Ag
CCDC No.			867206
Formula	C24 H26 N1 O5	C32 H50 N4 O8	C35 H33 AG3.50 F10.50 N4 O11.50
Formula Weight	408.47	618.77	1270.68
Crystal System	Triclinic	Monoclinic	Triclinic
Space group	P-1 (No. 2)	P21/n (No. 14)	P-1 (No. 2)
a,b,c [Å]	9.6761(3), 10.5020(4), 10.8995(4)	12.9998(3), 12.8094(2), 21.2617(4)	14.0250(5), 17.7490(5), 20.1285(6)
α,β,γ [°]	76.6(19), 80.44(18) 76.7(2)	90, 90.60(11), 90	111.40(16), 105.03(16), 96.52(17)
V [$Å^3$]	1041.37(6)	3540.29(12)	4382.7(3)
Z	2	4	4
D(calc) [g/cm^3]	1.303	1.251	1.926
Mu(MoKα) [mm^{-1}]	0.091	0.080	1.650
F(000)	434	1432	2488
Crystal Size [mm]	0.12 x 0.19 x 0.43	-	0.13 x 0.17 x 0.34
Temperature (K)	120	298	120
Radiation [Å,MoKα]	0.71073	0.71073	0.71073
Theta Min-Max [°]	2.5, 29.5	0.0, 30.0	1.3, 30.1
Dataset	-13: 13 ; -14: 14 ; -12: 15	-18: 18 ; -18: 18 ; -29: 29	-19: 19 ; -24: 24 ; -27: 28
Tot., Uniq. Data, R(int)	12101, 5777, 0.061	32489, 11214, 0.107	52266, 25276, 0.060
Observed data [I > 2.0 sigma(I)]	4746	7163	14993
Nref, Npar	4463, 271	7117, 433	14993, 1180
R, wR2, S	0.0539, 0.0808, 1.06	0.0650, 0.2060, 1.87	0.0829, 0.0622, 1.26
Min. and Max. Resd. Dens. [e $Å^{-3}$]	-0.38, 0.46	0.00, 0.00	-0.96, 0.88

Radical	BPNO	TPNO	BPTMP
CCDC No.	1001620	1001622	1001621
Formula	C10 H13 N1 O1	C26 H30 N2 O2	C40 H42 N2 O6
Formula Weight	163.22	402.54	646.78
Crystal System	Monoclinic	Monoclinic	Monoclinic
Space group	P21/a, (No. 14)	P21/a, (No. 14)	C2/c, (No. 15)
a,b,c [Å]	8.614(5),9.107(7), 11.338(9)	8.840(2), 8.988(3), 13.346(4)	18.130(8), 11.229(3), 17.613(8)
α,β,γ [°]	90, 101.9 (4), 90	90, 94.8(2), 90	90, 113.4(1), 90
V [$Å^3$]	870.21(11)	1056.79(5)	3290.6(2)
Z	4	2	4
D(calc) [g/cm^3]	1.246	1.265	1.306
Mu(MoKa) [mm^{-1}]	0.081	0.080	0.088
F(000)	352	432	1376
Crystal Size [mm]	0.09 x 0.16 x 0.41	0.09 x 0.29 x 0.42	0.13 x 0.20 x 0.39
Temperature (K)	120	120	120
Radiation [Å,MoKa]	0.71073	0.71073	0.71073
Theta Min-Max [°]	3.5, 27.6	3.5, 30.0	2.7, 28.7
Dataset	-11: 10 ; 0: 11 ; 0: 14	-12: 11 ; -12: 12 ; -18: 18	-24: 24 ; -15: 14 ; -19: 23
Tot., Uniq. Data, R(int)	6606, 1987, 0.056	13179, 3090, 0.055	13979, 4234, 0.088
Observed data [I > 2.0 sigma(I)]	1764	2464	3411
Nref, Npar	1764, 109	2304, 136	3137, 218
R, wR2, S	0.0577, 0.4001, 0.84	0.0505, 0.0643, 1.07	0.0664, 0.1024, 0.91
Min. and Max. Resd. Dens. [$eAng^{-3}$]	-0.42, 0.49	-0.33, 0.31	-0.50, 0.54

Appendix-IV

ORTEP diagrams, 50 % probability temperature ellipsoid plot

NN1	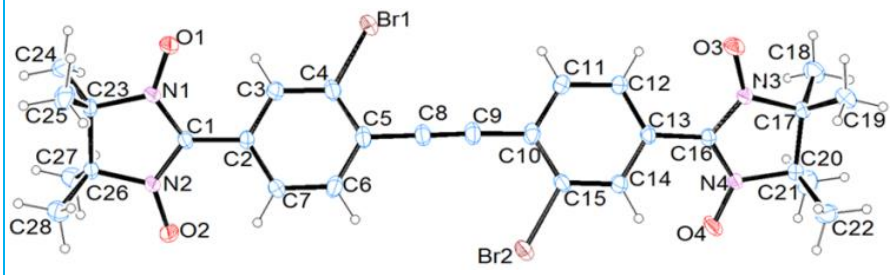
NN2	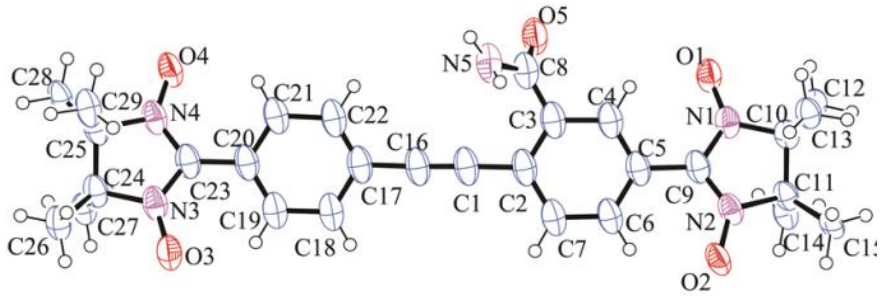
NN3	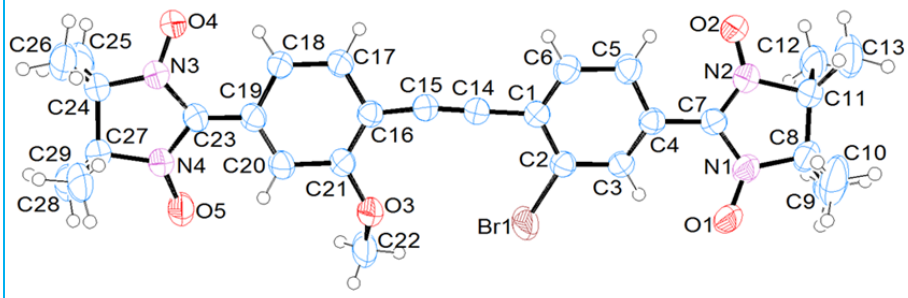

TMPNN	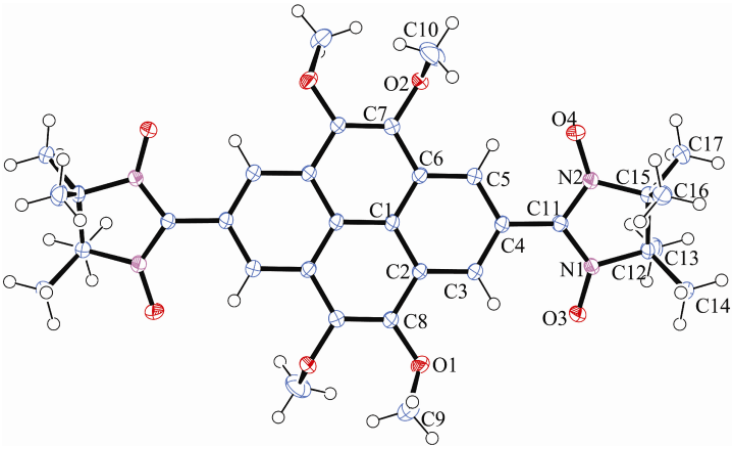
TMPIN	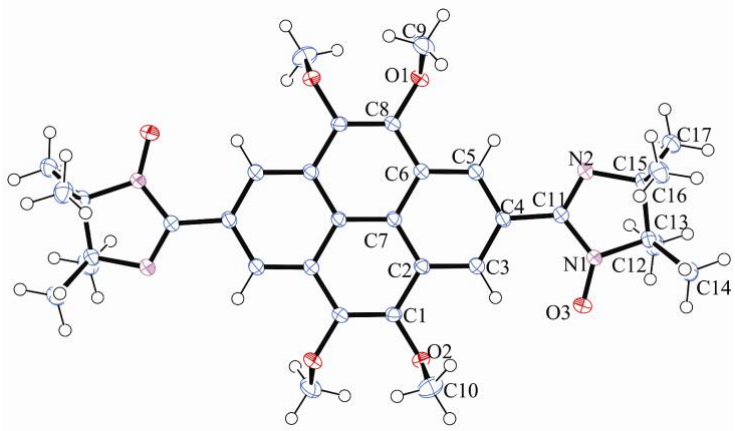
TMPIMIX	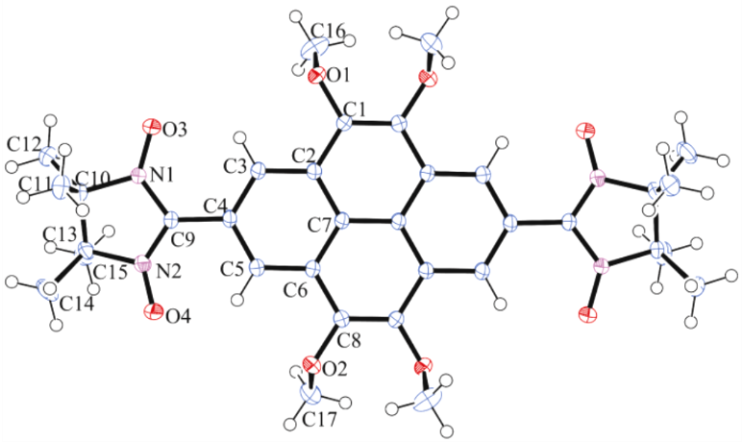

2,7-TMPNO	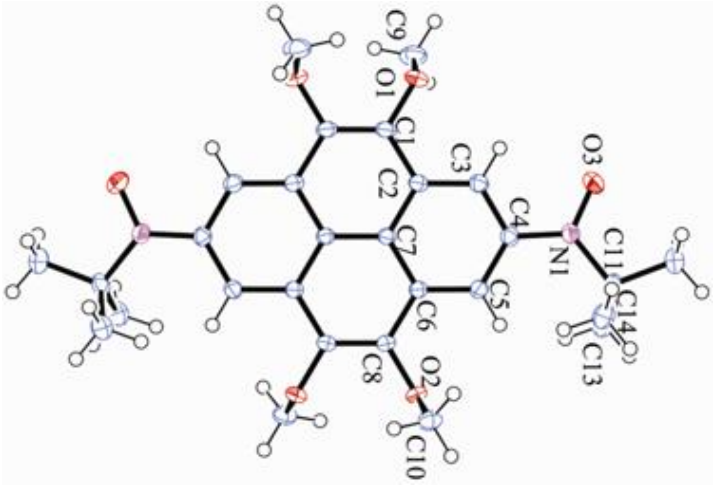
2-TMPNO	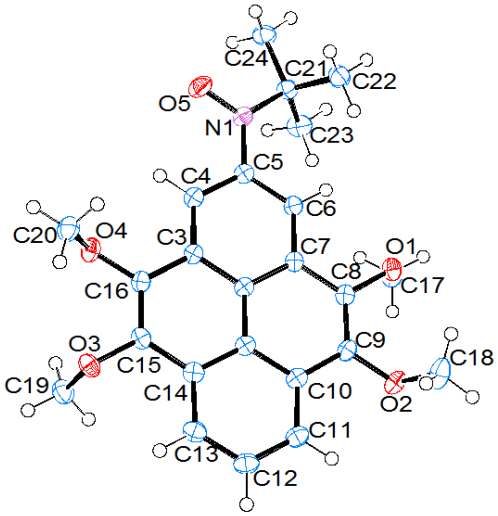
1-TMPNO	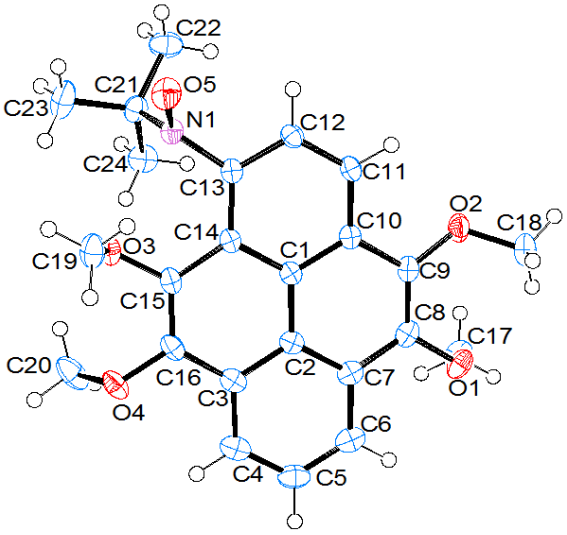

1,3,6,8-TMPNO	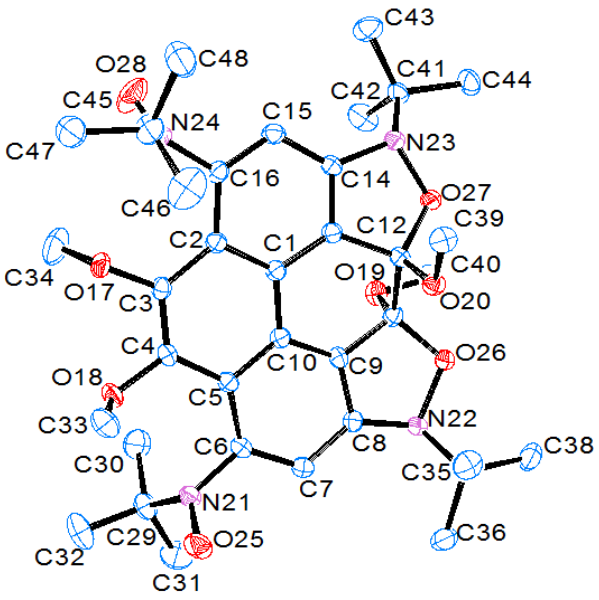
NN+Ag	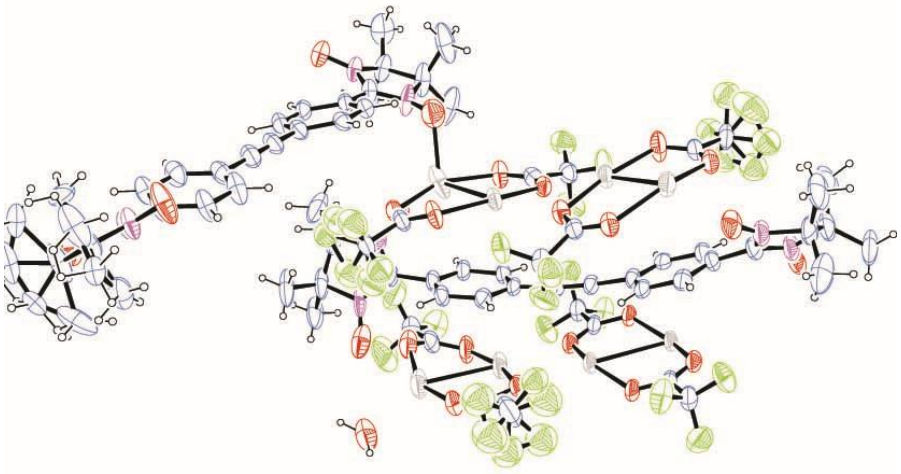
BPNO	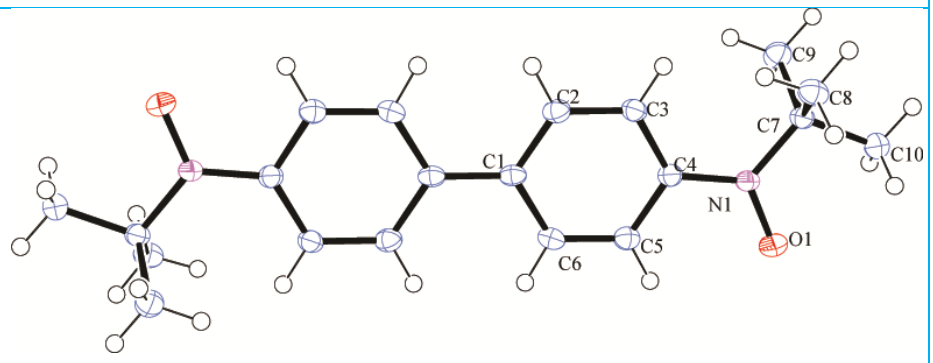

TPNO	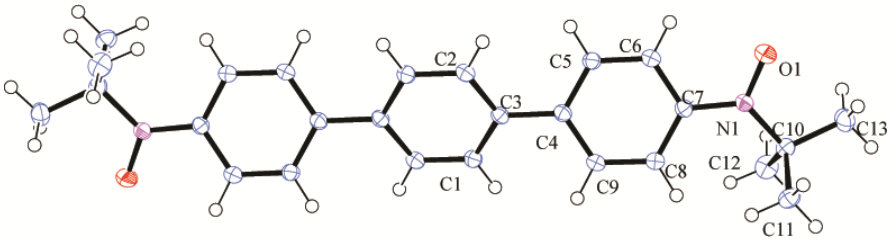 C2 C5 C6 O1 C3 C7 N1 C10 C13 C4 C12 C1 C9 C8 C11
BPTMP	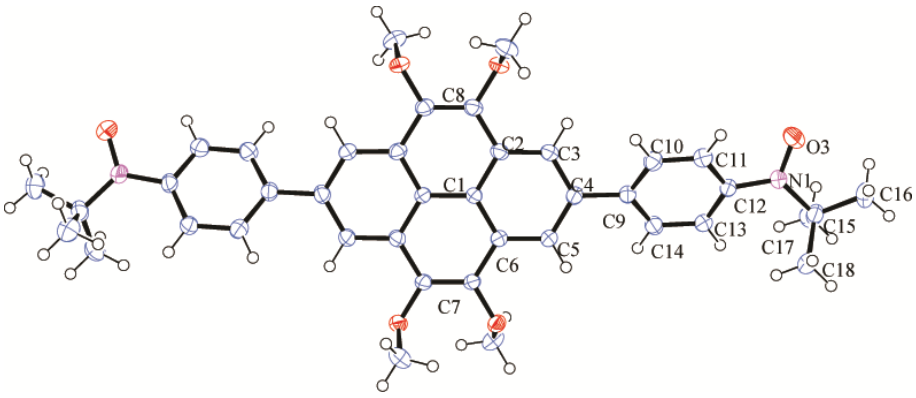 C8 C2 C3 C10 C11 O3 C1 C4 N1 C16 C12 C9 C15 C13 C17 C5 C14 C6 C18 C7

Appendix-V

Diamagnetic corrections

The total measured magnetic susceptibility, χ_T, is sum of these contributions from diamagnetic and paramagnetic species,

$$\boldsymbol{\chi_T = \chi_P + \chi_{Di}}$$

Thus diamagnetic correction can be performed as,

$$\boldsymbol{\chi_P = \chi_T - \chi_{Di}}$$

The diamagnetic susceptibility, χ_{Di} is temperature independent and calculated using the Pascal's formula,

$$\boldsymbol{\chi_{Di} = \sum_i \chi_{Di} + \sum_i \lambda_i}$$

Where, χ_{Di} and λ_i are known as "Pascal's constants".

Table 1. Values of χ_{Di} for Atoms in Covalent Species

Atom	χ_{Di}/(1 x 10^{-6} emu mol^{-1})	Atom	χ_{Di}/(1 x 10^{-6} emu mol^{-1})	Atom	χ_{Di}/(1 x 10^{-6} emu mol^{-1})	Atom	χ_{Di}/(1 x 10^{-6} emu mol^{-1})
Ag	–31.0	C (ring)	–6.24	Li	–4.2	S	–15.0
Al	–13.0	Ca	–15.9	Mg	–10.0	Sb(III)	–74.0
As(III)	–20.9	Cl	– 20.1	N (ring)	–4.61	Se	–23.0
As(V)	–43.0	F	–6.3	N(open chain)	–5.57	Si	–13
B	–7.0	H	–2.93	Na	–9.2	Sn(IV)	–30
Bi	–192.0	Hg(II)	–33.0	O	–4.6	Te	–37.3
Br	– 30.6	I	–44.6	P	–26.3	Tl(I)	–40.0
C	– 6.00	K	–18.5	Pb(II)	–46.0	Zn	–13.5

The details of diamagnetic corrections can be found in following paper[1]

[1] G. A. Bain, J. F. Berry, *J. Chem. Educ.* **2008**, *85*, 532.

Table 2. Values of λ_i for Specific Bond Types

Bond[a]	$\lambda_i/(1 \times 10^{-6}$ emu mol$^{-1})$	Bond	$\lambda_i/(1 \times 10^{-6}$ emu mol$^{-1})$	Bond	$\lambda_i/(1 \times 10^{-6}$ emu mol$^{-1})$	Bond	$\lambda_i/(1 \times 10^{-6}$ emu mol$^{-1})$
C=C	+5.5	Cl–CR2CR2–Cl	+4.3	Ar–Br	–3.5	Imidazole	+8.0
C≡C	+0.8	R2CCl2	+1.44	Ar–Cl	–2.5	Isoxazole	+1.0
C=C–C=C	+10.6	RCHCl2	+6.43	Ar–I	–3.5	Morpholine	+5.5
Ar–C≡C–Ar[b]	+3.85	C–Br	+4.1	Ar–COOH	–1.5	Piperazine	+7.0
CH2=CH–CH2–(allyl)	+4.5	Br–CR2CR2–Br	+6.24	Ar–C(=O)NH2	–1.5	Piperidine	+3.0
C=O	+6.3	C–I	+4.1	R2C=N–N=CR2	+10.2	Pyrazine	+9.0
COOH	–5.0	Ar–OH	–1	RC≡C–C(=O)R	+0.8	Pyridine	+0.5
COOR	–5.0	Ar–NR2	+1	Benzene	–1.4[c]	Pyrimidine	+6.5
C(=O)NH2	–3.5	Ar–C(=O)R	–1.5	Cyclobutane	+7.2	α- or γ-Pyrone	–1.4
N=N	+1.85	Ar–COOR	–1.5	Cyclohexadiene	+10.56	Pyrrole	–3.5
C=N–	+8.15	Ar–C=C	–1.00	Cyclohexane	+3.0	Pyrrolidine	+0.0
–C≡N	+0.8	Ar–C≡C	–1.5	Cyclohexene	+6.9	Tetrahydrofuran	+0.0
–N≡C	+0.0	Ar–OR	–1	Cyclopentane	+0.0	Thiazole	–3.0
N=O	+1.7	Ar–CHO	–1.5	Cyclopropane	+7.2	Thiophene	–7.0
–NO2	–2.0	Ar–Ar	–0.5	Dioxane	+5.5	Triazine	–1.4
C–Cl	+3.1	Ar–NO2	–0.5	Furan	–2.5		

[a]Ordinary C–H and C–C single bonds are assumed to have a λ value of 0.0 emu mol^{-1}. [b]The symbol Ar represents an aryl ring. [c]Some sources list the λ value for a benzene ring as –18.00 to which three times λ(C=C) must then be added. To minimize the calculations involved, this convention was not followed such that λ values given for aromatic rings are assumed to automatically take into account the corresponding double bonds in the ring.

Calculation of Diamagnetic susceptibility (X 10^{-6})

DBrNN

Pascal's constants

C ring	-6.24	Num C ring	12	Diamagnetism of C ring	-74.88
C	-6	Num C	16	Diamagnetism of C	-96
H	-2.43	Num H	30	Diamagnetism of H	-72.9
Br	-30.6	Num Br	2	Diamagnetism of Br	-61.2
N	-5.57	Num N	4	Diamagnetism of N	-22.28
O	-4.61	Num O	4	Diamagnetism of O	-18.44
				∑nAχA	-345.7

Constitutive Corrections

Benzene ring	-1.4	Num of benzene ring	2	Diamagnetism of Benzene ring	-2.8
Ar-C≡C-Ar	3.85	Num of Ar-C≡C-Ar	1	Diamagnetism of Ar-C≡C-Ar	3.85
C=N	8.15	Num of C=N	2	Diamagnetism of C=N	16.3
Ar-Br	-3.45	Num of Ar-Br	2	Diamagnetism of Ar-Br	-6.9
				∑ λ	10.45
		∑nAχA + ∑ λ=	**-335.25**		

MAMNN

Pascal's constants

C ring	-6.24	Num C ring	12	Diamagnetism of C ring	-74.88
C	-6	Num C	17	Diamagnetism of C	-102
H	-2.43	Num H	33	Diamagnetism of H	-80.19
N	-5.57	Num N	5	Diamagnetism of N	-27.85
O	-4.61	Num O	5	Diamagnetism of O	-23.05
				∑nAχA	-307.97

Constitutive Corrections

Benzene ring	-1.4	Num of benzene ring	2	Diamagnetism of Benzene ring	-2.8
Ar-C≡C-Ar	3.85	Num of Ar-C≡C-Ar	1	Diamagnetism of Ar-C≡C-Ar	3.85
C=N	8.15	Num of C=N	2	Diamagnetism of C=N	16.3
Ar-C(=O)NH2	-1.5	Num of Ar-C(=O)NH2	1	Diamagnetism of C(=O)NH2	-1.5
C(=O)NH2 bond	-3.5	Num of C(=O)NH2 bond	1	Diamagnetism of C(=O)NH2 bond	-3.5
				∑ λ	12.35
		∑nAχA + ∑ λ=	**-295.6**		

MNO2NN

Pascal's constants

C ring	-6.24	Num C ring	12	Diamagnetism of C ring	-74.88
C	-6	Num C	16	Diamagnetism of C	-96
H	-2.43	Num H	31	Diamagnetism of H	-75.33
N	-5.57	Num N	5	Diamagnetism of N	-27.85
O	-4.61	Num O	6	Diamagnetism of O	-27.66
				∑nAχA	-301.72

Constitutive Corrections

Benzene ring	-1.4	Num of benzene ring	2	Diamagnetism of Benzene ring	-2.8
Ar-C≡C-Ar	3.85	Num of Ar-C≡C-Ar	1	Diamagnetism of Ar-C≡C-Ar	3.85
C=N	8.15	Num of C=N	2	Diamagnetism of C=N	16.3
Ar-NO2	-0.5	Num of Ar-NO2	1	Diamagnetism of Ar-NO2	-0.5
NO2 bond	-2	Num of NO2 bond	1	Diamagnetism of NO2 bond	-2
				∑ λ	14.85
		∑nAχA + ∑ λ=	**-286.9**		

OMeBrNN

Pascal's constants

C ring	-6.24	Num C ring	12	Diamagnetism of C ring	-74.88
C	-6	Num C	17	Diamagnetism of C	-102
H	-2.43	Num H	33	Diamagnetism of H	-80.19
Br	-30.6	Num Br	1	Diamagnetism of Br	-30.6
N	-5.57	Num N	4	Diamagnetism of N	-22.28
O	-4.61	Num O	5	Diamagnetism of O	-23.05
				∑nAχA	-333

Constitutive Corrections

Benzene ring	-1.4	Num of benzene ring	2	Diamagnetism of Benzene ring	-2.8
Ar-C≡C-Ar	3.85	Num of Ar-C≡C-Ar	1	Diamagnetism of Ar-C≡C-Ar	3.85
C=N	8.15	Num of C=N	2	Diamagnetism of C=N	16.3
Ar-Br	-3.45	Num of Ar-Br	1	Diamagnetism of Ar-Br	-3.45
Ar-OMe	-1	Num of Ar-Ome	1	Diamagnetism of Ar-Ome	-1
				∑ λ	12.9
		∑nAχA + ∑ λ=	**-320.1**		

TMPNN

Pascal's constants

C ring	-6.24	Num C ring	16	Diamagnetism of C ring	-99.84
C	-6	Num C	18	Diamagnetism of C	-108
H	-2.43	Num H	40	Diamagnetism of H	-97.2
N	-5.57	Num N	4	Diamagnetism of N	-22.28
O	-4.61	Num O	8	Diamagnetism of O	-36.88

				∑nAχA	-364.2
Constitutive Corrections					
C share by 2 rings	-3.07	Num binuclear C	6	Diamagnetism of binuclear C	-18.42
Ar-OR	-1	Num of Ar-OR	4	Diamagnetism of Ar-OR	-4
C=N	8.15	Num of C=N	2	Diamagnetism of C=N	16.3
				∑ λ	-6.12
		∑nAχA + ∑ λ=	**-370.32**		

TMPMIX

Pascal's constants					
C ring	-6.24	Num C ring	16	Diamagnetism of C ring	-99.84
C	-6	Num C	18	Diamagnetism of C	-108
H	-2.43	Num H	40	Diamagnetism of H	-97.2
N	-5.57	Num N	4	Diamagnetism of N	-22.28
O	-4.61	Num O	7	Diamagnetism of O	-32.27
				∑nAχA	-359.59
Constitutive Corrections					
C share by 2 rings	-3.07	Num binuclear C	6	Diamagnetism of binuclear C	-18.42
Ar-OR	-1	Num of Ar-OR	4	Diamagnetism of Ar-OR	-4
C=N	8.15	Num of C=N	2	Diamagnetism of C=N	16.3
				∑ λ	-6.12
		∑nAχA + ∑ λ=	**-365.71**		

TMPIN

Pascal's constants					
C ring	-6.24	Num C ring	16	Diamagnetism of C ring	-99.84
C	-6	Num C	18	Diamagnetism of C	-108

H	-2.43	Num H	40	Diamagnetism of H	-97.2
N	-5.57	Num N	4	Diamagnetism of N	-22.28
O	-4.61	Num O	6	Diamagnetism of O	-27.66
				∑nAχA	-354.98
Constitutive Corrections					
C share by 2 rings	-3.07	Num binuclear C	6	Diamagnetism of binuclear C	-18.42
Ar-OR	-1	Num of Ar-OR	4	Diamagnetism of Ar-OR	-4
C=N	8.15	Num of C=N	2	Diamagnetism of C=N	16.3
				∑ λ	-6.12
		∑nAχA + ∑ λ=	**-361.1**		

TMPNO

Pascal's constants					
C ring	-6.24	Num C ring	16	Diamagnetism of C ring	-99.84
C	-6	Num C	12	Diamagnetism of C	-72
H	-2.43	Num H	34	Diamagnetism of H	-82.62
N	-5.57	Num N	2	Diamagnetism of N	-11.14
O	-4.61	Num O	6	Diamagnetism of O	-27.66
				∑nAχA	-293.26
Constitutive Corrections					
C share by 2 rings	-3.07	Num binuclear C	6	Diamagnetism of binuclear C	-18.42
Ar-OR	-1	Num of Ar-OR	4	Diamagnetism of Ar-OR	-4
				∑ λ	-22.42
		∑nAχA + ∑ λ=	**-315.68**		

List of Publications

(1) **Ravat, P**.; Ito, Y.; Gorelik, E.; Enkelmann, V.; Baumgarten, M., Tetramethoxypyrene-Based Biradical Donors with Tunable Physical and Magnetic Properties. **Org. Lett. 2013, *15*, 4280-4283**.

(2) **Ravat, P**.; Teki, Y.; Ito, Y.; Gorelik, E.; Baumgarten, M., Breaking the Semi-Quinoid Structure: Spin-Switching from Strongly Coupled Singlet to Polarized Triplet State. ***Chem. Eur. J.*** **2014, *20*, 12041-12045.**

(3) Berger, R.; Giannakopoulos, A; **Ravat, P**.; Wagner, M.; Beljonne, D.; Feng, X.; Müllen, K., Synthesis of Nitrogen Doped ZigZag-Edge Peripheries: Dibenzo-9a-azaphenalene as Repeating Unit ***Angew. Chem. Int. Ed.*****, 2014, *53*, 10520-10524.**

(4) **Ravat, P**.; Marszalek, T.; Pisula, W.; Müllen, K.; Baumgarten, M., Positive Magneto-LC Effect in Conjugated Spin-bearing Hexabenzocoronene. ***J. Am. Chem. Soc.*** **2014, *136*, 12860-12863.**

(5) **Ravat, P**.; Borozdina, Y.; Ito, Y.; Enkelmann, V.; Baumgarten, M., Crystal Engineering of Tolane Bridged Nitronyl Nitroxide Biradicals: Candidates for Quantum Magnets**. *Cryst. Growth Des.*** **2014, DOI: 10.1021/cg5010787.**

(6) **Ravat, P**.; Baumgarten, M., "Tschitschibabin type Biradicals": Benzenoid or Quinoid? (submitted to **PCCP, 2014**).

Curriculum Vitae

Personal Details

Name:	Prince Ravat
E-mail:	prince.ravat@gmail.com
Date of birth:	5th June, 1986
Place of birth:	Vadodara, India
Nationality:	Indian
Marital status:	Single

Education

May 2011 – August 2014	PhD studies, Max Planck Institute for Polymer Research Mainz Research adviser: Prof. Dr. Martin Baumgarten Group Director: Prof. Klaus Müllen
July 2008 – April 2011	Research Fellow, Supramolecular Chemistry, National Chemical Laboratory, Pune, India
August 2006 – May 2008	M.Sc. in Organic Chemistry, Department of Chemistry, M.S.University of Baroda, India
July 2003 – May 2006	B.Sc. in Chemistry, Department of Chemistry, M.S.University of Baroda, India

Awards and Fellowships

July 2014	**Best Poster Award**- International Conference on Molecule-Based Magnets (ICMM 2014), Saint Petersburg, Russia.
May 2011 – August 2014	**PhD Studentship**, Max-Planck Institute for Polymer Research, Germany.
March 2010	**Carl Storm International Diversity Fellowship Award**, Gordon Research Conference (Crystal Engineering), United States.
March 2008	**Graduate Aptitude Test in Engineering (GATE)-2008**, Department of secondary and higher education, Ministry of Human Resource Development, Government of India.
December 2007	**Junior Research Fellowship**, Council of Scientific & Industrial Research, New Delhi-110012, India.

Acknowledgements

First of all I would like to thank Prof. Dr. Martin Baumgarten for giving me an opportunity to work in his research group on exciting and challenging research topic on organic biradicals. I sincerely appreciate his continuous and kind support, helpful and inspiring suggestions, and his trust in my research work.

Prof. Dr. Klaus Müllen is gratefully acknowledged for the permission to join his unique research group and important scientific suggestions on quarterly reports.

Many thanks to all the members of the groups of Prof. Dr. Klaus Müllen for the exciting discussions, critical advices, encouragements, inspirations, a lot of fun, uncountable nice evenings, and the best working environment.

I would like to next acknowledge all the cooperation partners in the Max Planck Institute for Polymer Research, Mainz inside and outside our research group for great support and fruitful collaboration works, which could never been done without their involvements:

Dr. Yulia Borozdina for prior developments of the biradical project and her helpful guidance and kind encouragements when I started the project.

Dr. Yoshikazu Ito for SQUID measurements.

Dr. Volker Enkelmann for the single crystal X-ray measurements.

Dr. Wojciech Pisula, Dr. Tomasz Marszalek, and Dr. Sreenivasa Reddy Puniredd for the X-ray analysis.

Khaled Parvez for fabrications of FET devices.

Dr. Rongjin Li for fabrications of Memory device.

Dr. Zhong-Shuai Wu for the collaboration on ongoing project on Organic radical polymers for energy storage devices.

Jutta Schnee for synthesizing the tetramethoxy pyrene, and diiodo-

tetramethoxy pyrene, and for state fluorescence measurements.

Dr. Manfred Wagner for NMR analysis.

Stefan Spang for NMR measurement at low temperatures.

Dr. Frédéric Laquai, and Dominik Gehrig for time-resolved transient absorption analysis of the pyrene based biradical.

My sincere thanks also go to cooperation partners outside the MPIP for the exciting and fruitful collaboration works and discussions:

Prof. Yoshio Teki (Division of Molecular Material Science, Graduate School of Science, Osaka City University, Japan) for TREPR measurements and analysis.

Dr. Elena Gorelik (Johannes-Gutenberg-University Mainz, Germany) for some DFT calculations using ORCA software.

Prof. Gerd Schönhense and Alisa Chernenkaya (Johannes-Gutenberg-University Mainz, Germany) for UHV deposition of biradicals on silicon substrates.

My special thanks to Prof. Shubhangi Soman (M.S. University of Baroda, Vadodara) for her constant support and encouragement since my master studies.

Finally, I would like to thank my family and friends for their continuous and considerate support and understanding during my PhD studies.

Many thanks also to everybody I might have unintentionally forgotten to mention here.